Modeling microsegregation and nonmetallic inclusion formation based on thermodynamic databases

A thesis submitted in partial fulfillment of the requirements for the degree of a Doctoral of Metallurgical and Mining Sciences at the Montanuniversität Leoben

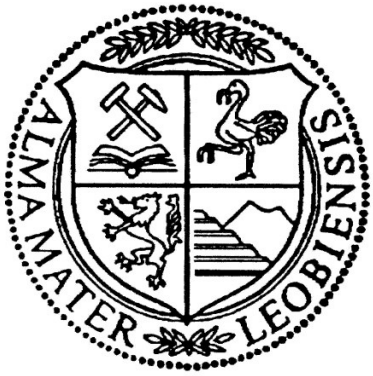

Presented by:

Dali You

Chair of Ferrous Metallurgy

Leoben, December 2016

Preface

First of all, I would like to express my special thanks to Ao. Univ. Prof. Dr. Christian Bernhard for your patient guidance and continuous taking care in the last three years. The regular discussions with you broaden my horizon and offer the clear advance direction to the research work. Your valuable suggests and comments on the work promote the improvements and our successful publications. The 'step by step' theory taught from you not only helps me firmly precede the research topic but also benefits my life. Following your encouragement, I learnt that fresh air outside of the office rather than longtime sitting lead to high efficiency.

I would like to thank Univ. Prof. Dr. Adreas Ludwig: reviews the thesis and provides the professional comments, constructive suggestions during the thesis preparation. I am grateful to your kind and detailed introduction on the aspects related to numerical simulation.

The deep gratitude goes to Ass. Prof. Dr. Susanne Michelic whom I regard as my 'big sister'. Your sustaining assistance and encouragement contribute the smooth and successful accomplishment of the present dissertation. It is grateful that we can publish our nice results in the journals under your guidance. Together with the invaluable advice on the scientific topics, you show me a nice model on how to project the work schedule, as well teach me how to write a 'Love Letter' to others.

My sincere thanks are due to Gerhard Wieser for introducing and always supporting me on modeling and coding; for your constructive suggests on the research topics; for your considering my both academic and daily life; for sharing your stories with me and teaching me life lessons; for listening to me and encouraging me.

I am grateful for the financial support from the Federal Ministry for Transport, Innovation and Technology (bmvit) and the Austrian Science Fund (FWF) [TRP 266-N19]. I sincerely acknowledge the laboratories at voestalpine Stahl GmbH in Linz for assistance in the analysis of samples.

I would like to thank the Chair of Ferrous Metallurgy and all collogues I spend time with. Thank you very much, Univ. Prof. Dr. Johannes Schenk, for your help on my study application and further consideration on my life in Leoben. To Denise, many thanks for your assistance at my beginning period of both life and research, and further help on exploring the nonmetallic inclusion world. I am grateful to Gregor (A) and Michael (B) for introducing me the SSCT experiments and post techniques. Thanks Peter for the meaningful suggests on microsegregation and phase transformation programming. To Michael (R), thanks for your important instruction

on the thesis preparing and sharing your experiences. I also would like to say thank you to Lukas (S) and Matthias (T) for your kindly consideration and offering me the chance to practice my German. For Toni and Philip, it is grateful and enjoyable to discuss with you on the studies, works and life. Again, I wish to express my gratitude to the professors, sectaries, scientific staffs, technicians, cleaners and student staffs in the chair who contribute my colorful academic and daily life in Leoben.

Special thanks go to Prof. Jianhua Liu who promotes my study in Leoben and continutes to support me. I also would like to thank the associate professors in USTB, Heng Cui, HuajieWu, Feng Yue, who offer me kind suggests of the future academic career. I am grateful to the Chinese families and students who live in Leoben, help and accompany me in the past three years. To Maximilian Erker, thank you very much, it is really enjoyable and healthy to join your football and run training. Many thanks to my friends, Zhiqiang Gao, Shilong Zhang, for listening to me and sharing with me on almost everything. To Fangfei and Hong, thank you very much for your encouragement and suggests on my work and life.

Finally, I want to deeply thank my parents for your forever support and care me. As the floating boat in the sea, whenever and whatever, you offer me the happy harbor.

The journey is the reward, I am grateful to meet you.

Affidavit

I declare in lieu of oath that I wrote this thesis and performed the associated research myself using only literature cited in this volume.

……

Dali You

Leoben, December 2016

Abstract

English Abstract

In steelmaking, the reaction of alloying elements with dissolved oxygen, sulfur and nitrogen involves the formation of non-metallic inclusions. Inclusions are usually detrimental for product properties such as fatigue resistance or surface appearance. Hence, steelmakers strive to minimize the number and size of inclusions or to reduce their harmful effect by modifying their composition or shape. More recently, researchers have determined the positive effect of fine dispersed inclusions as grain refiners or heterogeneous nuclei. However, inclusions affect the properties of steel, and adjusting their size, shape and chemistry is crucial to producing advanced steel grades.

The present thesis focuses on the computational solution of inclusion kinetics. The thermodynamic library-ChemApp is applied to connect the solution of kinetics in a FORTRAN source code and the thermodynamic databases in FactSage. Kinetics comprises not only the enrichment of solute elements in the solidification process, but also the nucleation and growth of particles. Ohnaka´s analytical microsegregation equation is solved numerically with local partition coefficients coming from thermodynamic databases. The homogeneous nucleation of particles and their subsequent growth is considered; thus, the simulation of single-phase inclusion formation becomes possible. In the present work, manganese sulfides were selected for experimental validation of the modeling results.

By incorporating the core concept of the single-phase inclusion model, the competitive formation and dissolution of multi-phase inclusions during cooling and solidification is also modeled. The influences of cooling rate and initial composition on the evolution of the mass fraction of complex oxides, their size, chemistry and number density were investigated in calculations and experiments.

The accordance of the results for single-phase inclusions is excellent and still remarkably significant for multi-phase inclusions. In the future, the model will be used to predict experimental conditions for the reliable adjustment of inclusions in ongoing research projects regarding inclusion metallurgy.

Deutsche Kurzfassung

In der Stahlherstellung kommt es bedingt durch Reaktionen von Legierungselementen mit gelöstem Sauerstoff, Schwefel und Stickstoff zur Bildung von nichtmetallischen Einschlüssen.

Diese beeinflussen in der Regel die Werkstoffeigenschaften, wie etwa Dauerfestigkeit oder Oberflächenbeschaffenheit, negativ. Ziel der Stahlhersteller ist es daher, sowohl Anzahl als auch Größe von nichtmetallischen Einschlüssen möglichst gering zu halten oder deren schädliche Wirkung durch gezielte Modifikation von Zusammensetzung oder Gestalt zu minimieren. Zunehmend bestätigen Forschungsergebnisse aber auch einen möglichen positiven Einfluss fein verteilter Einschlüsse als Kornfeinungsmittel oder heterogene Keimstellen. Unabhängig vom konkreten Anwendungsfall, nimmt die gezielte Einstellung von Einschlüssen hinsichtlich Größe, Form und Zusammensetzung eine Schlüsselrolle in der Herstellung hochqualitativer Stählen ein.

Die vorliegende Arbeit konzentriert sich auf die rechnergestützte Lösung von Fragen der Einschlusskinetik. Unter Anwendung der thermodynamischen Bibliothek ChemApp wird ein Fortran Quellcode für kinetische Betrachtungen mit den thermodynamischen Datenbanken von FactSage verknüpft. Die kinetischen Berechnungen beinhalten die Anreicherung von gelösten Elementen während der Erstarrung als auch Keimbildung und Partikelwachstum. Mikroseigerungsberechnungen erfolgen numerisch auf Basis der analytischen Lösung von Ohnaka und unter Einbeziehung lokaler Verteilungskoeffizienten. Die Berücksichtigung von homogener Keimbildung und anschließendem Partikelwachstum ermöglicht die Simulation der Bildung von einphasigen Einschlüssen. In der vorliegenden Arbeit wurden Mangansulfide für die experimentelle Validierung der Simulationsergebnisse herangezogen.

Basierend auf dem Simulationskonzept für einphasige Einschlüsse, erlaubt das entwickelte Modell auch die Berechnung konkurrierender Vorgänge der Bildung und Auflösung von mehrphasigen Einschlüssen während Abkühlung und Erstarrung. Die Einflüsse von Kühlrate und Stahlzusammensetzung auf die Entwicklung des Massenanteils komplexer Oxide als auch deren Größe, Zusammensetzung und Anzahl können experimentell sowie numerisch untersucht werden.

Ein Vergleich zwischen Experiment und Simulation zeigt für einphasige Einschlüsse eine ausgezeichnete Übereinstimmung. Auch betreffend mehrphasiger Einschlüsse sind die Ergebnisse äußerst aussagekräftig. Das entwickelte Modell soll zukünftig für die Konzeption experimenteller Bedingungen zur gezielten Adaptierung von nichtmetallischen Einschlüssen hinsichtlich verschiedener Fragestellungen aus dem Themengebiet ‘Inclusion Metallurgy’ verwendet werden.

Contents

1 Introduction

Steel cleanness is a measurable value comprising the size, number, morphology and shape of nonmetallic inclusions in steel. The cleanness demand of certain steel grades may widely vary: For example, concrete steels are more or less insensitive against inclusions whereas purity is the most important quality feature of roller bearing steels.

Nonmetallic inclusions are generally considered to be detrimental to the properties of steels such as ductility, fatigue, strength and corrosion. In the past, studies have mainly focused on the control and removal of nonmetallic inclusions through the further development of steelmaking technologies. In parallel, new tools such as computational thermodynamics or higher-sophisticated material analysis methods have became available; consequently, the knowledge of relationships between nonmetallic inclusions and microstructure and mechanical properties of steels has increased [1]. In the 1980s, Takamura and Mizoguchi [2,3] introduced the concept of 'oxides metallurgy' in steels. It was illustrated that the finely dispersed oxides could act as heterogeneous nuclei for other – and less harmful – precipitates and for intragranular (acicular) ferrite which may contribute to the improved mechanical properties of steel. This topic was further extended to the 'inclusion engineering' concept, which is explained in Figure 1.1: Key objectives, on the one hand, include modifying harmful inclusions into harmless particles and, on the other hand, to producing inclusions with adjusted composition, structure, size and number density to optimize the microstructure [4–6].

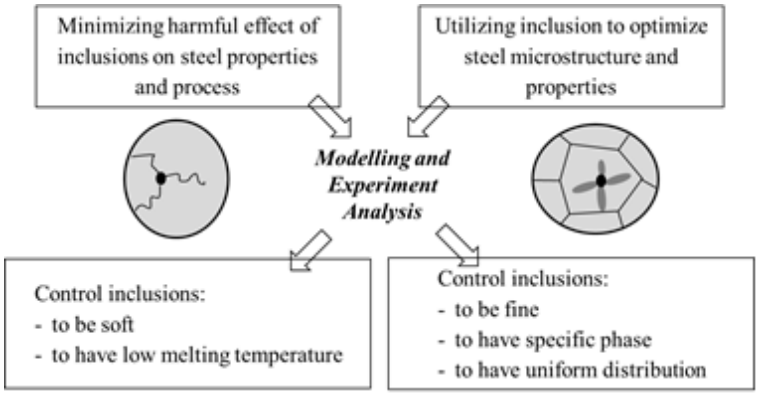

Figure 1.1. Concept of inclusion engineering [4].

In steelmaking, the first population of inclusions forms during deoxidation. The high content of dissolved oxygen is precipitated as oxide by the addition of oxygen affine elements, such as Aluminum, Manganese or Silicon. This process is well understood and the formed inclusions can be partly separated later into the ladle slag. The control of fluid flow and slag compositions during ladle treatment are important. The residual oxide inclusions and the inclusions generated

in the casting process – these are also sulfides and nitrides – will mostly remain in the solid steel. These inclusions are usually small but may also play a significant role in determining the quality of the steel products. It is therefore important to study inclusion formation during the cooling and solidification process.

The online control of steel cleanness is still extremely difficult. The methods for the analysis of micro-inclusions in steel samples are time consuming whereas the methods for the online inclusion detection (e.g. OES/PDA) are still unreliable. The increasing development of computer science and computational thermodynamics offers a powerful and valuable tool to simulate metallurgical processes. By combining thermodynamic databases and the related metallurgical model, the aforementioned inclusion features, such as the reaction with liquid steel as well as the chemical composition, size and number density of the formed inclusions can be predicted and investigated. These properties of nonmetallic inclusions can be controlled by adjusting the steel composition and thermal history based on the calculations. Consequently, this approach is applied to enhance the qualities of steel products through reducing the negative effects of inclusions and utilizing them to optimize microstructure.

Concentrations of the initial concentration of solute elements in the steel are regarded as fundamental inputs for simulating inclusion formation during cooling and solidification. In the solidification process, under the assumption of non-equilibrium, concentration gradients of solutes are generated in the solid and liquid phase. These uneven distributions of solutes contribute to the formation of constitutional under cooling and dendritic structure, and the solutes segregate in the interdendritic liquid. According to the length scale for back diffusion, this is termed as microsegregation. While microsegregation is a consequence of non-equilibrium processes, local equilibrium at the solid/liquid interface is always assumed. Thermodynamic equilibrium data is thus necessary for predicting the concentrations. The enriched concentrations can lead to the transformation of pre-existing inclusions and the nucleation of new precipitations. In addition, this phenomenon results in the formation of defects during the casting process (e.g. hot tearing) and negatively affects product quality (inhomogeneous microstructure). Hence, it is not surprising that this research topic has already been intensively investigated by several research groups in the past [7–12]. For microsegragtion predictions, analytical models have been widely applied. In most of the published models, several important aspects are considered in simplified ways but sometimes with limited equilibrium data: most partition coefficients are calculated from binary or ternary systems and are assumed as temperature- and concentration-independent; diffusion coefficients of solutes in solid are assumed to be constant over temperature; liquidus temperatures are mainly calculated according to the Fe-C binary phase diagram; and precipitations are estimated using single empirical Gibbs energy equations. These limitations leave further room for developing the analytical models.

Computational thermodynamics can provide comprehensive equilibrium calculations. Coupling microsegregation models with thermodynamic databases is an appropriated approach to improve the quality of microsegregation calculations and to consider inclusion formation during solidification. Yamada et al. [13] coupled the Clyne-Kurz microsegregation model [12] with thermodynamics for the formation of oxide phases and CaS in liquid steel. Subsequently, several similar coupled models have been developed [14–18]. Nevertheless, the full coupling of the solidification kinetics and the thermodynamics for inclusion formation as well as the quality of the underlying thermodynamic data can help to further improve the reliability of the results.

An additional method to improve the information is to consider the kinetics of inclusion nucleation and growth. While thermodynamic equilibrium defines the stability and formation driving forces of inclusion, kinetics determines the nucleation and growth speed. J. Lemann et al. [19–21] reported a model accounting microsegregation and the formation kinetics of single-phase nitrides and oxides. However, the complex deoxidation practice and the combination with Ca-treatment of the liquid steel results mostly in complex, multiphase inclusions. The prediction of these types of inclusions demands the consideration of heterogeneous nucleation. This is a highly challenging endeavor, not only due to the mathematical formulation and the solving procedure, but also due to the need for not yet available data, such as interfacial tensions between inclusion/inclusion or inclusion/steel.

The aim of the present work is to advance the fully coupled simulation of microsegregation and inclusion formation during cooling and the solidification process. The core concept of the current work is coupling the metallurgical models with thermodynamic databases to obtain more reliable predictions. The thermodynamic library ChemApp, commercial software FactSage and FORTRAN as programming language are applied during the modeling process. Fundamentally a microsegregation model with local partition coefficients is proposed based on Ohnaka´s model [10]. The microsegregation model is also coupled with nucleation and growth kinetics of single-phase inclusions in the solidification process. By incorporating the features of the single-phase inclusion model, a comprehensive model simultaneously considering thermodynamics and kinetics of various inclusions is finally developed. In the comprehensive model, a sub-model on multi-phase-inclusions formation thermodynamics is included which is also a powerful tool when independently applied.

In the course of this thesis, Chapter 2 describes the fundamental concepts and modeling works on microsegregation, and the typical and widely applied microsegregation models are briefly reviewed. In Chapter 3, the inclusion formation in liquid steel is presented from the perspectives of both thermodynamics and kinetics. In this context, inclusion origins, classifications and the roles on steel properties are introduced as the primary aspect. With the theoretical background, the representative models on inclusion formation in liquid steel are concisely introduced. Based

on the literature study in Chapter 2 and 3, the structure of the current modeling work is depicted in Chapter 4. The progressive modeling on the microsegregation and inclusion formation during cooling and solidification process is precisely explained in Chapter 4, and systematic parameter studies are also performed for the proposed models. Chapter 5 offers the experimental and calculated evaluations on the models in a step-wise manner, and the calculations using the models for typical cases are discussed. Finally, Chapter 6 summarizes the whole work and provides suggests for future studies.

2 Microsegregation

Microsegregation is an essential aspect when dealing with solidification, which inclusion formation is not an exception. In this chapter, the fundamental concepts on microsegregation including solute partitioning, diffusion and dendritic structure are introduced. In addition, the importance of microsegregation on the following metallurgical process and steel properties are summarized. Mathematical models offer powerful tools for analyzing the solute enrichments in the solidification process, and the widely applied analytical solutions are introduced based on these models. Compared with numerical methods, the analytical solutions are easy to handle and to couple so they will be the foundation for this work.

2.1 Fundamentals of microsegregation

A dendritic structure is observed in etched alloy samples as shown in the Figure 2.1. The skeleton of the dendrites illustrates the difference of solute concentrations which exist within the dendrites. These various concentrations on the dendritic scale are caused by the solute enrichment at the solid/liquid interface and the solute redistribution after solidification in a non-equilibrium state. This phenomenon is termed as microsegregation. Microsegregation of an element in an alloy mainly depends on the following factors: equilibrium partition coefficient, diffusion coefficient, dendrite arm spacing and cooling rate.

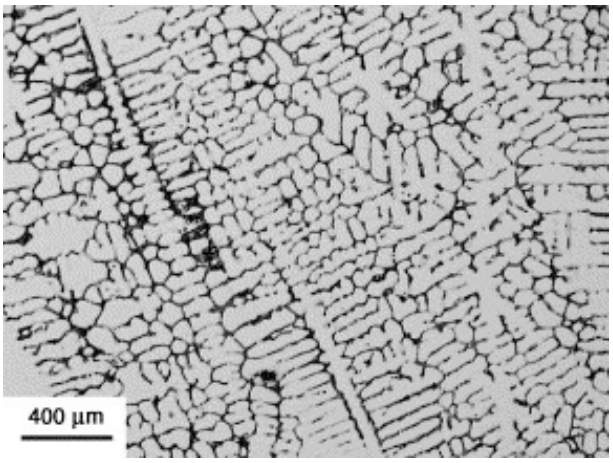

Figure 2.1. A dendritic structure for a cast steel with 0.4% carbon [22].

2.1.1 Concepts on microsegregation

2.1.1.1 Solute partitioning

Due to the differences of the solubility of elements in the solid and liquid matrix, the solutes will redistribute at the solid/liquid interface. For technical solidification processes, the existence of a local equilibrium at the solid/liquid interface is assumed. The interfacial equilibrium is not

valid in the case of rapid solidification (the advancing speed of the solidification front is larger than 1 cm/s) which is out of the range of this work. The enrichment of solutes at the interface is described by the equilibrium partition coefficient (k) which is the ratio of interfacial concentration in solid (C_S^*) and liquid (C_L^*), as given in Eq. (2.1). Note that the concentrations of solutes are all referred to 1% dilute solution in this work. Those elements with equilibrium partition coefficients smaller than unity are enriched in the residual liquid, which is known as positive segregation. In contrast, the elements with equilibrium partition coefficients larger than unity diffuse from liquid to solid during solidification, which is called negative segregation. Most elements in the steels show positive segregation, while only few elements such as aluminum in specific high alloy steels show negative segregation.

$$k = \frac{C_S^*}{C_L^*} \tag{2.1}$$

Since the partition coefficient is defined under the assumption of thermodynamic equilibrium, at least the following two thermodynamic approaches can be applied to determine the partition coefficients [23]: the simplest and most straightforward method is using a phase diagram. For instance, Figure 2.2 displays the schematic of calculating the partition coefficient from a binary phase diagram. In the solidification process, at solid fraction (f_s), the concentrations in both solid (α) and liquid (L) phases can be obtained from the solidus and liquidus slope. The simplest approach is to assume the solidus and liquidus lines as straight (solid lines in Fig. 2.2). Then, the equilibrium partition coefficient becomes constant and independent from temperature. The values of the constant partition coefficients are shown Section 4.3.3. This makes the calculation with analytical models much easier. For most Fe-X-binary systems, however, the solidus and liquidus slopes are the curves represented by the dash-dot line in Figure 2.2. In these curves, the partition coefficients are temperature dependent. A simple analytical model hence cannot handle a temperature dependent partition coefficient. In multi-components systems, the situation is even more delicate. The partition coefficient is not only temperature dependent, but also depends on the concentration of other solute elements. This makes the simple determination from binary systems impossible and higher developed tools for computational thermodynamics are needed.

The second technique is the deriving partition coefficient from the fact that the chemical potentials of solute in solid and liquid phase are equal. Eq. (2.2) gives the general expression of the chemical potential (μ_i) for solute i in one phase. By applying Eq. (2.2) to both solid and liquid phases and combining them, Eq. (2.3) is achieved for evaluating the partition coefficient of the solute. Eq. (2.3) shows that partition coefficient relies on compositions and temperature. The activity coefficients and chemical potentials in solid and liquid phases are needed for the determining partition coefficient using this approach.

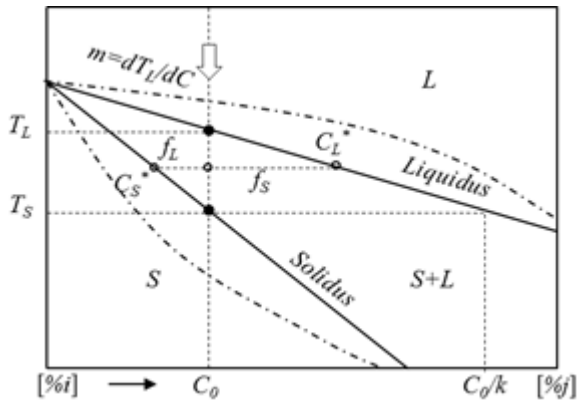

Figure 2.2. Schematic of the partition coefficient calculation using binary phase diagram.

$$\mu_i = \mu_i^0 + RTln(f_i C_i) \tag{2.2}$$

$$k_i = \frac{f_i^L}{f_i^S} exp[(\mu_i^{0,S} - \mu_i^{0,L})/RT] \tag{2.3}$$

where μ_i^0 is the standard chemical potential of the solute i, R is the gas constant, T is the temperature, γ_i is the activity coefficient, C_i is the concentration of the solute, and superscripts L and S represent liquid and solid, respectively.

2.1.1.2 Dendritic structure

The discussion in the last section shows that the concentrations of solutes considerably increase ahead of solidification interface when the partition coefficients lower than unity. As displayed in Figure 2.3, this increase (ΔC_0) will result in the decrease of the local liquidus temperature (ΔT_0) and the formation of the constitutional undercooling layer (the shade zone). Within the constitutional undercooling zone, the real liquidus temperature (T_L) gradually decreases approaching to the solid/liquid interface. This trend is directly corresponding to the enrichment degree of the solutes. T_q is the temperature after heat flux removing, which is lower than liquidus temperature and the driving force of the subsequent solidification.

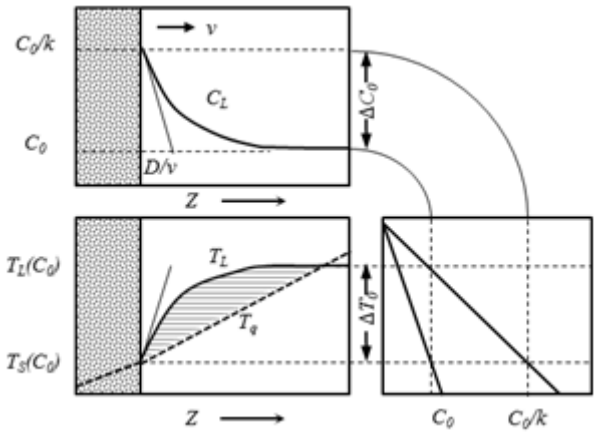

Figure 2.3. Constitutional undercooling in alloys [24].

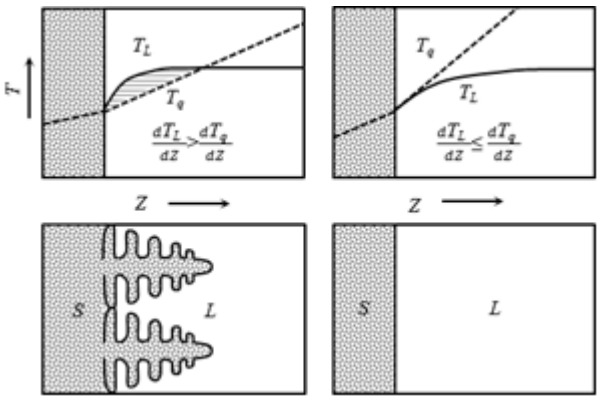

(a) (b)

Figure 2.4. Condition for (a) no-constitutional undercooling (b) constitutional undercooling at the Solid/Liquid interface and the resultant structures [24].

Solute segregation does not generally result in a dendritic morphology. Figure 2.4 displays the context between constitutional undercooling and resultant structures. The existence of a constitutionally undercooled zone depends on the temperature gradient at the solidification interface which is imposed by the heat extraction (dT_q/dZ) and the liquidus temperature change in the solidification direction (dT_L/dZ). Figure 2.4 (a) shows that when $dT_L/dZ > dT_q/dZ$, the local constitutional undercooling generates and further promotes solid dendrites. Subsequently, the further enriched solutes lead to an even steeper concentration gradient and increasrd liquidus temperature slope. Consequently, the dendrites growth will be stabilized. In the direction perpendicular to the primary dendrites, the solute enrichment and constitutional undercooling induces the formation of secondary dendrites. In contrast to the dendritic structure, when $dT_L/dZ \leq dT_q/dZ$, the solidification remains in the planar morphology as described in Figure 2.4 (b).

Secondary Dendrite Arm Spacing (SDAS) is considered as the objective region in most studies on microsegregation. Both theoretical and empirical determinations of the secondary dendrite arm spacing are directly related to the solidification variables. Linking with the local solidification time, Feurer and Wunderlin [25] proposed a model for estimating SDAS as given in Eq. (2.4):

$$\lambda_2 = 5.5(M_c t_f)^{1/3} \tag{2.4}$$

$$M_c = \frac{\Gamma_g D_L ln\left(\frac{C_L}{C_0}\right)}{m_l(1-k)(C_0 - C_L)} \tag{2.5}$$

where λ_2 is the secondary dendrite arm spacing, t_f is the local solidification time, the pre-exponent '5.5' is a numerical factor, M_c is coarsening parameter calculated with Eq. (2.5), Γ_g is the Gibbs-Thomson coefficient, D is the diffusion coefficient in the liquid, C_L and C_0 are the

liquid and initial concentrations, m_l is the liquidus slope, and k is the equilibrium partition coefficient.

This kind of theoretical model is developed based on the concept of Fick´s law and the Gibbs-Thomson equation as well as the coarsening models [26–28]. In the following, with different coarsening models, similar formulas for calculating SDAS were reported [29,30]. On the evaluation of the SDAS in steels, the carbon content is also a factor according to the experimental results [31,32]. Considering the influence of initial carbon content ($[\%C]$), Pierer and Bernhard [28] suggested an SDAS equation through fitting the local solidification time dependent model with the experimental results.

In addition to the local solidification time, cooling rate is another parameter used to define SDAS. The general form of the equations is given in Eq. (2.6). Bealy and Thomas [32] evaluated SDAS as a function of cooling rate when the initial carbon content is lower that 0.53%. This function was fitted to the former reported experimental results. In addition, Won and Thomas [33] proposed an SDAS equation accounting to the change of initial carbon concentration through fitting a wide range of research results.

$$\lambda_2 = A(R_C)^B \tag{2.6}$$

where parameters A and B are decided by experimental data and R_C is the cooling rate.

2.1.1.3 Solute back diffusion

Solute diffusivity is another fundamental aspect to the microsegregation. According to Fick´s second law given in the Eq. (2.7), the concentration change of solute ($\partial C/\partial t$) is proportional to the diffusivity (D) and concentration gradient. Based on the microsegregation as described in the Figure 2.5, the solute enrichments at the solid/liquid interface lead to a concentration gradient and solute diffusion. Solute diffusion can further alter concentration distribution.

$$\frac{\partial C}{\partial t} = D\frac{\partial^2 C}{\partial z^2} \tag{2.7}$$

Eq. (2.8) provides the expression of Fourier number (Fo) which characterizes the solute back diffusion involving microsegregation. In the equation, D_S is the diffusion coefficient in the solid and the diffusion length (l) is half of SDAS. This dimensionless parameter also can be regarded as the ratio of solidification time and diffusion time ($Fo = t_f/t_{diffusion}$). When $Fo \gg 1$, solute diffusion is complete; in other words, solutes are well mixed with the matrix and there are no concentration gradients at the solidification interface; When $Fo \ll 1$, solute diffusion is negligible; in other words, concentration gradients persist and become steeper. These two situations of the diffusion are common assumptions in modeling studies on microsegregation. In the final solid steel, the solutes with higher diffusivity have less segregation while the ones with lower diffusivity display stronger segregation.

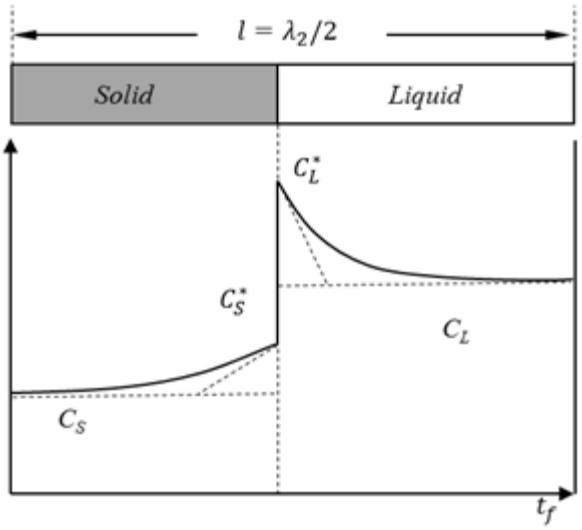

Figure 2.5 Concentration distributions of solutes during the solidification process [34].

$$Fo = \frac{D_S t_f}{l^2} \tag{2.8}$$

The solute diffusion ability is defined by the diffusion coefficient. It is decided by several physical chemistry properties of the system including temperature, matrix lattice type, size of solute atom, valence of the atoms, compositions and microstructure [35]. Normally, the diffusion coefficient is estimated by empirical equation in the form of Eq. (2.9) which is a function of temperature.

$$D = D_0 e^{-\frac{Q_D}{RT}} \tag{2.9}$$

where D is diffusion coefficient, Q_D is the activation energy, D_0 the maximum diffusion coefficient, R is the gas constant, T is the temperature. The formulas for calculating the diffusion coefficients in the solid steel can be referred to the Sections 4.3.2 and 4.3.3.

2.1.1.4 Cooling rate

Cooling rate affects the extent of enrichment in two ways:

- A higher cooling rate involves a lower local solidification time. The extent of back diffusion of a solute element in the solid is time dependant and a lower solidification time implies less back diffusion. This contributes to a more pronounced enrichment.
- A higher cooling rate involves smaller secondary dendrite arm spacing, and the diffusion length thus becomes smaller and the extent of back diffusion increases. This contributes to lowering the enrichment of dissolved elements.

Each of the two individual influences can be dominating and the enrichment could either increase or decrease with higher cooling rate. A typical example as shown in Figure 2.6; the higher cooling rate (R_C) leads to the stronger segregation of manganese (Mn) and lower solidus temperature under the assumption of Pierer and Bernhard´s equation [28] for SDAS. Thus, the

lower local solidification time decreasing the back diffusion is dominant compared with the influence of smaller secondary dendrite arm spacing in this case.

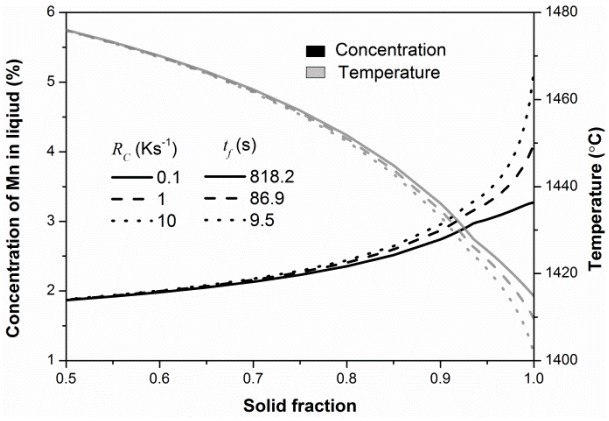

Figure 2.6. Influence of the cooling rate on microsegregation.

In total, the interactions of the aforementioned fundamental aspects result in microsegregation. The solute partitioning generates substantial concentration changes and concentration gradients ahead of the solid/liquid interface. This drives the back diffusion which influences the further redistribution of solutes. Under certain cooling conditions, the uneven distributions of solutes promote the formation of a dendritic structure. The cooling rate and the resultant local solidification time define the dendritic arm spacing which is regarded as the diffusion length. All together contribute the microsegregation in the solidified steel.

2.1.2 Influences of microsegregation

Microsegregation is an inevitable phenomenon in the solidification process. It has important influence on the subsequent metallurgical process and the final qualities of steel products as summarized by the following:

- Macrosegregation: though microsegregation is only significant in the short distance, the transport of the enriched interdendritic liquid is the main contribution of macrosegregation (Figure 2.7 (a)).
- Mesosegregation formation: the alloy elements enrichments caused by microsegregtion lead to mesosegregation close to the center of the continuous casting slab. Further after hot rolling the inhomogeneous concentration distribution results in the formation of a banded structure which causes the anisotropic products [35].
- Hot tearing formation (Figure 2.7 (b)): hot tearing is believed as a segregation phenomenon at mesoscopic scale which is consequently termed as 'Hot Tearing Segregation' [36]. Dendritic sregregations contribute more enrichment at the grain boundary. Under tensile stresses, hot tearing easily originates in the region [37,38].
- Inclusion precipitation: the increasing concentrations of solutes in the residual liquid promote the precipitation of inclusions between dendrites such as sulfides and nitrides.

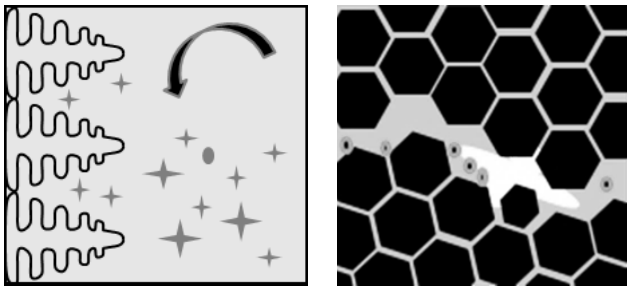

(a) (b)

Figure 2.7. Influence of microsegregaion (a) on macrosegregation (b) on hot tearing, mecrosegregation and precipitations [38,39].

- On phase transformation: the enriched alloy elements induce the reactions of phases such peritectic and eutectic reactions.

In total, microsegregation is one of the primary aspects when investigating the solidification process.

2.2 Analysis of microsegregation

Several mathematical models have been developed based on the discussed basic concepts. With these models, on one hand microsegregation process is simulated and studied; on other hand further complicated phenomena, such as microstructure development, macrosegregation and inclusion formation during solidification, can be modeled accounting microsegregation as their origin. The development of the models from simple and easy-solving analytical models to more dedicated numerical cases is overviewed in the context.

2.2.1 Analytical models on microsegregation

2.2.1.1 Lever Rule

The Lever Rule is a microsegregation model for equilibrium solidification process as described in Figure 2.8. In the model, complete diffusion in both solid and liquid is assumed. It means that at a specific solid fraction (f_S), the interfacial concentrations of solute in solid and liquid are equal to those in solid (C_S) and liquid (C_L) far away from the interface. A general mass balance can be given as Eq. (2.10). Note that the equilibrium partition coefficient (k) of the equilibrium solidification is constant. Consequently, the concentrations in the residual liquid are obtained from the Eq . (2.11).

In reality, the equilibrium solidification is never approached though the speed can be slow enough to satisfy $Fo \gg 1$. The microsegregation calculated by Lever Rule is therefore underestimated. For fast diffusion elements in steel, such as carbon, the Lever Rule predictions can be close to the real situation.

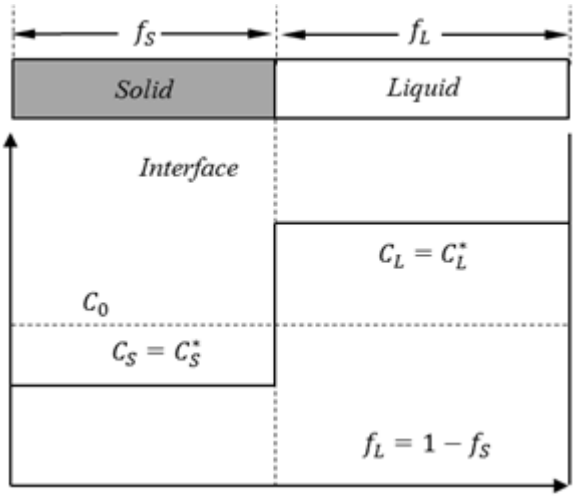

Figure 2.8. Schematic of Lever Rule.

$$C_S f_S + C_L f_L = C_0 \tag{2.10}$$

$$C_L = \frac{C_0}{1 + k f_S - f_S} \tag{2.11}$$

2.2.1.2 Scheil-Gulliver model

A more practical model on microsegregation is proposed by Scheil [9] which is also derived by Gulliver [8], as schematically shown in Figure 2.9. In contrast to Lever Rule, it assumes no diffusion in solid and well-mixed in liquid. Eq. (2.12) presents the mass balance at the solidification interface. With the interfacial equilibrium described in Eq. (2.13), the solute enrichments can be calculated with Eq. (2.14), which is the differential form of Scheil´s model [9].

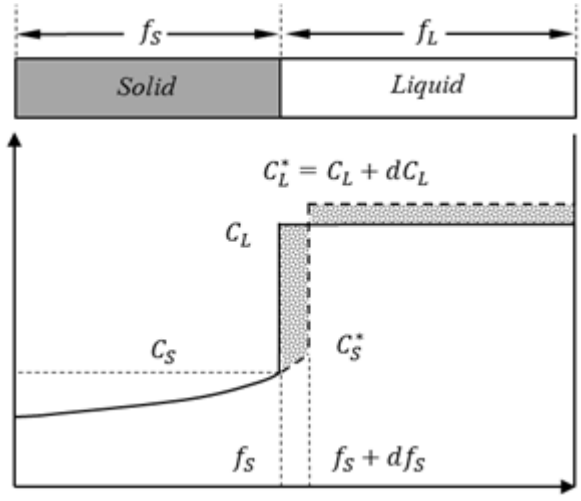

Figure 2.9. Schematic of Scheil-Gulliver model.

$$(C_L - C_S^*) df_S = (1 - f_S) dC_L \tag{2.12}$$

$$k = \frac{C_S^*}{C_L + dC_L} \approx \frac{C_S^*}{C_L} \tag{2.13}$$

$$C_L(1-k)df_S = (1-f_S)dC_L \tag{2.14}$$

$$C_L = C_0(1-f_S)^{k-1} \tag{2.15}$$

Note that in this case, the equilibrium partition coefficient changes with the proceeding solidification. In most subsequent applications, the partition coefficient was assumed as constant for simplification and absence of local values. Furthermore, the integrated form of Scheil´s model [9] is obtained in Eq. (2.15). Besides the concentrations in the residual liquid, the concentration profiles in solid are available. Due to the lack of diffusion in solid, the compositions of the formed solid phase remain unchanged.

Compared with the applied conditions of Lever Rule, Scheil´s model [9] is more appropriate for solutes with low diffusivity in solid and it overestimates the microsegregation for fast diffusing elements such as carbon and nitrogen. In addition, the interfacial concentrations would be infinite when solid fraction approaches one which also limits the application of Scheil´s model [9], because the final concentrations and solidus temperature would be important expectations. Considering the extreme characters of the Lever Rule and Scheil´s model [9], they are regarded as two limitations and widely applied to illustrate the reasonability of other predictions.

2.2.1.3 Brody-Flemings model

Brody and Flemings [7] proposed a model based on the analysis of Scheil´s model [9]. The characteristic of their model considers the diffusion in solid. They suggested that the three assumptions including no undercooling, no mass flow and complete diffusion in liquid applied in Scheil´s model [9] are valid to a wide range of casting and ingot making conditions. These three assumptions are also employed in their model, and some other assumptions are listed as the following,

(1) The diffusion geometry is planar;

(2) Solute transport within the solid phase is by volume diffusion;

(3) The thickening rate of dendrite plate is linear or parabolic;

(4) Densities of liquid and solid are the same and constant.

Figure 2.10 displays the schematic of the Brody-Flemings model [7]. The mass balance at the solid/liquid interface is given in Eq. (2.16). The figure shows that the solid diffusion is accounted in the form of back diffusion. The back diffusion layer (δ) is calculated by Eq. (2.17). In Eq. (2.17), D_s is the diffusion coefficient in solid and V is the interface advancing velocity. Combining Eq. (2.16) and (2.17), the differential solution of the model is obtained in Eq. (2.18).

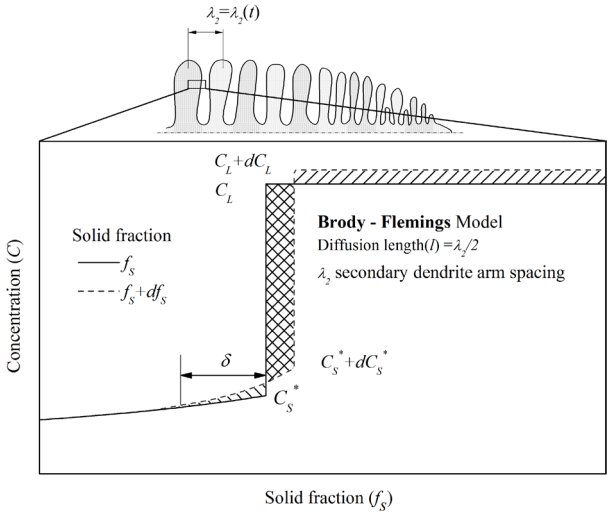

Figure 2.10. Schematic of Brody-Flemings model [12].

Solute rejected at interface

= solute increase in liquid + solute back diffusing to solid

$$(C_L - C_S^*)ldf_S = l(1-f_S)dC_L + \frac{1}{2}\delta dC_S^* \tag{2.16}$$

$$\delta = \frac{2D_S}{v} \tag{2.17}$$

$$\frac{dC_L}{C_L} = \frac{(1-k)}{(1-f_s)+\frac{D_S}{vl}} \tag{2.18}$$

where l is the diffusion length, δ is the thickness of the back diffusion layer, D_S is the solute diffusion coefficient in solid, v is the advancing velocity of solidification interface.

To achieve the integrated form, it is assumed that the partition and diffusion coefficients are constants during the whole solidification process. Providing that the interface advancing velocity is a constant with the value l/t_f, the integration of Eq. (2.18) leads to Eq. (2.19) for linear thickening of dendrite. In an alternative hypothesis, the interface advancing velocity decreases in a parabolic manner with dendrite thickening as given in Eq. (2.20) which is believed to be closer to the real situation. For this assumption, the resultant integration of Eq. (2.18) is Eq. (2.21).

$$C_L = C_0\left(1-\frac{f_S}{1+\alpha k}\right)^{k-1} \tag{2.19}$$

$$v = \frac{d\left(\frac{\lambda_2}{2}\sqrt{\frac{t}{t_f}}\right)}{dt} \tag{2.20}$$

$$C_L = C_0(1-(1-2\alpha k)f_S)^{\frac{k-1}{1-2\alpha k}} \tag{2.21}$$

with

$$\alpha = \frac{4D_S t_f}{\lambda^2} \tag{2.22}$$

In these equations, α is termed as the back diffusion coefficient which is also the Fourier number (Fo_S) in solid as given in Eq. (2.22). When α is equal to 0 and 0.5, the Brody-Flemings model [9] and Lever Rule respectively, which is found from Eq. (2.21). Based on the discussion in the Section 2.1.1.3, it is easily to understand that there is no diffusion in solid as assumed in Scheil´s model [9]. It is not reasonable for the situation of achieving Lever Rule (α=0.5), however, because back diffusion should be infinite in well mixed solid. As a result, this model is confined to the limited solid diffusion solutes.

2.2.1.4 Clyne-Kurz treatment

Clyne and Kurz [12] observed the aforementioned limitation of Brody-Flemings model [7]. When they calculated the same alloy with the Lever Rule and Brody-Flemings model [7], the predictions from Brody-Flemings model [7] did not conform to that from the Lever Rule with an increasing back diffusion coefficient (α), or Fo_S. Clyne and Kurz [12] presented a mathematical treatment for improving the Brody-Flemings model [7]. They replaced the back diffusion coefficient (α, Eq. (2.22)) with Eq. (2.23). With this treatment, when α is equal to zero and infinite Brody-Flemings model [7] approaches to the Scheil´s model [9] and Lever Rule, respectively, which is shown in Figure 2.11.

$$\Omega = \alpha\left\{1 - \exp\left(-\frac{1}{\alpha}\right)\right\} - \frac{1}{2}\exp\left(-\frac{1}{2\alpha}\right) \tag{2.23}$$

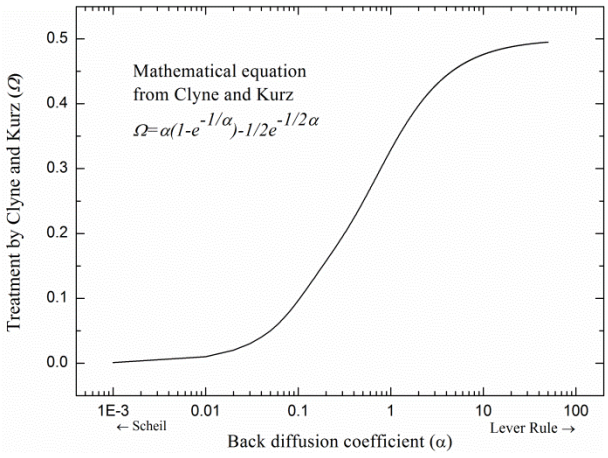

Figure 2.11. Schematic of mathematic treatment from Clyne and Kurz [12].

2.2.1.5 Ohnaka model

Considering the two-dimensional diffusion in the solid phase, Ohnaka [10] suggested a model for calculating solute enrichments during solidification. The geometry applied in the model (columnar dendrite model) as well as other geometries are described in Figure 2.12. In Figure 2.12, the dendrite models of (a), (b) and (c) are transverse cross section and (d) is longitudinal

cross section of primary or secondary dendrite. With the suggested microsegregation model, the columnar dendrite effect could be studied through comparing with plate geometry. An extension of the Brody-Flemings model [7] was made by defining the parabolic form of solute distribution in the solid (Eq. (2.24)). In Eq. (2.24), y^* is the location of solidification interface and c^* is a constant. Other important assumptions are similar with Brody-Flemings model [7]: complete diffusion in liquid, no density difference and the parabolic growth as expressed in Eq. (2.20). He also generalized the model accounting both the plate and columnar dendrites using distinct geometry parameters. Based on these assumptions, the approximate solution is obtained through solving the overall mass balance given in Eq. (2.25).

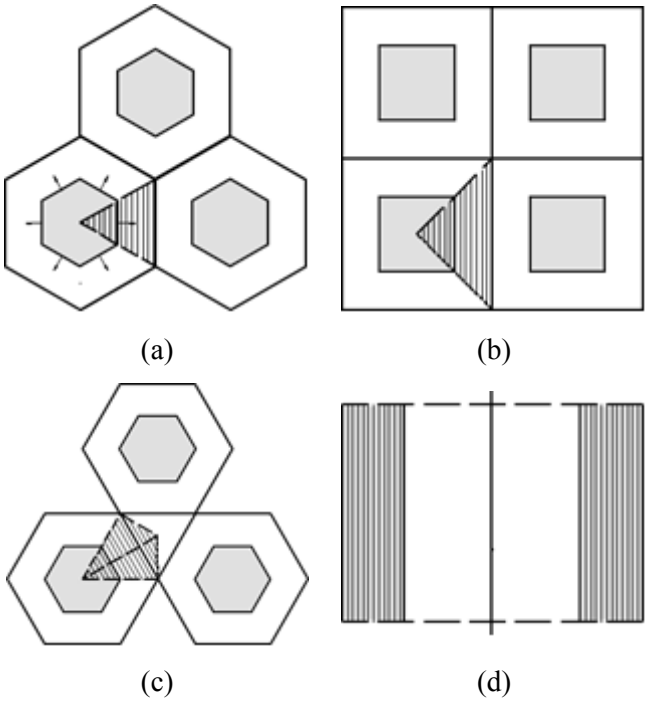

Figure 2.12. Dendrite models, (a) and (b) columnar dendrite model, (c) Matsumiya et al.´s model [40], (d) plate dendrite model.

$$C_S = C_S^* + c^*\left(l^2 - y^{*2}\right) \tag{2.24}$$

$$\frac{dC_L}{C_L} = \frac{(1-k)df_S}{\{1-\left(1-\frac{\beta k}{1+\beta}\right)f_S\}} \tag{2.25}$$

where β is equal to 2α and 4α for plate and columnar dendrite models, respectively; α is the back diffusion coefficient given by the former models; l is diffusion length.

Similarly, by providing the constant partition coefficients and diffusion coefficients, the following equation is obtained by integrating Eq. (2.26):

$$\frac{C_L}{C_0} = (1-\Gamma\cdot f_S)^{(k-1)/\Gamma}, \qquad \text{with } \Gamma = 1-\frac{\beta k}{1+\beta} \tag{2.26}$$

When sudden changes occur to partition coefficients and diffusion coefficients due to phase transformations such as the peritectic reaction in steel, the integration of Eq. (2.26) is no longer valid and the method of two regions integration would be applied as expressed in Eq. (2.27):

$$\frac{C_L}{C_0} = (1 - \Gamma_1 \cdot f_{S1})^{\frac{k_1 - 1}{\Gamma_1}} \left(\frac{1 - \Gamma_2 \cdot f_{S2}}{1 - \Gamma_2 \cdot f_{S1}}\right)^{\frac{k_2 - 1}{\Gamma_2}} \tag{2.27}$$

where $\Gamma_1 = 1 - \frac{\beta_1 k_1}{1+\beta_1}$, $\Gamma_2 = 1 - \frac{\beta_2 k_2}{1+\beta_2}$, $f_{S2} > f_{S1}$, the subscript of '1' and '2' correspond to the solid fraction of f_{S1} and f_{S2}, respectively, the solid fraction of f_{S1} is the step with sudden changes of parameters, f_{S2} is the current solid fraction.

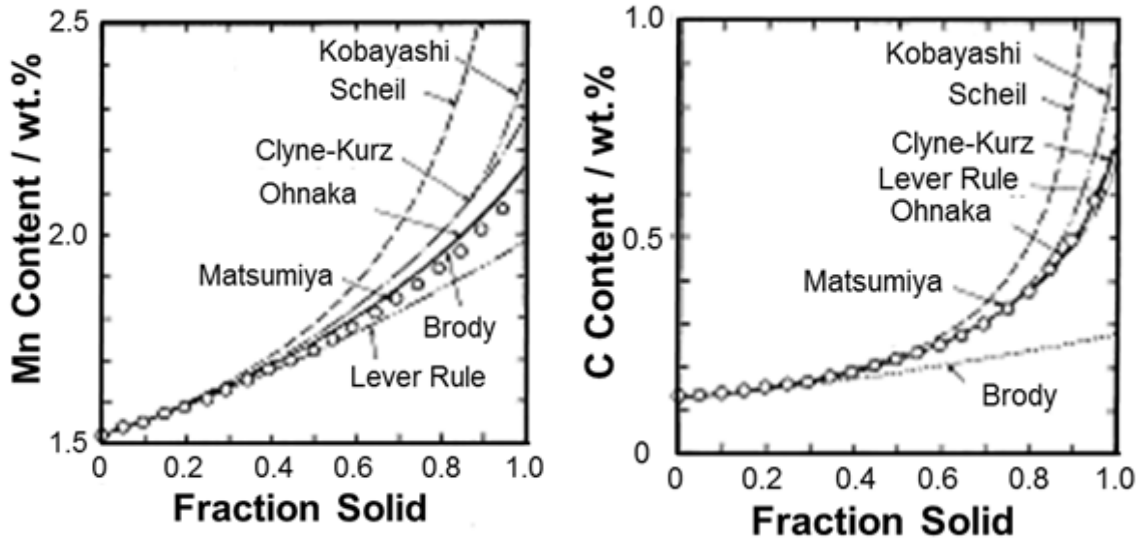

(a) (b)

Figure 2.13. Comparison of various microsegregation predictions for (a) Mn in a Fe-1.52wt% Mn alloy and (b) C in a Fe-0.13wt% C alloy.

Figure 2.13 compares the predicted concentrations in the liquid from different models for two alloys using different models with the same parameters. In addition to the aforementioned analytical solutions, the calculations using Kobayashi´s equation and Matusmiya´s numerical model are also compared. As a result, the segregation extents of Mn in Figure 2.13 (a) range from 1.52 to more than 2%, and for C (Figure 2.13 (b)), the concentrations enrich from 0.13 to 0.5%, which significantly influence the solidification temperature. In both cases, the predictions with Ohnaka´s model are quite close to those from the Matsumiya´s model. Figure 2.13 (b) shows the unrealistically lower segregation from Brody-Fleimings´s equation results from the increasing back diffusion as explained in Section 2.2.1.3. Furthermore the calculated results using Ohnaka´s model were compared with the experimental data, and a better estimation on the liquid concentration can be achieved than that of Brody-Flemings model [7].

2.2.1.6 Exact solutions from Kobayashi

Kobayashi [11] rigorously derived the exact solution of the Brody-Flemings model [7] under the conditions of constant partition and diffusion coefficients during the parabolic thickening process. It is a complex mathematical process which can be found in the original paper. The segregation behavior of alloy elements in steels estimated by the exact solution was compared with that from approximate solutions suggested by Brody-Flemings [7], Clyne-Kurz [12] and Ohnaka [10]. They concluded that all the approximate solutions underestimate the segregation of solutes, especially at the late stage of solidification. It was believed that the reason for the underestimation of Brody-Flemings [7] and Ohnaka´s models [10] is overestimating back diffusion caused by the ignorance of the second derivative involving the diffusion length.

At the same time, the exact solution of Ohnaka´s model [10] was also derived by Kobayashi [41]. The solution is for columnar dendrite model with the assumptions of constant partition and diffusion coefficients throughout the whole solidification process. While the exact solutions were more rigorously derived, it is uneasy to apply it to predict microsegregation of real alloys. That is why the analytical solutions are more widely applied for microsegregation estimation.

2.2.2 Numerical models on microsegregation

When entering the 'numerical world', the microsegregation phenomenon can be more elaborate. Different from the analytical models introduced above, numerical models are derived mainly based on Fick´s Second Law. Furthermore, the diffusion in the liquid is considered, which cannot be solved based on an analytical approach. The concentrations can be monitored without the limitations of solidification time and position. Consequently, newly formed phases and phase transformations could be easily detected. Kraft and Chang [42] reviewed a variety of microsegregation models. Later on the new works on numerically modelling were kept ongoing for different applications: using the mapping files linked with Thermo-Calc [43], Dore et al. [44] coupled microsegregation and phase diagram data for a ternary system; Du and Jacot [45] proposed a two-dimensional microsegregation model for describing the microstructure; Michelic et al. [46] developed a polydimensional model on dendritic growth and microsegregation in multicomponent alloys. Compared with analytical solutions, the numerical models are more dedicated to the complex phenomenon involving microsegregation instead of purely solute enrichments. It is unavoidable to attempt more efforts based on both computational mathematics and coding, which consumes a large amount of time to achieve the results. Meanwhile, the correctness on the concentrations in the residual liquid of numerical and analytical predictions is close to each other. Therefore, analytical solutions on microsegregation are preferable and simulate the inclusions formation in the solidification.

2.3 Summary

Microsegregation is essentially solute partitioning at the solid/liquid interface in the length scale of dendrites. Analytical models assume thermodynamic equilibrium at the solid/liquid interface; thus, the equilibrium partition coefficient becomes a decisive factor. Solute diffusion in the solid can decide the level of the segregation in the final solid, and the formation of a dendritic structure is promoted by the microsegregation. Because of the important role on further processing and the final qualities and properties of alloys, mathematical models are quite popular and widely applied to study this phenomenon. While numerical models have various advantages, they demand arduous mathematical computation and considerable time. Based on the simple solutes enrichments predictions, analytical models are more efficient. Meanwhile, the good calculation accuracies can be reached compared with those of the numerical models. This work therefore prefers the easy-to-handle analytical models. Among the analytical models, Ohnaka´s model [10] is closer to the real situation and achieves better agreement results. The existing limitations on applying the models, however, should be released: partition and diffusion coefficients are compositions and temperature dependent instead of constants, preferable equilibrium temperature is calculated based on multi-components and multi-phases rather than based on the Fe-C binary phase diagram. In addition, the influence precipitations in the solidification process should also be accounted. It is expected that using the improved model, more reliable and reasonable predictions can be obtained.

3 Formation of nonmetallic inclusions

Nonmetallic inclusions form as a result of the chemical reactions between different solutes in liquid steel or due to reactions with a slag or refractory phase. These inclusions are usually termed endogenous inclusions. The origin of inclusions might also be exogenous – e.g. the entrapment of slags or the erosion of refractories. The present work focuses on endogenous inclusions. In the last chapter, the mechanisms and models analyzing solutes concentrations in the residual liquid steel have been discussed. In this chapter, first, the origins and classifications of inclusions are briefly introduced. The effect of inclusions on selected steel properties is then described. Subsequently, the fundamentals of inclusion formation are presented from a thermodynamic and kinetic perspective. In the last section of this chapter, the thermodynamic and kinetic models for predicting the inclusion formation are reviewed.

3.1 Origins and classifications of inclusions

The liquid steel produced on the basis of iron ore or recycled scrap and Direct Reduced Iron (DRI) is called crude steel [47,48]. Two major routes for crude steel production according to the raw materials exist: The route taking different types of iron ores as primary materials is associated to Basic Oxygen Furnace (BOF). Alternatively, Electric Arc Furnace (EAF) as another route that uses recycled scrap and DRI to manufacture crude steel. In both BOF and EAF routes, liquid steel needs to undergo secondary metallurgy and continuous casting processes before becoming a solid product as schematically shown in Figure 3.1. The concerned nonmetallic inclusions originate in these processes.

According to the constituents of the nonmetallic particles in steel, it is generally divided between oxides, sulfides, nitrides and carbides as well as mixtures of the mentioned types. Most oxides are generated from deoxidizing process which is one of the main tasks of secondary metallurgy [50,51]. After oxygen blowing in BOF or EAF, the crude steel contains a large amount of oxygen which ranges from 200 to 800 ppm (0.02–0.08%) [52]. The solubility of oxygen decreases considerably with lower temperature. The maximum solubility for oxygen in pure liquid iron is about 0.23% at 1873K [50,52,53]; at 1773K (after solidification), the solubility is reduced to about 0.003%; and finally, the solubility amounts to only 2 ppm at 1173K [54]. Hence, it is necessary to decrease the high oxygen content down by deoxidation. Otherwise, the excess oxygen can promote the formation of CO bubbles and large quantities of inclusions during solidification which further causes defects such as porosities and cracks. To bind and remove the free oxygen, elements with high affinity towards oxygen are added to liquid steel in secondary metallurgy. Though most of the formed oxides are absorbed by the slag in the Ladle Furnace (LF), vacuum processes and tundish, certain amounts of oxides remain in

the melt and are present in the solid steel. Also alloying elements like Ti, Nb or Cr contribute to not only the formation of oxides, but also other inclusion types such as sulfides, nitrides and carbides. Due to the decreasing temperature and solute enrichments in the residual liquid; sulfides, nitrides and carbides mostly precipitate in the continuous casting process. During solidification, while the oxygen is quite low, some new oxides can form and pre-existing ones are possible to transform to other types. At the same time, heterogeneous inclusions form in the order of precipitation.

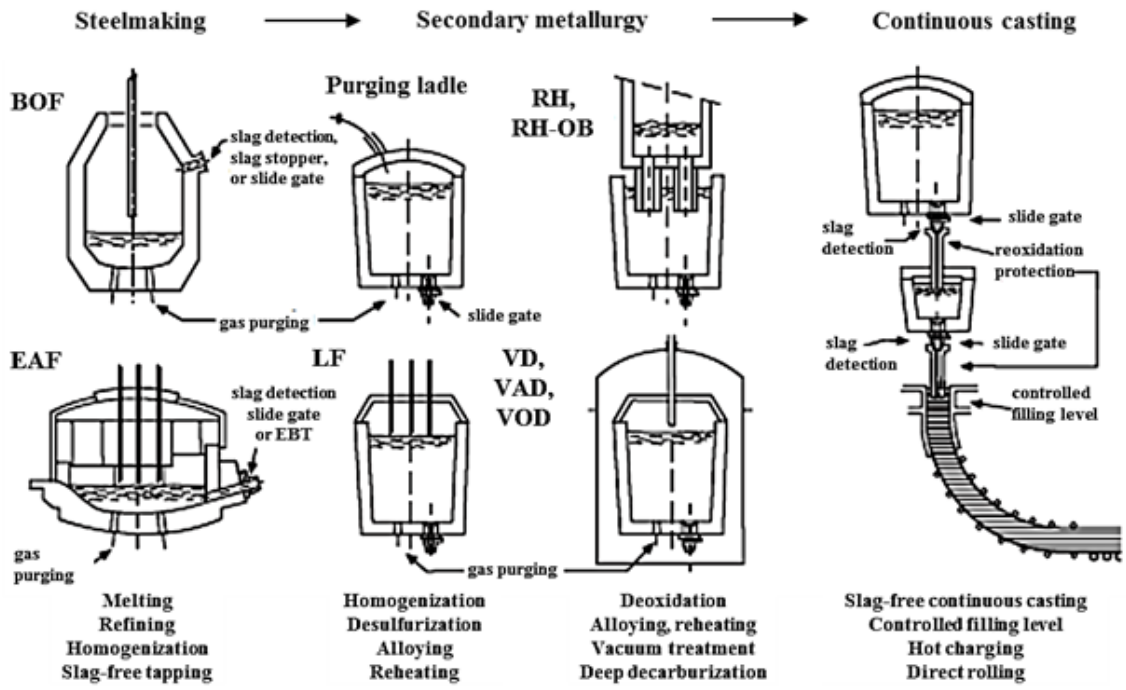

Figure 3.1. Schematic of metallurgical processes from liquid to solid steel [49].

In addition to chemical compositions, there are some other classifications. The aforementioned inclusions (products of deoxidation and alloying) are *endogenous* inclusions; There are some others inclusions resulting from reoxidation, ceramic corrosion and slag entrapment, termed as *exogenous* inclusions [55]. The size categories of inclusions are highly dependent on the steel applications. On possible classification based on the size is as follows [56,57]:

- Macro-inclusion: larger than 100µm
- Meso-inclusion: 20 to 100µm
- Micro-inclusion: 1 to 20µm
- Sub-micro-inclusion: less than 1µm

The inclusions forming before solidification are called *primary inclusions* and those generated during solidification are *secondary inclusions* [58]. The wide variety of inclusion types, sizes and formation origins opens a large field of research investigating the inclusion formation and

modification as well as their influence on the final product quality. The overall aim is to improve the steel cleanness specifically adapted to the requirements of the steel application.

3.2 Role of inclusions

Nonmetallic inclusions directly influence steel properties. Negative effects of inclusions are commonly known. Hence removing the impurities and pursuing 'clean steel' are important aspects in steelmaking. Gradual scientific progress in physical metallurgy widens the knowledge of the relationship between nonmetallic inclusions and the microstructure and mechanical properties of steels [1]. Since the concept of 'oxides metallurgy' has been introduced [2,3], the benefits of nonmetallic inclusions has gained more attention. Subsequently both, controlling and utilizing inclusions has been widely investigated and discussed [57,59,60].

3.2.1 Influences of inclusions

The presence of nonmetallic inclusions can be detrimental to the mechanical properties of steels such as the strength, toughness, fatigue and fracture [6,50]. The harmfulness of inclusions in the steel matrix originates from their different properties due to their compositions and structures. The plasticity of inclusions, as compared with steels, is the most important property affecting the steel performance [61]. The typical deformation formats of different inclusions under hot rolling conditions are described in Figure 2.1. The hard inclusions, as shown in Figure 3.2 (a), (b) and (c), can easily increase stress. Consequently, the crack forms and propagates at the inclusion and matrix interface. These inclusions are responsible for the ductile fracture and fatigue limitations [50,62]. The soft inclusions (Figure 3.2 (d) and (e)) are elongated after rolling and lead to the anisotropy of steels. This type of inclusions mainly produces negative effects on the toughness [63]. In the investigations, the Young´s modulus is used to indicate the plasticity of inclusions, and harder particles produce a higher Young´s modulus value. The Young´s moduli of the common inclusions are listed in Table 3.1 and shows that alumina is the hardest inclusion and its Young´s modulus is almost twice as that of steel matrix; consequently, the alumina should be avoided in the cracks sensitive steel. In contrast, sulfides are easier to be deformed and softer than the matrix while the resultant anisotropy should be prevented.

Different thermal expansions of inclusions and steels can also result in the harmfulness to the product. Steel production and application inevitably involves thermal processing. The circumferential stresses develop around the inclusions with lower thermal expansion coefficients. Furthermore, the circumferential stresses promote the formation of cracks. Essentially the potential defects are attributed to the deformation of inclusions and steels not occurring at the same 'pace'. The detailed mechanical explanations on the phenomenon can be found in a publication by Murakami [65].

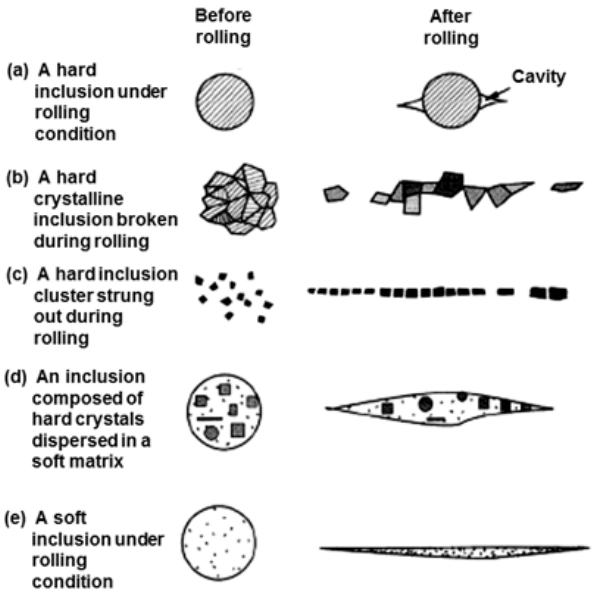

Figure 3.2. Typical deformation formats of different inclusions [64].

Table 3.1. Young´s modulus of different inclusions [65].

Inclusions	Chemical compositions	Young´s modulus (Gpa)
Sulfides	MnS	69~138
Aluminates	$CaS\cdot 2Al_2O_3$	113
Spinels	$MgO\cdot Al_2O_3$	271
Alumina	Al_2O_3	389
Nitrides	TiN	317
Oxides	MnO	178
	MgO	306
	CaO	183
Matrix	Austenite and Martensite	206

Apart from the chemistry of inclusions, the harmfulness usually increases with their content and size. The total amount of inclusions can be indirectly symbolized by the content of the formed elements. Through lowering the impurity elements, such as oxygen, sulfur and nitrogen, the amount of inclusions can be well controlled. The size distribution is quite important and the large inclusions are the most harmful to mechanical properties. A single large inclusion may cause a detrimental defect in whole heat of steel [66]. Hence, controlling the dimension of inclusions means not only decreasing their mean size, but also avoiding the presence of macro-inclusions. The critical content of impurity elements and permitted maximum inclusion size in different steel grades are summarized in Table 3.2.

In addition to the steel properties, nonmetallic inclusions also produce negative effects on the steelmaking process. The buildup of pre-existing inclusions on the nozzle wall is one of the main reasons for the clogging which is long-standing production problem in continuous casting. Nozzle clogging directly deteriorates the castability of steel and further reduces the productivity and increases cost [67]. At the same time, clogging results in the undesirable fluid flow which increases the risk of trapping mould flux. Consequently, the increasing content of macro-inclusions from both flux and dislodged clogs lead to defects in steel products [68].

Table 3.2. Typical elements requirements and permitted maximum inclusion size [66].

Steel grades	Permitted maximum inclusion size (μm)	Impurity elements requirements (ppm)
IF steel	100	[C] ≤ 10~30, [N] ≤ 40~50, T.O ≤ 10
Automotive and Deep drawing sheet	100	[C] ≤ 30, [N] ≤ 30
Drawn and Ironed cans	20	[C] ≤ 30, [N] ≤ 30, T.O ≤ 20
Alloy steel for Pressure vessels		[P] ≤ 70
Alloy steel bars		[H] ≤ 2, [N] ≤ 10~20, T.O ≤ 10
HIC resistant steel (sour gas tubes)		[P]≤ 50, [S] ≤10
Line pipe	100	[S] ≤ 30, [N] ≤ 35~50, T.O ≤ 30
Sheet for continuous annealing		[N] ≤ 20
Plate for welding		[H] ≤ 1.5
Bearings	15	T.O ≤ 10
Tire cord	10	[H] ≤ 2, [N] ≤ 40, T.O ≤ 15
Non-grain-orientated Magnetic Sheet		[N] ≤ 30
Heavy plate steel	13 (single inclusion) 200 (inclusion cluster)	[H] ≤ 2, [N] ≤ 30~40, T.O ≤ 20
Wire	20	[N] ≤ 60, T.O ≤ 30

The above discussion shows that it is necessary to control the nonmetallic inclusions to prevent and minimize their negative effects. On the other hand, the benefits of nonmetallic inclusions in the field of steelmaking were widely realized since ‘oxides metallurgy’ [3] being put forward.

This concept aims at emphasizing the positive role of nonmetallic inclusions as heterogeneous inoculants, which are veiled in the steelmaking process [3].

One important aspect of 'oxides metallurgy' is that nonmetallic inclusions offer heterogeneous nucleation sites for intragranular ferrite. Intragranular ferrite is also called inntragranular acicular ferrite or acicular ferrite due to its morphology. Compared with other ferrites such as Widmanstätten, acicular ferrite nucleating has a chaotic crystallographic orientation, which can effectively prevent the cleavage crack from propagating as schematically shown in Figure 3.3. Thus, the properties of steels can be enhanced using inclusions increasing the proportion of acicular ferrite.

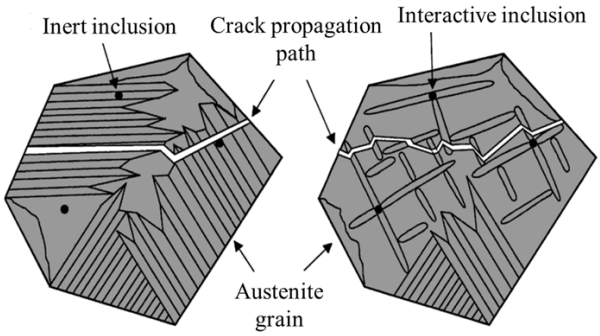

Figure 3.3. Illustration of the crack propagation in steel grains with acicular ferrite and side plate microstructure [69].

For yielding the optimum combination of strength and toughness, fine grain size is desirable to both carbon steels and high alloy steels such as ferritic stainless steel and austenitic high manganese steel. Non-metallic inclusions can refine grain by acting as nucleating agents and pinning the grain boundary [59]. In the first case, the inclusions with low planar lattice disregistry with respect to the matrix microstructure serve as the nucleation sites. Cerium containing oxides and sulfides have been illustrated to be effective on grain refining [70–72] and termed as first generation grain refiners [5,69]. Additionally, high number density of nucleating inclusions can further improve the microstructure [70]. To another case, the inclusions precipitating on the grain boundaries such as TiN [73] inhibit austenitic grain growth [74]. Thus small grain size is obtained.

3.2.2 Control and utilization of inclusions

For minimizing the negative effects of nonmetallic inclusions on steel process and properties, a variety of efforts have been made by steelmakers. In addition to limiting the total amount and avoiding exogenous inclusions, controlling the compositions of inclusions and modifying them to less harmful particles are popular methods. Regarding specific inclusion modification in order to improve product quality or to enable a continuous casting sequence, for selected steel grades, two frequently applied examples are given:

- One of the classic examples regarding inclusion modification is the case for Si/Mn deoxidation steel. The complex deoxidation using Si and Mn results in the formation of soft and deformable silicate inclusions and prevents pure SiO_2 which is non-deformable particle [6,52]. At the same time in this Si/Mn deoxidized steel, alumina cannot be completely avoided in practice, and there exists an equilibrium between it and silicate inclusions. It is reported that inclusions with MnO/SiO_2 mass% ratio near unity and Al_2O_3 content ranging from 10 to 20 mass% have low liquidus temperatures (1150–1200 °C) and their primary phases are $MnO{\cdot}SiO_2$ and $3MnO{\cdot}Al_2O_3{\cdot}3SiO_2$, which are soft [75,76].
- As a second example, calcium treatment is widely applied to modify inclusions. In the Al-killed steel, calcium addition can transform the hard aluminum and Mg-Al spinel into liquid calcium aluminates [49,52,77–79]. Consequently it is effective to prevent nozzle clogging and harmfulness on steel products caused by the inclusions. In the meantime, Ca hardens the easily deformed MnS through forming (Ca, Mn)S, which can eliminate the sulfide stringers and improve the toughness of steel [49,52,80,81].

In contrast to the negative effects, inclusions can be utilized to improve the microstructure of steel. As a typical example, the inclusions with specific compositions and size are needed to promote the nucleation of acicular ferrite. There are two possible approaches to realize this effect: obtaining effective inclusions through alloying and controlling metallurgical process [82–87]; adding the preferable inclusions to steel [88–91]. Though the mechanism of inclusion inducing the formation of acicular ferrite is still not completely understood, a wide range of dedicated work has been performed by different researchers. For instance, Shim et al. [87] investigated ferrite nucleation potency of nonmetallic inclusions in medium carbon steels. SiO_2, $MnO{\cdot}\ SiO_2$, Al_2O_3, Ti_2O_3, TiN and MnS were set as targeted inclusions and generated in the samples, respectively. The results showed that single SiO_2, $MnO{\cdot}\ SiO_2$, Al_2O_3, TiN and MnS are inert to formation of intragranular ferrite under the experimental conditions. Ti_2O_3 is effective to promoting the nucleation of intragranular ferrite in the Mn-containing steel through depleting Mn around the inclusions. In a later study, Byun et al. [86] confirmed the formation of Mn depletion zone around Ti_2O_3 and considered the absorption of Mn as the reason for Ti_2O_3 being a beneficial heterogeneous nucleus. As it is generally believed that titanium containing inclusions have higher potency on promoting acicular ferrite, Mu and Jönsson et al. [88–90] added titanium oxides and nitrides into steel and systematically studied the influence on acicular ferrite formation, involving not only chemistry but also the dimensions of inclusions. Nevertheless, the exploration on this topic is progressing.

In total, nonmetallic inclusions are important to steel properties and steelmaking processes. From the perspectives of both minimizing the negative effects and utilizing them, a broad

knowledge of inclusion formation is needed. Thus, thermodynamics and kinetics of inclusion formation, as fundamental aspects, are described in the following context.

3.3 Thermodynamics of inclusion formation

As described by Albert Einstein, thermodynamics is marked by its simplicity, the different kinds of things it relates to and the wide area of its applicability [92]. When applying to metallurgical processes, it mainly concerns on the state change of a system influenced by energy motion [48]. With the help of energy difference, the possibility and extent of chemical reactions are defined. Concerning an inclusion as a new phase in a steel matrix, the stability of it can be evaluated using thermodynamics.

3.3.1 General aspects of thermodynamics

The formation reaction of simple stoichiometric inclusion is generally described using Eq. (3.1). Here $[P]$ and $[Q]$ are the formed elements of inclusion P_xQ_y which are dissolved in liquid steel where x and y are the atom numbers in the molecule. Gibbs free energy change is the most popular thermodynamic criteria. At a constant temperature, the Gibbs energy change (ΔG) for the reaction is given by Eq. (3.2).

$$x[P] + y[Q] = P_xQ_y \tag{3.1}$$

$$\Delta G = \Delta G^0 + RTln\left(\frac{a_{P_xQ_y}}{{a_P}^x {a_Q}^y}\right) \tag{3.2}$$

where ΔG^0 is the standard Gibbs energy change which is a function of temperature, R is the Gas constant and a_i is the activity of species i. For formation of common inclusions, the empirical expressions of standard Gibbs energy change in liquid iron are available. According to Henry's law, the activity is proportional to solute concentration referred to 1% dilute solution $[\%i]$ as calculated in the following:

$$a_i = f_i \cdot [\%i] \tag{3.3}$$

where f_i is defined as activity coefficient in liquid iron which symbolizes the effects of other solutes on the activity of species i which is the basic way to consider multi-alloys. Using Wagner's formalism, the activity coefficient is calculated by Eq. (3.4).

$$\log(f_i) = e_i^i \cdot [\%i] + \sum_j e_i^j \cdot [\%j] \tag{3.4}$$

where e_i^j is the interaction coefficient of solute j on i.

When,

- $\Delta G < 0$, the reaction can happen in the right direction and the inclusion is stable.

- $\Delta G > 0$, the reaction proceeds towards the opposite direction. It means that the inclusion P_xQ_y will not precipitate.
- $\Delta G = 0$, the reaction reaches the equilibrium state, where Eq. (3.5) is achieved.

$$\Delta G^0 = -RTln\left(\frac{{a_{P_xQ_y}}^{eq}}{({a_P}^{eq})^x({a_Q}^{eq})^y}\right) \tag{3.5}$$

where the superscript eq means equilibrium.

Consequently, Eq. (3.2) can be written into Eq. (3.6):

$$\Delta G = RTln[\frac{a_{P_xQ_y}}{{a_{P_xQ_y}}^{eq}}\frac{({a_P}^{eq})^x({a_Q}^{eq})^y}{{a_P}^x{a_Q}^y}] \tag{3.6}$$

When assuming the inclusion P_xQ_y is a pure solid phase the activity of it is equal to one ($a_{P_xQ_y}$=${a_{P_xQ_y}}^{eq}$=1). Then the calculation of free energy change transfers to the evaluation of supersaturation (Eq. (3.7)). The supersaturation (S_{sat}) is defined as the ratio between activity products of constituents before and after inclusion formation (approaching equilibrium state) as expressed in Eq. (3.8). It is clear that the condition of obtaining stable inclusion is that the supersaturation is larger than one. In the dilute solution, the supersaturation is also estimated by the ratio of real concentration product (K) and solubility product (K^{eq}).

$$\Delta G = RTln\left[\frac{({a_P}^{eq})^x\left({a_Q}^{eq}\right)^y}{{a_P}^x{a_Q}^y}\right] = -RTln(S_{sat}) \tag{3.7}$$

$$S_{sat} = \frac{{a_P}^x{a_Q}^y}{({a_P}^{eq})^x\left({a_Q}^{eq}\right)^y} \approx \frac{K}{K^{eq}} \tag{3.8}$$

Simultaneously, thermodynamics decide the chemical driving force for the inclusion formation as displayed in Figure 3.4. It is found that supersaturation promotes the proceeding of reactions until the equilibrium state, while it gradually decreases due to the consumption of solutes. Correspondingly, the absolute value of free energy change approaches zero. To some extent, this driving force is the link between thermodynamics and kinetics. The detailed application of the chemical driving force to inclusion nucleation and growth is later discussed.

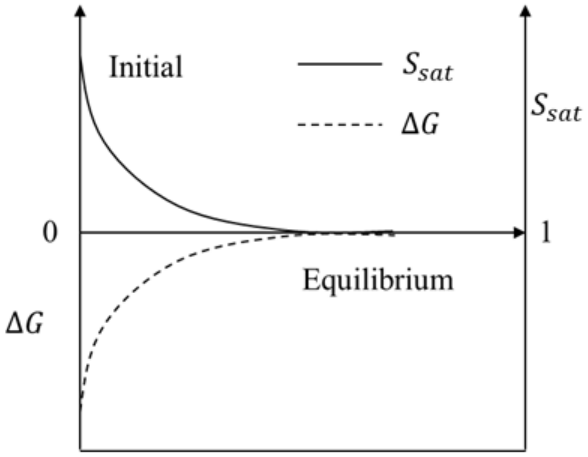

Figure 3.4. Schematic of driving force chemical reactions.

3.3.2 Computational thermodynamics

Steelmaking processes involve high temperature chemical interaction of multi-components and multi-phases. For not only phase stability, but also equilibrium compositions and temperatures, it is desirable to achieve thermodynamics based on comprehensive databases since the usage of the simple Gibbs energy data is quite limited. A strong database is normally constructed by a large amount of critically optimized binary and ternary phase diagrams [93]. For over 40 years, there has been an international group of scientists working closely on developing methods and producing data to describe the thermodynamic properties and phase diagrams of material systems [94]. This group is famous for the name associated with CALculation of PHAse Diagrams (CALPHAD) and the methodology is referred as 'CALPHAD Method' or 'CALPHAD Technique'. Together with the development of computer science, the continued dedicated work on the thermodynamic phase diagrams promotes the creation of thermodynamic databases. A French-funded project (CNRS, 1969–1974) jointed the AEA Harwell in the UK, the University of Grenoble and Institut de Recherche de la Sidérurgie (IRSID), Maizières-les-Metz, in France, and the RWTH in Germany to establish a common database [94]. In 1979, together with Sweden KTH, Scientific Group Thermodata Europe (SGTE) [95] was founded and created the SGTE database which is under continuous development. In addition to SGTE, Facility for the Analysis of Chemical Thermodynamics (FACT) started in 1976 by École Polytechnique and McGill University. The group developed its own database system to treat thermodynamic properties and calculations in chemical metallurgy [96]. In the following, several other databases have been developed for different systems [97–101]. All the aforementioned projects have greatly gained popularity for applying thermodynamic calculations.

Table 3.3. The applications of thermodynamics databases on steelmaking processes [108].

Steelmaking fields	Cases
Inclusion engineering	Inclusions compositions control: deoxidation, Ca treatment, promoting acicular ferrite formation, etc.
Slag/metal reactions	Desulfurization, dephosphorization, etc.
Refractories/slag reactions	Stabilities of refractories: thermal and chemical.
Slag/inclusions reactions	Inclusion dissolution in slag, inclusion capacity of slag.
Solidification of slag and mould flux	Investigation of solidification process to obtain preferable solid phases for applying.
Solidification of liquid steel	Predictions of segregation and precipitations
Process modeling	Coupling with CFD model to simulate fluid flow
Physical properties of slag	Evaluation of viscosity and surface tension of slag

Along with Gibbs energy minimization software, the databases are used to calculate the equilibrium of multi-components and multi-phases system. The well-known software with a variety of strong databases include FactSage [102], Thermo-Calc [103], CEQCSI [104,105], MPE [99] and MTDATA [106]. Taking FactSage as an example, it contains two series-compound and solution databases and includes 17 different databases [107]. By using these powerful software packages and databases, acceptable thermodynamic evaluations can be achieved and the chemical phenomenon in the steelmaking process is well understood and better controlled. Consequently, it saves considerable time and effort, which are needed to carry out complex experiments. The large advantages also lead to their wide applications. Based on the summary of In-Ho Jung [108], the applications of thermodynamics databases on steelmaking processes are listed in Table 3.3.

3.4 Kinetics of inclusion formation

On the basis of thermodynamics, kinetics defines the rate of chemical reaction. Specific to inclusion formation, the evolution of size and number density are described using kinetics. In this way, the size distribution of inclusions can be studied and controlled. Furthermore, inclusion composition and amount are simultaneously achievable.

3.4.1 Nucleation

The classical nucleation theory is widely used and illustrated to be valid to investigate precipitation related topics. The development of classical nucleation theory was mainly attributed to Volmer, Weber [109] and Becker, Döring [110] while many other researchers [111–113] also made significant contributions. When a new phase nucleates in liquid steel, the essential driving force is the difference of system free energies (ΔG_{hom}) between initial (G_1) and final (G_2) states as given by Eq. (3.9) to (3.12):

$$G_1 = (V_L + V_{in})G_V^L \tag{3.9}$$

$$G_2 = V_L G_V^L + V_{in} G_V^{in} + A_{inL}\sigma_{inL} \tag{3.10}$$

$$\Delta G_{hom} = G_2 - G_1 = -V_{in}\Delta G_V + A_{inL}\sigma_{inL} \tag{3.11}$$

$$\Delta G_V = G_V^{in} - G_V^L = \Delta G_{in}/V_{in} \tag{3.12}$$

where V_L and V_{in} are the molar volumes of liquid steel and inclusion, respectively; G_V^L and G_V^{in} are the volume Gibbs energies of liquid steel and inclusion, respectively; A_{inL} is interfacial area between liquid matrix and inclusion while σ_{inL} is the corresponding interfacial energy; and ΔG_V and ΔG_{in} are the volume and molar energy changes of inclusion formation.

When assuming a spherical nucleus with a radius of r, the free energy change of system is written into Eq. (3.13). In Eq. (3.13), the first term describes the Gibbs energy change caused by the chemical reaction of nucleus formation and ΔG_V can be calculated by Eq. (3.12). The second term is the energy obstacle resulting from the new interface formation. The free energy changes of different terms with the radius of nucleus are displayed in Figure 3.5. Since ΔG_V and σ_{inL} are constants, the critical radius for possibly stable inclusion nuclei (r^*) and corresponding to free energy change (ΔG_{hom}^*) are obtained through differentiating as given in Eq. (3.14) and (3.15). It is found that when $r < r^*$ the nucleus dissolves into liquid to minimize the system free energy; when $r > r^*$ the nucleus tends to grow up and become stable. To specific inclusions with certain radius, the driving force of nucleation depends on the formation Gibbs energy change (ΔG) or supersaturation of comprised elements (S) as given in Eq. (3.7) and (3.8). In this manner, the thermodynamics and kinetics of inclusion formation are connected.

$$\Delta G_{hom} = \frac{4\pi r^3}{3}\Delta G_V + 4\pi r^2 \sigma_{inL} \tag{3.13}$$

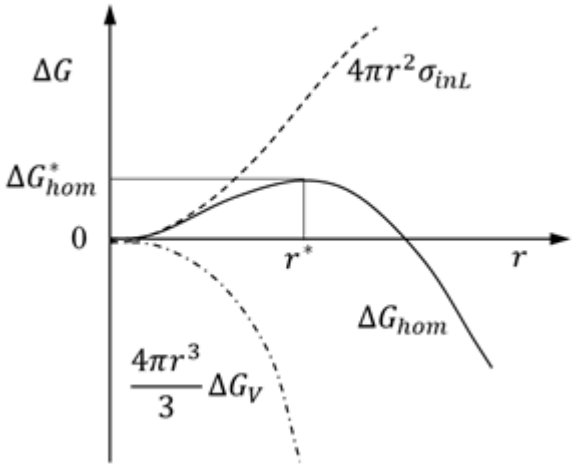

Figure 3.5. The free energy changes during nucleation [114].

$$r^* = -\frac{2\sigma_{inL}}{\Delta G_V} \tag{3.14}$$

$$\Delta G^*_{hom} = \frac{16\pi\sigma_{inL}}{3\Delta G_V^2} \tag{3.15}$$

As for the rate of nucleation, Volmer and Weber [109] first proposed an expression, and Becker and Döring [110] further improved it which is the basis for almost all the subsequent treatments as described in Eq. (3.16) [115].

$$I = I_A \exp\left[-\frac{\Delta G^*_{hom}}{k_b T}\right] \tag{3.16}$$

In Eq. (3.16), I_A is a frequency factor which is the product of the number of nucleation sites, the atom or molecule diffusion frequency across to the liquid and inclusion embryo interface and the probability of the particle successfully adsorbing on the embryo. ΔG^*_{hom} is the maximum Gibbs energy change for the homogeneous nucleation, T is temperature and k_b is the Boltzmann constant. For estimating the frequency factor, Turnbull and Fisher [111] proposed an expression as given in Eq. (3.17):

$$I_A = \frac{N_A k_b T}{h} \exp\left[-\frac{Q_D}{RT}\right] \tag{3.17}$$

where N_A is Avogadro constant, k_b is Boltzmann constant, h is Planck constant, and Q_D is the activation energy for diffusion.

Turpin and Elliott [116] applied the above method and estimated the frequency factor ($s^{-1}\cdot m^{-3}$) with the pertinent data [117] for several oxides in an iron melt: Al_2O_3, 10^{32}; $FeO\cdot Al_2O_3$, 10^{31}; SiO_2, 10^{34}; FeO, 10^{36}. Rocabois et al. [19] suggested the factor ranges from 10^{35} to 10^{45}. It was believed that the frequency factor could be considered as constant due to the nucleation number density is not sensitive to its variation [117].

One the other hand, based on Eqs. (3.15) and (3.16), nucleation rate is strongly influenced by the critical Gibbs energy change. Meanwhile the interfacial energy also plays an important role (σ_{inL}) which is calculated by Eq. (3.18) [118]. The interfacial energy of inclusion and pure liquid as well as contact angle can be both measured by the sessile drop method [119] and calculated by mathematical models together with phase diagrams [120]. The two methods for achieving interfacial energies are normally in binary or ternary systems. However, the multi-components and multi-phases in liquid steel influence the values.

$$\sigma_{inL} = \sigma_{in} - \sigma_L cos\varphi \tag{3.18}$$

where σ_{in}, σ_L are interfacial energies of inclusions, liquid with vapor, respectively, and φ is the contact angle between inclusions and liquid.

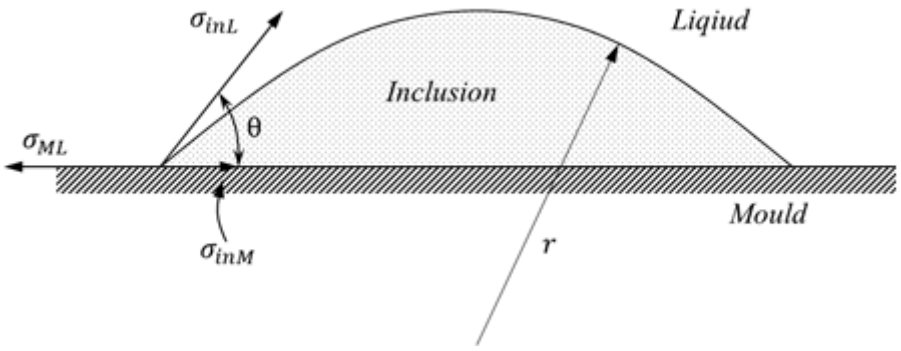

Figure 3.6. Inclusion nucleating on flat mould wall [115].

For simplification and using less uncertain parameters, the aforementioned homogeneous nucleation theory is applied in most simulations. In practice, heterogeneous nucleation is the dominant nucleation format due to the existence of impurity particles and boundaries. Compared with homogeneous nucleation, the smaller energy obstacle of heterogeneous nucleation earns its popularity. Figure 3.6 shows a sphere inclusion nucleating on a flat mould wall. The relationship of different interfacial energies is derived according to tension balance as given in Eq. (3.19):

$$\sigma_{ML} = \sigma_{inM} + \sigma_{inL} cos\theta \tag{3.19}$$

In Eq. (3.19), σ_{ML}, σ_{inM} and σ_{inL} are the interfacial energies between mould and liquid steel, inclusion and mould as well as inclusion and liquid steel, respectively. θ is the contact angle of inclusion and mould. Due to the appearance of new interfaces, the system Gibbs energy change of heterogeneous nucleation (ΔG_{het}) turns to be Eq. (3.20).

$$\Delta G_{het} = -V_{in}\Delta G_V + A_{inL}\sigma_{inL} + A_{inM}\sigma_{inM} - A_{inM}\sigma_{ML} \tag{3.20}$$

where A_{inL} and A_{inM} are the interfacial area between inclusion and liquid steel and inclusion and mould, respectively.

Combined with Eq. (3.19), Eq. (3.20) can be written into Eq. (3.21):

$$\Delta G_{het} = \left(-\frac{4\pi r^3}{3}\Delta G_V + 4\pi r^2 \sigma_{inL}\right) \cdot f(\theta) \tag{3.21}$$

$$f(\theta) = \frac{(2 + cos\theta)(1 - cos\theta)^2}{4} \tag{3.22}$$

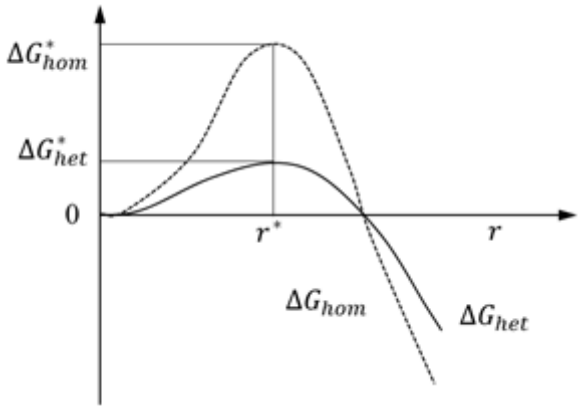

Figure 3.7. Comparison of critical Gibbs energy change for homogeneous and heterogeneous nucleation [114].

The critical free energy change ΔG^*_{het} can be obtained through differentiating as expressed in Eq. (3.23), and the corresponding critical radius is the same with homogeneous nucleation (Eq. (3.14)). Figure 3.7 compares the critical energy changes (maximum obstacles) of heterogeneous and homogeneous nucleation and shows that heterogeneous nucleation is much easier.

$$\Delta G^*_{het} = \frac{16\pi\sigma_{inL}}{3\Delta G_V^2} \cdot f(\theta) = \Delta G^*_{hom} \cdot f(\theta) \tag{3.23}$$

As for the heterogeneous nucleation rate, it has the similar form as that of homogeneous nucleation as given in Eq. (3.24) [121]. The contact angle θ needs to be defined when using heterogeneous nucleation, while it is impossible to decide it since it varies for different cases.

$$I = I_B f(\theta)^{1/6} \exp\left[-\frac{\Delta G^*_{het}}{k_b T}\right] \tag{3.24}$$

where I_B is the frequency factor and similar with I_A.

3.4.2 Growth

The final size of inclusions depends on the growth rate. Three mechanisms: diffusion controlled growth, collisions and coarsening contribute the size changes of inclusions. After an inclusion is thermodynamically stable and the supersaturation satisfies the condition of nucleation, the nucleus starts to grow. The growth is promoted by constituents diffusing towards the particle. In liquid steel, collisions of individual particles lead to further size enlargement with reducing

number density. Coarsening, referred as Ostwald ripening [122], is caused by larger inclusions growing at the consumption of smaller particles.

3.4.2.1 Diffusion controlled

One of the most frequently used expressions to evaluate the diffusion controlled growth rate of a spherical particle was derived by Zener as given in Eq. (3.25) [123]. The detailed derivation of this equation can be found in the original publication [123].

$$\frac{dr}{dt} = \frac{D_L}{r}\frac{C_L - C_{inL}}{C_{in} - C_{inL}} \tag{3.25}$$

where dr/dt is the growth rate of the particle with a radius of r; D_L is the solute diffusion coefficient in the liquid steel; C_L, C_{in} and C_{inL} are the solute concentrations in liquid steel, inclusion and at inclusion-liquid steel interface, respectively.

Figure 3.8 schematically displays the driving force for inclusion growth in this case. The figure shows that the driving force mainly depends on the solutes concentration difference in liquid and at the inclusion/liquid interface. For calculating the interfacial concentrations, it is assumed that there exists thermodynamic equilibrium at the interface as expressed in Eq. (3.26). In this equation, the superscripts P and Q represent the formed elements of the inclusions; K^{eq} is the solubility products of the inclusion under current conditions.

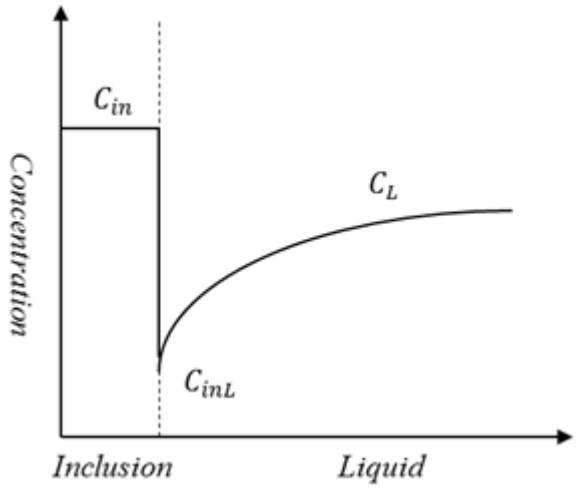

Figure 3.8. The driving force of inclusion growth.

$$C_{inL}^{P} \cdot C_{inL}^{Q} = K^{eq} \tag{3.26}$$

One more assumption to solve the interfacial concentrations has the following two possibilities: (1) mass balance according to the stoichiometric formula as given in Eq. (3.27);

(2) considering the diffusion of the formed elements as defined in Eq. (3.28) [124]. In both cases, it involves the selection of the controlled element.

$$\frac{C_L^P - C_{inL}^P}{C_L^Q - C_{inL}^Q} = \frac{xM^P}{yM^Q} \tag{3.27}$$

$$\frac{C_L^P - C_{inL}^P}{C_L^Q - C_{inL}^Q} = \frac{xM^P}{yM^Q} \cdot \sqrt{\frac{D_L^Q}{D_L^P}} \tag{3.28}$$

where M^P and M^Q are molar weights of elements P and Q, D_L^P and D_L^Q are the liquid diffusion coefficients for the elements P and Q.

In contrast, another expression to estimate the growth rate of a spherical particle does not consider the interfacial phenomenon as given in Eq. (3.29). The derivation of this mechanism can be found elsewhere [125]. It is found that the driving force for growth is the difference between liquid concentration (C_L^P) and equilibrium value (C_{eq}^P) instead of interfacial concentration. This simplification gains its popularity. Note that the growth is only controlled by the element P in this situation.

$$r\frac{dr}{dt} = \frac{M_{in}}{100 \cdot M^P}\frac{\rho_{Fe}}{\rho_{in}} D_P\left(C_L^P - C_{eq}^P\right) \tag{3.29}$$

where M is the molar weigh; ρ is the density; P stands for the controlled solutes; and in and Fe mean inclusion and liquid steel, respectively.

3.4.2.2 Collisions

The radius of particles generated by collisions is usually calculated using the unchangeable total volume and the decreasing number density. According to the theory of collisions, the collision frequency (N_{ij}, $m^{-3}s^{-1}$) can be calculated using Eq. (3.30) [126]:

$$N_{ij} = \beta\left(r_i, r_j\right) \cdot n_i \cdot n_j \tag{3.30}$$

where $\beta\left(r_i, r_j\right)$ (m^3s^{-1}) is a function of collision frequency of particles with radius of r_i and r_j, n_i and n_j are the corresponding number densities of these two group particles.

Normally there are three types of collisions contributing to the growth of inclusions in liquid steel and collision frequency functions of them are expressed as Eqs. (3.31) to (3.33) [127–129]:

Brownian motion:

$$\beta_B\left(r_i, r_j\right) = \frac{2k_bT}{3\mu} \cdot \left(\frac{1}{r_i} + \frac{1}{r_j}\right) \cdot \left(r_i + r_j\right) \tag{3.31}$$

Stokes collision:

$$\beta_S(r_i, r_j) = \frac{2\pi g(\rho_{Fe} - \rho_{in})}{9\mu} \cdot |r_i - r_j|(r_i + r_j)^3 \tag{3.32}$$

Turbulent collision:

$$\beta_T(r_i, r_j) = 1.3\alpha_T \pi^{1/2} (\varepsilon / v_k)^{1/2} (r_i + r_j)^3 \tag{3.33}$$

where $\beta_B(r_i, r_j)$, $\beta_S(r_i, r_j)$ and $\beta_T(r_i, r_j)$ are Brownian motion, Stokes and turbulent collision frequency functions, respectively, for the particles with radius of r_i and r_j; k_b is the Boltzmann constant; T is temperature; μ is the dynamic viscosity of liquid steel; π is circumference ratio; g is the gravitational acceleration; ρ_{Fe} and ρ_{in} are the densities of liquid steel and inclusion; α_T is the turbulent coagulation coefficient; ε is the turbulent dissipation rate; v_k is the kinematic viscosity of the melt.

Then, the total collision frequency function can be obtained:

$$\beta(r_i, r_j) = \beta_B(r_i, r_j) + \beta_S(r_i, r_j) + \beta_T(r_i, r_j) \tag{3.34}$$

Note that among the three formats of collisions, Brownian motion and Stokes collisions are the fundamental parts which can happen without liquid flow and turbulent collision decides the intensity of collisions in most cases with liquid flow. Based on Eqs. (3.30) to Eq. (3.34), the growth of particles resulting from collisions can be considered.

3.4.2.3 Coarsening

Coarsening is derived based on the reduction of the interfacial energy. This process is realized through shrinkage of smaller particles and growth of large ones. Coarsening is particularly important when the formation of inclusions reaches equilibrium. With constant volume fraction of inclusions, the theory to estimate the mean radius change was proposed by Lifshitz and Slysov [130,131], as expressed by Eq. (3.35):

$$\bar{r}^3 = \bar{r}_0^3 + \frac{4}{9} \frac{2\sigma_{inL} V_{in} C_0 D}{R(C_{in}^i - C_0)} \cdot t \tag{3.35}$$

where $\bar{r}_0$ and $\bar{r}$ are the mean radius before coarsening and at time t, respectively; σ_{inL} is the interfacial energy between inclusion and liquid steel; V_{in} is molar volume of inclusion; C_0 and C_{in}^i are the concentrations of controlled solute i at initial state and in inclusion, respectively; D is the diffusion coefficient of solute i in the matrix; R is gas constant.

3.4.3 Dissolution

When the formed inclusion is thermodynamically unstable, it starts to dissolve. Considering the dissolution as diffusion controlled process, Whelan [132] derived the following expression to calculate the dissolution rate as expressed in Eqs. (3.36) to (3.38):

$$\frac{dr}{dt} = -\frac{\alpha_d D}{2r} - \frac{\alpha_d}{2}\sqrt{\frac{D}{\pi t}} \tag{3.36}$$

with

$$\alpha_d = 2\frac{C_{inL} - C_L}{C_{in} - C_{inL}} \tag{3.37}$$

$$\frac{dr}{dt} = -\frac{\alpha_d D}{2r} \tag{3.38}$$

where D is the diffusion coefficient of solute in the matrix and, t is the time for dissolution.

Figure 3.9 schematically shows the driving force for inclusion dissolution. After the inclusion is unstable, the interfacial concentration (C_{il}) is higher than that in liquid steel. The elements diffuse from the inclusion/liquid matrix towards to liquid and the inclusion experience dissolution. If the transit item in the Eq. (3.36) is neglected, Eq. (3.38) is derived [133]. Compared with the diffusion controlled growth, the dissolution is believed as an inverse process. Note that when submitting Eq. (3.37) into Eq. (3.38), it turns to be the same as the growth rate suggested by Zener (Eq. (3.25)).

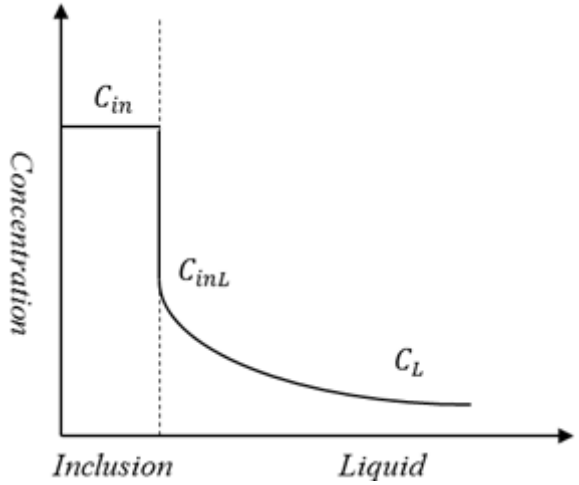

Figure 3.9. Schematic of driving force for inclusion dissolution.

3.5 Models on inclusion formation

Thermodynamic and kinetic models on inclusion formation are powerful tools to investigate the related topics. In a defined system, with thermodynamic models; the stability, compositions, constituents and the amount of the inclusions can be calculated under equilibrium conditions; the changes of inclusions during cooling and solidification process can be simulated; and the influences of solute concentrations on the formation of inclusions can be predicted. Based on the formation thermodynamics, kinetic models are able to evaluate the rate of inclusions evolution, and the size distribution and number density are achievable. The effects of cooling

conditions, concentrations of formed elements on inclusion size and amount can be investigated and controlled. In this section, different thermodynamic and kinetic models are briefly reviewed.

3.5.1 Thermodynamic models

In the 1980s, the first thermodynamic model to simulate the compositional changes of inclusions was reported by Yamada and Matsumiya [13]. The model coupled SOLAGSMIX [134] with additional thermodynamic data and the Clyne-Kurz microsegregation model [12]. SOLAGSMIX is a Gibbs energy minimization program which can calculate thermodynamic equilibrium for multicomponent systems. At that time, this program was still in the infancy of ChemSage [135]. Thus extra data of standard formation free energies for nonmetallic inclusions, activities coefficients of species in molten steel and compositions of liquid oxides had to be introduced into SOLAGSMIX. The basic assumptions of this coupled model are as follows: (1) solute enrichments in the residual liquid steel during solidification are estimated by the Clyne-Kurz model [12]; (2) there exists an equilibrium between segregated solutes and inclusions phases in residual liquid steel at each solidification step; (3) The formed inclusions distribute homogeneously in the residual liquid steel; (4) The inclusions are trapped by the solidification interface without pushing out and the inclusions in solid are inert in future solidification steps. The liquidus temperature is estimated by the reported empirical equations. In addition, the values of partition coefficients and diffusion coefficients are needed for microsegregation calculation. Using the proposed model, the formation process of calcium oxides and sulfide during the solidification of hydrogen-induced-crack resistant steel were analyzed. In this case, Ca was added to control the sulfide shape in the steel. One of the calculated results is shown in Figure 3.10. The figure shows that the compositions evolution of all inclusions types and stabilities of complex oxides can be obtained. Before achieving the solid fraction of 0.5, the amount of CaS increases gradually by consuming CaO. The mass fraction of the various inclusions changes little when the solid fraction ranges from 0.5 to 0.9. At end of the solidification, CaO becomes unstable and transforms to CaS due to the strong segregation of S and the corresponding decreased temperature. The released oxygen reacts with Al and forms Al_2O_3. Based on the calculation, the formation of CaS can suppress the formation of MnS and the shape can be controlled.

The research group at IRSID used the same technique as Yamada and suggested a model based on CEQCSI [105], an in-house developed software, and Clyne-Kurz model [14,15]. In the model, both the stoichiometric and complex solution inclusions can be considered based on the thermodynamic equilibrium calculation with CEQCSI. In one application, the compositions of oxides in semi-killed steel from different industrial processes were well predicted compared with experimental results [15]. In another case, the precipitation of the (Mn, Fe, Cr)S solution

phase during the solidification of high carbon steels were calculated [14], and both compositions and amounts showed good agreements with experiments.

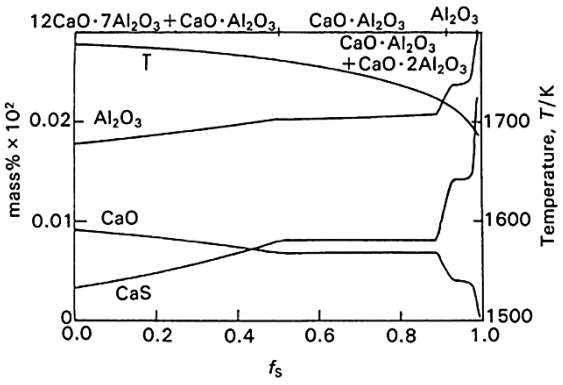

Figure 3.10. The calculated result for calcium containing inclusions using Yamada´s model [13].

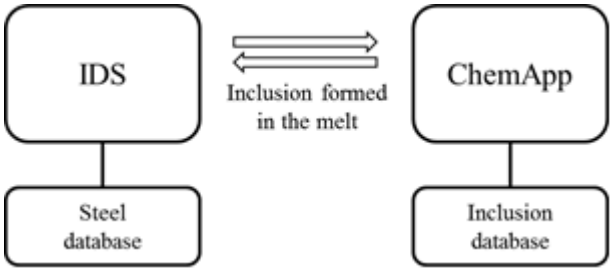

Figure 3.11. The concept behind the program ICA [17].

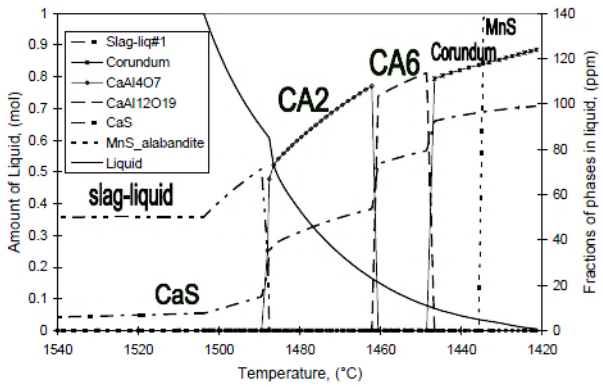

Figure 3.12. Formation of inclusions during cooling and solidification in high carbon steel [18].

Choudhary and Ghosh [16] reported a methodology to predict inclusions formation during cooling and solidification. In the cooling process, the inclusions changes were calculated using the Equilib module of FactSage. A sequential calculation was performed through coupling the Clyne-Kurz model [12] and FactSage. In this manner, the segregated solutes concentrations estimated by the microsegregation model were input parameters for FactSage to predict the

inclusions evolutions during solidification. The characters of the predicted inclusions fit well with the measured ones from industrial samples.

To simulate the inclusion behavior during casting and solidification, the researchers in Helsiniki University of Technology (now Aalto University) combined InterDendritic Solidification (IDS) software with the thermodynamic library ChemApp [136] (ICA [17,18]). The concept of ICA is shown in Figure 3.11. IDS is the more elaborate model for solidification and phase transformation compared with the simple mathematical models. This program was constructed based on a thermodynamic substitutional solution model, a magnetic ordering model and Fick's diffusion law. IDS has its own database so that it can provide solidification-related thermos-physical properties such as enthalpy and specific heat. In this case, ChemApp calculates the thermodynamic equilibrium for inclusions formation. Figure 3.12 displays an example for calculating the inclusion changes during casting and solidification in high carbon steel. In this example, the Ca treatment was expected to modify the hard alumina to the soft calcium aluminates. It shows that the formation of various inclusions including sulfides and complex oxides is predicted. The compositions of liquid slag oxide are also available, and the liquid slag phase and CaS are stable at the beginning of the solidification. With the decreasing temperature, the slag phase transforms to various calcium aluminates and finally transforms to corundum (Al_2O_3). Accompanying with these changes, the amount of CaS gradually increases. At the end of the solidification, the residual liquid contains high sulfide content due to the high sulfur content and its enrichment. The sulfides should be strictly controlled since they are likely to cause nozzle clogging during casting. The predictions using the model are in good agreement with the experimental results [137].

On the other hand, by possessing strong databases, the aforementioned commercial software [102–106] naturally has become the most powerful and popular thermodynamic tools. On inclusion studies, phase diagram and equilibrium at changing temperature and compositions are widely applied. As an example, Figure 3.13 displays the compositional trajectories of MnO-Al_2O_3-SiO_2 inclusions with different Mn/Si ratios where the total amount of soluble Mn and Si is equal to 1.0% mass. The main target of this case is to control the oxides into liquid region at 1200 °C which minimizes their harmfulness. Hence the liquidus region at 1200 °C is superimposed to assist steelmakers to obtain a proper Mn/Si ratio. For this commercial software, there exist limitations of flexibility when more practical cases need to be considered such as microsegregation during solidification and inclusions behavior at the liquid/solid interface. Even though FactSage and Thermo-Calc have embedded the Lever Rule and the Scheil´s model [9] to simulate the solidification process, they are only valid to extreme situations. In addition to the thermodynamics, more reasonable and flexible models with kinetics consideration such as the

diffusion geometries in the solidification process and nucleation of precipitations are desirable. That explains why several simple in-house models were developed.

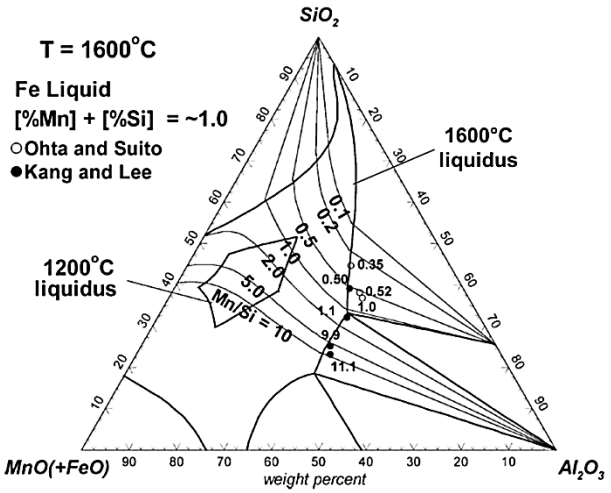

Figure 3.13. Calculated compositional trajectories of MnO-Al2O3-SiO2 inclusions in Si-Mn deoxidation steel at 1600 °C and 1200 °C [75,76,138].

3.5.2 Kinetic models

In addition to chemistry, the number density and size of inclusions are also important aspects in inclusion research. In 1966, Turpin and Elliot [116] first applied classical nucleation theory to investigate oxides nucleation in ternary steel melts. In the application, only homogeneous nucleation was considered to avoid the complication caused by the introduction of heterogeneous substrate. The nucleation frequency factor (pre-exponent) for a variety of oxides was estimated. On the basis of the critical nucleation Gibbs energy change, the critical nucleation concentrations of oxygen for supersaturation with the equilibrium concentrations of alloys in different ternary systems were calculated. By this method, the effects of super-cooling and interfacial tension on the nucleation of possible nuclei were investigated. At the same time, the corresponding cooling and solidification experiments were designed and the experimental results support the nucleation theory. It was also indicated that the interfacial tensions between the oxides and liquid iron were the main limitations on applying the theory to experiments.

In the same year with Turpin and Elliot [116], Turkdogan [139] analyzed the kinetics of nucleation growth and flotation of oxides inclusions in liquid melt. It was assumed that the nuclei resulted from the homogeneous nucleation of deoxidation products. The growth of inclusions was controlled by the solute diffusion and the growth rate was derived as given in Eq. (3.39).

$$\bar{r} = \bar{r}_0 \left(\frac{C_0 - C_L}{C_{in}} \right)^{\frac{1}{3}} \tag{3.39}$$

In Eq. (3.39), $\bar{r}$ is the oxide radius in after growing; $\bar{r}_0$ is the radius of reactant diffusion zone which is defined by the number density of growing inclusions; C_0 is the initial concentration of the solute; C_L and C_{in} are concentrations in bulk melt and inclusions, respectively. Since the existing equilibrium at the inclusion/steel interface and the flux of reactants are equal, only one reactant (oxygen) needs to be considered in the calculation. Furthermore, the flotation of oxides was accounted using Stokes law. With the practical consideration, this approach was applied to study deoxidation efficiency and remove inclusions through calculating different number densities of growing inclusions. The calculated results showed that a critical number density could be achieved to reach the highest deoxidation efficiency.

Afterwards, Mathew et al. [140] proposed the conceptions taking account not only nucleation and growth, but also stokes and gradient collisions. Their analysis concluded that the collisions of the inclusions is the main reason for deoxidation products growth. The importance of the interfacial energy between inclusions and steel were addressed.

Based on the aforementioned concepts, Babu et al. [141] extended the application of classical nucleation and diffusion controlled growth theories to the weld metal deoxidation. In their model, they additionally induced the overall kinetics to describe transformation extent (ζ) as given in Eq. (3.40). Using this model, the Time-Temperature-Transformation (TTT) curves for various oxides were calculated as an example shown in Figure 3.14. It shows that the reaction kinetics of Al_2O_3 are faster than that of SiO_2. The further calculations and analyses concerned the influence of oxygen content, deoxidizing element concentrations and temperature on the inclusions characters. In a subsequent publication [142], the researchers coupled thermodynamics and kinetics as well as cooling curves of weld to simulate the inclusion formation. The calculated results from the proposed model including the composition, size, number density and oxidation sequence were verified with experimental results. The preliminary work on the coupled heat transfer, fluid flow and inclusion model were also discussed. As a continuous work [124,143,144], the research group published a more elaborated model accounting growth, dissolution, collision and coarsening of inclusions in the weld pool. Al_2O_3 was selected as an example. The calculated size distributions agree with the experimental results which indicate that this kind of fundamental model can be used to simulate the inclusions formation.

$$\zeta = 1 - exp\left\{-I\left(\frac{8\pi}{15}\right)\left(2D_L^O\frac{C_L - C_{inL}}{C_{in} - C_{inL}}\right)^{\frac{1}{2}} t^{\frac{5}{2}}\right\} \tag{3.40}$$

where I is the homogeneous nucleation number density; D_L^O is the diffusion coefficient of oxygen in liquid melt; t is time for inclusion formation; C_L, C_{in} and C_{inL} are the solute

concentrations in liquid steel, inclusion and at inclusion-liquid steel interface, respectively; and the solute is oxygen in this case.

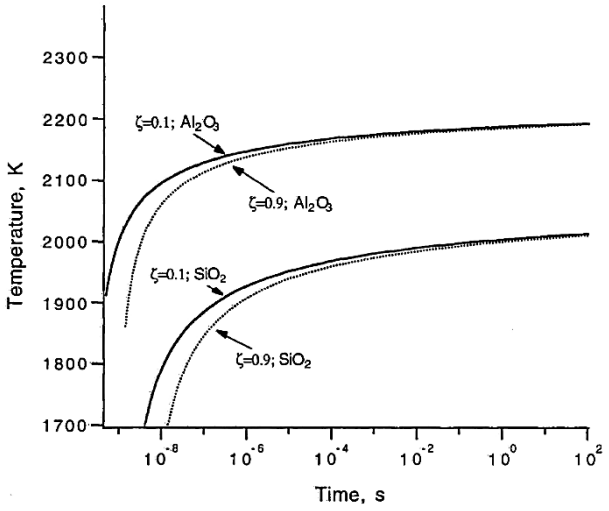

Figure 3.14. TTT curves of Al_2O_3 and SiO_2 with transformation extent ζ=0.1 and 0.9 [141].

Zhang et al. [145,146] established a model considering Ostwald ripening and collision growth instead of diffusion-controlled growth in the deoxidizing process. Another main character of their model is that the pseudomolecule of inclusions is assumed as the basic unit and the clusters of the pseudomolecule exist before nucleation. Using this model, the size distribution and evolution at different formation stages can be predicted. Later on, Zhang and Lee [127] improved the former model through considering more details on Ostwald ripening and various collisions. At the same time, a numerical method was introduced to reduce the load of the enormous computation. In the following, a similar mathematical model was proposed by Lei et al. [128]. In their model, the deoxidation products were divided into embryos and inclusion particles. The two parts with corresponding equations were separately solved to speed up the calculation. Their predictions on inclusion size distribution were consistent with the experimental results. In addition, the influence of diffusion coefficient and turbulent energy dissipation rate are also evaluated.

Apart from the formation in the melt, inclusions precipitating during solidification have received a large amount of attention, especially after introducing the concept of 'oxides metallurgy' [2,3]. Goto et al. [147–149] reported a coupled model of oxides growth and microsegregation for studying the precipitations during solidification as described in Figure 3.15. In the model, Eq. (3.29) is applied to estimate the growth of oxides and Ohnaka´s model [10] is used to predict solutes enrichments in the residual liquid. Figure 3.15 shows that oxides are assumed to form in the interdendritic liquid and grow with the driving force of segregated and equilibrium concentration difference. The consumptions of reactants were calculated with a local mass balance. Using the presented model the effects of cooling rate on the size evolution

and supersaturation for oxides were investigated. Note that in the calculation the number density of oxides was set as constant based on the experimental results.

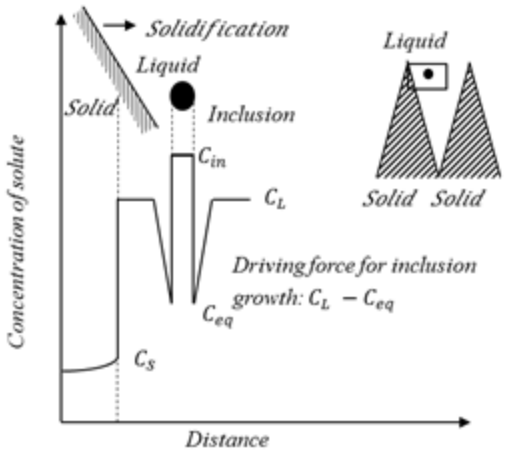

Figure 3.15. Schematic of inclusion precipitation and growth during solidification [149].

In the following, Ma and Janke [150] predicted the inclusion growth through mass balance without considering the role of oxygen in solid steel. They also calculated microsegregation with Ohnaka´s model [10]. Based on the former models, Liu et al. [151] applied the Ueshima´s model [152] to predict the solutes concentration changes in both solid and liquid. Then using overall mass balance to consider the consumption of solutes due to inclusion growing up, the oxygen content in solid can be accounted. Providing different constant number densities, the influences of cooling rate on the growth of inclusion with various initial radii were studied.

Rocabois et al. [19,20] combined nucleation and growth of inclusions with microsegregation to describe the formation process of titanium nitride. In the model, the classical nucleation theory is applied; thermodynamic equilibrium is calculated using CEQCSI [105]; the microsegregation is calculated with Lever Rule; and a mixed control of diffusion and interfacial reaction for inclusion growth is assumed as described in Eq. (3.41) and (3.42). With Eq. (3.41), the interfacial concentrations and flux can be solved. Using the presented model, the size distribution of the inclusions can be obtained, and the predicted TiN amounts evolution fit well with the experimental results. Then the model was extended to one complex solution for oxides by Lehmann et al. [21] which enables the calculation of size evolution as shown in Figure 3.16. In this case, a Al-Ti alloyed low carbon steel was calculated. It shows that at 1492 °C which is initial stage of the inclusion formation, the most numerous inclusions are always the smallest ones. With the growing, the particles size with the peak number densities obviously increases. When the temperature decreases from 1491 °C to 1484 °C, the size distribution shape remains due to the decreases of the supersaturation and nucleation rate, and the inclusions can continue to enlarge.

$$J = \frac{D_L^{Ti}}{r}\frac{\rho_{Fe}}{100M^{Ti}}([\%Ti]_L - [\%Ti]_{inL})$$
$$= \frac{D_L^{N}}{r}\frac{\rho_{Fe}}{100M^{N}}([\%N]_L - [\%N]_{inL})$$
$$= k_c\left(a_{inL}^{Ti}\cdot a_{inL}^{N} - K_{TiN}^{eq}\right) \quad (3.41)$$

$$4\pi r^2 M_{TiN} J dt = \frac{4}{3}\pi\rho_{TiN} d(r^3) \quad (3.42)$$

where J is the molar flux; D_L^{Ti} and D_L^{N} are the diffusion coefficients in liquid steel of Ti and N, respectively; ρ_{Fe} and ρ_{TiN} are the densities of liquid steel and TiN; M^{Ti}, M^{N} and M_{TiN} are the molar weights of Ti, N and TiN, respectively; $[\%Ti]$ and $[\%N]$ are the concentrations of Ti and N referred to 1% dilute solution; a_{inL}^{Ti} and a_{inL}^{N} are the activities of Ti and N at the interphase of inclusion and liquid steel; k_c is the kinetic constant; t is time; r is the radius of the particle.

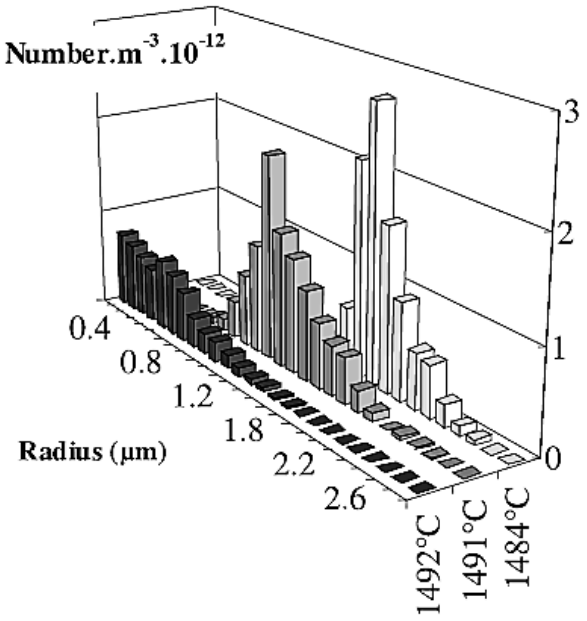

Figure 3.16. The size evolution histogram of the complex oxides during solidification [21].

3.6 Summary

Nonmetallic inclusions formation is unavoidable in modern steelmaking process, although continuous effort is pursued to improve steel cleanness in the final product. Inclusions are classified into different types from various perspectives: chemistry, source, size and formation period. Different types of inclusions have distinct characters which determine their effect. These effects are either negative effects on steel properties and processing or for the positive effects on creating a specific steel microstructure, and nonmetallic inclusions are of particular interest. A large amount of effort has therefore been made to adjust existing inclusions to preferable ones or utilize them through additions to the melt. For investigating inclusion formation,

thermodynamics and kinetics are fundamental. By using thermodynamics, it is possible to calculate the stability of inclusion phases and the chemical driving force. Furthermore, kinetics defines the growth rate and extent. On investigating the topic, the rapid development of computer sciences promotes the realization of developing and applying the powerful thermodynamic databases and mathematical models. The reviewed characteristic models are summarized in Table 3.4 and Table 3.5. Though these models have made tremendous contributions to controlling and understanding inclusion formation, further developments are still possible. For the models listed in Table 3.4, the microsegregation prediction can be optimized by an advanced model with reasonable dendrite structure and the local thermodynamic and kinetic parameters. A thermodynamic consistency progress is necessary for complete coupling the microsegregation and inclusion formation. Furthermore the unified thermodynamics offer more reliable calculations of inclusion stability and nucleation driving force. At the meantime, a comprehensive consideration on inclusion formation thermodynamics and kinetics can be made not only for single inclusion but also for multi-phase-inclusions.

The chemical reactions of inclusion formation mainly depend on the compositions in liquid steel. Thus the well calculated concentrations of solutes in the modeling process are necessary. When simulating the inclusion formation during solidification, microsegregation is essential as summarized in Chapter 2.

In the present work, through linking with thermodynamic databases, solute enrichments in the residual can beestimated using local partition and diffusion coefficients. Subsequently a completely coupled microsegregation and inclusion formation model using one thermodynamic data-file is designed to predict the precipitation process during cooling and solidification. The concepts and frame of the current thesis are described in Chapter 4.

Table 3.4. List of thermodynamic inclusion models [13,15,16,18].

Process	Author	Year	Inclusion stability	Microsegragtion		Annotations
				Model	Temperature	
Solidification	Yamada	1990	SOLGASMIX	Clyne-Kurz	Based on Fe-C phase diagram	Additional thermodynamic data
	Wintz	1995	CEQCSI	Clyne-Kurz	-	Solution phase is possible
	Choudhary	2009	FactSage	Clyne-Kurz	Based on Fe-C phase diagram	Methodology
	ICA	2010	ChemApp	IDS	Multi-components	Solution phase is possible

Table 3.5. List of kinetic inclusion models [19,116,139–141,146,149,150].

Process	Author	Year	Inclusion stability	Number	Size			Annotations
					Growth	Collision	Dissolution	
Liquid	Turpin	1966	Empirical	CN	-	-	-	On nucleation
	Turkdogan	1966	Empirical	CN	Diffusion	-	-	On deoxidation
	Mathew	1974	-	CN	Diffusion	Yes	-	Conceptions
	Babu	1995	Empirical	CN	Diffusion	Yes	Yes	Complete
	Zhang	2002	Empirical	CN	Coarsening	Yes	-	Pseudomolecule as basic unit
Solidif-ication	Goto	1994	Empirical	Constant	Diffusion	-	-	Mean size
	Ma	1998	Empirical	Constant	Diffusion	-	-	Mean size from mass balance
	Rocabois	1999	CEQCSI	CN	Diffusion and reaction	-	-	Single inclusions

Note: ‘CN’ means Classical Nucleation; ‘Empirical’ stands for empirical free energy equation; ‘Yes’ indicates the item was considered.

4 Modeling Process

After reviewing the work on microsegregation and inclusion modeling, the direction for advancing on studying this topic is clearly defined. In this chapter, as a map for the entire work, the core concepts and the steps to reach the final objective are described. Furthermore, the tools applied to construct the models are introduced. Subsequently, the progressive modeling work is depicted. First, a microsegregation model is developed based on the Ohnaka´s model [10] with local partition coefficients and diffusion coefficients. The effects of different parameters in the proposed model are discussed through comparing the calculations with the measured characteristic temperatures. Combining with this microsegregation model, a coupled model on MnS formation during solidification is proposed. The influences of the main related parameters on the formation of MnS are investigated. Additionally, the multi-phase-inclusions formation during cooling and solidification is modeled on the basis of the single inclusion (MnS) formation model. The comprehensive model contains a sub-model on inclusion formation thermodynamics. As a preliminary model, the parameters used in the calculations included both reported values and the adjusted ones, and the step values are defined by comparing the different calculations. These modeling works are progressively tested via experiments and simulations in Chapter 5.

4.1 Modeling concepts

Figure 4.1 displays the basic concept of the present modeling processes. Heat and mass transfer at the macroscopic scale, enrichment of elements, and the kinetics of the precipitation of phases at the microscopic scale are solved in a FORTRAN program. The initial conditions and parameters such as compositions, diffusion coefficients and cooling rates are put into the source code of the metallurgical models before calculation. For each calculation step, the composition is transferred to ChemApp [136] based on the thermodynamics of the FactSage [107], and the program libraries are used to determine the liquidus temperature, equilibrium partition coefficients at the solid/liquid interface, and volume fraction of the stable phases.

In this process, ChemApp plays an important role connecting the metallurgical model with thermodynamic databases. ChemApp is interface software developed by GTT Technologies, Herzogenrath, Germany, and this interfacial software can be linked to a source code written in FORTRAN, C/C++, Visual Basic® and Borland Delphi®. In this case, FORTRAN is applied as the programming language. Microsoft Visual Studio 2013 was used as the main frame provider and modern compiler. FactSage offers the powerful databases through an output ChemSage datafile. In this manner, the subroutines of ChemApp work together with the datafile to perform

thermodynamic calculations and post treatments. It is the connected ChemApp and database application that characterize the present modeling work.

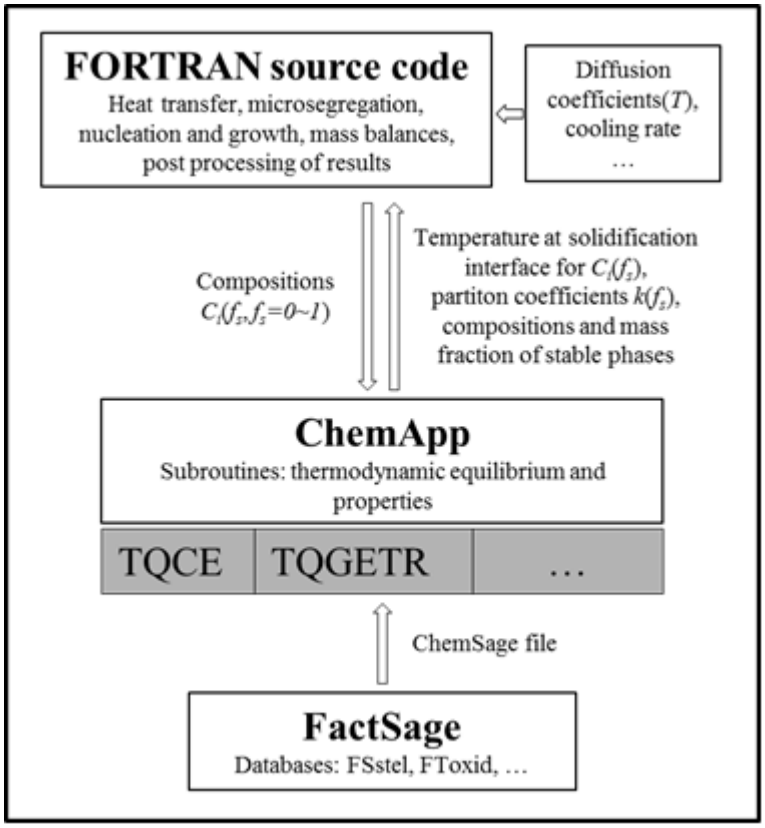

Figure 4.1. Concept of the modeling work [153].

4.2 Modeling structure

The modeling structure of the present work is displayed in Figure 4.2. As a first step, the microsegregation model is developed. Using the proposed model, systematic investigations are made to obtain the importance of various parameters on the predictions. The calculated results with the optimizing parameters are validated by the reported experimental results and other calculations. After achieving the acceptable correctness, the model is applied to provide feedback for database optimization and further development of inclusion models. At the second step, single inclusion formation during solidification is modeled where MnS is selected as the target, and this model couples microsegregation, thermodynamics and kinetics of inclusion formation. The parameters in the model are calibrated by the measured particle size distribution. Furthermore, the model is used to study the influences of cooling conditions and compositions on MnS formation. Finally, the multi-phase-inclusions competitively formation process is programmed based on the single inclusion case. As a precondition for the kinetics, the multi-oxides formation thermodynamics are calculated and confirmed with the experimental results. Then, a preliminary comprehensive model considering the microsegregation as well as thermodynamics and kinetics of multi-oxides formation is proposed. Additionally, there are

considerable difficulties to calibrate the comprehensive model from both carrying on experiments and measurements. The final case study using this model, however, can offer a valuable reference and deepen understanding on the multi-phase-inclusions formation.

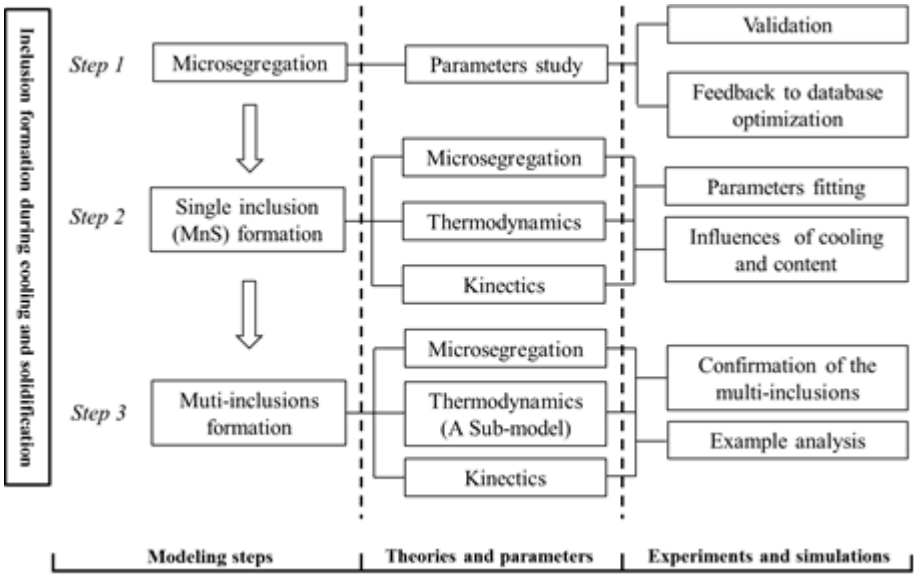

Figure 4.2. Modeling structure of the present work.

4.3 Microsegregation model

In previous predictions of steel microsegregation, the partition coefficients of solutes were assumed as constants and integrated analytical equations were applied. Additionally, most partition coefficients were calculated from binary and ternary systems. Partition coefficients however actually depend on the concentrations of various chemical components and temperature rather than being constants. Local partition coefficients for different compositions and temperatures are therefore desired for predicting microsegregation more accurately in various steels. Second, temperatures during the solidification process were often estimated using empirical equations from limited experiments in the aforementioned models. In the present model, the analytical equation in differential form from Ohnaka [10] was semi-integrated and applied with local partition coefficients and temperature-dependent diffusion coefficients. Additionally, multicomponent alloy effects and the formation of inclusions were considered, and the peritectic reaction was realized with the help of the thermodynamic library ChemApp [136]. In the model, thermodynamic equilibrium was calculated using ChemApp, which can access related databases from FactSage [135] such that the liquidus temperature at the solidification interface and local partition coefficients were achieved at each solidification step. In the model, the various parameters are of highest important to the prediction quality. A systematic investigation was thus performed on the influences of the parameters in this part.

4.3.1 Analytical equations

Ohnaka introduced a columnar dendrite diffusion model [10]. In this model, one-dimensional diffusion in the triangle area is considered as an approximation for the three-dimensional diffusion as shown in Figure 2.12. For considering the changes of the partition and diffusion coefficients, the solution of Ohnaka´s model (Eq. (2.25)) [10] was integrated into Eq. (4.1).

$$C_L^+ = C_L\{\frac{1-\Gamma\cdot f_S}{1-\Gamma\cdot(f_S+\Delta f_S)}\}^{\frac{1-k}{\Gamma}}, with\ \Gamma = 1-\frac{4\alpha k}{1+4\alpha} \tag{4.1}$$

where f_S represents the solid fraction; C_L^+ and C_L are the concentrations of solutes in the residual liquid at solid fractions of $f_S+\Delta f_S$ and f_S, respectively; k is the equilibrium partition coefficient between solid and liquid; α is the back diffusion coefficient, which can be calculated using Eq. (2.22); D_S is the solute diffusion coefficient in solid; t_f is the local solidification time; and λ_2 is the secondary dendrite arm spacing.

4.3.2 Parameters in the model

In the applied model, temperatures at the solidification interface and partition coefficients (k) were calculated using ChemApp. At each solidification step, for a multicomponent system, the phase transformation point from liquid to solid was detected after the activity of δ-ferrite or austenite approached one. Then, the concentrations of solutes in both liquid and solid and the temperature were determined. For simplification, Figure 4.3 describes a binary system of the above process. The diffusion coefficients (D) applied in the calculations are listed in Table 4.1, and the thermodynamic data file used in ChemApp was provided by the FSstel database of FactSage 7.0.

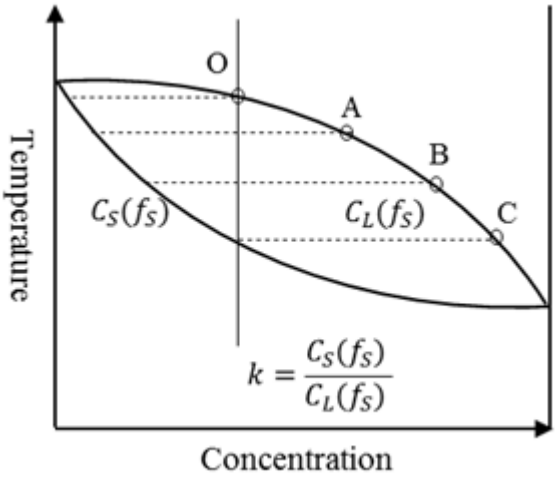

Figure 4.3. Schematic illustration of the determination of partition coefficients and temperatures.

The partition and diffusion coefficients used for the calculations were the average of the values between the current and former steps. The temperatures were updated in a loop until the difference between two adjacent values was less than 10^{-3} °C.

Secondary dendrite arm spacing was estimated using Eq. (4.2) [28], which is influenced by the local solidification time and initial carbon content. In the first step, the local solidification time is estimated. In the second step, the local solidification time is calculated after obtaining the solidus temperature. This process was repeated until the difference between two adjacent local solidification times was less than 10^{-4} seconds,

$$\lambda_2 = \left(27.3 - 13.1[\%C]^{\frac{1}{3}}\right) t_f^{\frac{1}{3}} \tag{4.2}$$

$$t_f = \frac{T_L - T_S}{R_C} \tag{4.3}$$

where λ_2 (μm) is the secondary dendrite arm spacing, $[\%C]$ is the initial concentration of carbon in weight percent, t_f (s) is the local solidification time, R_C (Ks^{-1}) is the cooling rate, and T_L and T_S (°C) are the liquidus and solidus temperatures, respectively.

Table 4.1. Diffusion coefficients of solutes [13,152,154].

Elements	D_δ (m^2s^{-1})	D_γ (m^2s^{-1})
C	0.0127Exp(-81301/RT)	0.0761Exp(-134429/RT)
Si	8.0Exp(-248710/RT)	0.3Exp(-251218/RT)
Mn	0.76Exp(-116935/RT)	0.055Exp(-249128/RT)
P	2.9Exp(-229900/RT)	0.01Exp(-182666/RT)
S	4.56Exp(-214434/RT)	2.4Exp(-212232/RT)
O	0.0371Exp(-96349/RT)	5.75Exp(-168454/RT)
Al	5.9Exp(-241186/RT)	5.15Exp(-245800/RT)
Ti	3.15Exp(-247693/RT)	0.15Exp(-251000/RT)
Ca	0.76Exp(-224430/RT)	0.055Exp(-249366/RT)

R: 8.314 $Jmol^{-1}K^{-1}$; T: temperature in Kelvin.

In addition, the peritectic reaction was considered in a simple way similar to other analytical models: If ChemApp detects that the solid phase at the solidification interface changed from δ-ferrite to austenite, the peritectic reaction temperature and the corresponding solid fraction are defined by the model. When exceeding the solid fraction for the peritectic reaction, the partition and diffusion coefficients of austenite were applied. The peritectic transformation, the subsequent transformation of δ-ferrite to austenite, is neglected.

Due to the solubility limit of manganese and sulfur, manganese sulfide could precipitate in the residual liquid during solidification. In the present model, the thermodynamic stability of manganese sulfide in the residual liquid was computed by ChemApp at each solidification step. Once the sulfide formed, it was treated as inert in the subsequent calculations. The concentrations of corresponding solutes in the residual liquid would decrease due to the formation of the sulfide. Then, equilibrium compositions in the residual liquid were obtained for the next calculation step. Within this work, elements most important related to microsegregation are discussed: C, Si, Mn, P and S. More complex alloying systems and the consideration of the thermodynamic stability of oxides will be discussed in future publications and a flow chart of the present model is presented in Figure 4.4.

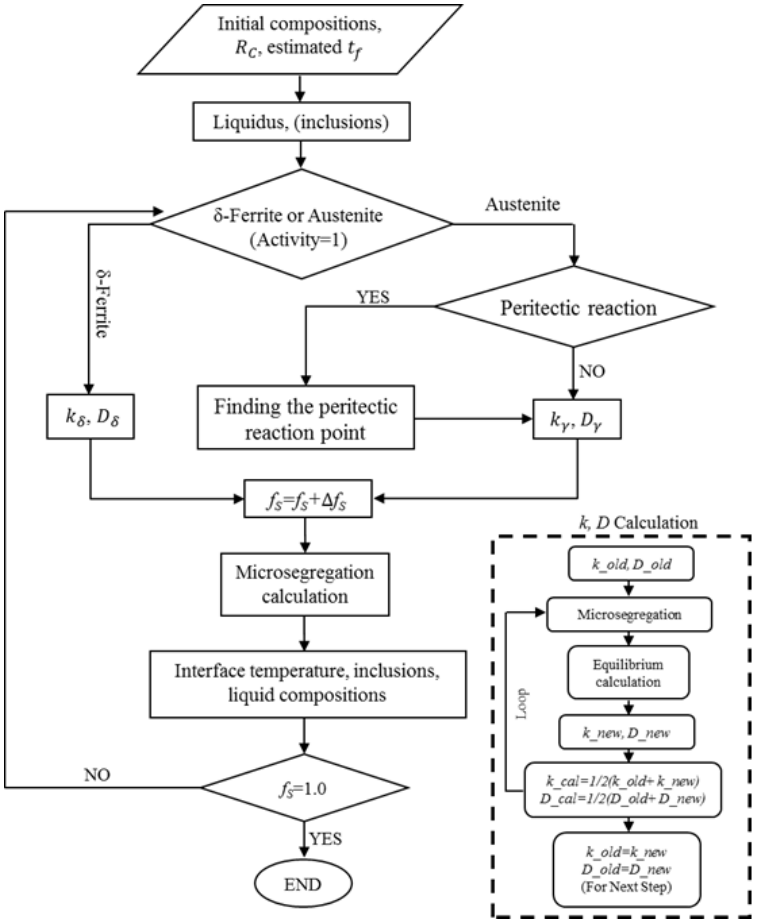

Figure 4.4. Flow chart of the microsegregation model.

4.3.3 Influences of the parameters

For investigating the influences of various parameters on microsegregation predictions, a series of carbon steels reported by Schmidtmann and Rakoski [155] was selected to calculate using the suggested model under the cooling rate of 10 Ks^{-1}. The chemical compositions the steels are listed in Table 4.2. Meanwhile, Schmidtmann and Rakoski [155] measured Zero Strength Temperature (ZST) and Zero Ductility Temperature (ZDT) by high temperature tensile testing

which are indirect benchmarks for the microsegregation models. ZST is the critical temperature below which solidifying materials start to transmit strength inside the dendritic structure of both solid and liquid steel. ZDT is defined as the temperature at which ductility first starts to increase during the solidification process. The schematic of ZST and ZDT is shown in Figure 4.5. Note that ZDT also stands for the non-equilibrium solidus temperature. Both ZST and ZDT are strongly influenced by solute enrichments and can comprehensively reflect the phenomenon. Additionally, hot tears generally form between ZST and ZDT; thus, it is also desirable to reasonably estimate ZST and ZDT through solidification modeling. Thus, in this section the ZST and ZDT analyzed from the present model with different parameters were compared with the reported experiment results. According to the statistical analysis and experimental results from Won et al. [156], the temperatures at solid fractions of 0.75 and 0.99 were considered as ZST and ZDT. Note that the experimentally determined ZST values correspond with the calculated solid fractions of between 0.65 and 0.8, whereas ZDT commonly varies just between 0.98 and 1.0. Therefore, it cannot be expected that the ZST fits to the calculated temperature for a solid fraction of 0.75.

Table 4.2. Chemical compositions of the steels from Schmidtmann (mass%) [155].

Sample series	C	Si	Mn	S	P	Number
S1	0.015–1.00	0.210–0.420	1.48–1.66	0.0110–0.0170	0.0090–0.0130	15
S1-1	0.05	0.35	1.56	0.013	0.011	
S1-2	0.32	0.37	1.54	0.015	0.011	
S1-3	0.59	0.40	1.62	0.017	0.011	

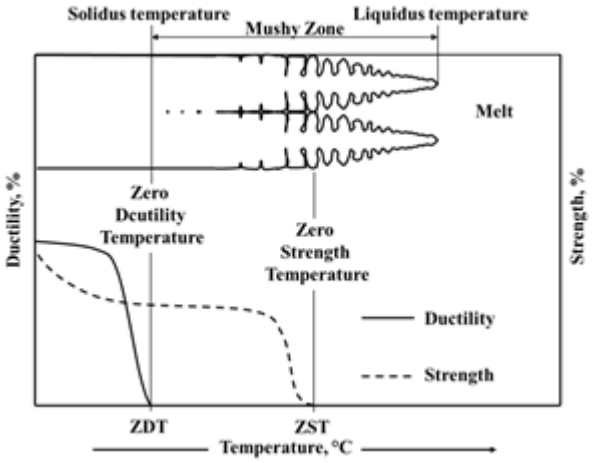

Figure 4.5. Schematic of ZST and ZDT [157].

4.3.3.1 Solid fraction step

For each modeling study, the step value for calculation is a pre-requisite parameter which needs to be carefully defined. The simulated phenomenon is a continuous progress, and models with the finer steps are more close to real situation, while they spend more time. In contrast, the rough step may lead to low quality predictions. Therefore, the proper step value is appreciated. In current case, the calculations with different solid fraction steps (5×10^{-2}, 1×10^{-2}, 5×10^{-3} and 1×10^{-3}) for the S1-1, S1-2 and S1-3 steels from S1 series (Table 4.2) were compared and the calculated results of the S1-1 are shown in Figure 4.6. Figure 4.6 (a) shows that that the temperature profile predicted with step value of 5×10^{-2} displays an obvious difference with others after the solid fraction 0.9, and the estimated carbon concentrations with the step values of 5×10^{-2} and 1×10^{-2} are different with those with the finer step values. In Figure 4.6 (b), the enrichments of sulfur calculated with the step values of 5×10^{-2} and 1×10^{-2} shows considerable differences with other predictions after solid fraction of 0.95; note that the sharp decreases of sulfur is caused by the precipitation of manganese sulfide (MnS) and it indicates that the calculations with different step values can also affect the predictions of precipitations. For the concentrations of manganese, the predictions with the step values of 5×10^{-2} and 1×10^{-2} are similar but distinct with others while the main reason for their soars and difference at the late stage of solidification are caused by the peritectic reaction. On both concentrations profiles of solutes and temperatures, the calculations with the step values of 5×10^{-3} and 1×10^{-3} are nearly the same.

Figure 4.7 shows the predicted Mn and S concentrations for S1-2 and S1-3 which have higher carbon contents. Figure 4.7 (a) reveals that the calculated S and Mn concentrations of sample S1-2 with the step value of 5×10^{-2} are different with those from other calculations at the late stage of solidification, particularly after the formation of MnS (sharp decrease of S). Similar with S1-2 steel, Figure 4.7 (b) shows that due to the rough step value the precipitation chance of MnS are not well predicted in the case of 5×10^{-2} and this leads to further differences of concentrations of sulfur. The predicted carbon concentrations and temperature profiles with various step values for these two steels are quite close, respectively, which are not displayed.

Based on the above discussion, using the step values of 1×10^{-3} can obtain good accurateness but with longer time. The calculated results with the step value of 5×10^{-3} present no difference with those with the step values of 1×10^{-3}. From the perspectives of both accurateness and efficiency, the step value of 5×10^{-3} is applied to further calculations.

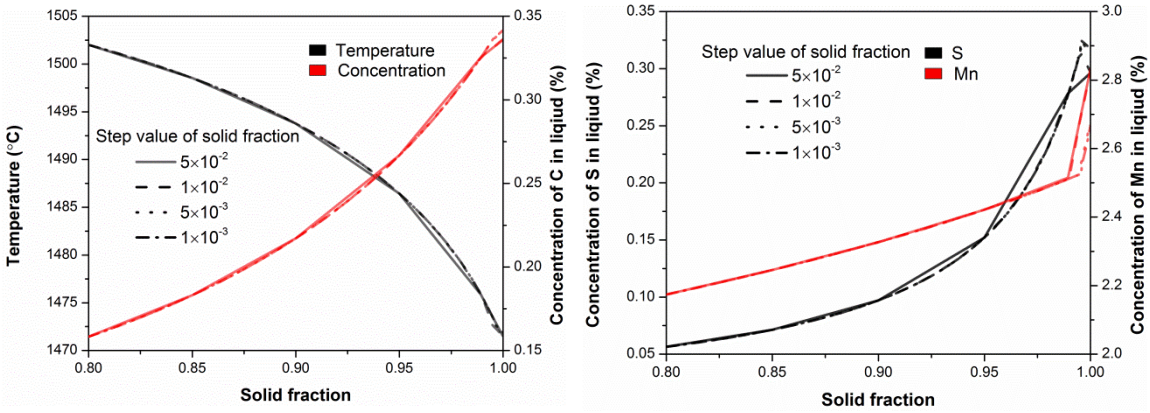

(a) (b)

Figure 4.6. Influence of step values on predictions (a) temperature and C concentration (b) Mn and S concentrations for S1-1 steel: note that the sharp changes of Mn and S concentrations at the solid fraction of approximate 0.99 are due to peritectic reaction; afterwards the sudden decreases of S concentration are caused by MnS formation.

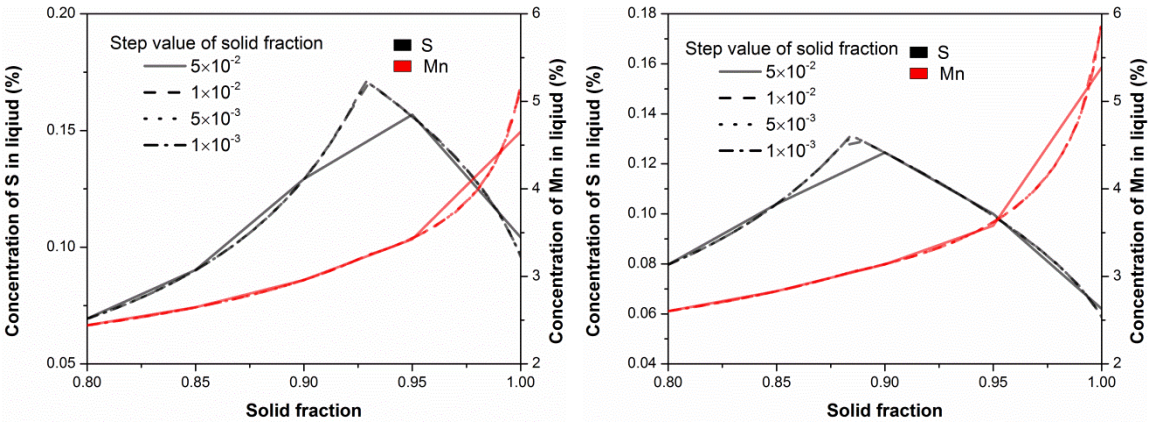

(a) (b)

Figure 4.7. Influence of step values on predicted Mn and S concentrations for (a) S1-2 and (b) S1-3 steel: the sharp decreases of S concentration are caused by MnS formation; the changes of Mn concentration resulted from MnS formation are not noticeable.

4.3.3.2 Partition coefficients

In this section, differences of the partition coefficients between the present model and literature values (see Figure 4.8) are studied, and their influence on microsegregation is discussed. Note that for comparisons, only partition coefficients calculated by concentrations in mass percent unit were selected.

As the first example, S1-2 steel (see Table 4.2) was calculated with variable partition coefficients from the present model referred to as locals in the diagrams. The calculation process for the local partition coefficients has already been explained in Figure 4.3. The calculation results for the solid fraction-dependent partition coefficients were compared with constant partition coefficients from the literature (listed in Table 4.3) and first calculated values

of local partition coefficients (given in Figure 4.8), which were set as the initial values when the solid phase appears. Differences in partition coefficients and their influence on solute microsegregation are shown in Figure 4.8.

Table 4.3. Constant equilibrium partition coefficients used in other models [13,152,154].

Elements	$k^{\delta/L}$	$k^{\gamma/L}$
C	0.19	0.34
Si	0.77	0.52
Mn	0.77	0.785
P	0.23	0.13
S	0.05	0.035

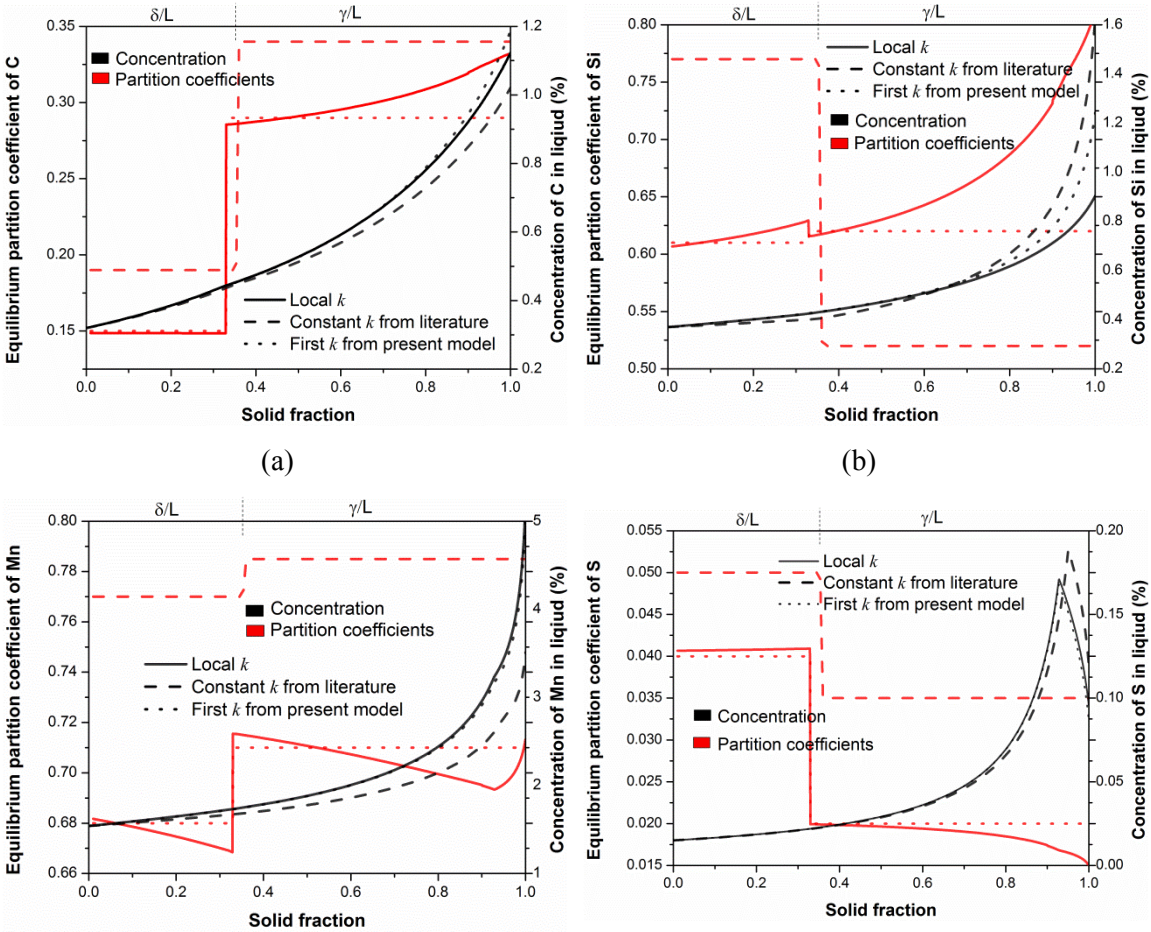

Figure 4.8. Different partition coefficients (left axis) and their influences on microsegregation (right axis) of (a) C, (b) Si, (c) Mn and (d) S in S1-2: 'Local k' mean the partition coefficients calculated at each solidification step; 'First k from present model' are the first calculated values and taken as constants in the following solidification process.

Figure 4.8 shows there are distinct differences between the partition coefficients calculated by the present model and those from the literature. In detail, the partition coefficients of carbon, manganese and sulfur from the current calculations are lower than those from the literature (Figure 4.8 (a), (c), and (d)). The calculated partition coefficient of silicon between δ-ferrite (δ) and liquid steel (*L*) is lower, but that of austenite (γ) and liquid is higher than the value from the literature (Figure 4.8 (b)). In addition, through comparison with the first *k* values, it is suggested that the partition coefficients of solutes change differently during the solidification process. The partition coefficient of carbon at the δ/*L* interface almost remains constant and that of γ/*L* increases gradually; the partition coefficient of silicon of δ/*L* increases slightly and to a large degree in the case of γ/*L*; the partition coefficient of manganese at both δ/*L* and γ/*L* interfaces decreases at a small scale, but it suddenly increases because of the formation of manganese sulfide; regarding sulfur, its partition coefficient of δ/*L* remains almost constant and that of γ/*L* decreases gradually. The changes of the partition coefficients can be explained by Eq. (2.3). During solidification, the solute standard chemical potentials in both liquid and solid and activity coefficients in liquid and solid change with compositions and temperature, which comprehensively lead to partition coefficient changes.

Additionally, the solute concentration profiles predicted with different partition coefficients exhibit obvious differences. On the one hand, compared with the concentrations calculated with constant partition coefficients from the literature, the concentrations of carbon and manganese in the residual liquid calculated with the local partition coefficients are higher because of the lower partition coefficients, as shown in Figure 4.8 (a) and (c). The concentration of Si is first higher and then decreased as a result of the differences of partition coefficients, as described in Figure 4.8 (b). For sulfur in Figure 4.8 (d), the concentration is lower at a late stage of solidification, although the local partition coefficient of sulfur is always lower than that from the literature, which is attributed to the formation of manganese sulfide. Note that the difference in partition coefficients also influences the formation of manganese sulfide, as indicated by the different points of sharp decreases in the sulfur concentration. On the other hand, the influence of the partition coefficient changes on microsegregation should also be considered. In this case, compared with the results calculated with the first *k* values, the carbon and silicon concentrations calculated with the local partition coefficients are considerably lower, which results from the significant increases in the partition coefficients. Regarding manganese and sulfur, little concentration differences are observed because of small changes in their partition coefficients. It therefore appears to be very important to apply reliable partition coefficients when predicting microsegregation with models.

Figure 4.9 displays the temperature profiles predicted with different partition coefficients for steel S1-2 and it shows the clear differences of temperature changes during solidification. The

differences result from the together work of different segregations of solutes. Especially at the late stage, the roles of different partition coefficients on temperatures are magnified with the increasing serious segregation.

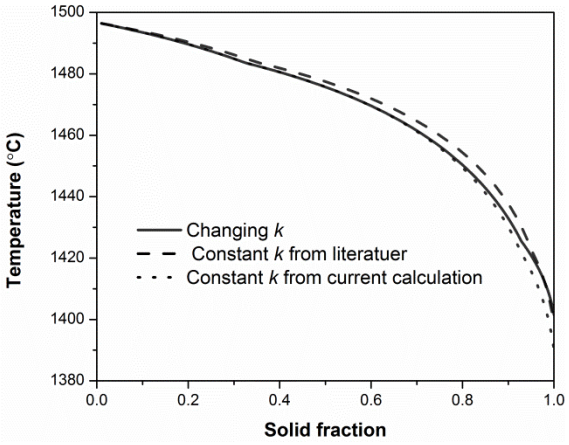

Figure 4.9. Temperature changes with solid fraction.

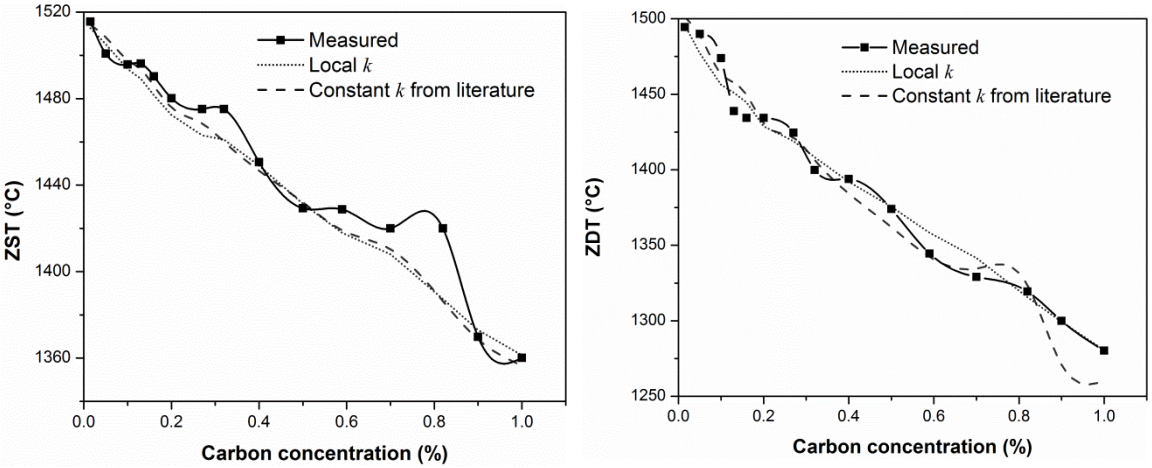

(a) (b)

Figure 4.10. Predicted (a) ZST and (b) ZDT with different partition coefficients along with measurements [155].

ZST and ZDT were analyzed with local partition coefficients and constant values and compared with measurements from Schmidtmann [155] under the above-described conditions. The comparison is given in Figure 4.10. This figure shows that both ZST and ZDT from the microsegregation analysis are consistent with the measured data, but distinct differences exist for the results calculated with different partition coefficients. To identify the predictions that agree closer to the experimental results, statistical differences between predictions and experimental data for ZST and ZDT, including maximum (Max), minimum (Min), mean values (Mean) and standard deviations, were analyzed and are listed in Table 4.4.

Table 4.4. Differences in characteristic temperatures between the measured data and calculations with different partition coefficients.

Partition coefficients	Local *k*		Constant *k*	
Measured-Calculated (°C)	ZST	ZDT	ZST	ZDT
Max	**32.77**	**17.66**	33.70	28.99
Min	**-3.89**	**-13.61**	-7.52	-18.82
Mean	7.66	**0.14**	**5.60**	3.88
Standard Deviation	**9.41**	**9.49**	9.58	13.43

As shown in Table 3, the ZST and ZDT calculated with local partition coefficients exhibit smaller differences with the measured data than those calculated with constant partition coefficients. In detail, with regard to ZST, the differences between the predictions with local partition coefficients and the measured data have smaller Max and standard deviation values compared with those calculated with constant partition coefficients, although a larger but closer Mean value. For ZDT, all of the discussed statistical values calculated with local partition coefficients are smaller than those calculated with constant ones. In particular, the mean difference of ZDT between predictions with local partition coefficients and measured data is only approximately 0.14 °C. Therefore, it is suggested that the predictions with local partition coefficients are more reliable.

4.3.3.3 Liqiudus temperatures

Temperature is an important parameter and desirable result when applying a microsegregation model to simulate solidification of steels. In former models, liquidus temperatures were estimated by empirical equations from limited experiments. In the present model, liquidus temperatures of the residual liquid were determined by means of Gibbs energy minimization with the help of ChemApp. Additionally, multicomponent and multiphase effects were considered during the calculation. In this part, some common liquidus temperature equations from literature were applied to the present model and the estimated characteristic temperatures were compared with those calculated by ChemApp, and S1 steels in Table 4.2 were calculated. The temperature equations discussed in this part can be found in *references [158–161]*. Similar to the previous section, ZST and ZDT predicted by different temperature equations were compared with experimental data from Schmidtmann [155] as shown in Figure 4.11.

As demonstrated in Figure 4.11, ZST and ZDT calculated by ChemApp fit the closest to the measured data and the estimations from Kawakami [158] are similar to those from ChemApp. For ZST and ZDT from other equations, considerable differences to the measured data exist, especially for high carbon steels. To quantify the difference between calculations and

measurements, the statistical differences of ZDT were analyzed which is in the same way as the data given in Table 4.4. The results are listed in Table 4.5. ZDT calculated from ChemApp show the smallest differences and the estimations by Kawakami´s equation also provides good reference values. In particular, the mean difference of calculations from ChemApp and measurements is only 0.14 °C which indicates that ChemApp could well predict the liquidus temperature during the solidification process.

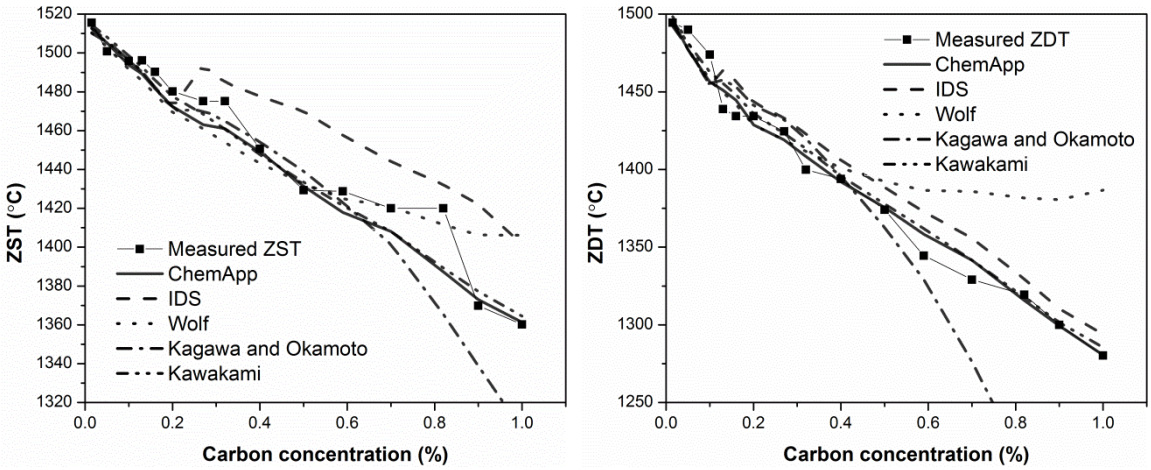

(a) (b)

Figure 4.11. Predicted (a) ZST and (b) ZDT with different empirical equations and ChemApp.

Table 4.5. Differences of ZDT between measured data and calculations [158–161].

Different predictions	ChemApp	IDS(REG)	Wolf	Kagawa	Kawakami
ZDT (Measured-Calculated,°C)					
Max	17.66	19.79	16.68	181.93	**11.24**
Min	**-13.61**	-28.11	-106.40	-19.95	-17.29
Mean	**0.14**	-11.29	-24.68	31.30	-4.22
Standard Deviation	9.49	13.85	36.47	62.28	**8.72**

4.3.3.4 Diffusion coefficients

To investigate the influence of diffusion coefficients on microsegregation predictions, S1 steels were calculated by the proposed model with different diffusion coefficients from literature (Table 4.1) and IDS (Table 4.6). Compared with those from literature, the diffusion coefficients from IDS depend on not only temperature, but also solute concentrations.

Taking S1-2 steel (0.32% C) as an example, the differences of the diffusion coefficients and their influences on corresponding solutes enrichments are displayed in Figure 4.12. There are obvious differences of diffusion coefficients in ferrite of C, Si and S from IDS and literatures but they are close to each other in austenite as shown in Figure 4.12 (a), (b) and (d). The predicted microsegregation using the different diffusion coefficients are similar and indicate that

the diffusion coefficient in ferrite has little influence on microsegregation. Additionally, the diffusion coefficients of Mn from both estimations are similar (Figure 4.12 (c)). In addition, considering the effects of concentrations do not change decreasing trends of diffusion coefficients with decreasing temperature, the sharp decreases of the diffusion coefficients result from a peritectic reaction. To identify the situation in austenite, S1-3 steel with higher carbon content (0.59%) was studied, and the effects of diffusion coefficient on C and Mn segregations are displayed in Figure 4.13.

Table 4.6. Diffusion coefficients from IDS.

Elements	D_δ (J/mol)	D_γ (J/mol)
C	0.11448Exp(-95612/RT)	0.22748Exp[-(147901 -232634*X_C)/RT]
Si	1.06044Exp[-(225655-194642*X_{Si})/RT]	0.05241Exp(-228114/RT)
Mn	0.64688Exp(-222320/RT)	0.15394Exp[-(264583-356861*X_C -42912*X_{Mn})/RT]
P	1.68416Exp[-(221525-320887*X_P-86797*X_{Mn}+427012*X_{Si})/RT]	0.00214Exp[-(163392-80434*X_C -25097*X_{Mn})/RT]
S	2.51924Exp(-207941/RT)	15.69238Exp(-245992/RT)

Where X_i is the mole fraction of element i.

As shown in Figure 4.13 (a), while there are distinct differences of diffusion coefficients of C from the two estimations, the concentration profiles are nearly coincident. As for Mn (Figure 4.13 (b)), the diffusion coefficient from literature is smaller than that of IDS and the corresponding predicted segregation is stronger. This can be explained by the less back diffusion for the case using the literature diffusion coefficient. Compared with the situation of C and Mn, it is believed that the diffusion coefficient plays a more important role on the segregation of large atoms and weak diffusivity solutes. Although the difference of diffusion coefficients of Mn decreases with solid fraction, the difference of segregation is more evident due to the high content. Particularly, the difference of final Mn segregation is considerable. Hence, to clarify the effect of diffusion coefficient on Mn nominal segregation, S1 steels were calculated with the diffusion coefficients as compared in Figure 4.14.

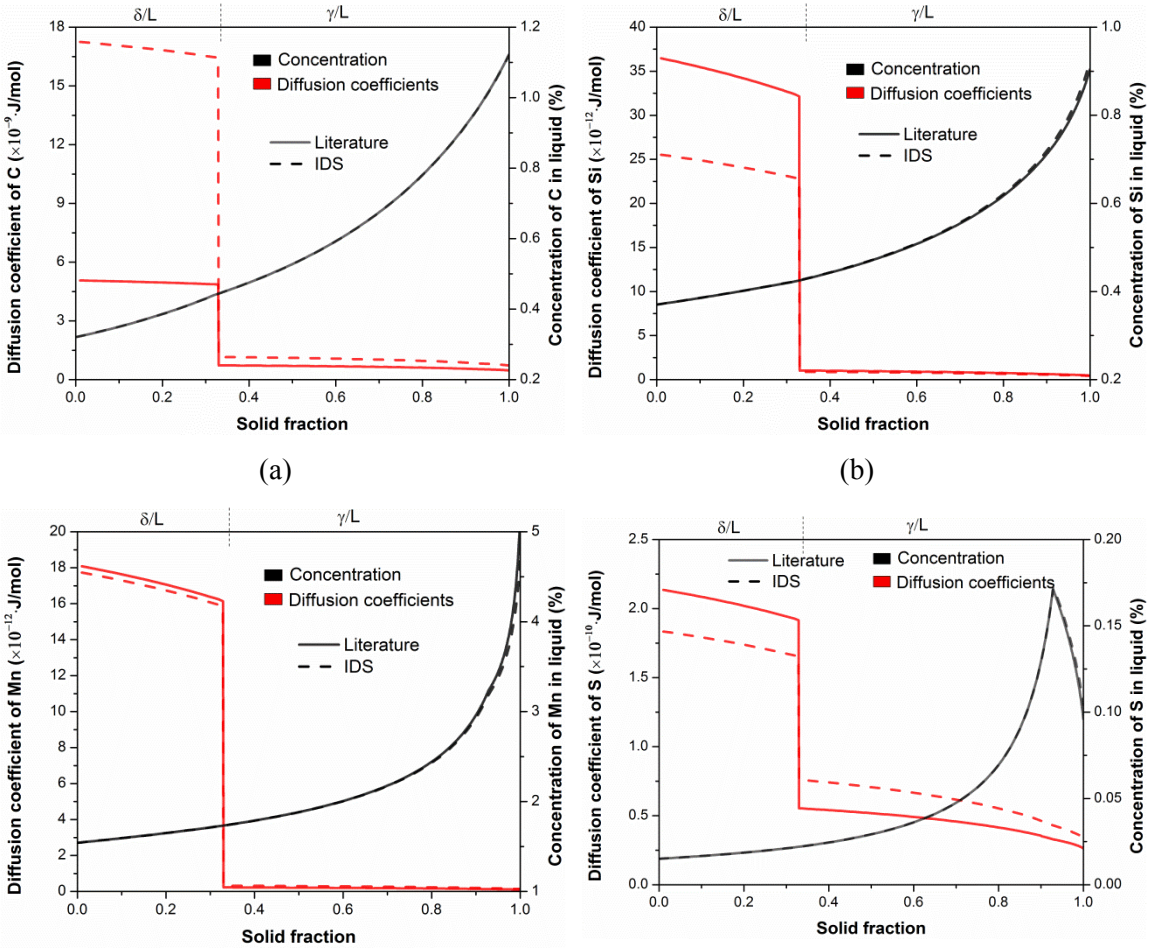

Figure 4.12. Different partition coefficients and their influences on microsegregation of (a) C, (b) Si, (c) Mn and (d) S in S1-2 steel: the sharp deceases of S concentration are due to MnS formation.

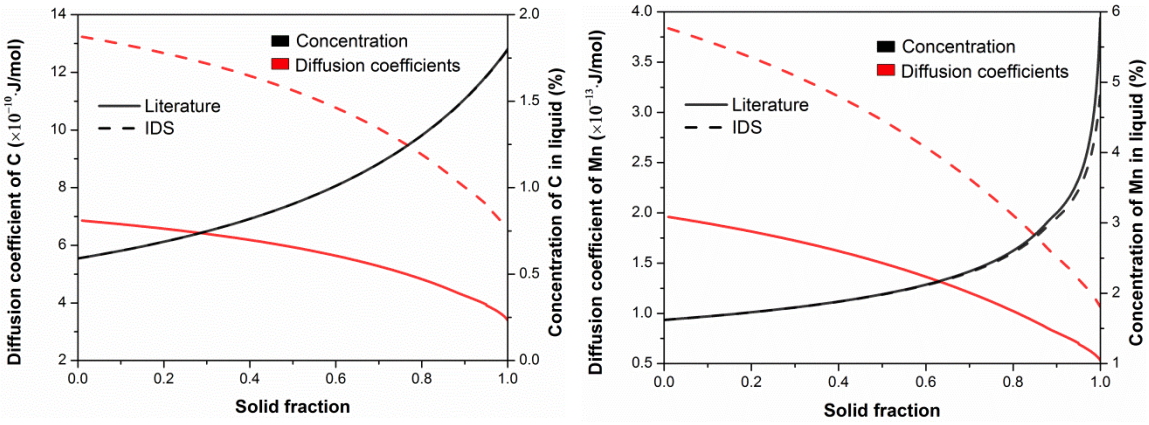

Figure 4.13. Different partition coefficients and their influences on microsegregation of (a) C and (b) Mn in S1-3 steel.

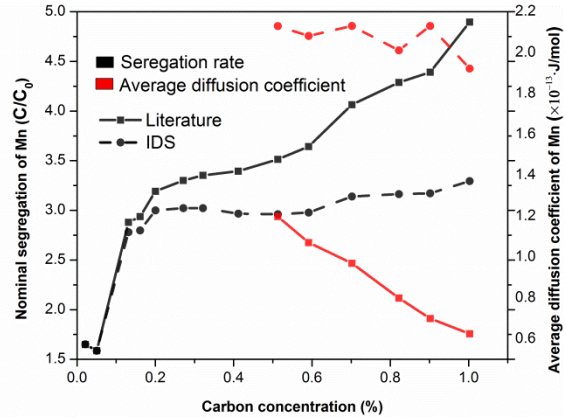

Figure 4.14. The predicted nominal segregations of Mn using different diffusion coefficients for S1 steels.

Figure 4.14 shows that the differences in nominal segregation enlarge with increasing differences between the diffusion coefficients in literature and IDS. The diffusion coefficients from IDS are larger than those from literature resulting in a lower calculated nominal segregation. The consideration of solutes concentrations in diffusion coefficients from IDS leads to the relatively constant and slight-fluctuation profile, while those from literature linearly decrease with lower temperature and higher C content. Note that here just the average diffusion coefficients in the austenite are presented. The diffusion coefficients in ferrite from literature and IDS are similar. The relatively higher diffusivity of solutes in ferrite cannot be mixed with those in austenite, since the characters of diffusion coefficients in austenite would be hindered.

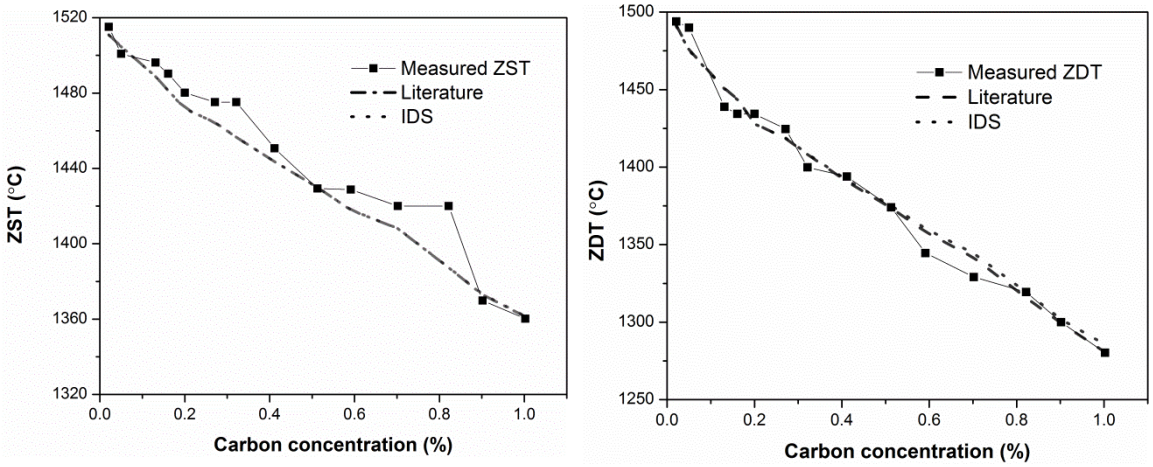

(a) (b)

Figure 4.15. Predicted (a) ZST and (b) ZDT with different diffusion coefficients along with measurements [155].

Figure 4.15 compares the measured characteristic temperatures (ZST and ZDT) with the analyzed values using different diffusion coefficients. The figure shows that the ZST and ZDT calculated from different diffusion coefficients are similar and agree with the measured data. To

achieve clear comparisons, a statistical analysis was made on the difference of characteristic temperatures between measured data and calculations with different diffusion coefficients as listed in Table 4.7. For all the comparing items, the values analyzed using the two types of diffusion coefficients have marginal differences, and the calculations using the diffusion coefficients from literature have the smallest mean difference with the measured data for both ZST and ZDT. The comparisons of other items support that the predicted characteristic temperatures using IDS diffusion coefficients are closer to measured data.

Table 4.7. Difference of characteristic temperatures between measured data and calculations with different diffusion coefficients.

Diffusion coefficients	Literature		IDS	
Measured-Calculated (°C)	ZST	ZDT	ZST	ZDT
Max	32.77	17.66	**32.59**	**14.71**
Min	-3.89	**-13.61**	**-3.77**	-15.72
Mean	**7.66**	**0.14**	8.02	-2.54
Standard Deviation	9.41	9.49	**9.58**	**8.86**

In total, the above discussion suggests that the diffusion coefficient only has a relatively small influence on the microsegregation of solutes if studying carbon steels. An exception is the final nominal segregation of Mn which is affected strongly by the diffusion coefficient particularly in high carbon steels. Another point is that the influence of diffusion coefficient becomes stronger with increasing solid fraction and segregation. This indicates that the influence of diffusion coefficients on microsegregation in high alloy steels should be paid attention. For conventional carbon steels the diffusion coefficients from IDS accounting concentrations effects bring few changes, while it is more reasonable to apply such kind of both temperature and concentration dependent diffusion coefficients for predicting microsegregation of high alloy steels.

4.3.3.5 Secondary dendrite arm spacing

Secondary Dendrite Arm Spacing (SDAS) as diffusion field in the microsegregation model is another primary parameter. In addition to the empirical equation from Bernhard [28] (Eq. (4.2)), another two typical equations from Thomas [33] (Eq. (4.4)) and IDS [17] (Eq. (4.5)) are introduced in this section. Compared with Eq. (4.2), Eq. (4.4) and Eq. (4.5) depend on cooling rate (R_C) instead of local solidification time (t_f). Furthermore besides carbon concentration ($[\%C]$), the estimation of SDAS from IDS (Eq. (4.5)) also accounts for the concentrations of silicon ($[\%Si]$) and manganese ($[\%Mn]$) but they have much less importance than carbon

concentration. All these equations are based on the measured final secondary dendrite arm spacing. The discussed three equations have been applied to study the influence of SDAS on the microseregation of S1 steels.

$$\begin{aligned}\lambda_2 &= [169.1 - 720.9[\%C]]{R_C}^{-0.4935} \quad (for\ 0 < [\%C] \leq 0.15) \\ &= 143.9{R_C}^{-0.3616} \cdot [\%C]^{[0.5501-1.996[\%C]]} \quad (for\ 0.15 < [\%C])\end{aligned} \tag{4.4}$$

$$\begin{aligned}\lambda_2 = 200{R_C}^{-0.33}\, exp[&-(0.6844[\%C] - 0.14788[\%C]^2 + 0.0069[\%Si] \\ &+ 0.0674[\%Mn])^{0.4}]\end{aligned} \tag{4.5}$$

Figure 4.16 displays the calculated SDAS of various steels in S1 series using the equations provided by Bernhard (Eq. (4.2)), Thomas (Eq. (4.4)) and IDS (Eq. (4.5), where the steels are characterized by the different carbon contents. It is seen that SDAS from different estimations have considerable difference and change differently. Calculated SDAS from the equations of both Bernhard and IDS decrease gradually with carbon content, though estimations from IDS´s equation are much larger than those from Bernhard´s equation. The SDAS calculated using Thomas´s equation fluctuate with the increase of carbon content and reach the minimum and maximum values at carbon content of 0.1% and 0.6%, respectively. The SDAS are set as constants during microsegregation predictions so that the final nominal segregations are used to instruct the influence of SDAS in this part as shown in Figure 4.17.

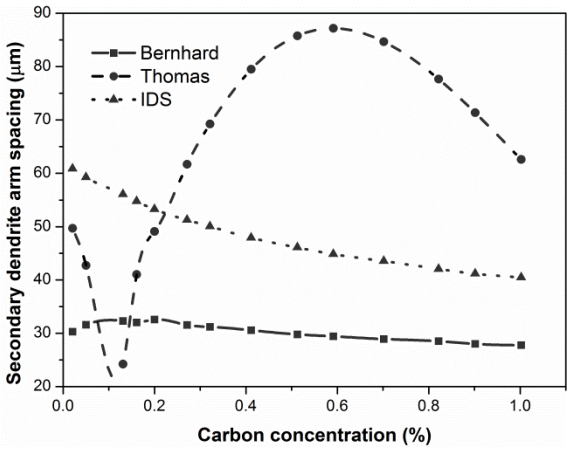

Figure 4.16. Different SDAS of various steels in S1 series (characterized by carbon content).

Figure 4.17 shows that SDAS has little influence on C nominal segregation (Figure 4.17 (a)), while significant influences on Mn, P and S segregation (Figure 4.17 (b), (c) and (d)) which is related to the diffusion abilities of the solutes. Combined with Figure 4.16, Figure 4.17 (a), (b) and (c) suggest that larger SDAS lead to stronger nominal segregations of C, Mn and P. For instance, the estimated SDAS using Thomas´ equation are the largest ones in the steels containing 0.3–1.0%C which results to the highest segregation of C, Mn and P. The situation for S is inverse, which means calculating with larger SDAS results in less segregation as shown in Figure 4.17 (d). This inverse trend of sulfur is attributed to the formation of sulfide.

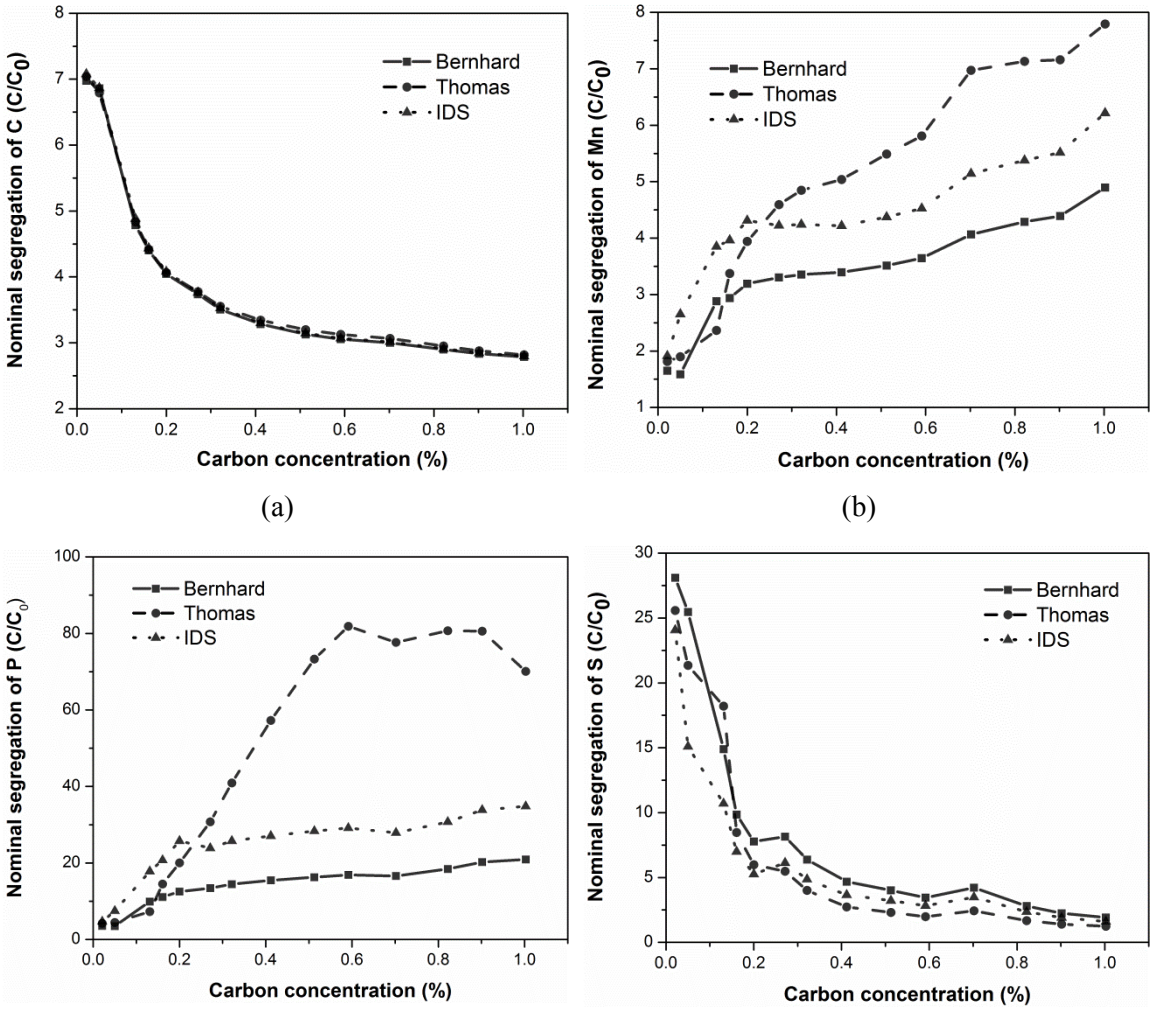

Figure 4.17. Influence of SDAS on (a) C, (b) Mn, (c) P and (d) S nominal segregations for S1 steels.

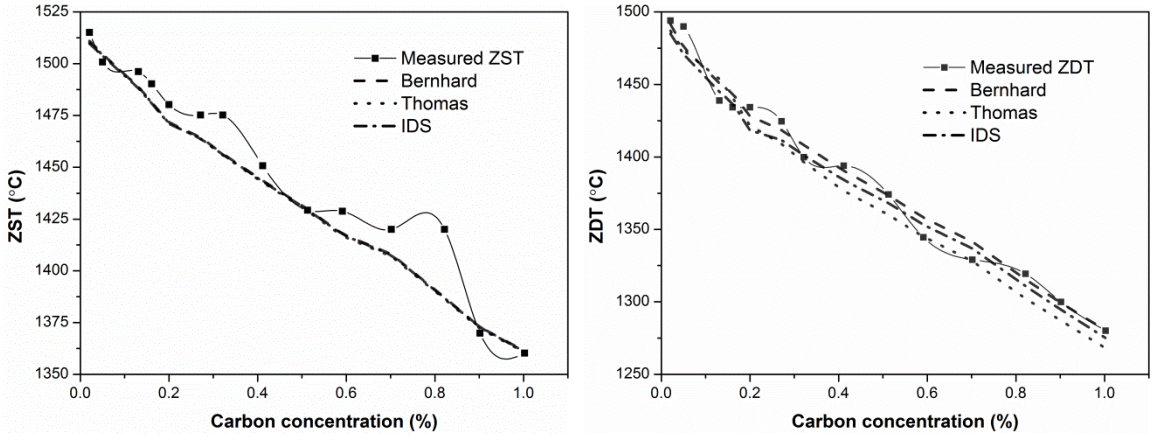

Figure 4.18. Comparisons of (a) ZST and (b) ZDT predicted with different SDAS and measured values [155].

The comparisons of characteristic temperatures calculated with different SDAS and measured values are shown in Figure 4.18. The figure shows that SDAS has little influence on ZST but considerable influence on ZDT. Both ZST and ZDT calculated with different SDAS agree well with the measured data. Using the same technique as for studying other parameters, the difference between analyzed results with different SDAS and measured data was calculated as listed in Table 4.8. About ZST, most compared items of difference (Max, Mean and Standard Deviation) support that the calculations with the SDAS estimated by Bernhard´s equation are closer to the experimental results. As for ZDT, the predictions using Bernhard´s SDAS equation have just 0.14 °C mean difference to the measured data; other compared items predicted with different SDAS are similar. Hence the calculations using Bernhard´s equation are satisfying.

Table 4.8. Difference of characteristic temperatures between measured data and calculations with different SDAS Equations.

SDAS Equations	Bernhard		Thomas		IDS	
Measured-Calculated (°C)	ZST	ZDT	ZST	ZDT	ZST	ZDT
Max	**32.77**	17.66	33.65	**17.31**	33.06	19.00
Min	-3.89	-13.61	-3.47	-14.83	**-2.98**	**-8.65**
Mean	**7.66**	**0.14**	8.71	7.70	8.57	4.66
Standard Deviation	**9.41**	9.49	9.65	9.88	9.52	**8.78**

Overall, a microsegregation model linked to the thermodynamic databases was suggested. Using the present model to calculate the microsegregation for S1 series steels and comparing the analyzed ZST and ZDT with the experimental results, the reasonability of parameters selection are illustrated to some extent. The influences of various model parameters on the microsegregation predictions are realized after comparing different calculations. Due to the high sensitivity of microsegregation to solute partitioning, the local partition coefficient is preferable and reasonable. Though the diffusion coefficient has little influence on the solutes microsegregtion in carbon steels, the roles of it on solute enrichments in high alloy steels should be paid adequate attention. Meanwhile, applying both concentration and temperature dependent diffusion coefficients is preferred. Normally larger SDAS lead to stronger segregation and the influence is more significant for high segregation elements. Temperature is also important to microsegregation which can comprehensively reflect the phenomenon and influence the calculations of other parameters such partition and diffusion coefficients. The temperature considering multi-components and multi-phases is more reliable. The above systematic

investigation on the related parameters in this model is in favor of further modeling work and application.

4.4 Model of MnS formation during solidification

As a second step of the present modeling work, a program on single inclusion formation was developed on the basis of the above described microsegregation model. Manganese sulfide (MnS) was selected as the target inclusion. MnS forms in nearly every steel grade and is highly influenced by microsegregation. The latter can lead to anisotropy of the steel matrix and act as a possible starting point for crack formation or corrosion [162,163]. Apart from these negative effects, in the field of 'Oxide Metallurgy' [2,3], MnS – as single-phase inclusion or together with titanium oxides – is known to act as potential nuclei for the formation of acicular ferrite [86,87]. In addition, the formation of MnS prevents internal cracks resulting from the appearance of FeS and reduces the hot tearing segregation [164]. Two factors have a significant impact on number density, size distribution and total amount of formed MnS: Cooling rate and sulfur content. Both parameters play an important role for process control and optimization, especially during casting and can therefore directly affect the final product quality. It is not surprising that MnS formation has thus been intensively studied in the last few decades. Mathematical modeling provides a useful tool to investigate the formation of inclusions during the solidification of steel. However, an enhanced model covering microsegregation, thermodynamics and kinetics has not been published thus far.

A deeper understanding of the nucleation and growth of manganese sulfide during the solidification of steels is desirable to reduce, control, and even benefit from them. To simplify the calculations, the physical assumptions of the present model are as follows:

- Only MnS forming in residual liquid is considered in this work. The particles trapped into the solid are assumed to be inert. The particles distribute homogeneously in liquid steel.
- MnS are independent particles. Nucleation, growth and collision occur separately for the particles.
- The morphology of the particles is spherical.
- Diffusion controlled growth is assumed. A local equilibrium exists at the interface of the inclusions and liquid steel.

Figure 4.19 describes the flow chart of the proposed model. The present model combines microsegregation and MnS formation thermodynamics and kinetics. The solute enrichments are calculated using the proposed model based on Ohnaka´s model [10] which has been described

in Chapter 4.3. An empirical equation for MnS formation thermodynamics is applied after the selecting calculations. The Particle Size Distribution (PSD) [165] and Particle Size Grouping (PSG) [166] methods are applied to model the size evolution process. For each solidification step, in the residual liquid, the number density of nuclei was calculated by Becker´s theory [110]; the growth of existing particles was calculated with Zener´s model [123], and the collision of particles was treated in a simple way based on Brownian motion. After each step, the particle size distribution of MnS and its total amount were obtained. The concentrations of solutes accounting for the consumption of inclusion formation were used in the next microsegregation calculation.

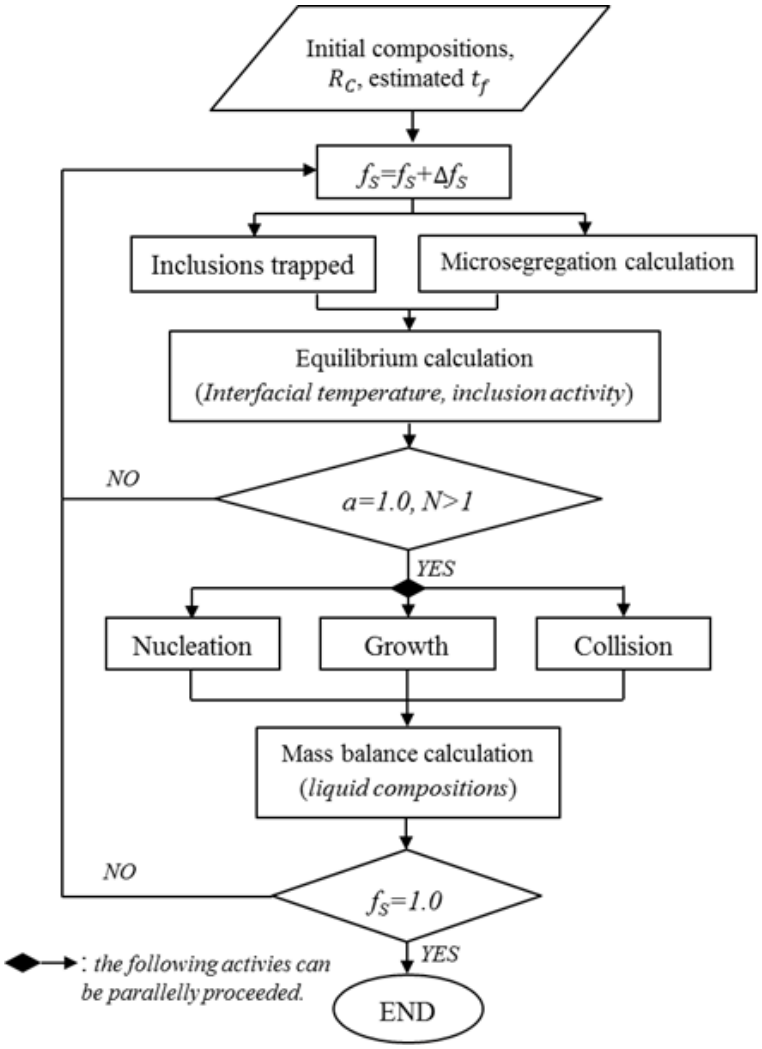

Figure 4.19. The flow chart of the model on MnS formation.

4.4.1 Thermodynamics

As discussed in Chapter 3.4, thermodynamics define the stability of inclusion phase and the chemical driving force for the formation kinetics. The reliable thermodynamics of inclusion formation is necessary. Due to the microsegregation of manganese (Mn) and sulfur (S), MnS forms in the residual liquid as given in Eq. (4.6). It is believed that MnS is

thermodynamically stable when the real concentration product (K) is larger than the solubility product (K^{eq}). The solubility and real concentration products can be calculated using Eq. (4.7) and Eq. (4.8), respectively, which are further used to calculate the chemical driving force of nucleation. Note that the description of MnS formation in the databases is not mature and under development. So in this part, five empirical equations in the format of Eq. (4.7) reported by different authors were applied to thermodynamically evaluate the MnS formation as listed in Table 4.9.

$$[Mn] + [S] = MnS \tag{4.6}$$

$$\log(K_{MnS}^{eq}) = -A/T + B \tag{4.7}$$

$$K_{MnS} \approx C_L^S \cdot C_L^{Mn} \tag{4.8}$$

where A and B are two constants, where $[Mn]$ and $[S]$ represent the soluble manganese and sulfur in the residual liquid; MnS represents solid manganese sulfide formed in the liquid steel; and C_S and C_{Mn} (mass%) are segregated concentrations in the liquid.

Figure 4.20 shows the solubility products estimated by different equations at 1500 °C. The figure shows that the solubility products reported by the authors show significant differences. In this figure, the lower value of solubility product means the easier formation of MnS. For example, with 2% Mn, the necessary concentrations of S for MnS formation range from 0.2% to 0.8%. The estimations using Xia´s equation has lowest values and are the most favorable to the MnS precipitation, while the solubility products calculated from Choudhary´s equation offer the most demanding formation concentrations. In addition, with the decreasing temperature, solubility product of MnS formation will decrease, which is obtained from Eq. (4.7).

Table 4.9. Equations for calculating solubility products of MnS formation.

Author	$\log(K_{MnS}^{eq}) = -A/T + B$		Reference
	A	B	
Ueshima	8625	4.74	[167]
Choudhary	8817	5.16	[16]
Oikawa	9200	5.30	[168]
Valdez	8431	4.61	[169]
Xia	8750	4.63	[170]

To select the proper equation for evaluating the MnS formation thermodynamics, the MnS amount for P1 and P3 steels was predicted and compared with experimental results. The chemical compositions of selected steels are listed in Table 4.10. The calculations were

performed using the present microsegregation model coupling with the equations of MnS formation (listed in Table 4.9). The microsegregation model itself can also thermodynamically predict the inclusion amount using ChemApp, whose predictions are also compared. When using the outside empirical equation to evaluate the MnS formation, this original function in the model is set as dormant. Once MnS formed, it is inert and accumulates in the further calculation. At each step, the equilibrium concentrations in the residual liquid were taken for the next calculation, which is the way of solutes consumptions.

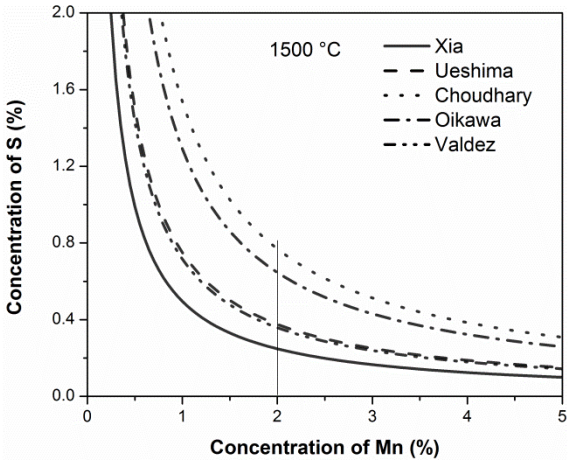

Figure 4.20. The equilibrium concentrations of Mn and S from different solubility products of MnS formation.

The samples were from the Submerged Split Chill Tensile (SSCT) experiment and measured with Scanning Electron Microscope (SEM), which is described in detail in Chapter 5.2.1. Note that it is difficult to accurately identify the amount of MnS with experiments and measurements so the experimental results offer the references of 'trend'. The calculated and experimental results are compared in Figure 4.21 and Figure 4.22, respectively.

Table 4.10. Chemical compositions of analyzed steels for MnS formation.

Samples	C	Si	Mn	S	P
P1	0.22	0.03	1.40	0.0060	0.0055
P2	0.22	0.03	1.46	0.0050	0.0048
P3	0.21	0.04	1.50	0.0021	0.0036

Figure 4.21 (a) shows that the predicted MnS forms at higher temperature with the higher mass fraction which leads to the higher solidus temperature. Note that the curves in Figure 4.21 (a) end at the solid fraction of one. Coinciding with the explanation on the solubility products (Figure 4.20), the predication with Xia´s equation has the largest MnS amount while that from

Choudhary´s equation shows the least. The calculation using ChemApp has a medial value. Figure 4.21 (b) compares the predicted final amount with the measured values (labeled as M1 and M2) from different laboratories. For both cases, the measured MnS amounts are larger than the calculated ones, and indicate that Xia´s equation provides the result closest to measured values.

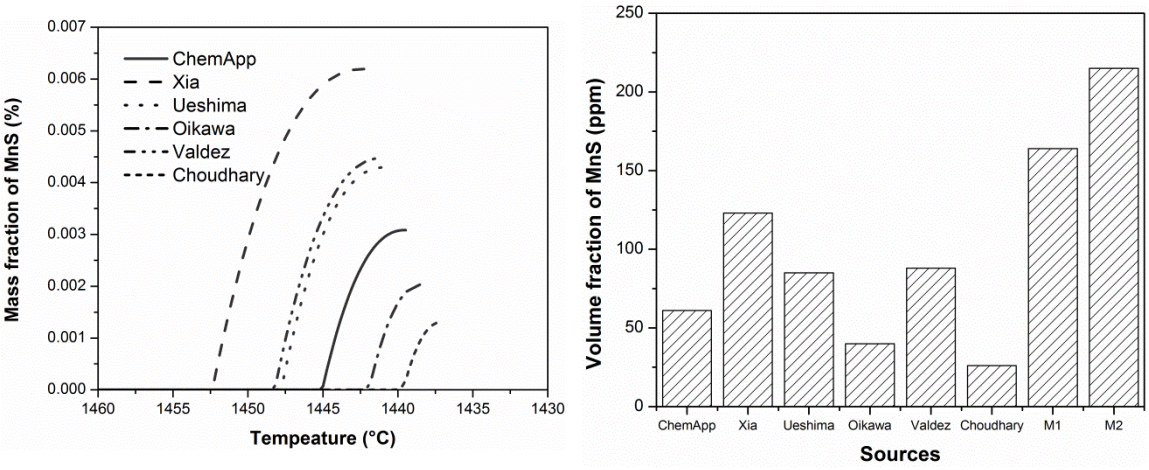

(a) (b)

Figure 4.21. Calculated and measured MnS amounts for P1 steel with different empirical equations (a) calculated precipitation process and (b) comparisons of final amount: M1 and M2 are the different measured values.

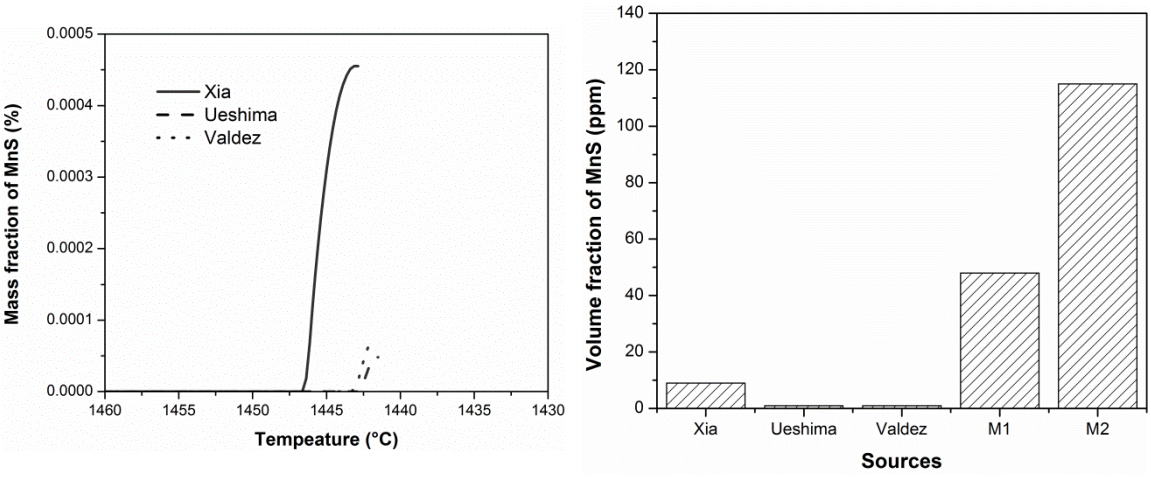

(a) (b)

Figure 4.22. Calculated and measured MnS amounts for P3 steel with different empirical equations (a) calculated precipitation process and (b) comparisons of final amount: M1 and M2 are the different measured values.

In contrast to P1 steel, P3 steel has less sulfur content and only three equations predict that MnS can form in this steel as shown in Figure 4.22 (a). The predicted amount from Xia´s equation is still the largest one while the others are almost zero. In practice, there are considerable MnS amounts being measured (M1, M2 in Figure 4.22 (b)). As aforementioned, while the measured

amounts of MnS just offer the 'trend' references, Xia´s equation offer the most reasonable thermodynamic predictions for MnS formation according to the above discussion. It will be thus applied for the further calculations on MnS nucleation and growth during solidification. Note that though ChemApp and the corresponding thermodynamic database cannot offer favorable prediction on MnS formation, the large advantages of them cannot be denied.

4.4.2 Kinetics

4.4.2.1 Nucleation

Classical nucleation theory is applied to the model. For simplicity, homogeneous nucleation is considered in the current case. The chemical driving force is calculated with Eq. (4.9) which is corresponding to the Gbiibs energy change of inclusion (ΔG_{in}) in Eq. (3.12). Combining Eq. (3.15) to Eq. (3.17), the nucleation number density of the system at each solidification step is determined by Eq. (4.10).

$$\Delta G = RTln(\frac{K_{MnS}^{eq}}{K_{MnS}}) \tag{4.9}$$

$$N(f_S) = I(f_S) * \frac{(1-f_S)*100}{\rho_{Fe}} * \tau \tag{4.10}$$

where K_{MnS}^{eq} and K_{MnS} are solubility and real concentration products, respectively; $N(f_S)$ and $I(f_S)$ ($m^{-3}s^{-1}$) are the number and nucleation rate at the solid fraction of f_S, respectively; and τ is the time period for one solidification step; '100' means the total amount of steel is 100 g.

4.4.2.2 Growth

The growth of the spherical particle is assumed to be controlled by diffusion of the solutes in liquid steel. Zener´s equation [123], as given in Eq. (3.25), is used to calculate the growth rate. There also exists a local equilibrium at the inclusion/liquid steel interface. According to previous studies [171,172], the diffusion flux (J) towards the inclusion is proportional to the concentration gradient and can be calculated using Eq. (4.11). For the given reaction of MnS formation (Eq. (4.6)), it is assumed that at the interface, the diffusion fluxes of Mn and S are equal as given in Eq. (4.12). From Eq. (4.11) and Eq. (4.12), Eq. (4.13) is derived. Eq. (4.14) is from the thermodynamic equilibrium at the inclusion-liquid steel interface. Combining Eq. (4.13) and Eq. (4.14), the interfacial concentrations of the solutes can be solved.

$$J = \frac{D_L}{r}\frac{\rho_{Fe}}{100M}(C_L - C_{inL}) \tag{4.11}$$

$$J^{Mn} = J^S \tag{4.12}$$

$$\Longrightarrow \frac{C_L^{Mn} - C_{inL}^{Mn}}{C_L^S - C_{inL}^S} = \frac{M^{Mn}}{M^S} \cdot \frac{D_L^S}{D_L^{Mn}} \tag{4.13}$$

$$C_{inL}^{Mn} \cdot C_{inL}^{S} = K_{MnS}^{eq} \tag{4.14}$$

where J is the diffusion flux of solute; D_L is the diffusion coefficient in liquid steel; r is the particle radius; ρ_{Fe} is the density of liquid steel; M is the molar weight of the solutes, and the superscripts Mn and S stand for manganese and sulfur, respectively; the concentrations (C) in the equiations are in mass percent (mass%).

4.4.2.3 Collisions

Collisions of the particles in liquid steel have important effects on the inclusion size distribution. Brownian motion, Stokes collision and turbulent collision are normally considered when studying the inclusion coalescence in steelmaking vessels, such as RH degasser and casting tundish [128,129]. During the solidification process at the dendritic scale, however, it is difficult to calculate the collision frequencies in the same manner as in metallurgical vessels due to the lack of corresponding parameters. For turbulent collision, in particular, it is impossible to determine the turbulent energy caused by the solidification interface movement, which is non-negligible. To reasonably consider collision, therefore, a collision factor (f) is introduced based on Brownian motion collision. This is a factor for enhancing the value of collision frequency function by considering other types of collisions in a simple manner. Brownian motion collision is more representative in the studied radius range compared with Stokes collision, as shown in Figure 4.23.

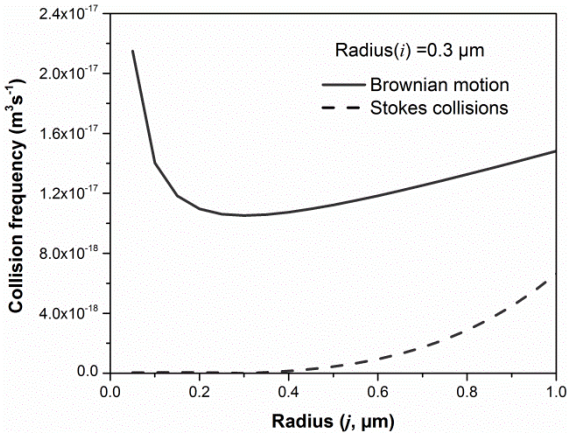

Figure 4.23. Comparison of the values of Brownian motion and Stokes collision frequency functions.

In Figure 4.23, the values of Brownian motion and Stokes collision frequency functions are calculated using Eq. (3.31) and Eq. (3.32). It is assumed that the average radius of MnS is 0.3 μm and the size ranges from 0 to 1.0 μm in the targeted system. It is found that Brownian motion causes collision that is several times stronger than Stokes collision in the particle size range. The nominal total collision frequency function in the model is hence calculated based on the Brownian motion collision frequency function together with the collision factor as given in

Eq. (4.15). The collision frequency is calculated with Eq. (4.16). The radius of particles generated by collisions is calculated according to the volumes of particles before collisions. Eqs. (4.15) and (4.16) are derived based on Eqs. (3.30), (3.31) and (3.34). Note that the collision factor is an adjustable parameter and fitted to the experimental results.

$$\beta'(r_i, r_j) = f \cdot \beta_B(r_i, r_j) \tag{4.15}$$

$$N_{ij} = \beta'(r_i, r_j) \cdot n_i \cdot n_j \tag{4.16}$$

where $\beta_B(r_i, r_j)$, $\beta'(r_i, r_j)$ (m^3s^{-1}) are the Brownian motion and the nominal total collision frequency functions, respectively, for particles with a radius of r_i and r_j (m) and N_{ij} ($m^{-3}s^{-1}$) is the collision frequency of the particles with number densities of n_i and n_j (m^{-3}).

4.4.2.4 Class model

Particle Size Distribution (PSD) [165] is a useful and widely applied method to describe the evolution process of inclusion formation and precipitation. In the method, the size histogram is characterized by the size classes and corresponding number density of each class. For the classification of size during nucleation and growth, Maugis and Gouné [173] suggested an approach in which each radius defines one size class. At each calculation step, a new size class is generated due to nucleation and existing classes of particles that grow simultaneously. For a phenomenon involving collision, however, it is difficult to consider each radius as a one size class because of the breadth of the particle size distribution. Fortunately, it has been illustrated that the Particle Size Grouping (PSG) method is effective for solving this problem [166]. Inspired by the aforementioned approaches, the following method (Figure 4.24) is applied to treat size classes for MnS formation in the solidification process:

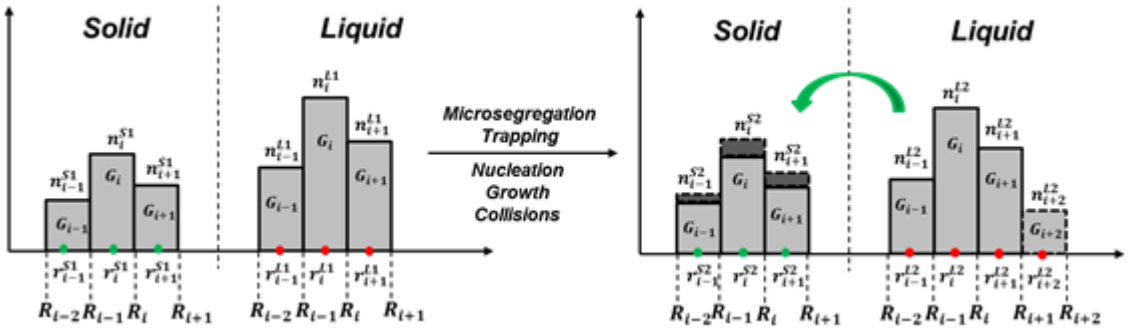

Figure 4.24. Schematic illustration of the Particle-Size-Grouping.

- The size of the particles is classified into several groups (G_i) according to the boundary values (R_i) in both solid and liquid steel. The groups are characterized by the average radius (r_i) and related number density (n_i). The superscripts $S1$ and $L1$ indicate that it is in the Solid and Liquid at the current ('1') calculation step, respectively. $S2$ and $L2$

represent the subsequent ('2') step after a series of activities, such as trapping, nucleation and growth.

- Nucleation: The particles created by nucleation with the radius and number density (r_0, n_0) are classified into the first group (G_1). As given by Eq. (4.20), the number density (n_1^{L2}) of G_1 at the second step is the sum of n_0 and existing number density (n_1^{L1}). The average radius changes to r_1^{L2} based on the calculation with total volume and number (Eq. (4.21)).

$$n_1^{L2} = n_1^{L1} + n_0 \tag{4.17}$$

$$r_1^{L2} = \sqrt[3]{\frac{(r_1^{L1})^3 \cdot n_1^{L1} + {r_0}^3 \cdot n_0}{n_1^{L1} + n_0}} \tag{4.18}$$

- Growth: The particles after growing from $(r_{i-1}^{L1}, n_{i-1}^{L1})$ to (r_g, n_g) can be grouped into G_{i-1} or G_i. If $R_{i-2} < r_g \leq R_{i-1}$: they belong to G_{i-1} (the same group before growing); the size of this group is $r_g (r_{i-1}^{L2} = r_g)$ and the number is n_g $(n_{i-1}^{L2} = n_g)$. If $R_{i-1} < r_g \leq R_i$, they upgrade to the larger group G_i; the number of the group (n_i^{L2}) becomes the sum of n_i^{L1} and $n_g (n_i^{L2} = n_i^{L1} + n_g)$; and the radius of this group renews to r_i^{L2} as calculated in Eq. (4.19).

$$r_i^{L2} = \sqrt[3]{\frac{(r_i^{L1})^3 \cdot n_i^{L1} + {r_g}^3 \cdot n_g}{n_i^{L1} + n_g}} \tag{4.19}$$

- Collision: The new size class (G_{i+2}) is easier to create due to collisions compared with diffusion controlled growth. The calculation of the radius and number are similar to that described in the aforementioned method, and the number of particles contributing to the collisions is reduced.

- The inclusions in solid steel are trapped particles and inert in the following solidification process. Therefore, at each calculation step, the number densities of the particles in different classes increase according to the trapped number (dark volumes in Figure 4.24) in the corresponding classes. The trapped number or amount of each group in the liquid is proportional to the step value of the solid fraction as given in Eq. (4.20) [13]. The average radius of each class is obtained based on the total volume and number of particles in the group.

$$\text{Amount}_{\text{trapped}} = \text{Amount}_{\text{in liquid}} * \Delta f_S/(1 - f_S) \tag{4.20}$$

- At one solidification step, the radius and number of particles in different size groups, as well the size classes, are refreshed once after the inclusions experience all of the activities (trapped, nucleation, growth and collision). Note that the boundary values of

the size group (R_i) are settled during the calculation. Hence, the particles can be classified into the suitable group according to their own radius (r_i) and the boundary values.

4.4.2.5 Mass balance

Figure 4.25 schematically describes the behaviors of inclusions during solidification. As already mentioned, only the inclusions formed in the residual liquid are considered. The trapping of particles by the solidification interface is treated in a simple manner which is calculated using Eq. (4.20).

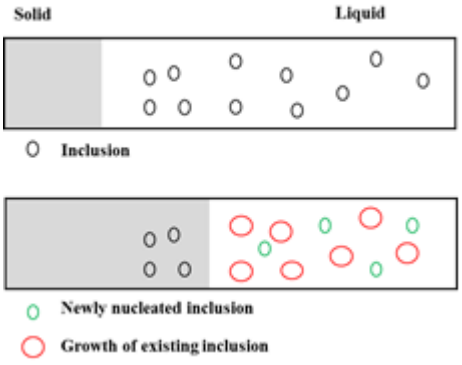

Figure 4.25. Schematic of inclusion behaviors during solidification.

At each solidification step, the nucleation and growth happen to the inclusions and the increase of inclusion amount is calculated using Eq. (4.21). This further causes the decreases of the Mn and S amount as calculated in Eqs. (4.23) and (4.24). The changes of solute concentration are accounted with Eqs. (4.21) to (4.25). The new concentrations of solutes in the residual liquid (C_i') are used for the next calculation.

$$\Delta m_{in} = \frac{4}{3}\pi\rho_{in}\left\{N_{nu}r_{nu}^3 + \sum_{i=1}^{n_{class}} N(i)[(r(i)+\Delta r(i))^3 - r(i)^3]\right\} \tag{4.21}$$

$$m^j = C^j m_L \tag{4.22}$$

$$m^{Mn} = C^{Mn}m_L - \frac{M^{Mn}}{M^{Mn}+M^S}\Delta m_{in} \tag{4.23}$$

$$m^S = C^S m_L - \frac{M^S}{M^{Mn}+M^S}\Delta m_{in} \tag{4.24}$$

$$C'^j = \frac{m^j}{m_L - \Delta m_{in}} \times 100\% \tag{4.25}$$

Where Δm_{in} is the increase of inclusion mass (kg); ρ_{in} is inclusion density; N_{nu} and r_{nu} are the number and radius of nuclei at this solidification step, respectively; $N(i)$ is the number of the particles corresponds to size class with a radius of $r(i)$; n_{class} is the number of size classes in liquid before inclusion growth and nucleation; $\Delta r(i)$ is the increase of the particles with a radius

$r(i)$; m^j and C^j are the amount and concentration of solute j in the liquid steel before inclusion growth and nucleation; m_L is the liquid amount before inclusion growth and nucleation; and C'^j is concentration of solute j in liquid after inclusion formation.

4.4.3 Parameters study

Table 4.11 lists the parameters used in the model for the present calculations. While these parameters are well measured or estimated from former studies and widely applied, the influences of the important parameters on the calculations are needed to understand the inclusion formation process. In this section, the effects of step value, interfacial energy, pre-exponent and collision factor on MnS formation are studied. Note that the adjustable parameter-collision factor is assumed as 200 in this section which will be fitted using experimental results in Chapter 5. As the example, P1 (Table 4.10) are calculated with various parameters under the cooling rate 25.4 Ks^{-1} in the following table.

Table 4.11. Parameters applied in the kinetic model of MnS formation [19,168,174,175].

Symbol(Unit)	Name	Values	Symbol(Unit)	Name	Values
V_{MnS} (m^3mol^{-1})	Molar volume of manganese sulfide	2.2×10^{-5}	ρ_{MnS} (kgm^{-3})	Density of manganese sulfide	4.0×10^{3}
R ($JK^{-1}mol^{-1}$)	Gas constant	8.314	μ ($kgm^{-1}s^{-1}$)	Dynamic viscosity of liquid steel	6.2×10^{-3}
k_b (JK^{-1})	Boltzmann constant	1.38×10^{-23}	ρ_{Fe} (kgm^{-3})	Density of liquid steel	7.9×10^{3}
D_L^{Mn} (m^2s^{-1})	Manganese(Mn) diffusion coefficient in liquid	1.3×10^{-9}	D_L^S (m^2s^{-1})	Sulfur(S) diffusion coefficient in liquid	2.1×10^{-9}
M^{Mn} ($gmol^{-1}$)	Manganese(Mn) molar weight	55.0	M^S ($gmol^{-1}$)	Sulfur(S) molar weight	32.0
Δf_S	Solidification step ($f_S < 0.96$)	5.0×10^{-3}	Δf_S	Solidification step ($f_S \geq 0.96$)	2.5×10^{-5}
I_A ($m^{-3}s^{-1}$)	Pre-exponent	10^{42}	σ (Jm^{-2})	Interfacial energy	0.2
f	Collision factor	200	ΔR (μm)	Group width	0.01

4.4.3.1 Group size

When applying the PSG methods, the appropriate group size should be defined. Calculations with two group widths (0.01 and 0.03 μm) were compared with the calculation without the grouping approach. For comparing, collisions of MnS were not considered. Note that considering collisions in non-grouping calculation can create huge amount of size classes. The calculation process can refer to Figure 4.19 and Eqs. (4.6) to (4.25). The predicted results are shown in Figure 4.26. Figure 4.26 (a) displays the comparisons of final size distributions calculated with different group widths. The particle size distributions are described by the histograms with the lognormal group sizes. The particle size distributions predicted with group sizes of 0.01 and 0.03 μm fit well with that calculated without grouping. In Figure 4.26 (b), the predicted amount evolutions of MnS and concentration changes of reactants with different group widths are respectively coincident. Through the above comparison, it is believed that the PSG method is valid. The group size of 0.01 μm is considered as reasonable and used by the present model.

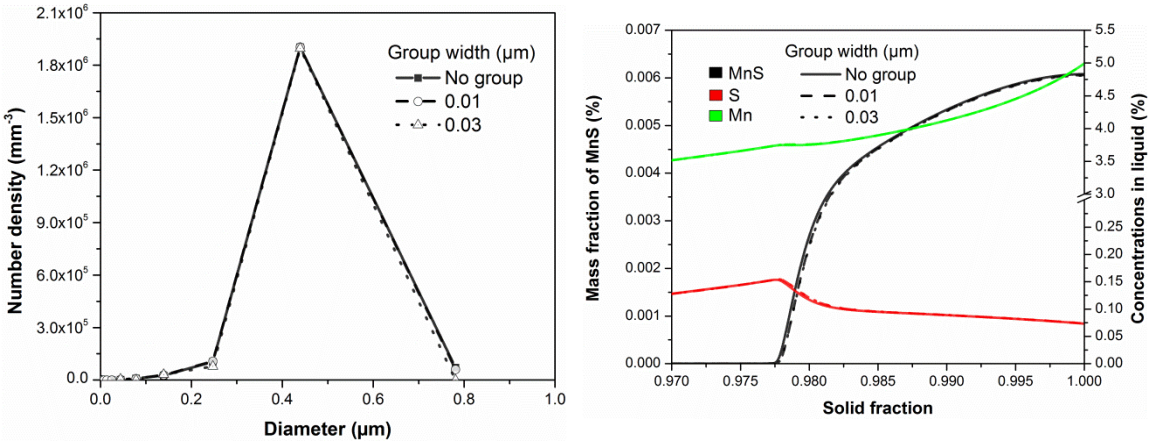

(a) (b)

Figure 4.26. The calculated results on MnS formation with different group widths (a) size distribution at the end of solidification and (b) amount and concentrations changes of the reactants.

4.4.3.2 Solid fraction step

MnS form at the late stage of solidification and nucleate and grow up in quite high speed. Thus, the finer step value is necessary after the solid fraction of 0.96 where MnS is thermodynamically stable for the investigated steels. Here the step value refers the solid fraction, and four step values, 1.0×10^{-3}, 5.0×10^{-4}, 2.5×10^{-4} and 1.0×10^{-4} after the solid fraction of 0.96 were applied to the calculations. Before the solid fraction of 0.96, the step value of 5.0×10^{-3}, which has been illustrated to be an appropriate value in Chapter 4.4.3.1, is taken as constant in the calculations. The calculated results with different step values are shown in Figure 4.27. As shown in Figure 4.27 (a), the entire size distributions of MnS predicted with various step values

are in similar arrangements. Only the peak number densities of diameters differ with each other. With the finer step values, the peak number density decreases while the corresponding diameter increases. This can be explained by that the larger step value results to the more concentrated nucleation and less nucleation steps which further affects the growth. When the step value of solid fraction is refined from 2.5×10^{-4} to 1.0×10^{-4}, there are few changes in the whole size distribution. Figure 4.27 (b) shows the mass fractions changes and the concentrations changes of the reactants calculated with different step values. The figure shows that the maximum differences of predicted MnS amount is within 2 ppm. The concentrations profiles of Mn and S from different predictions almost coincide, respectively. Combining Figure 4.27 (a) and (b), the simulations with step value of 2.5×10^{-4} and 1.0×10^{-4} can achieve similar results. When performing simulations, time used is another important aspect that should be considered and finer step values indicate longer calculation times. Thus in the current case, the solid fraction step of 2.5×10^{-4} is selected based on the above comparisons.

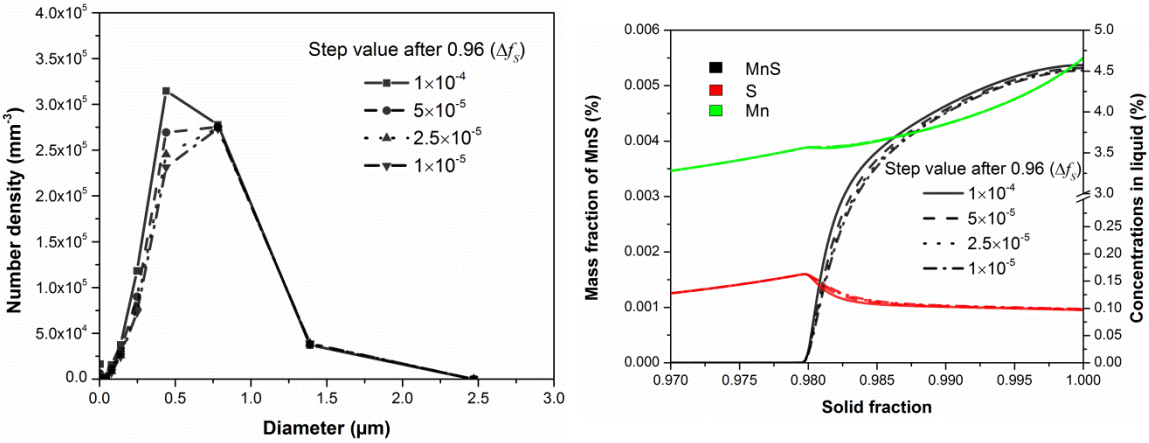

(a) (b)

Figure 4.27. The calculated results on MnS formation with different step values (a) size distribution at the solidus temperature and (b) amount and concentrations changes of the reactants.

4.4.3.3 Interfacial energy

Interfacial energy between inclusions and liquid steel is an important parameter on the nucleation of inclusions as given in Eqs. (3.15) and (3.16). To study the sensitivity of the nucleation and formation of MnS to the interfacial energy, calculations with three different values: 0.15, 0.2 and 0.25 J·m^{-2} were performed. The calculated results are shown in Figure 4.28. In Figure 4.28 (a), the nucleation rates estimated with different interfacial energies have distinct differences. The highest nucleation rates reduce to half with interfacial energy increasing by 0.05 J·m^{-2}. Meanwhile, the smaller interfacial energy results to the earlier nucleation but shorter duration. Figure 4.28 (b) displays the final size distributions of MnS calculated with different values of interfacial energy. With increasing interfacial energies, the peak number densities

decrease and the related diameters increase, and all the size distributions remain lognormal arrangement. Figure 4.29 shows the influences of interfacial energies on the MnS amount evolution and the concentration changes of Mn and S. The predicted MnS with the lower interfacial energy precipitate earlier and has a large final amount while the amount profiles are similar. Corresponding well to the trends of MnS amount, the concentrations of Mn and S sharply decrease when MnS starts to form. In total, the nucleation rate has high sensitivity to change of interfacial energy which contributes to the obvious variations of size distribution and MnS evolution.

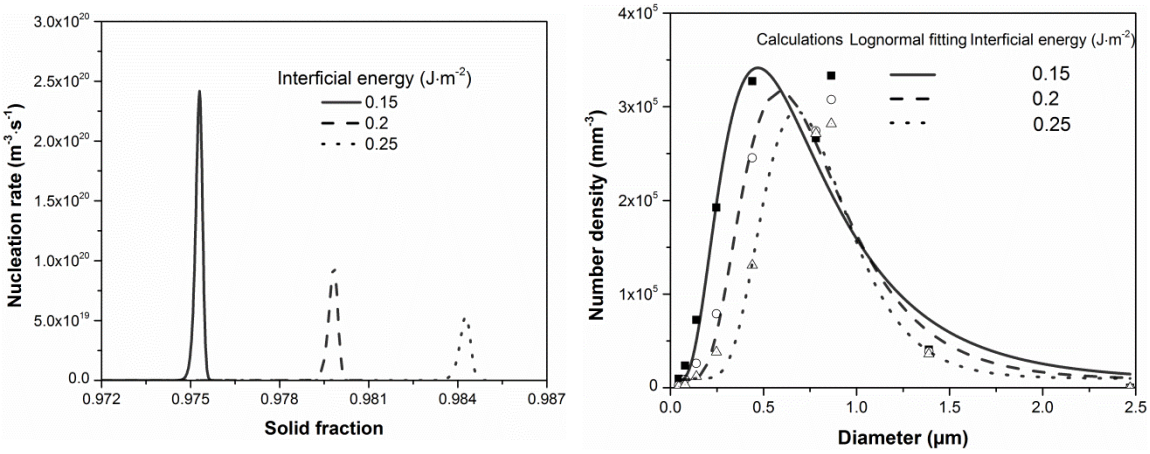

(a) (b)

Figure 4.28. The calculated results on MnS formation with different interfacial energies (a) nucleation rate and (b) size distribution at the solidus temperature.

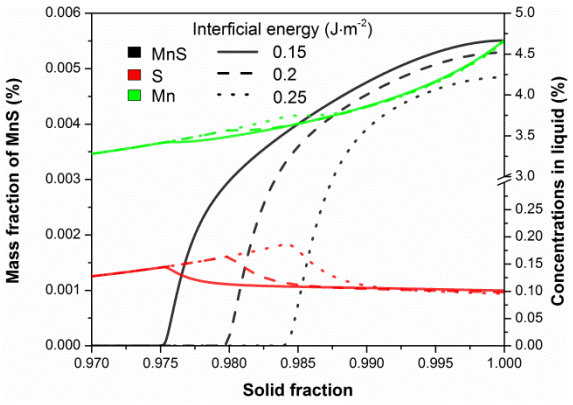

Figure 4.29. The formation of MnS and concentrations changes of reactants calculated with different interfacial energies.

4.4.3.4 Pre-exponent

Pre-exponent is another primary parameter on nucleation rate calculation which is defined by the atom collision frequency as expressed in Eqs. (3.16) and (3.17). The influences of pre-exponent on the MnS formation were studied through calculating with three selected values of 10^{39}, 10^{42} and 10^{45}. The calculated results are displayed in Figure 4.30 and Figure 4.31. Figure

4.30 (a) shows that the peak nucleation rate enhances with the increasing pre-exponent. In addition, it can be imagined that the more active movement of reactants atoms is more favorable to the MnS nucleation so that it can precipitate earlier (Figure 4.30 (a)). At the same time, the nucleation range becomes narrower with the increasing pre-exponent. In Figure 4.30 (b), the particle size distributions predicted with different pre-exponent values are close to each other. It means that though the pre-exponent value has considerable influence on nucleation, and the effects on size distribution are relatively smaller.

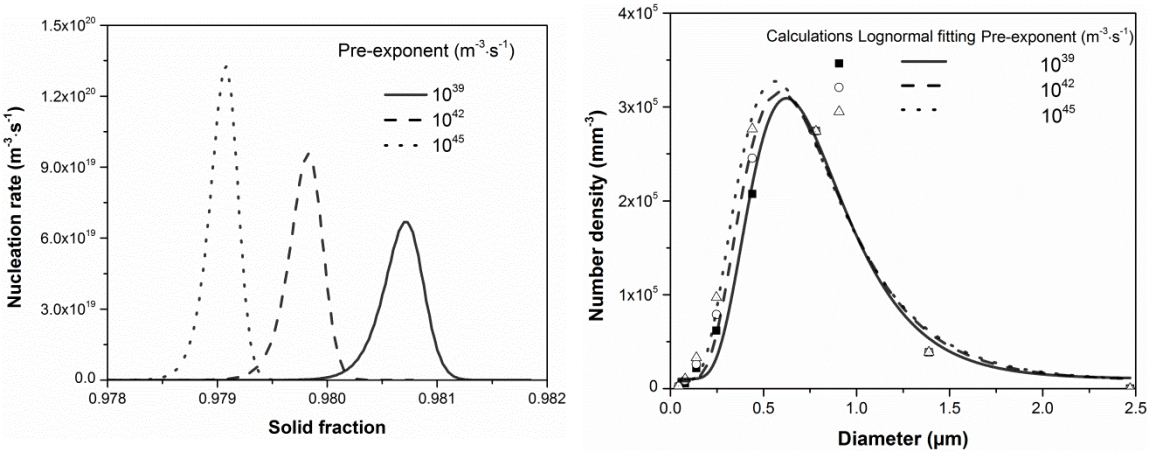

(a) (b)

Figure 4.30. The calculated results on MnS formation with different values of pre-exponent (a) nucleation rate and (b) size distribution at the solidus temperature.

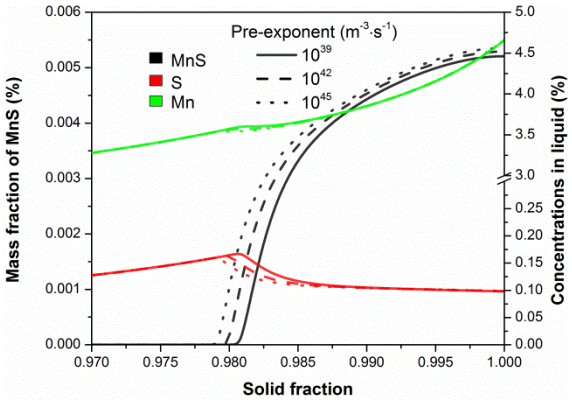

Figure 4.31. The formation of MnS and concentrations changes of reactants calculated with different values of pre-exponent.

Figure 4.31 shows that the predicted MnS amounts with different values of pre-exponent are distinct at an initial stage and then tend to be close. The concentration profiles of Mn and S calculated with different values of pre-exponent are similar. Compared with the influences of interfacial energy (Figure 4.28 and Figure 4.29), the nucleation and further growth are relatively less sensitive to the variations of pre-exponent.

4.4.3.5 Collision factor

In the proposed model, the influences of the collision factor (Eq. (4.15)) are desirable, which are the basis to adjust it according to experimental results. Figure 4.32 displays the calculated results of MnS formation with different collision factors. Figure 4.32 (a) shows that the size ranges become broader and the peak number densities decrease with an increasing collision factor. This means that the stronger collision results in larger and smaller number of particles. In addition, all of the size distributions are in a reasonable lognormal arrangement. Figure 4.32 (b) shows that different collision factors also cause the variations of MnS amount and reactants consumptions. The predicted MnS has a fewer amount of particles with the larger collision factor and the corresponding concentrations of Mn and S are higher. In Chapter 5, the collision factor is fitted to experimental results based on these calculations.

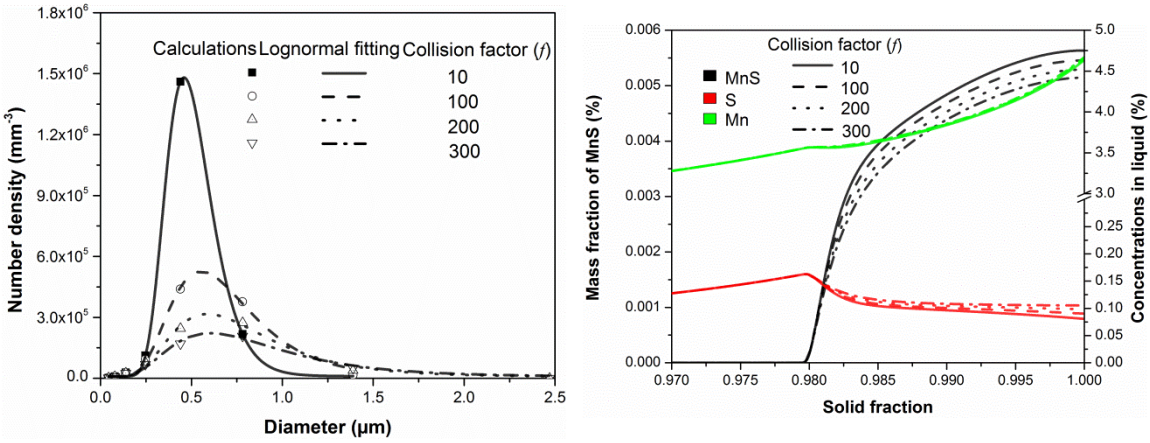

(a) (b)

Figure 4.32. The calculated results on MnS formation with different collision factors (a) size distribution at the solidus temperature and (b) mass fractions and concentrations changes of reactants.

In summary, the proposed model coupled MnS formation thermodynamics and kinetics with the developed microsegregation model. The predicted nucleation and growth of inclusion are highly influenced by the various parameters in the model. The influences of the group size in the PSG method and the solid fraction step for the calculation were firstly studied and the most applicable values were determined. Subsequently, the calculations with different interfacial energies showed that the nucleation rate is highly sensitive to the changes of interfacial energy which further results in the distinct variations of size distribution and total amount. Compared with interfacial energy, pre-exponent has relatively less influence on the nucleation and growth of MnS. Larger collision factors can promote the growth of particles and cause the reduction of number density. The collision factor is further evaluated in Chapter 5.2.2 by comparing with experimental results.

4.5 Model of multi-phase-inclusions formation during cooling and solidification

On the basis of the modeling on single inclusions formation during solidification, the preliminary model on multi-phase-inclusions formation during cooling and solidification was programmed. This model followed the core concept of the single inclusion model. It accounts for the inclusion formation thermodynamics and kinetics as well as microsegregation by considering competitive nucleation, growth and dissolution of multi-phase-inclusions which most refer oxides. Thermodynamics of inclusions formation were calculated with the sub-model which was developed using ChemAPP. The classical nucleation theory and diffusion controlled growth model from Zener [123] were continuously applied. The model reported [132] (Eq. (3.38)) was used to calculate the dissolution, and the collisions of particles were accounted using the above introduced collision factor. The size and number density evolutions were still recorded with PSG and PSD methods. The step values in the presented model were defined in this section. Due to the using the same concept and similar theories with single inclusion model, the influences of other parameters on nucleation and inclusion formation were not repeated, while the parameters applied in the calculations were listed.

4.5.1 Thermodynamics of inclusions formation during solidification

Thermodynamics offer the information of inclusion stability, compositions and chemical driving force for further kinetic calculations. Meanwhile, the thermodynamic prediction itself is valuable to inclusions investigations and that is why several thermodynamic models have been suggested as listed in Table 3.4. The sub-model on inclusions thermodynamics presented in this section plays the aforementioned roles. The model coupled the inclusions formation thermodynamics with the suggested microsegregation model. The thermodynamic equilibrium calculations were performed using ChemApp and the ChemSage datafile. In this manner, it determines the liquidus temperature, solute partition coefficients at the solidification interface and inclusion formation in the residual liquid. Trapping of inclusions by the solidification interface was treated in a simple manner as suggested by Yamada et al. [13] (Eq. (4.20)). The flow chart of the model is described in Figure 4.33.

In addition, during the cooling process, a similar technique is applied with decreasing temperature instead of microsegregation. Using this sub-model, the inclusions formation thermodynamics during cooling and solidification can be simulated. The stabilities, compositions and formation process of various inclusions can be obtained. At the same time the chemical driving forces for the kinetics are achieved. The logarithm of the coupling microsegregation and inclusion formation is tested through an overall mass balance and the predictions are compared with experimental results in Chapter 5.

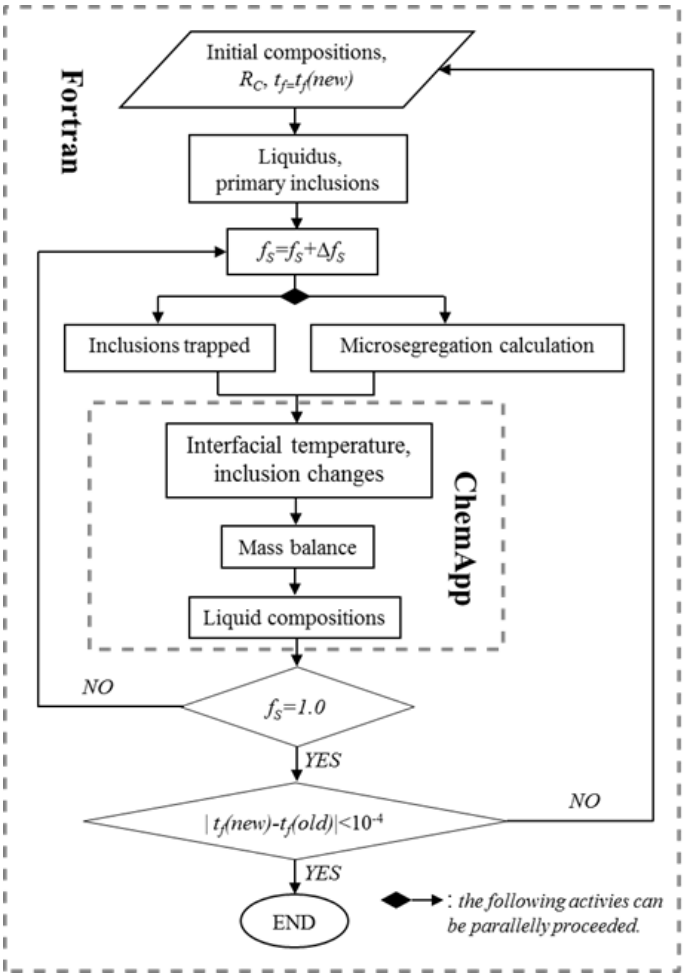

Figure 4.33. Flow chart of the coupled thermodynamic model predicting inclusion formation during the solidification of steels.

4.5.2 Kinetics of multi-phase-inclusions formation

4.5.2.1 Nucleation

Combing with the inclusion formation kinetics, the sub-model on inclusion formation thermodynamics was added to the comprehensive model. In analogy to Chapter 4.4.2.1, this model also employed the homogeneous nucleation theory as given in Eqs. (3.15) to (3.17). Simulating the heterogeneous formation of different inclusions is out of the ability of the present model. When calculating the nucleation rate of inclusions (Eq. (3.16)), the chemical driving force which is expressed by the formation Gibbs energy change of the inclusion is necessary. For a stoichiometric phase, the formation Gibbs energy change is easily estimated by the solubility and concentration products as MnS with Eq. (4.9). Regarding the solution phase, the situation is more complex. The nucleation of a solution phase should fulfill the condition that the affinities of the components formation reaction are equal [21]. Additionally, detailed explanation of this condition includes the concept of affinity can be found elsewhere [176]. Afterwards, the formation of a solution phase finds its equilibrium compositions. In the

proposed model, this problem can be solved using ChemApp. After calculating the multi-components and multi-phases equilibrium based on thermodynamic databases, ChemApp can offer the components and compositions of various phases. The Ti-Al containing liquid oxide is an example whose formation is assumed in Eq. (4.26).

$$b \cdot Ti_2O_3 + c \cdot TiO_2 + d \cdot Al_2O_3 = (Ti_2O_3)_b \cdot (TiO_2)_c \cdot (Al_2O_3)_d \tag{4.26}$$

In Eq. (4.26), b, c and d are the molar fractions of the components Ti_2O_3, TiO_2 and Al_2O_3, respectively. The types of the components and the corresponding proportions are all obtained from ChemApp. Hence, the formation Gibbs energy changes of the solution phase (ΔG_{sol}) can be estimated using the following equations:

$$\Delta G_{sol} = b \cdot \Delta G_{Ti_2O_3} + c \cdot \Delta G_{TiO_2} + d \cdot \Delta G_{Al_2O_3} \tag{4.27}$$

$$\begin{aligned} \Delta G_{sol} \approx RT[b \cdot \ln\left(\frac{[Ti\%]^{eq\,2} \cdot [O\%]^{eq\,3}}{[Ti\%]^2 \cdot [O\%]^3}\right) + c \\ \cdot \ln\left(\frac{[Ti\%]^{eq} \cdot [O\%]^{eq\,2}}{[Ti\%] \cdot [O\%]^2}\right) + d \cdot \ln\left(\frac{[Al\%]^{eq\,2} \cdot [O\%]^{eq\,3}}{[Al\%]^2 \cdot [O\%]^3}\right)] \end{aligned} \tag{4.28}$$

where $\Delta G_{Ti_2O_3}$, ΔG_{TiO_2} and $\Delta G_{Al_2O_3}$ are the molar Gibbs energy changes for the components Ti_2O_3, TiO_2 and Al_2O_3; $[i\%]$ and $[i\%]^{eq}$ are the real and equilibrium concentrations of reactants in liquid steel, respectively.

4.5.2.2 Growth and Dissolution

The schematic of inclusions competitive growth and dissolution is described in Figure 4.34. It shows that the inclusion which is thermodynamically more stable will grow up (in red color) and/or nucleate (green ones) at the consumption of unstable particles. The unstable phase (purple particles) gradually dissolves. The growth and dissolution rate were calculated with Eqs. (3.25) and (3.38), respectively. The calculations of the interfacial concentration for both growth and dissolution can apply the similar method as used for MnS growth (Eqs. (4.11) to (4.14)). While it is not displayed in Figure 4.34, the collision of the same inclusion type also contributes to their growth, which is considered by using the former introduced collision factor. The collisions between different inclusions were not accounted in the model. Note that these behaviors of inclusions only can happen in the liquid steel during the cooling and solidification process. The trapped inclusions by the solidification interface are proportional to the solid fraction (Eq. (4.20)) and inert in the following process.

On recording the size changes of various inclusions, the class model described in Figure 4.24 was applied to each inclusion type separately and with consideration of inclusion dissolution. Similar with the treatment of other activities, the particles that dissolved were reclassified according to the size and boundary values of the groups.

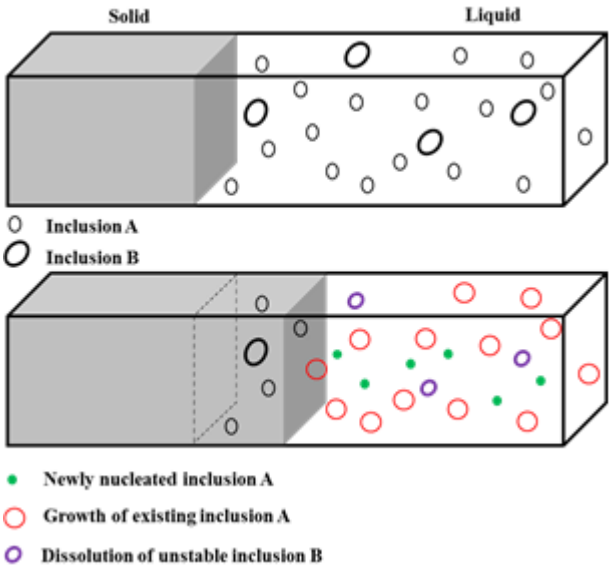

Figure 4.34. The schematic of inclusions competitive growth and dissolution.

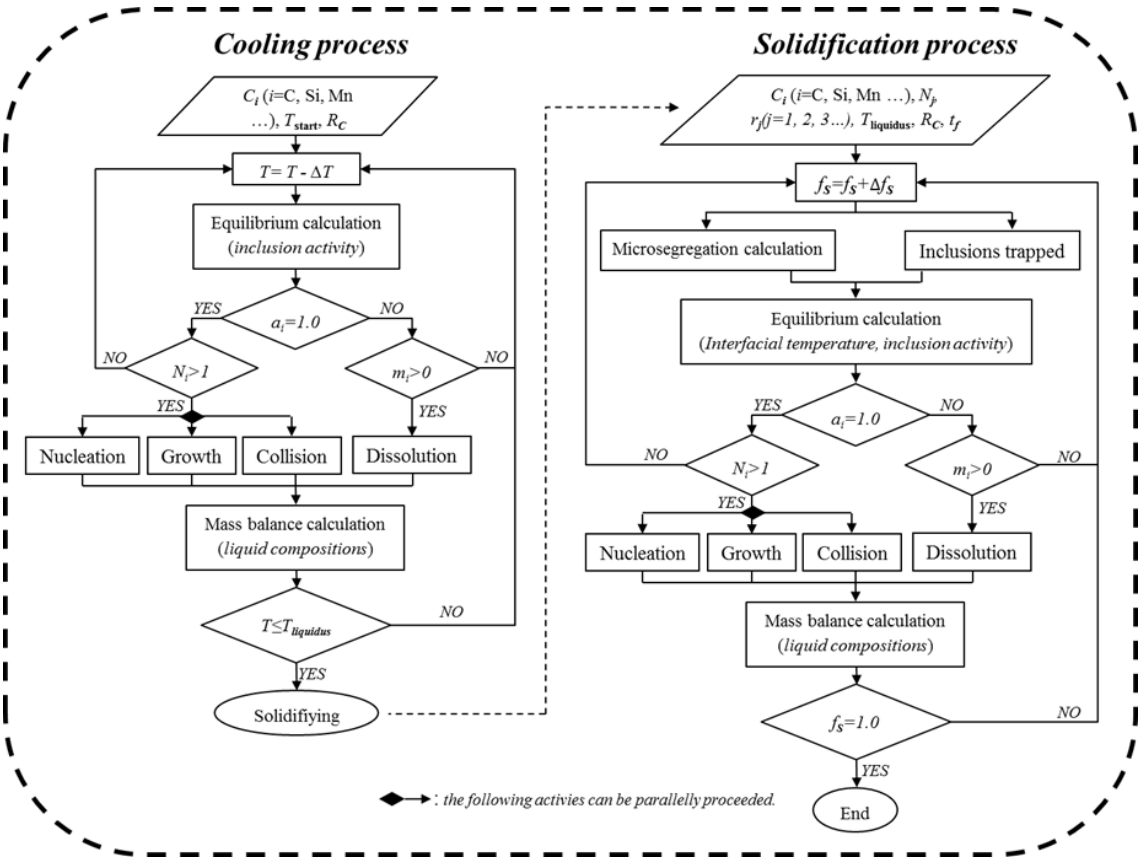

Figure 4.35. The flow chart of the comprehensive model on multi-phase-inclusions formation during cooling and solidification of steel.

At each solidification step, after all activities, such as nucleation, growth, collision and dissolution were completed, the changes of inclusions amounts were calculated.

Considering the consumptions and increases caused by the changes of inclusions, the new concentrations of solutes in the liquid steel were obtained and applied to next step.

Figure 4.35 displays the flow chart of the presented comprehensive model on multi-phase-inclusions formation and it is assumed that the inclusions formation starts in the cooling process. The initial steel compositions, temperature and cooling rate are input to the model. With the decreasing temperature, the thermodynamics and kinetics of inclusions formations are predicted until the solidification starts (the liquidus temperature). Combing with microsegregation, the inclusions formations during solidification process are continuously simulated based on the information of the existing inclusions including size and number density as well as steel compositions.

4.5.2.3 Parameter definition

The parameters used in the following calculations are listed in Table 4.12. Note that the general constants and the properties of MnS are not listed in this table, but it is listed in Table 4.11. The molar volumes of solution phase are calculated according to the components and their molar volumes. The diffusion coefficient of oxygen in the liquid steel is calculated by Eq. (4.29) due to its high sensitivity to temperature change [124]. The comparably smaller values of interfacial energy are applied to promote the nucleation because the heterogeneous nucleation is dominant in practice. Due to employing the same nucleation and growth theory with the single inclusion model, the influences of interfacial energy, pre-exponent collision and group size on the each inclusion formation should be similar to that found in Chapter 4.4.3. In the following the temperature step during cooling and solid fraction step during solidification are determined through comparing the different calculations.

One Ti-Al containing steel with the following chemical compositions: 0.23% C, 0.02% Si, 1.48% Mn, 0.0074% S, 0.004% P, 0.0051% Al, 0.05% Ti and 0.005% O, is calculated using the presented model with different temperature steps for liquid cooling process and solid fraction steps for solidification process. The assumed cooling rate is 10 Ks^{-1}. The calculated results of inclusion formation during the cooling process are shown in Figure 4.36. Note that the temperature differences are set as step values for the calculation. Figure 4.36 (a) shows that the amount evolutions of the solution phase-ASlag predicted with different cooling steps are close to each other. ASlag is the only stable inclusion in current case and its components are mainly Ti_2O_3 (29%–30%), TiO_2 (35%–36%), Al_2O_3 (24%–25%) and MnO (8%–9%). The size distributions at the liquidus temperature are almost the same for both size ranges and number densities (Figure 4.36 (b)). The figure illustrates that the studied cooling steps are fine enough under the current conditions. From the perspectives of calculation efficiency and fineness, the cooling step of 5.0×10^{-2} °C is selected for subsequent calculations.

Table 4.12. Parameters applied in comprehensive model for the multi-phase-inclusions formation calculations. [174,175]

Symbol(Unit)	Name	Values	Symbol(Unit)	Name	Values
Δf_S	Solidification step ($f_S < 0.96$)	2.5×10^{-4}	Δf_S	Solidification step ($f_S \geq 0.96$)	2.5×10^{-5}
ΔT (°C)	Cooling step	5.0×10^{-2}	ΔR (μm)	Group width	0.01
f	Collision factor	200	I_A ($m^{-3}s^{-1}$)	Pre-exponent	10^{33}
D_L^O (m^2s^{-1})	O diffusion coefficient in liquid	$6.0\sim12.0\times10^{-9}$	D_L^{Al} (m^2s^{-1})	Al diffusion coefficient in liquid	3.0×10^{-9}
D_L^{Ti} (m^2s^{-1})	Ti diffusion coefficient in liquid	3.5×10^{-9}	$\sigma_{Ti_3O_5}$ (Jm^{-2})	Interfacial energy of Ti_3O_5	0.7
$\sigma_{Al_2O_3}$ (Jm^{-2})	Interfacial energy of Al_2O_3	0.7	σ_{sol} (Jm^{-2})	Interfacial energy of solution phase	0.57
$V_{Ti_3O_5}$ (m^3mol^{-1})	Molar volume of Ti_3O_5	5.3×10^{-5}	$V_{Al_2O_3}$ (m^3mol^{-1})	Molar volume of Al_2O_3	2.6×10^{-5}
$V_{Ti_2O_3}$ (m^3mol^{-1})	Molar volume of Ti_2O_3	3.2×10^{-5}	V_{TiO_2} (m^3mol^{-1})	Molar volume of TiO_2	1.9×10^{-5}
V_{MnO} (m^3mol^{-1})	Molar volume of MnO	1.5×10^{-5}	$\rho_{Ti_3O_5}$ (kgm^{-3})	Density of Ti_3O_5	4.89×10^3
$\rho_{Al_2O_3}$ (kgm^{-3})	Density of Al_2O_3	3.97×10^3	$\rho_{Ti_2O_3}$ (kgm^{-3})	Density of Ti_2O_3	4.49×10^3
ρ_{TiO_2} (kgm^{-3})	Density of TiO_2	4.26×10^3	ρ_{MnO} (kgm^{-3})	Density of MnO	4.80×10^3
M^O ($gmol^{-1}$)	Oxygen(O) molar weight	16.0	M^{Al} ($gmol^{-1}$)	Aluminum (Al) molar weight	27.0
M^{Ti} ($gmol^{-1}$)	Titanium(Ti) molar weight	48.0	M^{Si} ($gmol^{-1}$)	Silicon(Si) molar weight	28.0

$$D_L^O = 1.05 \times 10^{-6} \cdot Exp(-\frac{72.5}{RT}) \quad (4.29)$$

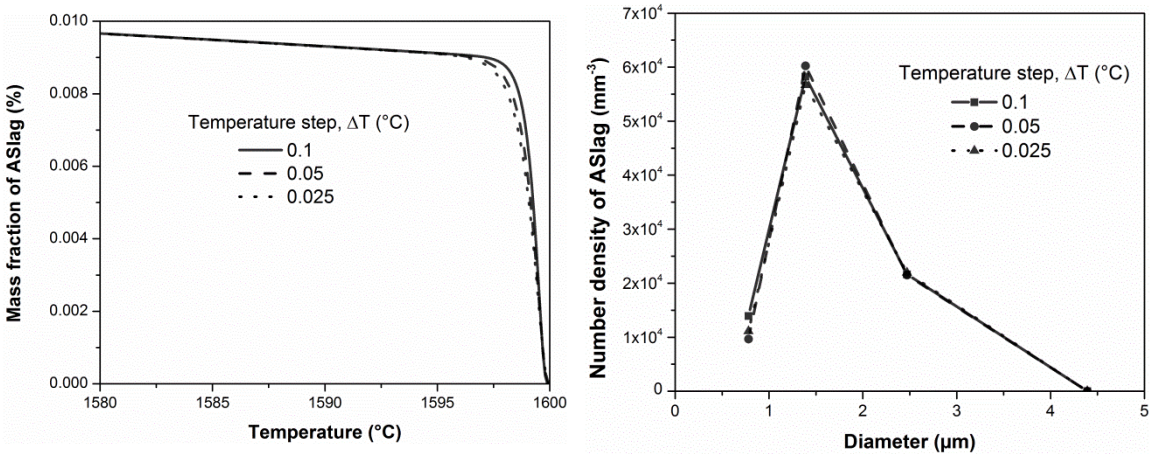

(a) (b)

Figure 4.36. The calculated results of inclusion formation with different cooling steps (a) amount changes and (b) size distribution at the liquidus temperature: the components of ASlag are Ti_2O_3 (29%–30%), TiO_2 (35%–36%), Al_2O_3 (24%–25%) and MnO (8%–9%).

Note that in the calculations of solidification process, the different step values are taken before and after the solid fraction is equal to 0.96. Here, the step value before the solid fraction of 0.96 is determined. After the solid fraction is equal to 0.96, the tested and finer step (2.5×10^{-5}) is applied for the intensive precipitation of MnS. Figure 4.37 shows the inclusions and oxygen concentrations evolutions during the subsequent solidification process. The profiles of all the three inclusions predicted with different solid fraction steps coincide with each other and the same situation is faced to the oxygen concentrations. In addition, the profiles of both ASlag and Al_2O_3 amounts predicted with the step values of 2.5×10^{-4} and 1.0×10^{-4} are smooth curves. In contrast, for the simulations with larger step values, the amounts of ASlag from solid fraction 0 to 0.1 and Al_2O_3 from solid fraction 0.1 to 0.3 show large fluctuations. The fluctuating extents decrease with the finer step values. Meanwhile these fluctuations also cause the variations of oxygen concentrations. The fluctuation phenomenon can be explained by the balance of growth and dissolution as well as the larger step values of 5.0×10^{-4} and 1.0×10^{-3}. At the current step, one inclusion is stable and can increases in size, while the next step is due to the consumptions of reactants (such as oxygen). Additionally, as the temperature changes, the inclusion becomes unstable and dissolves which leads to increased concentration and the inclusion reaching a stable condition. The circulation of the above process results in the fluctuations, which larger calculation steps promote the phenomenon formation while the ‘step value’ in the real reaction is infinitesimal.

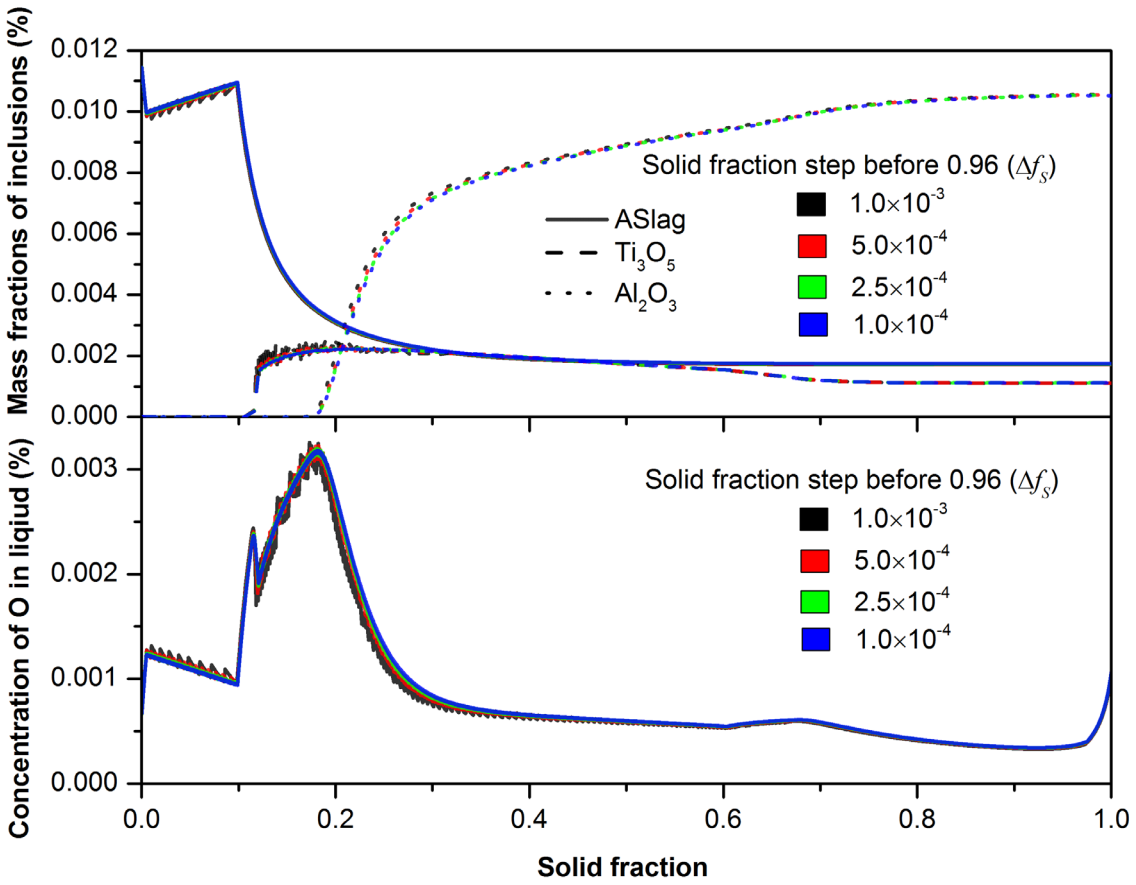

Figure 4.37. The evolutions of inclusions amounts and the corresponding oxygen concentration changes predicted with different solid fraction steps.

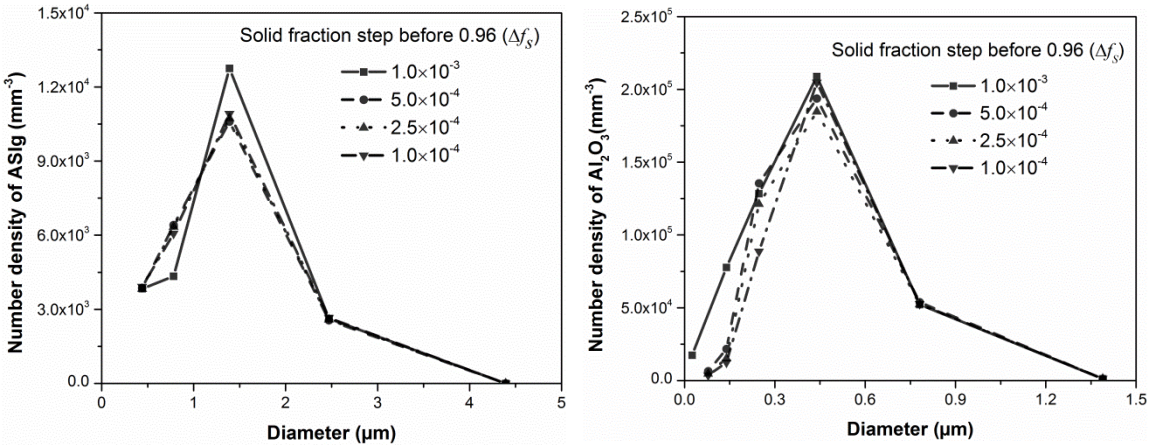

(a) (b)

Figure 4.38. The calculated size distributions at the solidus temperature with different solid fraction steps (a) ASlag and (b) Al_2O_3.

Figure 4.38 displays the size distribution of ASlag and Al_2O_3 at the solidus temperature. Figure 4.38 (a) shows that the size distributions of ASlag with the finer step values are distinct with that calculated with 1.0×10^{-3}. In contrast, reducing the step value from 5.0×10^{-4} to 1.0×10^{-4} has little influence on ASlag size distribution. In Figure 4.38 (b), the size distributions of Al_2O_3

predicted with various step values have slight discrepancies and all the distributions are in the same arrangement. Thus on the size distributions of Al_2O_3, refining the step value of solid fraction establishes few changes. In the view of simulation, with acceptable correctness, it is necessary to enhance calculation efficiency through selecting a proper step value. In the current case, combined with the description in Figure 4.37, the calculation with step value of 2.5×10^{-4} can obtain quite close results to those predicted with 1.0×10^{-4}, while the consuming time are shorten about 2.5 times (3 hours). Thus, the step value of 2.5×10^{-4} for solid fraction before 0.96 is believed to be appropriate for the following simulations.

The comprehensive model on multi-phase-inclusions formation during cooling and solidification was depicted in detail in this section. Appling the same modeling theory with the single inclusion formation, the model further considered the competitive nucleation, growth and dissolution of various oxides. While the influences of various parameters have been investigated in the last section, the calculation step values for cooling and solidification process were defined in this section. Using this model, an illustrative example is calculated in the next chapter.

4.6 Summary

Based on the modelling concept introduced at the beginning of Chapter 4, progressive work including microsegregation, single inclusion formation and multi-phase-inclusions formation thermodynamics was performed and finally promoted the construction of the comprehensive model on multi-phase-inclusions formation. By linking to the thermodynamic database, the step-wise Ohnaka´s model [10] can offer microsegregation predictions while considering the local partition coefficients, temperature dependent diffusion coefficients, multi-components and multi-phases based temperatures and various precipitations. The advantage of the model and the reasonability of parameters selections were well illustrated through the systematic parameters study. Meanwhile, the influences of the various parameters were realized. The following model on single inclusion formation during solidification was developed through coupling with the microsegregation model, and MnS was taken as the target inclusion. The thermodynamic stability, nucleation, growth and collision of MnS during solidification process were programmed. Additionally, the effects of the related parameters in this model, including step values, interfacial energy, pre-exponent and collision factor on the MnS formation were investigated. The parameter study provides the foundation for further fitting calculations and applications. Based on the core concept of the single inclusion model, the comprehensive model on multi-phase-inclusions formation during cooling and solidification was developed. Afterwards, a sub-model on the thermodynamics of multi-phase-inclusions formation is presented. The thermodynamic model provides the stabilities, chemical driving force, compositions and equilibrium amount of the studied inclusions which is also a powerful tool when applying it separately. The comprehensive model further considered the competitive

nucleation, growth and dissolution of various oxides and can be applied to investigate influences of several metallurgical parameters such as cooling conditions and chemical compositions on the formation behaviors of various inclusions. While the present preliminary model is mainly used to tendency study, it can offer valuable references for inclusion control and utilization. In Chapter 5, the developed models are evaluated and applied.

5 Model evaluation and application

In this chapter, the models proposed in Chapter 4 are evaluated using experiments and simulations and further applied to case studies. First the modelling on microsegregation is tested through comparing the calculated results with the predictions from FactSage and other models, as well as the measured temperatures from the former publications. In addition to being applied to the subsequent modeling process, the microsegregation model can offer feedback for the database optimization. In this section, the adjustable parameter -collision factor- in the modeling of single inclusion (MnS) formation is fitted to the experimental results, and the model is used to investigate the influences of cooling rate and sulfur content. Using the similar methodology with simulating a single inclusion, a multi-phase-inclusions formation model was originally developed considering the competition of different inclusions. After checking the overall mass balance and the confirmation of formation thermodynamics of the multi-phase-inclusions, an illustrative example is calculated and the influences of cooling rate and oxygen content are discussed.

5.1 Evaluation on microsegregation modeling and application

5.1.1 Model test

The first objective of this section is to test the convergence of the algorithm for the semi-integrated analytical equation in ChemApp and the proper transfer of the partition coefficients from FactSage to ChemApp by comparison with calculation results from the Scheil-module of FactSage. At last the calculations are faced to the reported characteristic temperatures measured by the hot tensile experiments for a variety of carbon steels.

5.1.1.1 On the 'communication' with FactSage

When setting the back diffusion coefficient (α) in the present model to zero, Eq. (4.1) becomes Eq. (5.1), which is the semi-integrated analytical equation of Scheil´s model [9]. By solving this equation numerically, the results may then be compared with the results from the analytical Scheil model as offered by FactSage on the basis of identical partition coefficients. The microsegregation of C, Mn, Si, P and S for three selected carbon steels, 0.05%C, 0.32%C and 0.59%C (Table 4.2, S1-1~3) was calculated and it was assumed that solidification completed at a solid fraction of 0.95. The results are shown in Figure 5.1.

$$C_L^+ = C_L\{\frac{1-(f_S+\Delta f_S)}{1-f_S}\}^{k-1} \tag{5.1}$$

Figure 5.1 (a) shows that the solidification temperatures versus solid fraction during the solidification of the three selected steels predicted by the current model fit very well with those

from FactSage. The maximum difference in the calculated temperature amounts to 0.85, 1.59 and 2.74 °C. Figure 5.1 (b), (c) and (d) show good agreement between the concentration curves of C, Mn and S predicted by the present model and FactSage. Note that for the calculation results presented, the solute concentrations of Mn and S in the residual liquid are limited by the solubility product of MnS. For the present case, the concentration ratio of Mn and S results in a sharp decrease in the solute S-concentrations as soon as the concentrations exceed the solubility product, as shown in Figure 5.1 (d). This is a simplifying assumption, but in a further step, the present model is extended to consider the inclusion of nucleation and growth kinetics.

In summary the results prove the stability and convergence of the algorithm for the semi-integrated solution of the microsegregation equation in ChemApp as well as the proper transfer of the local partition coefficients from FactSage to ChemApp.

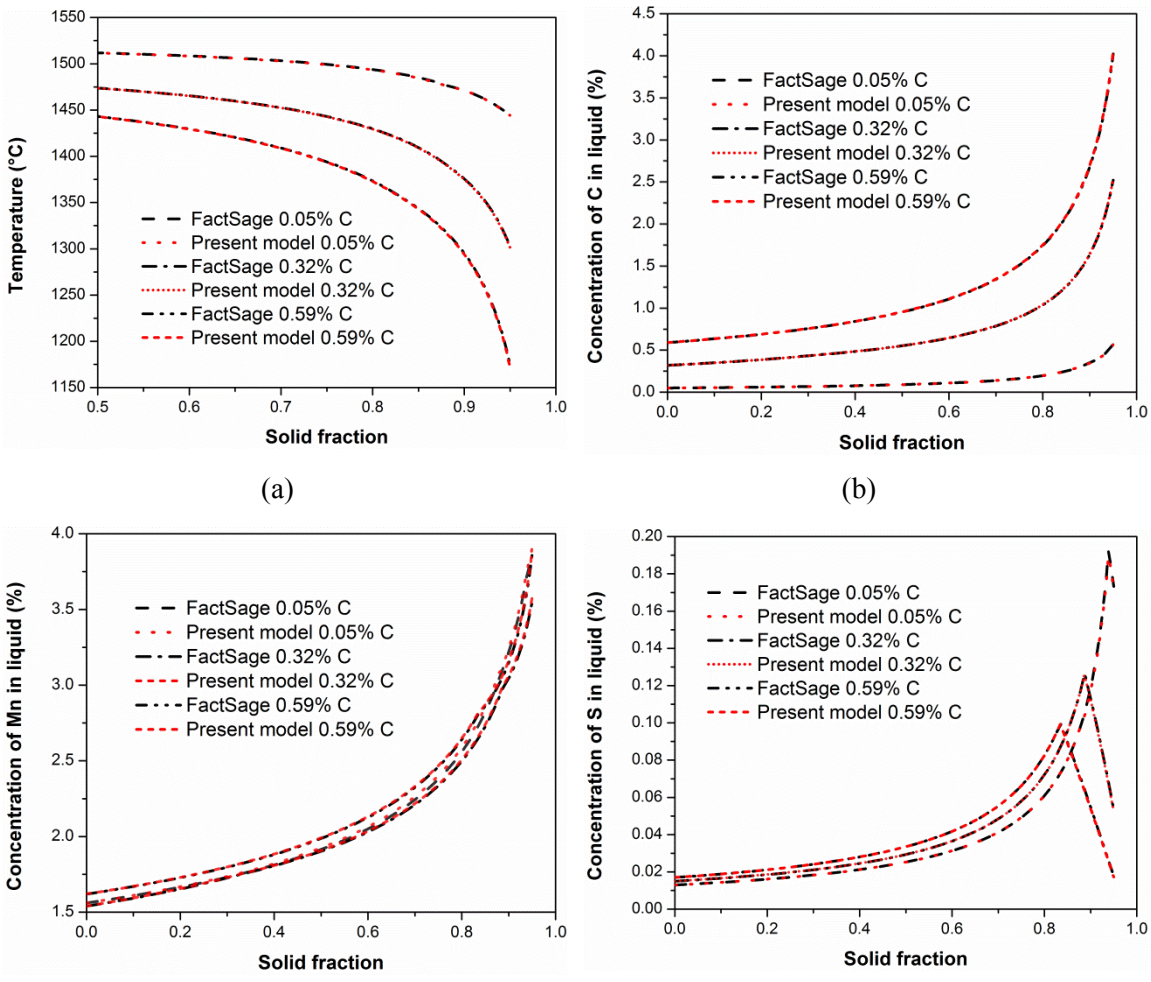

Figure 5.1. (a) Temperature and (b) carbon, (c) manganese, (d) sulfur concentrations in residual liquid calculated by FactSage and the present model with $\alpha = 0$: the sharp decreases of S concentrations are due to the MnS formation; the changes of Mn concentrations caused by MnS formation are not noticeable.

5.1.1.2 On the concentrations

In the second step, the carbon and manganese microsegregation predicted by the present model was compared with the solutions from the Lever Rule and Scheil´s model [9], the two extreme cases of the present equation. In this comparison, S1-2 steel in Table 4.2 was calculated assuming a cooling rate of 10 Ks^{-1}. Calculations of the Lever Rule and Scheil´s model [9] were performed using FactSage. It was assumed that the solidification terminated at a solid fraction of 0.95 in Scheil´s equation, and the results are shown in Figure 5.2.

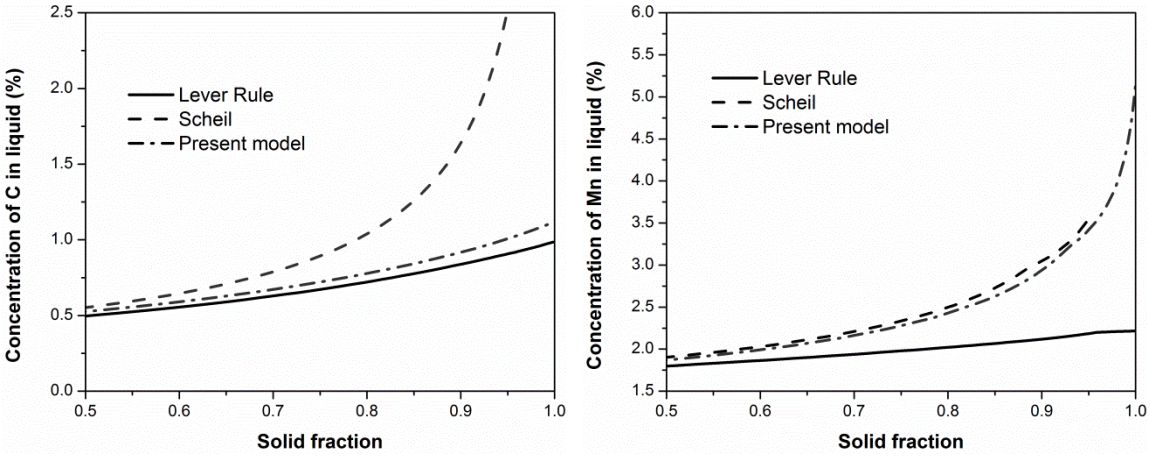

(a) (b)

Figure 5.2. (a) Carbon and (b) manganese microsegregation predicted by different models for S1-2 steel.

As shown in Figure 5.2, the concentration curves for both carbon and manganese from the present model are between the curves calculated by the Lever Rule and Scheil´s model [9]. In detail, the microsegregation profile of carbon from the present model is closer to that from the Lever Rule (Figure 5.2 (a)) because carbon is known to diffuse fast in solid phases of steel and the Lever Rule assumes infinite diffusion in solid; in contrast, the manganese enrichment predicted by the present model is more similar to the result from the Scheil´s model [9] (Figure 5.2 (b)) because the back diffusion of the large manganese atoms is much slower.

These results present only a qualitative indication for the correctness of the results: The calculation results lie within the Lever and Scheil solutions, the two extreme cases for microsegregation, and the solution for carbon comes closer to the Lever rule whereas the solution for manganese is closer to Scheil. Additionally, FactSage does not offer an analytical solution for microsegregation with consideration of back diffusion in the solid state. Hence, it is a common practice to predict the enrichment of carbon by the lever rule and the enrichment of manganese by the Scheil model.

5.1.1.3 On the temperatures

As described and applied in Chapter 4.3.3, the measured ZST and ZDT were used to indicate the correctness of the microsegregation calculations. In addition, further experimental results from Schmidtmann [155] and from Shin [177] were used for the comparison with calculations as listed in Table 5.1.

Table 5.1. Chemical compositions of steels tested by Shin (mass%) [177].

Sample series	C	Si	Mn	S	P	Number
S2	0.060–0.60	0.008–0.150	1.03–1.06	0.0005–0.0008	0.0005–0.0009	6

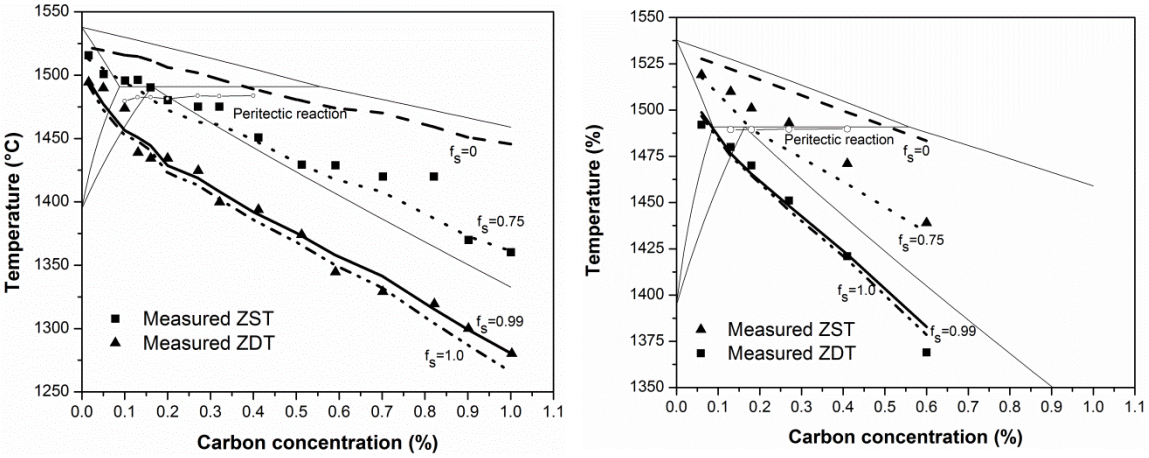

(a) (b)

Figure 5.3. Fe-C equilibrium phase diagrams along with characteristic temperatures from microsegregation analysis and measured ZST and ZDT (a) from Schmidtmann [155] and (b) from Shin [177]: the thick lines are the calculed results using the proposed model; the thin lines are the calculated Fe-C equilibrium phase diagrams with FactSage.

In Figure 5.3 (a) and (b), Fe-C equilibrium phase diagrams calculated by FactSage are compared with the predicted characteristic temperatures and measured ZST and ZDT from Schmidtmann [155] and Shin [177], and the authors tested their samples using a high-temperature tensile machine under cooling rates of 10 Ks^{-1} and 0.17 Ks^{-1}, respectively. Microsegregation analysis is performed using the present model for these two series of steels (S1in Table 4.2 and S2 in Table 5.1) under the experimental cooling rates. Same with the discussions in the last chapter, ZST and ZDT correspond to the solid fractions of 0.75 and 0.99, respectively. As shown in Figure 5.3 (a) and (b), the characteristic temperatures from the analysis of both experimental series are in good agreement with the calculated values. The calculated non-equilibrium solidus temperatures range far below the Fe-C equilibrium values.

The correspondence between the solidification temperature for solid fraction 0.99 and 1.0 and the measured ZDT is excellent. The correspondence of calculated values for solid fraction 0.75 with ZDT is however rather limited as ZDT is often associated with a solid fraction between 0.6 and 0.8, depending on steel composition [177]. Furthermore, the liquidus temperatures from the microsegregation analysis are approximately 10 °C and 5 °C lower than equilibrium temperatures due to the consideration of other alloying elements (Mn, Si, P, and S).

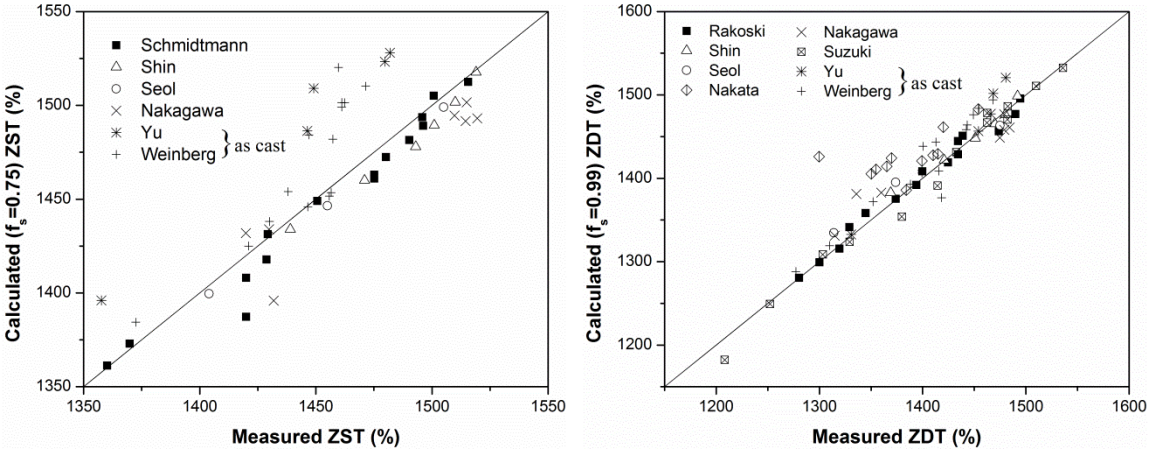

(a) (b)

Figure 5.4. Comparisons of (a) ZST and (b) ZDT between microsegregation analysis and measured data [155,177–183].

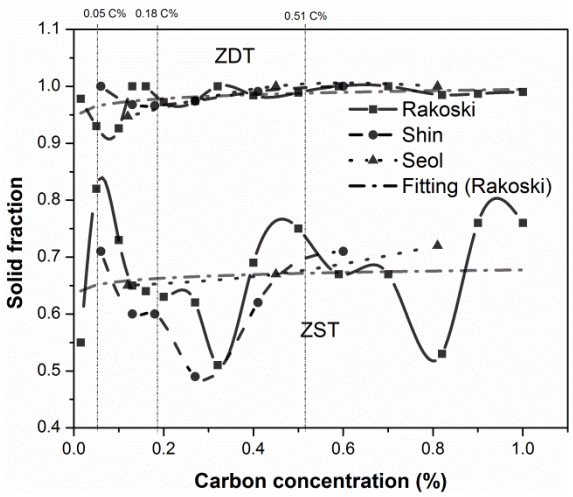

Figure 5.5. The corresponding solid fraction of ZST and ZDT varies with carbon contents [155,177,183].

Figure 5.4 (a) and (b) compare the ZST and ZDT from the microsegregation analysis and measured data by different authors [155,177–183] for a wide range of steel compositions. Under the same given conditions of steel compositions and cooling rates, the calculated ZST and ZDT are in reasonable agreement with the experimental results. Note that the correspondence between the ZST from analysis and measured data is of rather poor quality. In contrast, the

correspondence of the calculated and measured ZDT is excellent. The main reason is that the ZST does not necessarily coincide with a solid fraction of 0.75 but rather depends on the steel composition as displayed in Figure 5.5. For the studied three steels [155,177,183] in Figure 5.5, carbon concentration was established as the only variable. The figures show that ZST had greater fluctuations in considerable extent with the changing carbon contents while the profiles of ZDT are rather flat. In summary, the above described results demonstrate that the proposed model can reasonably predict the microsegregation of steels.

5.1.2 Applications

One of the main characteristics of the presented microsegregation model is the use of so-called local partition coefficients (temperature dependant and concentration dependant) from thermodynamic databases. For most carbon steels, the benefit of applying local partition coefficients is only minor as their variation in temperature and concentration is rather small. Nevertheless, an increasing number of advanced steel grades contain considerable amounts of alloying elements, mainly manganese, silicon or aluminum, but also nickel or chromium. For these alloys, even the quality of commercial databases is partly questionable as demonstrated by DSC measurement, as shown by Presoly [185]. One of the successful strategies to overcome these limitations is to optimize excerpts of commercial databases by means of OptiSage [102]. In the following, an in-house optimized database was applied to predict the enrichment of alloying elements during the solidification of TRIP (Transformation Induced Plasticity) steel. An important element is that the Fe-C-Mn system is identical in all three databases and was not optimized. In the in-house database, however, the manganese interaction with Si and Al were selectively optimized, based on DSC measurements on model alloys [184,185]. The chemical composition of the selected steel is listed in Table 5.2. For comparing with the following measured results, secondary dendrite arm spacing was set to 18 μm and the local solidification time was calculated using Eq. (4.2).

Table 5.2. Chemical compositions of the TRIP steel (mass%).

C	Si	Mn	Al
0.21	0.54	2.12	0.77

Figure 5.6 compares the results calculated with different databases and shows that both solute concentrations and partition coefficients exhibit significant differences. The C concentration profiles (Figure 5.6 (a)) are similar until a solid fraction of 0.7 is reached, and then they differ; concentrations of Si and Mn (Figure 5.6 (b) and (c)) predicted with FSstel database are close to those predicted with SGTE2014 database, while they are higher than those calculated by the in-house developed database; for Al, all the three calculations show its negative segregation, and

the concentration in the residual liquid estimated with the optimized database is higher than those estimated with the other two databases. Different databases have their own parameters for the Gibbs energy minimization and thermodynamic equilibrium calculations. The partition coefficients and equilibrium concentrations therefore calculated with different databases vary with each other.

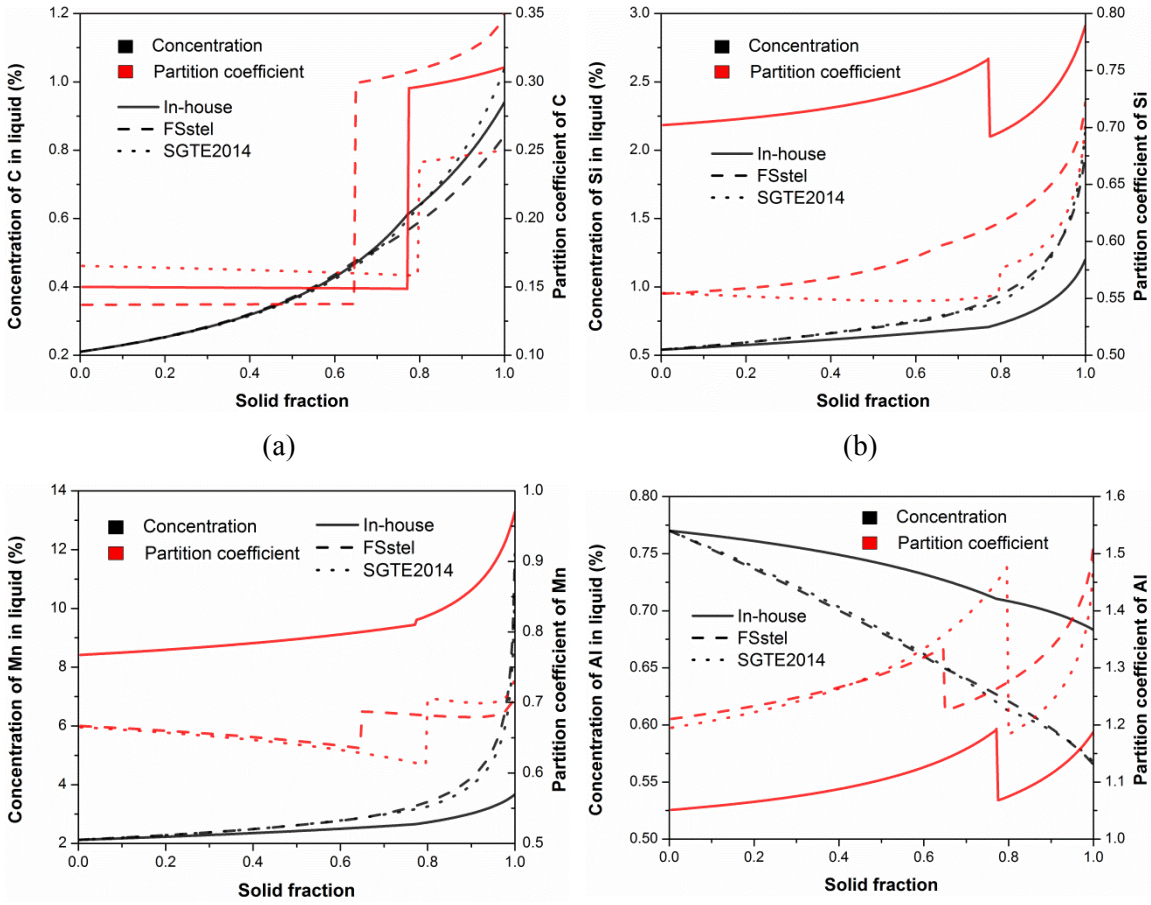

Figure 5.6. Predictions of segregated concentrations and partition coefficients with different databases (a) C, (b) Si, (c) Mn and (d) Al.

The differences in the concentration profiles can be well explained by the differences in the corresponding partition coefficients. For positive segregation (C, Si and Mn), the smaller partition coefficients indicate higher segregation; while for negative segregation (Al), the smaller partition coefficients lead to a lower segregation. Taking Mn as an example (Figure 5.6 (c)), the partition coefficient calculated using the in-house database is always higher than those calculated using the FSstel and SGTE2014 databases, which results in a lower concentration profile calculated with the in-house database. Note that the sharp changes of partition coefficients in Figure 5.6 are caused by the peritectic reaction, and the results indicate that the calculated onset of the peritectic reaction varies significantly. The partition coefficients for the transformation from liquid to austenite are always higher for the austenite forming elements

carbon and manganese whereas the partition coefficient for silicon and aluminum, both ferrite forming elements, are higher for the transformation from liquid to ferrite. At the same time, the peritectic reaction leads to a decrease of back diffusions, which further increases the concentrations in the residual liquid. This explains the higher concentrations calculated with the FSstel database for Si and Mn between solid fraction 0.63 and 0.79, though their partition coefficients are larger (Figure 5.6 (b) and (c)).

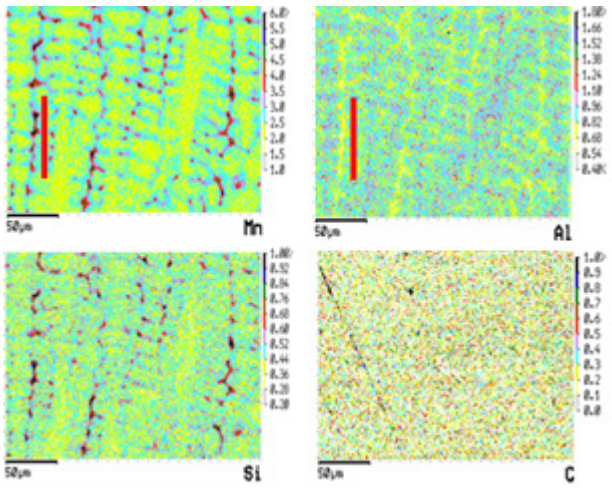

Figure 5.7. The concentration mappings of the solutes for the TRIP steel.

To compare with the predictions, a sample with the same compositions as listed in Table 5.2 was produced by means of high-frequency remelting and spin-casting. The small sample (60 g) was solidified with high speed and water-quenched so that the back diffusion of solutes was minimized. Then, the microprobe analysis was performed on a selected cross section, and the concentration mappings of the solutes are shown in Figure 5.7.

From Figure 5.7, it can be seen that both primary and secondary structures are clearly drawn by the segregated concentrations of Mn, Al and Si. The C concentration distributes quite evenly due to its fast diffusion. To evaluate the calculations, the concentration profile between two secondary dendrite arms was investigated in detail. A line scan was performed on the secondary dendrites as indicated by the red line in Figure 5.7.

Figure 5.8 describes the concentration distributions of Mn and Al over the line scan distance, and concentrations of Mn and Al reflect the microsegregation. Mn gets enriched in inter-dendrite zones and approaches the highest concentrations. By contrast, Al shows a negative segregation and reaches the lowest concentrations in inter-dendrite zones. Compared with the measurements, the trends of the enrichment of elements are predicted well by the proposed model. For the values, the measured inter-dendritic concentrations of Mn range from 3.4% to 4.0%. Figure 5.6 (c) shows the segregated concentration of Mn calculated with the in-house database is about 3.5% which fits well with the measured results. For the predictions with the

FSstel database and the SGTE2014 database, the final segregated concentrations exceed 10% which seems to be unrealistic. For Al, the measured inter-dendritic concentrations vary from 0.65% to 0.75%. The inter-dendritic concentration predicted with the in-house database of 0.68% is closer to the measured value than the results calculated with the other two databases (0.57%).

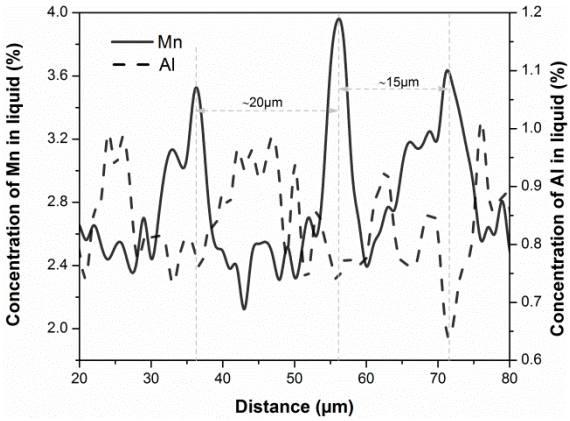

Figure 5.8. Concentration distributions of Mn and Al from line scan of secondary dendrites.

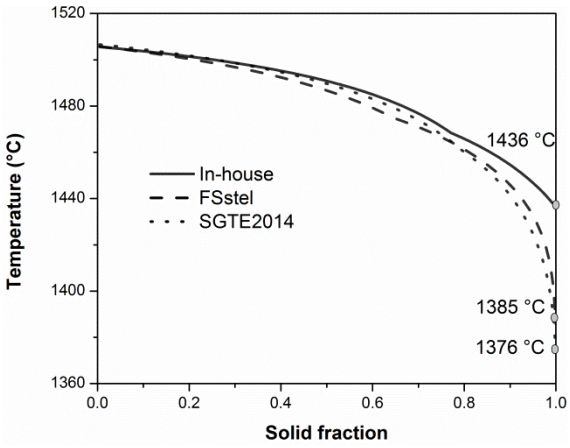

Figure 5.9. Predicted temperature profiles with different databases.

The liquidus temperature during solidification highly depends on microsegregation. Figure 5.9 shows the calculated temperature profiles based on different databases. The remarkable overestimation of the Manganese and Silicon enrichment in the FSstel and SGTE2014 results in the prediction of an extremely low solidus temperature of 1385 °C and 1375 °C, respectively. The in-house optimized database calculates a solidus temperature of 1436 °C, approximately 60 degrees above the other values. In continuous casting, this difference corresponds to a variation of the metallurgical length in many meters. This makes the precise control of the position of the metallurgical length, which is a prerequisite for the dynamic adjustment of the soft reduction position, impossible.

Based on the above discussion, the proposed model can better predict the microsegregation of the investigated TRIP steel with the in-house database. Optimization of the database is

necessary to better describe the thermodynamic equilibrium of selected steels and this work is still ongoing in the research group.

5.2 Evaluation on the single inclusion formation modeling and application

In this part, to fit the adjustable parameter -collision factor- in the single inclusion model, the Submerged Split Chill Tensile (SSCT) experiment is used to simulate the formation of MnS during solidification process of steel. First, the experimental procedure is described in Section 5.2.1. The parameter fitting is performed through comparing different calculated results with the experimental results. With the fitted parameters, the model is applied to investigate the influences of cooling rate and sulfur on MnS formation, and the predictions are also compared with the measured ones to illustrate the correctness.

5.2.1 Experiments

The SSCT experiment was initially developed to investigate the high temperature mechanical properties of alloys [36,186,187]. The schematic of the SSCT experimental and sampling process are explained in Figure 5.10. As shown in Figure 5.10 (a), liquid steel is pre-melted in an induction furnace (25 kg), and a cylindrical chill body is submerged into liquid steel. A steel shell starts to solidify on the cylindrical body with the Zr-Oxide coating surface. The crystallographic growth of the shell mainly originates perpendicular to the cylinder. After approximately 30 s, the sample is lifted out of the liquid melt. The temperature changes during shell solidification are measured by thermocouples inside the test body. The measured temperatures serve as input data for thermo analysis and heat flux calculation. Further shell growth, cooling rates, solid fractions and temperature distributions are obtained using an in-house developed solidification model. The detailed descriptions of SSCT and the interpretation of the results can be found elsewhere [36,186]. Figure 5.10 (b) displays the sample preparation procedure. The solidified shell is cut into 16 pieces at room temperature. The piece with a relatively even shell thickness is selected. Then, the sample is metallographically prepared for observation.

In the current case, three steels with different sulfur content are melted and solidified using the SSCT experiment. The chemical compositions of the steels are listed in Table 4.10. After the aforementioned sample preparation process, the inclusions in the samples are measured using automated SEM/EDS analysis. This method consists of a Scanning Electron Microscope (SEM), that is, a ZEISS ultra55 in the present case, equipped with an Energy Dispersive X-ray Spectrometer (EDS) system (SEM/EDS) from Oxford Instruments. This method has been widely applied to investigate the steel cleanness [4,5,57,188,189]. With this method, the size distribution and number density of inclusions, as well as compositions, can be determined and the measured fields and corresponding cooling rates are shown in Figure 5.11. For sample P1, three fields (A, B and C) of different shell thicknesses, but with the same height, are measured

to study the influence of cooling rate on MnS formation. In samples P2 and P3, each has a field with the same thickness and height as field B to investigate the influence of the sulfur content. For each field, an area of 1.02 mm^2 is measured. The minimum detectable particle size in the measurements is 0.1 µm ECD (Equivalent Circle Diameter). While the measured area is relatively small to keep inclusions from forming under similar cooling conditions, at least 1000 particles are checked to ensure quality. From the cooling curve calculated based on the measured temperature, the cooling rates of the measured fields are defined as shown in Figure 5.11 (b).

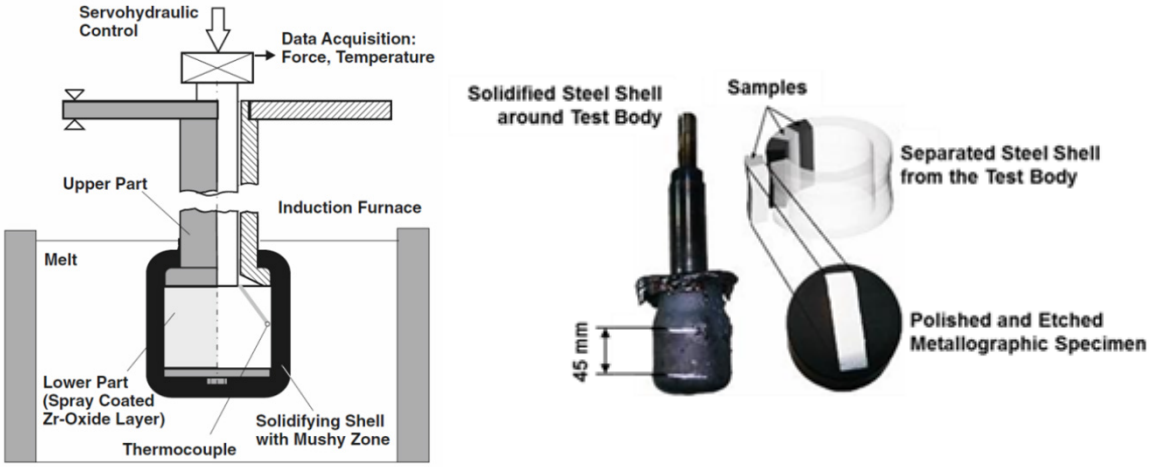

(a) (b)

Figure 5.10. Instruction of the (a) SSCT experiment and (b) sampling process [28].

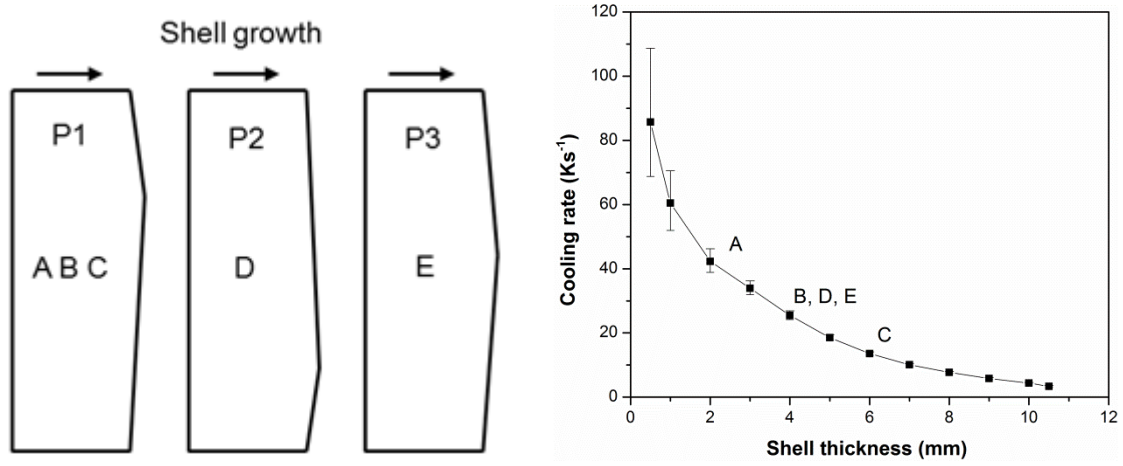

(a) (b)

Figure 5.11. (a) Measured fields by automated SEM/EDS and (b) corresponding cooling rates.

5.2.2 Parameter fitting

The collision parameter as given in Eq. (4.15) is fitted in this section using the experimental results. Note that all other parameters applied in the calculations have been listed in Table 4.12. In Chapter 4.4.3.5, the P1 steel was calculated with varying collision factors under a cooling rate of 25.4 Ks^{-1} (corresponding to field B). Additionally, stronger collisions result in larger less

number of particles. In Table 5.3, the calculated mean diameters and total number densities with different collision factors are compared with the measured value of field B in Figure 5.11 (a).

Table 5.3. Comparisons of the measured and calculated mean diameter and number density of MnS.

Sources	Collision factor (f)	Mean diameter (μm)	Number (mm^{-3})
Calculations	1	0.48	2.12×10^{6}
	10	0.49	1.83×10^{6}
	100	0.60	9.67×10^{5}
	200	**0.67**	**6.78×10^{5}**
	300	0.71	5.34×10^{5}
Experiment		0.54~0.65	$5.05\sim6.22\times10^{5}$

Note that for the comparison between measurements and calculations, the measured 2-dimensional diameter and number density from the analyzed cross section are converted into volumetric values using the program CSD Corrections v.1.50 [190,191]. In this program, corrections are made for the intersection probability and cut section effects. The measured 2D diameters and area are inputted into the software. Before conversion, the morphology information of the particles should be defined by 'short', 'intermediate' and 'long' aspect ratios and roundness. In the case of MnS particles, they are assumed to be isotropic. The class size settings for the histogram are also needed, because different choices of bin size settings vary the converted results. The last row of Table 5.3 gives the range of the mean diameters and number densities estimated with different bin settings. Table 5.3 shows that both the mean diameter and number density predicted with the collision factor of 200 agree well with the experimental values. As an output, in addition to the 3D size distribution, its Population Density Function (PDF, described in Eq. (5.2)) can be obtained from the CSD Corrections to minimize the influence of the bin size selection, which has already been applied in the study of the inclusion size distribution [192,193]. Figure 5.12 compares both the 3D size distribution and PDF of MnS from the measurement and calculation with a collision factor of 200. The PDF is defined as following,

$$PDF = \frac{n_V}{\Delta l} \tag{5.2}$$

where n_V is the volume number density of a size class and Δl is the size class width.

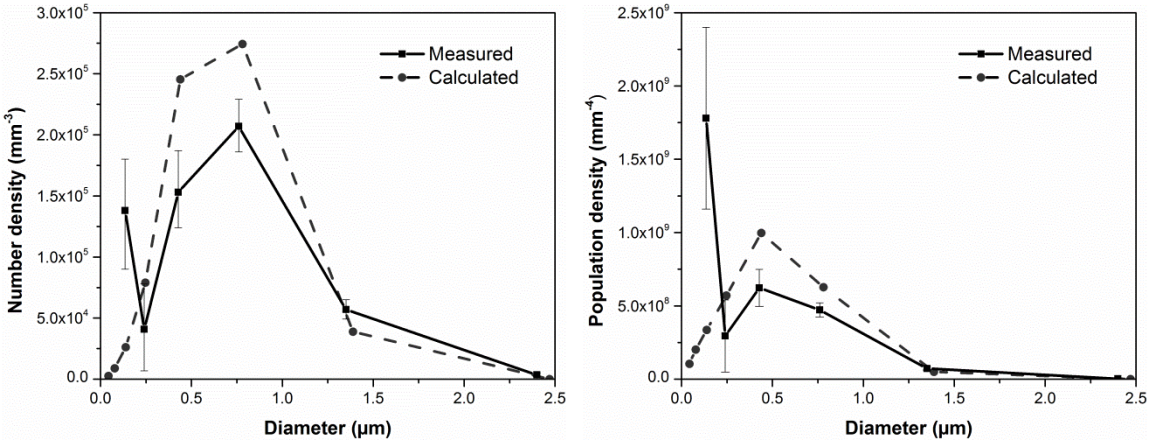

(a) (b)

Figure 5.12. Comparison of the measured and calculated size distribution *vs*. the (a) number density and (b) population density.

In Figure 5.12 (a), the predicted and measured size distributions are reclassified with a lognormal bin size. The figure shows that the calculated size distribution of MnS is in good agreement with the experimental one. The diameter class of 0.75 μm contains the most particles for both calculation and measurement, and the predicted and measured maximum particle sizes are also similar, with a diameter of approximately 2.5 μm. The measured number densities of the particles in the first several size classes (smaller than 0.12 μm) are higher than the predicted ones. This relatively larger discrepancy is attributed to the measured limitation (0.1 μm) and the further conversion to the 3D size distribution. For the population density shown in Figure 5.12 (b), the situation is similar with the number density, that is, the distributions fit well with each other, except for the first several size classes. Note that the present model cannot consider MnS precipitations in the solid steel, which can be smaller than 0.1 μm and may lead to discrepancies in the comparison.

Figure 5.13 displays the MnS formation process, including the size and amount evolutions as well as concentration changes of Mn and S. In Figure 5.13 (a), the entire distribution shifts to the direction of a larger size when solidification proceeds. The size distribution at a solid fraction of 0.980 has a narrow range from 0 to 0.5 μm and a high number density when MnS just starts to form. The distribution curve subsequently becomes flatter and broader due to growth and collision. At the end of solidification (solid fraction of 1), the maximum size reaches 2.5 μm and the maximum number density is approximately 3.0×10^{6} mm^{-3} with a diameter of 0.75 μm. Figure 5.13 (b) shows that MnS precipitates at a solid fraction of 0.98 and the amount soars. The concentration of sulfur decreases due to the relatively lower content and small liquid fraction, while the Mn concentration continues to increase but at a slower speed. At the late stage of precipitation, MnS grows slowly due to the consumption of S and the reduced amount of liquid steel.

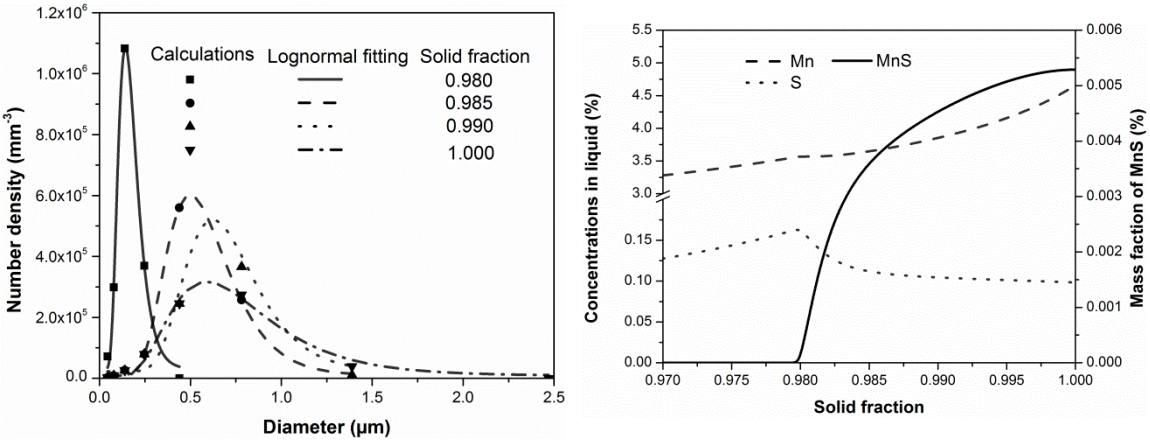

(a) (b)

Figure 5.13. Evolutions of (a) the size distribution and (b) the mass fraction of MnS and concentrations of Mn and S.

As a whole, a collision factor equal to 200 is regarded to be effective for simulating MnS formation using the present model under the SSCT experimental conditions. In the following calculations, therefore, a collision factor of 200 is applied to study the influence of cooling rate and sulfur content.

5.2.3 Application on studying the influences of process factors

After fitting the parameters to the experimental results, the present model gives high quality predictions for MnS formation during the solidification process. Furthermore, the model is utilized to investigate the influences of two important process parameters on MnS formation: the cooling rate and sulfur content. For reasonable comparisons of the calculated and experimental results, the measured 2D size distributions from the SSCT samples are also converted into 3D distributions using the described CSD Corrections v. 1.5 with the lognormal bin size setting; size classes smaller than 0.1 μm are not considered to avoid differences caused by the measurement limitations and precipitation in the solid steel.

5.2.3.1 Influence of cooling rate

Sample P1 (in Table 4.10) is calculated for three different cooling rates (42.3, 25.4 and 13.5 Ks^{-1}), which correspond to the measured fields A, B and C, respectively (Figure 5.10). The influence of the cooling rate on size distributions from the calculations and experiments is shown in Figure 5.14 (a) and (b), respectively. Figure 5.14 (a) shows that the size of inclusions has an increasing trend with a decreasing cooling rate. When the cooling rate slows from 42.3 to 13.5 Ks^{-1}, the maximum particle size class increases from approximately 1.3 to 2.5 μm; the diameter of particles with peak frequencies enlarges from 0.42 to 0.76 μm; and the frequency of particles with diameters of approximately 0.25 μm (the smallest size class) decreases from 20% to 5%. In Figure 5.14 (b), the experimental size distributions display similar trends with the

predicted results with decreasing cooling rates. The calculated and predicted size ranges and the diameter of particles with the largest proportion are the same.

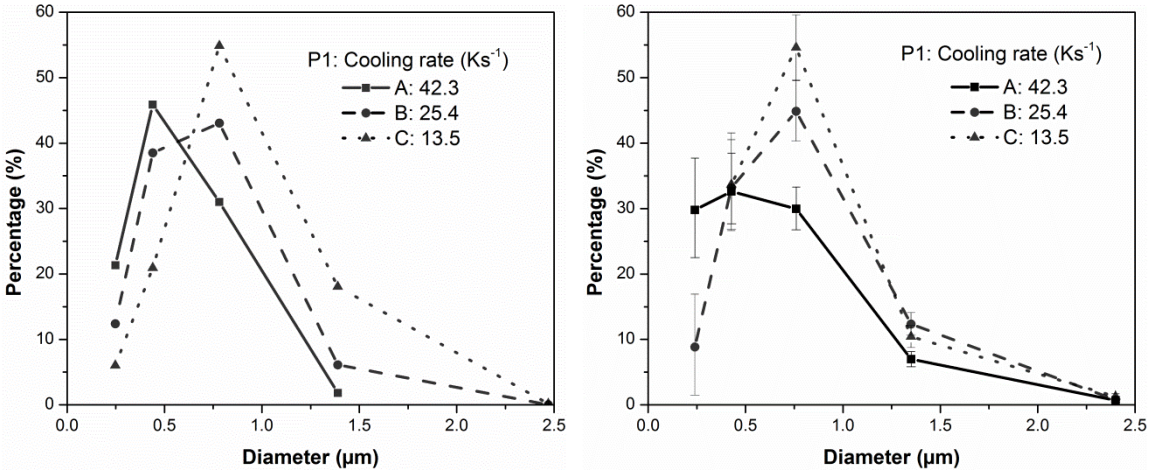

(a) (b)

Figure 5.14. Influence of the cooling rate on the size distribution of MnS from (a) calculations and (b) experiments.

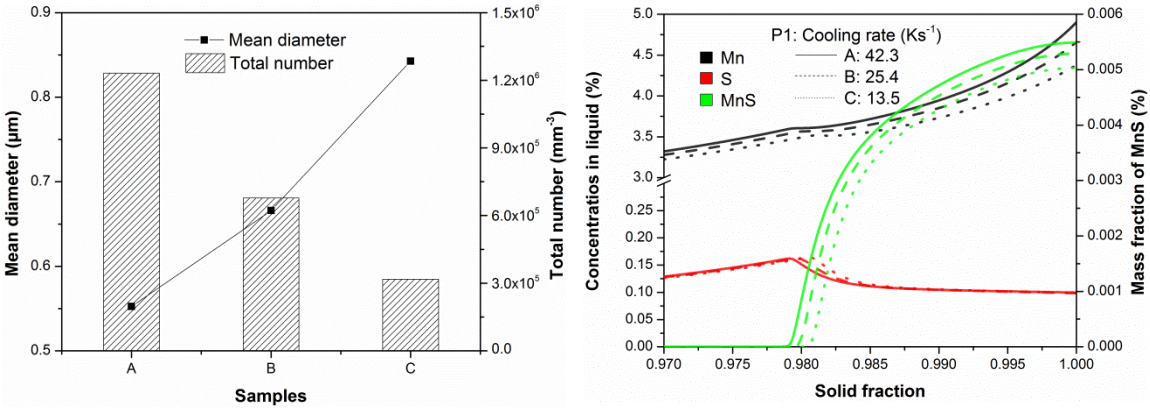

(a) (b)

Figure 5.15. Influence of the cooling rate on (a) the number and mean diameter and (b) the mass fraction of MnS and concentrations of Mn and S.

Figure 5.15 shows the calculated changes of the total number, mean diameter and amount of MnS, as well as the concentrations of Mn and S, with different cooling rates. Figure 5.15 (a) shows that the number density decreases, while the mean diameter increases with the decreasing rate. The amount of MnS decreases slightly when the cooling rate slows down, which is attributed to fewer segregations of Mn and S, as shown in Figure 5.15 (b). The simulations together with the experimental results demonstrate that the variations of cooling rate will significantly change the MnS size distributions, mean diameter and total number. At the same time, this indicates that the preferable features of MnS are achievable through controlling the cooling conditions and referring the corresponding predictions.

5.2.3.2 Influence of sulfur content

In addition to the cooling rate, the sulfur content is another key factor for MnS formation. Three samples with different sulfur contents (P1, P2 and P3 in Table 4.10) are calculated under a cooling rate of 25.4 Ks^{-1}. Figure 5.16 shows the influence of the sulfur content on the size distributions from the simulations and experiments.

As shown in Figure 5.16 (a), the size significantly increases with the increase of sulfur content from 20 ppm to 50 and 60 ppm. In the sample containing 20 ppm sulfur (P3), a diameter of approximately 0.25 μm, that is, the smallest size class, has a peak frequency of 80%, which is only approximately 15% in the other two samples with higher sulfur contents; the maximum size of the particles is approximately 0.76 μm, while it is 2.5 μm in the higher sulfur samples. The size distributions of the samples with 50 and 60 ppm sulfur are close to each other. Comparing the predicted size distributions with experimental distributions (Figure 5.16 (b)), the agreement can be considered to be satisfactory when bearing in mind the complexity of the phenomenon and uncertainty of the physical properties and measurements.

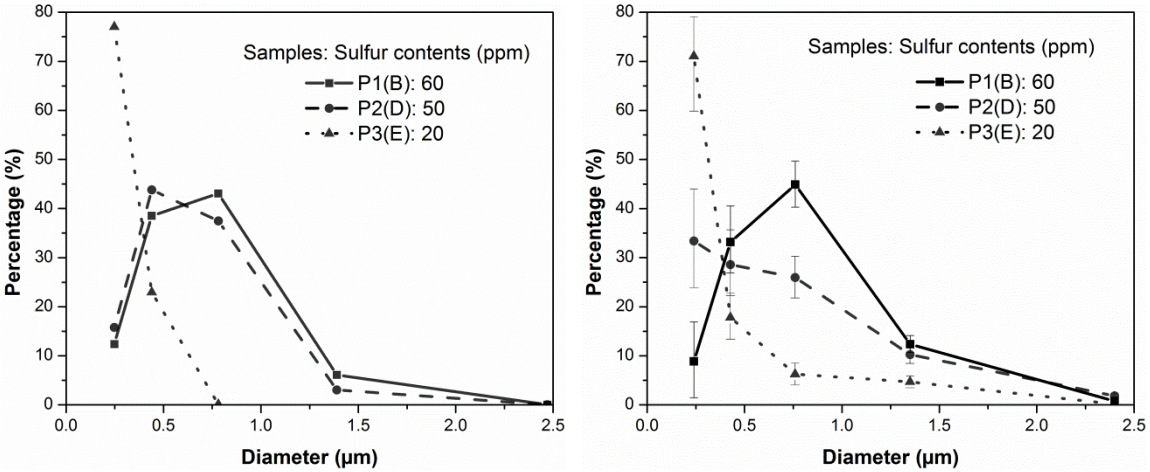

(a) (b)

Figure 5.16. Influence of the sulfur content on the size distribution of MnS from the (a) calculations and (b) experiments.

In Figure 5.17, the influence of the sulfur content on the number density, mean diameter and amount of MnS is predicted. Figure 5.17 (a) shows that with increasing sulfur content, the number density of MnS in the samples is comparable, while the mean diameter increases. The amount of MnS decreases considerably due to the decreasing sulfur content and less segregation. In the meantime, MnS in the sample containing higher sulfur content precipitates earlier than that in the sample with lower sulfur content.

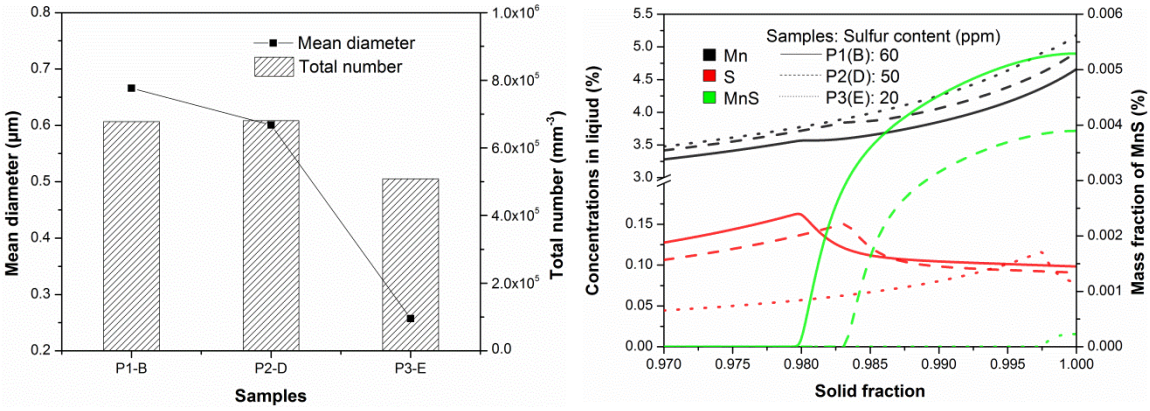

(a) (b)

Figure 5.17. Influence of the sulfur content on (a) the number and mean diameter and (b) the mass fraction of MnS and concentrations of Mn and S.

Based on the above discussion in this section, the cooling rate and sulfur content are important process parameters on deciding the MnS formation, final size distribution and number density. Fine dispersed MnS is desirable for both controlling and utilizing the inclusions. Faster cooling and reducing the sulfur content are two approaches for obtaining finer particles. For instance, the small size can effectively relieve the steel anisotropy due to MnS elongation after rolling; meanwhile, it can retain the austenite growth through pinning grain boundaries and further improve the steel properties. Faster cooling and reducing the sulfur content are two approaches for obtaining finer increasingly particles. At the same time, the other effects of these two methods should be considered, such as the serious manganese microsegregation, as shown in Figure 5.15 (b) and Figure 5.17 (b), which is detrimental to steel properties. Additionally, there is a favorable diameter ranging from approximately 0.3 to 0.9 μm when utilizing inclusions as heterogeneous nucleation sites for acicular ferrite [194,195]. In industrial solidification processes, the local cooling rate varies between several hundred degrees per second for welding and strip casting whereas for continuous casting or ingot casting, the local cooling rate might decrease to less than 0.1 degree per second close to the center of the cast part. The presented model allows for the precise evaluation of solidification processes with respect to the formation of sulfides with prescribed diameter or, vice-versa, the adjustment of manganese and sulfur content for the cooling conditions of a certain solidification process. Thus, the proper cooling rate and sulfur content should be defined.

5.3 Evaluation on multi-phase-inclusions formation modeling and application

Thermodynamics are the foundations for kinetic calculations. Hence, the thermodynamics of multi-phase-inclusions formation is first evaluated. This can be considered as an independent sub-model. The algorithm of coupling microsegregation and inclusion nucleation and growth kinetics is tested through overall mass balance. Then, the predictions from the sub-model for

three Ti-Al alloyed steels are compared with the experimental results on the inclusion types, compositions and the precipitation order. After confirming the thermodynamics, by using the proposed comprehensive model, the influences of cooling rate and oxygen content on competitive multi-phase-inclusions formation for the selected steel are investigated.

5.3.1 Thermodynamics validation

5.3.1.1 Overall mass balance

In this section, the algorithm of the fully coupled microsegregation and inclusion formation thermodynamics (the sub-model) is tested according to an overall mass balance for steel M1 with the composition listed in Table 5.4. To simplify the calculation of the solute amount in solid steel, the semi-integrated analytical equation of Scheil´s model [9] as given in Eq. (5.1) was applied for the microsegregation calculation in this test. It was assumed that solidification was completed at a solid fraction of 0.95. The results are shown in Figure 5.18.

Table 5.4. Chemical compositions of studied steels on multi-phase-inclusions formation (mass%).

Steels	C	Si	Mn	S	P	Al	Ca	Ti	O	N
M1	0.2	0.05	1.00	0.0060	0.0010	0.0300	0.0020	-	0.0020	-
M2	0.23	0.02	1.48	0.0074	0.0040	0.0051	-	0.0500	0.0050	-
M3	0.24	1.80	1.91	0.0060	0.0040	0.0040	-	0.0310	0.0029	0.0039
M4	0.26	1.84	2.07	0.0050	0.0040	0.0040	-	-	0.0040	0.0022

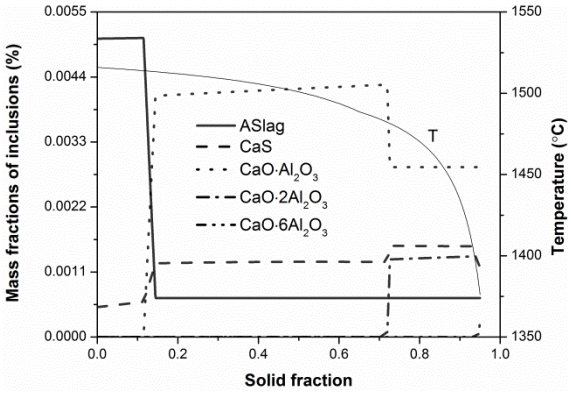

Figure 5.18. Changes of the inclusions during solidification for M1 steel.

Figure 5.18 describes the changes of inclusions during the solidification process. ASlag and CaS are found to be stable at the liquidus temperature. Here ASlag is a solution phase whose components are mainly Al_2O_3, CaO, Al_2S_3, CaS and SiO_2. At the solid fraction of 0.1, the ASlag phase transforms into CaS and $CaO{\cdot}Al_2O_3$. Next, with the stronger enrichment of solutes and decreasing temperature, $CaO{\cdot}Al_2O_3$ becomes unstable and becomes $CaO{\cdot}6Al_2O_3$ at solid fraction

of 0.7. During the changing of inclusions and enriching of solutes, the overall mass balances of all of the solutes were calculated. Compared with the input amount, a maximum relative difference of 0.05% was found for oxygen, whereas for the other elements, the maximum relative difference remains below 0.02%. With respect to the initial oxygen content in steel A of 0.002%, the inconsistency in the mass balance amounts to only 10^{-2} ppm. The observed differences can be primarily explained as the sum of the residuals in the iteration steps and by the abrupt increase of the partition coefficient during the peritectic reaction. With respect to the five involved inclusion types and continuous changes of their mass fraction as well as the change in partition coefficients due to the peritectic reaction the inconsistency in the mass balance is apparently in an acceptable range.

5.3.1.2 Experimental procedure

Steels M2, M3 and M4 (in Table 5.4) were produced on a laboratory scale. To achieve specific inclusion types and a possibly homogeneous distribution of non-metallic inclusions in the steel matrix, an easily controllable small-scale furnace is used for all experiments. The Tammann type furnace (Ruhrstrat HRTK 32 Sond.) is a high-temperature electric resistance furnace that can be heated to 1700 °C. Due to the carbon heating tubes inside the furnace and their reaction with the residual oxygen, the final oxygen content in the furnace vessel is extremely low (0.001 ppm). The schematic experimental setup before starting the experiment is schematically shown in Figure 5.19. All experiments are conducted under an inert gas atmosphere. The experimental procedure consists of the following main steps:

- Approximately 100 g of unalloyed steel (0.004wt% C, 0.066wt% Mn and 0.006wt% S, rest Fe) is placed in an Al_2O_3 crucible together with an oxygen-rich pre-melt (0.001wt% C, 0.075wt% Mn and 0.009wt% S, 0.175wt% O, remainder Fe). Due to the thermal and mechanical stresses during the experiment, the Al_2O_3 crucible is also placed into a graphite crucible. A Mo-wire which is used to remove the crucible from the furnace is fixed at the top of the graphite crucible (‘elevator system’).

- The crucible with the raw materials is heated to 1600 °C at a rate of 10 $Kmin^{-1}$, resulting in a melt that has a defined oxygen content of approximately 300 ppm. After 6 min the melt is stirred with an Al_2O_3 bar and C, Mn and Si are added according to the desired final chemical composition. This process also involves a decrease in the oxygen content and the formation of non-metallic inclusions.

- After another 8 min, the melt is stirred again and FeTi75 is added (only for steels M2 and M3), which again provokes the formation of new inclusions and the modification of pre-existing inclusions. FeTi75 means the Fe-75wt% Ti alloy. After holding for another 5 min at 1600 °C and a final stirring, the crucible is quickly removed from the heating

zone of the furnace by the use of the Mo-wire and then quenched rapidly through casting into a mold to prevent distinct inclusion flotation during solidification.

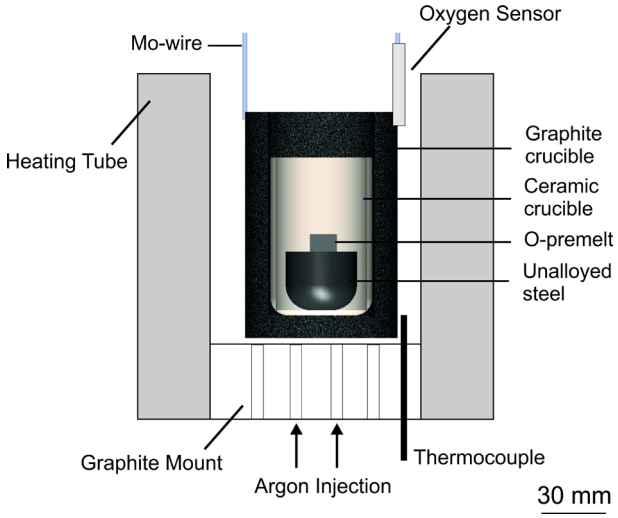

Figure 5.19. Schematic illustration of the experimental set-up for Tammann Furnace experiments.

The total experimental time of 19 min at the experimental temperature was the same for all experiments. The only difference consisted of the addition of FeTi75 alloy for steels M2 and M3, whereas for steel M4, no FeTi75 was alloyed. Note that Al was not added directly in any of the experiments. The presence of Al in the melt and consequently in the inclusion is the result of reactions with the crucible material used as well as the bar for stirring the melt.

The final cast sample has a spherical shape with a diameter of 50 mm. In the first step, the chemical composition of the sample was determined using classical optical emission spectrometry. The sample was then cut into equal halves: one part was used for inclusion analyses; the other part was used to produce small slices (cut from the part) for the determination of the oxygen and nitrogen contents via LECO analyses. The final chemical compositions of the examined samples are listed in Table 5.4. Further details regarding the Tammann Furnace experiments can be found elsewhere [196,197].

Automated SEM/EDS analyses using an FEI Quanta 200 MK2 scanning electron microscope (SEM), equipped with an energy dispersive X-ray spectrometer (EDS) system from Oxford Instruments, were performed to characterize the inclusion number, size and type in the produced samples of steels M2, M3 and M4. The latter method is the state-of-the-art method concerning the determination of steel cleanness in steels. Based on the automated SEM/EDS analysis, inclusions are detected due to the material contrast differences in the backscattered electron (BSE) image. Usually, non-metallic inclusions are displayed as darker compared to the steel matrix. The automated analyses are performed at an accelerating voltage of 15 kV and are

limited to a minimum particle size of 1.1 µm Equivalent Circle Diameter (ECD). Principally, a measurement area of 100 mm^2 is defined on the sample surface. However, because samples that are in the as-cast condition are not deformed after the melting experiment, the analysis is limited to a maximum of 6000 particles on the defined area to avoid an extensive measurement time caused by the presence of micropores. The inclusion distribution over the analyzed sample area was found to be very homogeneous, and in all cases, more than 90 mm^2 was analyzed.

5.3.1.3 Calculated results

The three steels M2, M3 and M4 were calculated using the proposed coupled model. The cooling rate was assumed to be 10 Ks^{-1} for all three steels considered, but the exact cooling rates of the aforementioned experiments are difficult to define. For this reason, taking Steel B as an example, the influence of the cooling rate on the inclusion formation during solidification also are discussed in this section.

(1) Steel M2

Figure 5.20 (a) shows the calculated inclusion formation behavior at a cooling rate of 10 Ks^{-1}. Four types of inclusions are predicted: ASlag, MnS, Al_2O_3 and Ti_3O_5. The components of the solution phase -of ASlag- are mainly Al_2O_3, MnO, Ti_2O_3 and TiO_2. The exact compositions of ASlag will be discussed in Section 5.3.1.5. The primary inclusions before solidification are ASlag and Al_2O_3. Next, ASlag increases and Al_2O_3 decreases at a small scale until reaching a solid fraction of 0.1. At the solid fraction of 0.1, ASlag becomes unstable and then decomposes into Ti_3O_5 and Al_2O_3, leading to the sharp increases of Ti_3O_5 and Al_2O_3. These sudden changes are not reasonable however when considering the kinetic processes. In the subsequent process, Ti_3O_5 is more stable than Al_2O_3 in the following process and precipitates with the consumption of Al_2O_3. MnS forms at the late stage of solidification due to the microsegregation of sulfur (S) and manganese (Mn). Finally, in addition to Ti_3O_5 and MnS, small amounts of ASlag and Al_2O_3 still exist due to trapping by solid steel.

To investigate the influence of the cooling rate on the inclusion formation thermodynamics, another calculation is performed for Steel B applying a cooling rate of 0.1 Ks^{-1}. The calculation result is shown in Figure 5.20 (b). Compared with the result assuming a cooling rate of 10 Ks^{-1}, as shown in Figure 5.20 (a), the inclusion types are the same when including Ti_3O_5, MnS, ASlag and Al_2O_3, and their evolution processes are also the same. The amount of oxides calculated with different cooling rates is similar. The amount of MnS under a cooling rate of 10 Ks^{-1} is approximately twice that of the cooling rate of 0.1 Ks^{-1} because of the higher enrichment of S and Mn. The higher cooling rate also yields to a lower solidus temperature because of stronger microsegregation. A reasonable cooling rate therefore must be selected especially for the

prediction of microsegregation-induced precipitations (such as MnS), whereas the influence of the cooling rate on the formation of oxides can practically be neglected for the present case.

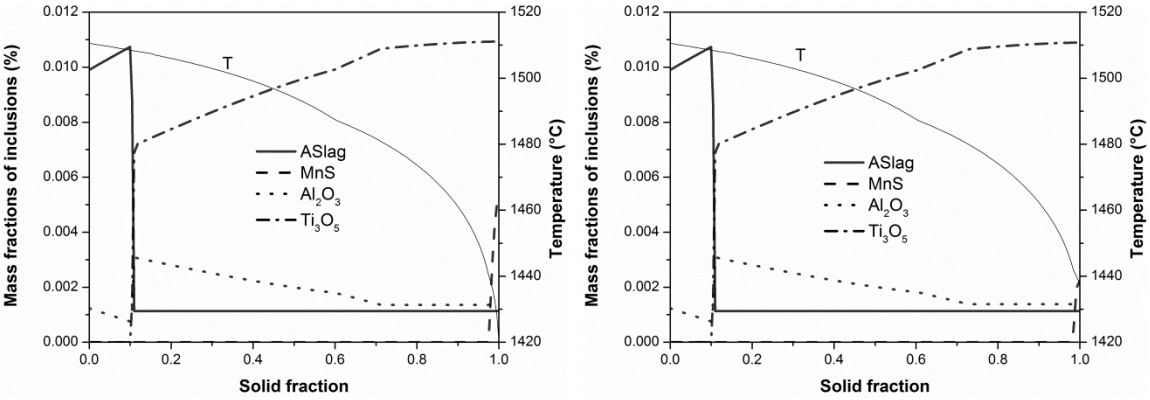

(a) (b)

Figure 5.20. Calculated inclusion formation behavior during the solidification of M2 (a) at a cooling rate of 10 Ks^{-1} and (b) at a cooling rate of 0.1 Ks^{-1}.

(2) Steel M3

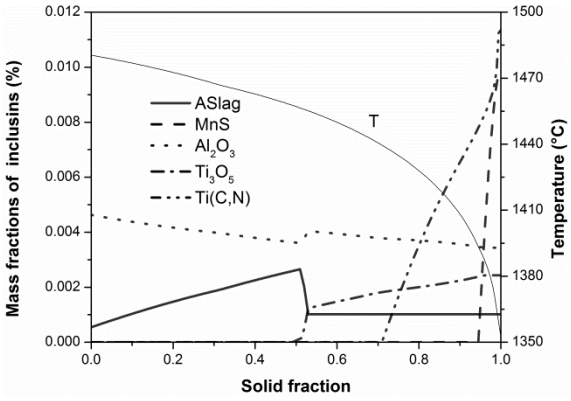

Figure 5.21. Calculated inclusion formation behavior during the solidification of M3 at a cooling rate of 10 Ks^{-1}.

Figure 5.21 displays the inclusion changes that occur during the solidification of Steel C. Five types of nonmetallic inclusions are observed: ASlag, MnS, Al_2O_3, Ti_3O_5 and Ti(C, N). The ASlag phase is composed of Al_2O_3, SiO_2, MnO, Ti_2O_3 and TiO_2. In addition to ASlag, Ti(C, N) is also a solution phase, in which the amount of carbon (C) increases gradually because of microsegregation. ASlag and Al_2O_3 already exist in liquid steel. After solidification starts, the amount of ASlag increases, whereas that of Al_2O_3 decreases. ASlag transforms into Ti_3O_5 and Al_2O_3 at a solid fraction of 0.5. Similar to ASlag in Steel B, the sudden decomposition results in only a small amount of ASlag in the solid steel. Ti_3O_5 starts to precipitates from this point and the content of Al_2O_3 continues to decrease. Next, Ti(C, N) forms at a solid fraction of 0.7 due to the microsegregation of titanium (Ti) and nitrogen (N). The enrichments of Mn and S promote the precipitation of MnS after reaching a solid fraction of 0.94. The formation of Ti(C, N) and

MnS highlights the importance of microsegregation. Note that the amount of different inclusions from the calculation only offers a basic reference. For an accurate estimation of the absolute contents, the kinetics must be considered.

(3) Steel M4

Figure 5.22 describes the inclusions formation during solidification of Steel D. ASlag, Al_2O_3 and MnS compose the inclusions in Steel D. Without Ti addition, Al_2O_3, SiO_2 and MnO are the primary components of the ASlag phase. ASlag and Al_2O_3 form before solidification. During the solidification process, ASlag gradually increases and Al_2O_3 decreases. MnS precipitates at the late stage of solidification. Compared with Steels B and C, the types and changes of inclusions are relatively few due to the absence of Ti addition.

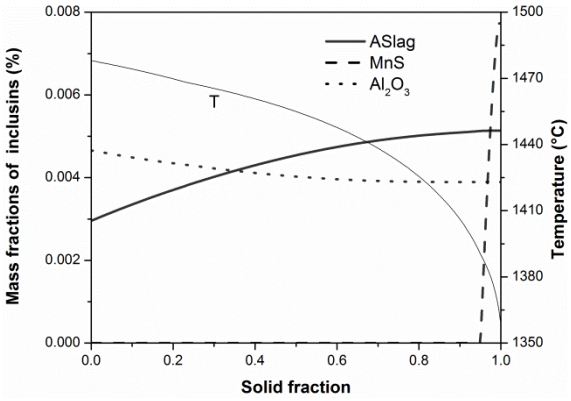

Figure 5.22. Calculated inclusion formation behavior during the solidification of M4 at a cooling rate of 10 Ks^{-1}.

5.3.1.4 Experimental results

Figure 5.23 shows the inclusion types and frequencies of inclusions in the three steels obtained from automated SEM/EDS analyses. For each type of steel, the main inclusion types are listed; inclusion types with a relative frequency of less than 2% were summarized in the class 'others'. For Steel M2, the predominant inclusion types are (Ti, Al, Mn)$_x$O$_y$, TiO$_x$, MnS and Al_2O_3-TiO$_x$. The other types are mainly the heterogeneous inclusions of the aforementioned oxides and sulfides; among them, the frequency of (Ti, Al, Mn)$_x$O$_y$ and TiO$_x$ account for approximately 90% of the total inclusion amount.

In Steel M3, (Ti, Al, Si, Mn)$_x$O$_y$, MnS and Ti(C,N) are the main inclusions. Compared with Steel B, the frequencies of oxides are decreased, in agreement with the lower oxygen content in steel C. The enrichments of nitrogen (N) and carbon (C) result in the precipitation of Ti(C,N). Carbonitrides and sulfides are likely to nucleate heterogeneously.

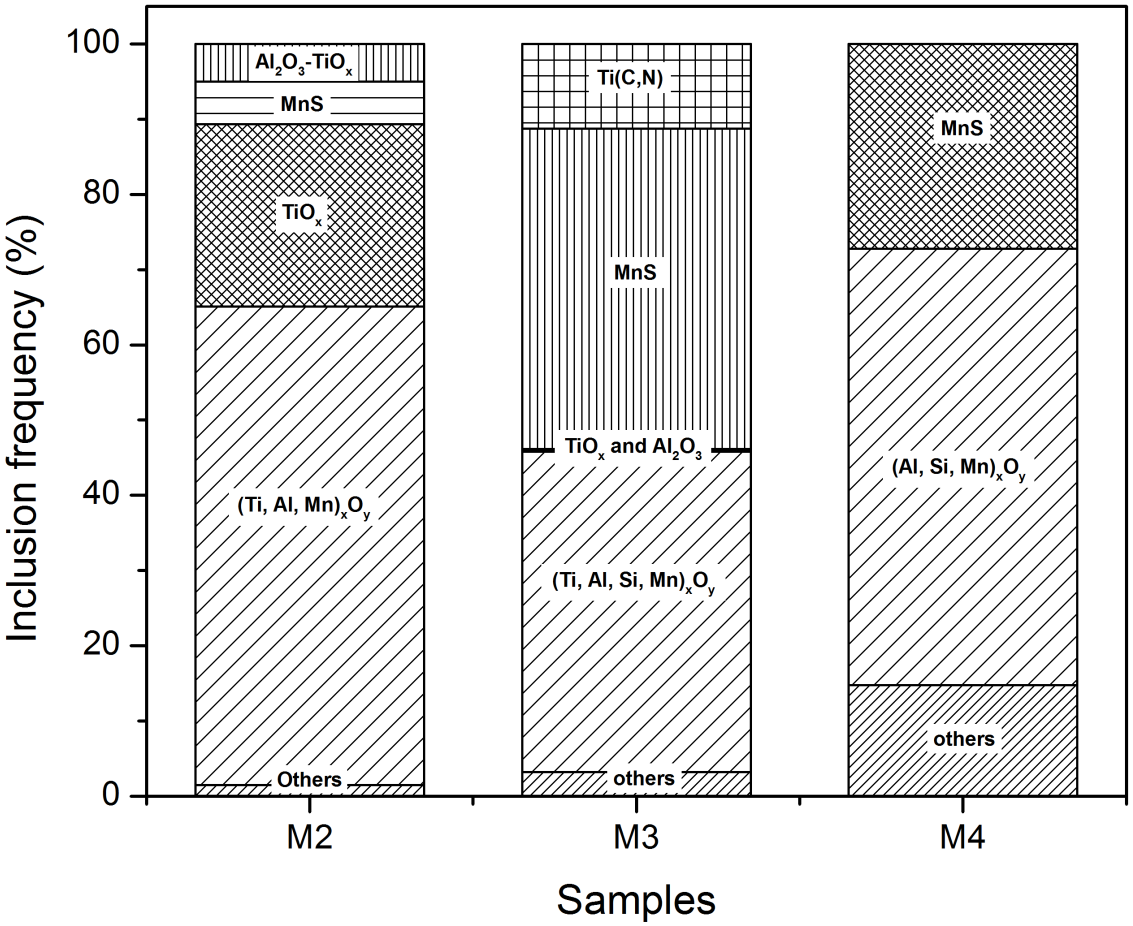

Figure 5.23. Results of automated SEM/EDS analyses for the investigated steels M2, M3 and M4.

For Steel M4, the types of inclusions are significantly different due to the absence of Ti. (Al, Si, Mn)$_x$O$_y$, MnS and oxysulfides are the prevailing types. Similar with Steel C, the microsegregation of solutes contribute to the high frequency of MnS. Hardly any pure Al_2O_3 was detected in any of the three steels considered.

5.3.1.5 Confirmation of the formation thermodynamics of the multi-phase-inclusions

In this section, the calculated results are compared with the experimental ones and their correspondence is discussed. Meanwhile, the inclusion formation processes in M2, M3 and M4 steels were analyzed based on the calculations and measurements.

(1) Steel M2

For comparing the measured and predicted types of inclusions, it is important to realize that the model cannot picture heterogeneous nucleation. Consequently, a direct comparison between the measured and calculated inclusions is not approvable for all types. In detail, a comparison between measured and calculated inclusion types leads to the following results:

- The solution phase (Ti, Al, Mn)$_x$O$_y$ reflects the largest percentage in Steel M2. Figure 5.24 shows the morphology and the corresponding EDS spectrum of the (Ti, Al, Mn)$_x$O$_y$ phase. The shape and nature of this inclusion type suggests its liquid occurrence at the processing temperature. As illustrated in Figure 5.25, the average composition of this measured phase (measurement of the whole particle) is in very good agreement with the calculated ASlag Phase, which is the predominant phase at low solid fraction in the calculations (see Figure 5.20 (a)). Thus, a correspondence between the measured and calculated results for this type can be assumed.

- TiO$_x$ and MnS are found by both measurement and calculation as shown in Figure 5.20 (a) and Figure 5.23. As stated in the literature, Ti$_3$O$_5$ can transform into other titanium oxides in solid steel [198]. In addition, a clear distinction between different titanium oxides in the automated measurement results is also difficult to obtain due to unavoidable effects, such as the dependence of the excitation of the inclusions´ surrounding matrix with the size of the inclusions´. Thus, the exact fit of predictions and measurements regarding the stoichiometry of the oxides cannot be expected, although the comparison showed a satisfying accordance.

- Table 5.5 summarizes the correspondence of the predicted and measured inclusion types in Steel B. The homogeneous inclusions (Types 1, 2, and 3) are in good agreement. For the heterogeneous inclusions, Al$_2$O$_3$-TiO$_x$ and TiO$_x$-MnS (Types 4 and 5), no direct accordance is found because, as previously stated, heterogeneous nucleation is not considered by the presented model. The order of inclusion formation, however, can be predicted, which can be indirectly used to explain the formation of these inclusion types.

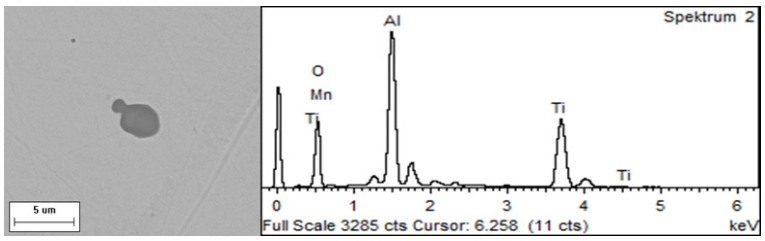

Figure 5.24. Morphology and EDS analysis of (Ti, Al, Mn)$_x$O$_y$ in steel M2.

Al$_2$O$_3$ is likely to act as a heterogeneous nucleus for TiO$_x$ and other oxides, whereas TiO$_x$ itself can also act as a potential nucleus for the precipitation of MnS (see Figure 5.26 (a) and (b)). In the automated measured results (Figure 5.23), heterogeneous TiO$_x$-MnS (Figure 5.26 (a)) inclusion is classified into others. Based on the assumptions and explanations above, the following inclusion formation order is proposed: Al$_2$O$_3$, Ti$_3$O$_5$, and MnS. The same order is described by the calculations as shown in Figure 5.20 (a).

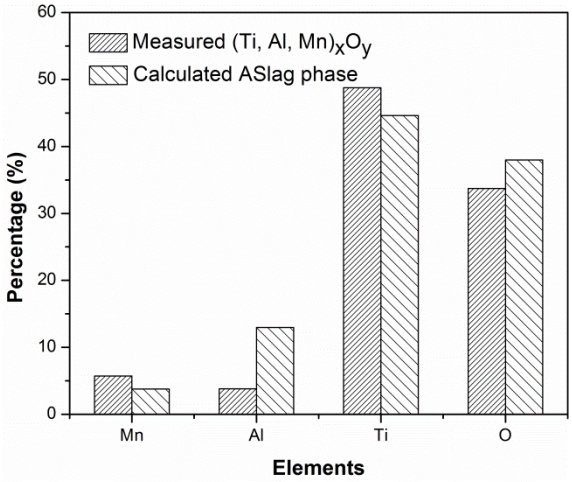

Figure 5.25. Comparison of the calculated and measured compositions of (Ti, Al, Mn)$_x$O$_y$ (named ASlag in the calculation results) in steel M2.

Table 5.5. Correspondence of the predicted and measured inclusions in Steel M2.

Types	1	2	3	4	5
Measured	(Ti, Al, Mn)$_x$O$_y$	TiO$_x$	MnS	Al_2O_3-TiO$_x$	TiO$_x$-MnS
Calculated	ASlag	Ti_3O_5	MnS	Al_2O_3	-
Corresponding	Yes	Yes	Yes	Possible	Possible

Regarding the inclusion frequencies, Figure 5.23 shows that the contents of homogeneous inclusions in Steel M2 occur in the following order according to the measurements: (Al, Ti, Mn)$_x$O$_y$, TiO$_x$, and MnS. For the predictions (Figure 5.20 (a)), the content decreases from Ti_3O_5 to MnS and to ASlag. Note that this difference results from the transformation balance between TiO$_x$ and ASlag. One possible reason for the discrepancy is that instead of thermodynamically sudden decomposition shown in Figure 5.20 (a), the (Al, Ti, Mn)$_x$O$_y$ (ASlag) could transform into TiO$_x$ with low speed. Thus, in solid steel, there is a larger amount of (Al, Ti, Mn)$_x$O$_y$ oxide than TiO$_x$.

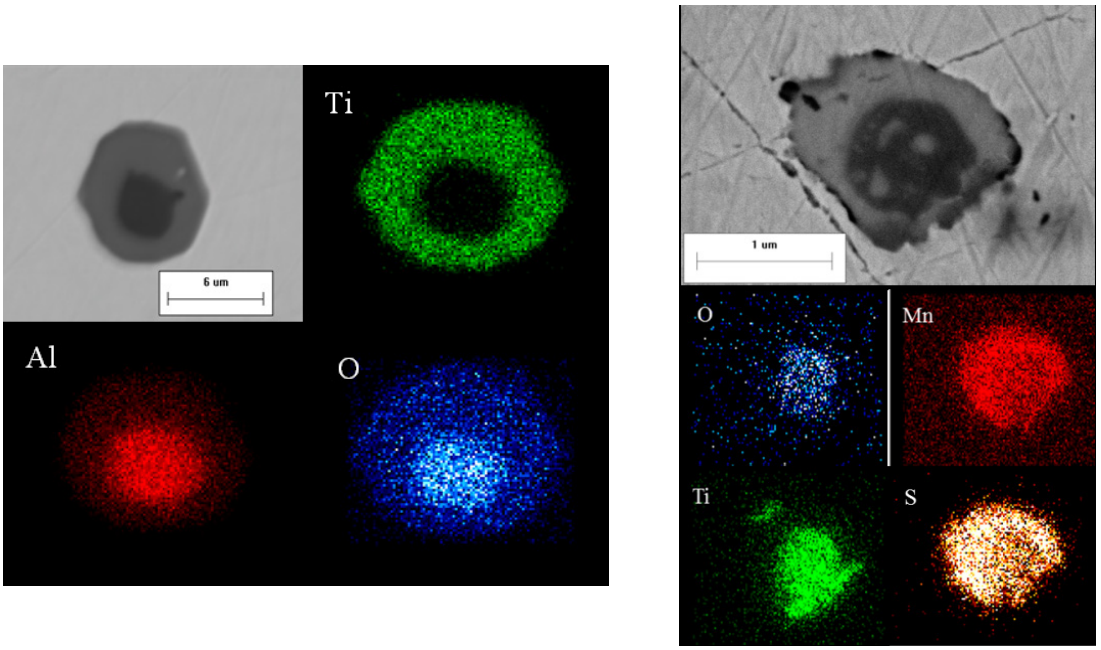

(a) (b)

Figure 5.26. Typical heterogeneous inclusions in steel M2: (a) Al_2O_3-TiO_x and (b) TiO_x-MnS.

(2) Steel M3

- For studying the correspondence of the inclusion types, it is necessary to define the solution phase (Ti, Al, Si, Mn)$_x$O$_y$. The spherical shape and chemical composition of the solution phase given in Figure 5.27 indicate the possibility of corresponding to the ASlag phase. Figure 5.28 compares the average measured compositions of (Ti, Al, Si, Mn)$_x$O$_y$ (measurement of the whole particle) and calculated ASlag. The good agreement illustrates their correspondence.

- Table 5.6 lists the corresponding inclusion types from the predictions and measurements in Steel C. In addition to the (Ti, Al, Si, Mn)$_x$O$_y$ solution phase, TiO_x, Al_2O_3, MnS and Ti(C, N) are also identified in both calculations and experiments. Note that it is difficult to compare the compositions of Ti(C, N) due to the largely changeable nature in the microsegregation process of solutes.

Regarding the inclusion formation order, various oxides form before MnS and Ti(C, N). MnS and Ti(C, N) precipitate at the late stage of solidification because of segregation. It is also possible for pre-existing (Ti, Al, Si, Mn)$_x$O$_y$ to transform into TiO_x and Al_2O_3. However, when considering the transformation kinetics, the occurrence of sudden and complete decomposition appears to be unreasonable.

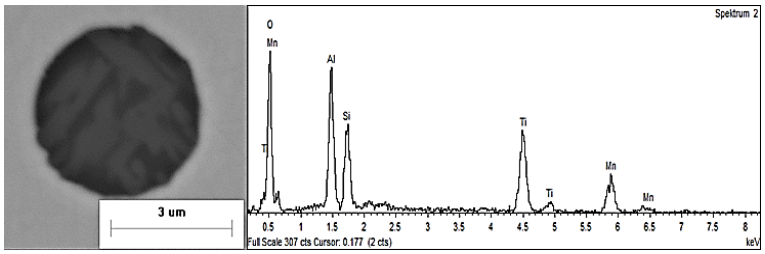

Figure 5.27. Morphology and EDS analysis of (Ti, Al, Si, Mn)$_x$O$_y$ in steel M3.

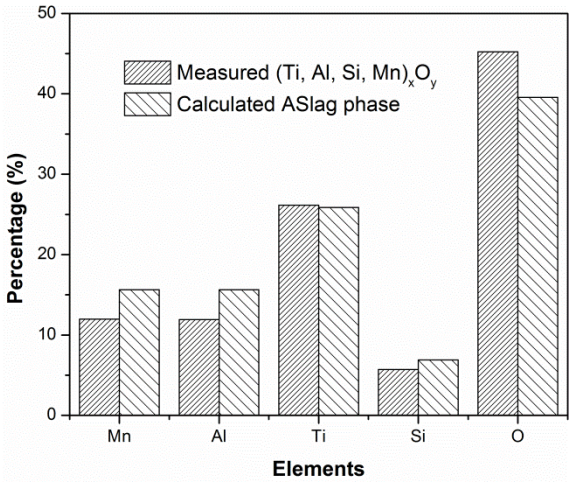

Figure 5.28. Comparison of the calculated and measured compositions of (Ti, Al, Si, Mn)$_x$O$_y$ (named ASlag in the calculation results) in steel M3.

Table 5.6. Correspondence of the predicted and measured inclusions in Steel M3.

Types	1	2	3	4	5
Measured	(Ti, Al, Si, Mn)$_x$O$_y$	TiO$_x$	Al$_2$O$_3$	MnS	Ti(C, N)
Calculated	ASlag	Ti$_3$O$_5$	Al$_2$O$_3$	MnS	Ti(C, N)
Corresponding	Yes	Yes	Yes	Yes	Yes

For the inclusion frequency, the prediction (Figure 5.21) shows that the oxides, manganese sulfide and titanium carbonitride share similar frequencies, and the measurement (Figure 5.23) displays similar frequencies of to those of the oxides and manganese sulfide as well as a smaller percentage of carbonitrides. For a simple comparison, the applicability of the calculation and experiment is considered to be acceptable. Among the oxides, TiO$_x$ and Al$_2$O$_3$ are rarely detected, which is attributed to the interaction between the melt and the Al$_2$O$_3$ crucible. The local saturation of solutes results in the preferable formation of (Ti, Al, Si, Mn)$_x$O$_y$ instead of the existence of Al$_2$O$_3$. In addition, there is less transformation from (Ti, Al, Si, Mn)$_x$O$_y$ to TiO$_x$ and Al$_2$O$_3$ with consideration of the kinetics.

(3) Steel M4

In steel M4, the same approach as for Steels M2 and M3 is taken for the inclusion type comparison:

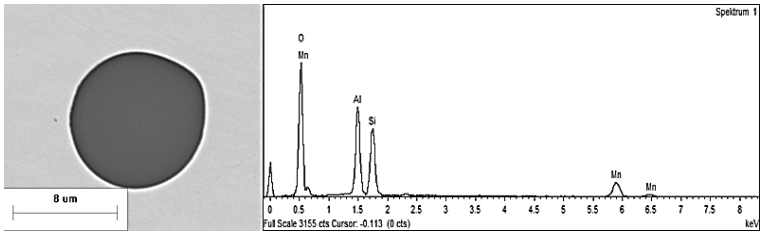

Figure 5.29. Morphology and EDS analysis of (Al, Si, Mn)$_x$O$_y$ in steel M4.

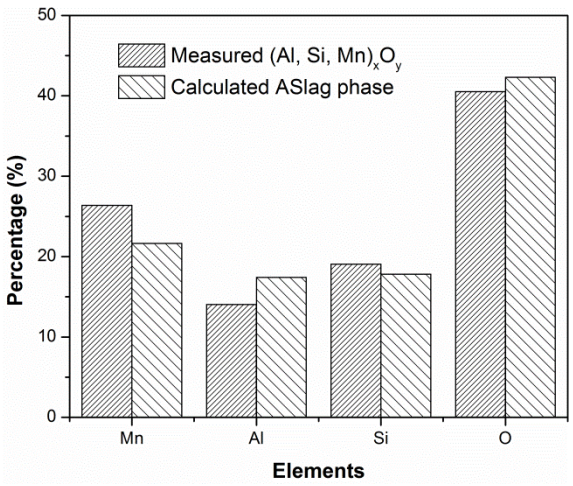

Figure 5.30. Comparison of the calculated and measured compositions of (Al, Si, Mn)$_x$O$_y$ (named ASlag in the calculation results) in steel M4.

- As shown in Figure 5.28, (Al, Si, Mn)$_x$O$_y$ in Steel M4 shares similar spherical shape to that of the solution oxides in Steels M2 and M3. Figure 5.29 shows the good accordance of the average compositions of (Al, Si, Mn)$_x$O$_y$ (measurement of the whole particle) and the ASlag phase.

- In addition to (Al, Si, Mn)$_x$O$_y$, MnS are also identified in the calculated and experimental results as summarized in Table 5.7. Pure Al_2O_3 was not detected in the measurements.

In contrast with the oxides, MnS always precipitates at end of the solidification. Without Ti addition, (Al, Si, Mn)$_x$O$_y$ and MnS account for the largest part of the inclusions. The absence of Al_2O_3 in the measurement is comparable to the situation in Steel M3. Without Ti addition, however, the high concentration of Si and Mn would promote the formation of (Al, Si, Mn)$_x$O$_y$ near the crucible rather than Al_2O_3.

Table 5.7. Correspondence of the predicted and measured inclusions in Steel M4.

Types	1	2	3
Measured	$(Al, Si, Mn)_xO_y$	MnS	-
Calculated	ASlag	MnS	Al_2O_3
Corresponding	Yes	Yes	Possible

Overall, the predicted inclusion types, compositions and formation orders of all the three steels are in good agreement with the experimental results. Even for the inclusion frequencies, the calculations offer meaningful references. The measurements, however, do not reflect the entire inclusion spectrum in the sample. Inclusions smaller than 1.1 μm ECD are not considered in the measurements. Furthermore, although the inclusion distribution was homogenous over the measured sample area, certain deviations due to the comparable small measured area and some limitations of the laboratory experiment itself (e.g. flotation and separation effects during the experiment) must be considered when comparing measurements and calculations. For more accurate and detailed predictions, the coupled model thus must be further developed and improved regarding the kinetic aspects.

5.3.2 Multi-phase-inclusions formation kinetics: an illustrative example

The tested sub-model for thermodynamics is in the following used to investigate the competitive nucleation and growth kinetics of multi-phase-inclusions during cooling and solidification. The M2 steel (in Table 5.4) was selected as an illustrative example.

Figure 5.31 displays the mass fraction of the various inclusion types versus temperature and the corresponding oxygen concentration in the residual liquid. During the cooling process, the ASlag phase is the only stable phase; its mass fraction increases already close to 1600 °C and ASlag forms continuously during cooling due to the decreasing solubility for oxygen. ASlag is a solution phase containing Al_2O_3, MnO, Ti_2O_3 and TiO_2, and the detailed composition is shown in Figure 5.25. During cooling of the liquid, Al_2O_3 is thermodynamically stable but the chemical driving force is not high enough for nucleation of pure Al_2O_3. After the start of solidification at about 1510 °C, ASlag becomes thermodynamically unstable and starts to dissolve quickly which results in minor stability problems and mass fraction fluctuates; the amount of Al_2O_3 increases rapidly, reaches its maximum and then decreases slowly with the precipitating of Ti_3O_5. Below 1480 °C, the mass fraction of Ti_3O_5, ASlag and Al_2O_3 remains constant even though ASlag and Al_2O_3 are thermodynamically unstable and get completely dissolved in the residual liquid steel. Their existence in the solid steel is only attributed to the entrapment by the solidification interface. While the oxygen concentration increases slightly at the latest stage of

solidification due to microsegregation, the limited content in the residual liquid does not result in significant growth of the oxides. MnS forms at the end of solidification in the current case. The size evolution of the inclusions at the selected temperatures which are marked by the points in Figure 5.31, are shown in Figure 5.32.

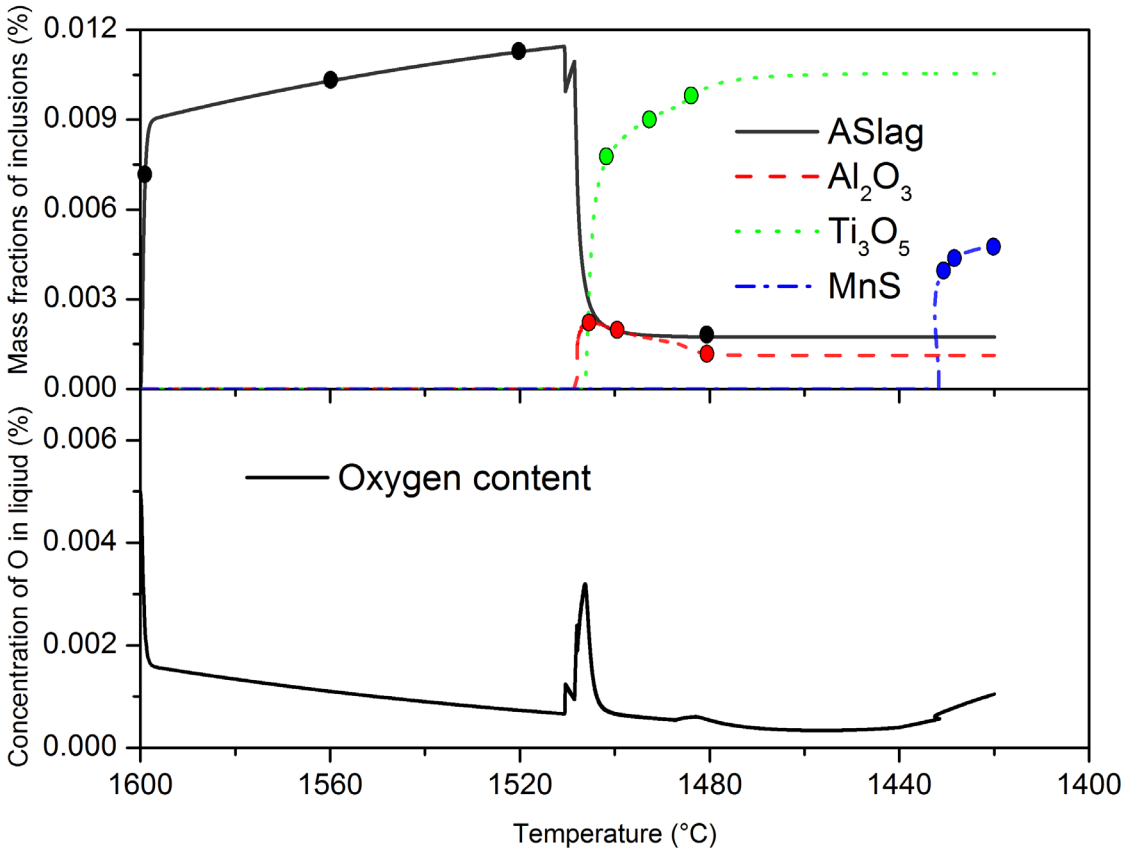

Figure 5.31. The changes of inclusions amounts and oxygen concentration during cooling and solidification of M2 steel.

Figure 5.32 (a) displays the size distributions of ASlag at the decreasing temperatures. At 1599 °C, ASlag just starts to form and the maximum number density of the nucleated particles is smaller than 1 µm. At this stage, nucleation and diffusion controlled growth lead to the further increase of the mass fraction of ASlag (Figure 5.31). Later on, the size of the particles increases and the maximum number density decreases as described by the size distributions at 1560 and 1520 °C. While diffusion controlled growth slows down as the supersaturation of oxygen decreases, collision growth becomes the dominating growth effect. With the start of solidification, both number density and size of ASlag decrease due to the thermodynamic instability and the following dissolution in the liquid. Particles which are entrapped by the liquid do not change their size or composition anymore. Figure 5.32 (b) shows the size evolution of Al_2O_3. The figure shows that the Al_2O_3 inclusions are much smaller than the ASlag particles due to the low oxygen supersaturation and the lack of gradient growth. After the temperature falls below the liquidus temperature (1505, 1500 and 1480 °C), the maximum number density

decreases due to the collision growth and the corresponding sizes are similar to approximate 0.45 μm. The maximum size of Al_2O_3 is only 1.4 μm. Compared with the size distribution at 1505 °C, the two size distributions at lower temperature of Al_2O_3 have a broader size range though the particles dissolve at the temperatures, which attributes to the collisions promoting the formation of the larger particles. The size distribution histograms of Ti_3O_5 are shown in Figure 5.32 (c), and shows that the size distribution of Ti_3O_5 does not change significantly with temperature. The maximum number density decrease with solidification proceeding and the number of larger inclusions increases. At the initial stage of MnS formation, the size distributions changes rapidly due to the strong segregations of Mn and S (Figure 5.32 (d)). This study focuses on the competitive formation of various oxides, while the influences of the conditions on MnS formation are not discussed in the following sections. These details can be found in Chapter 5.2.3.

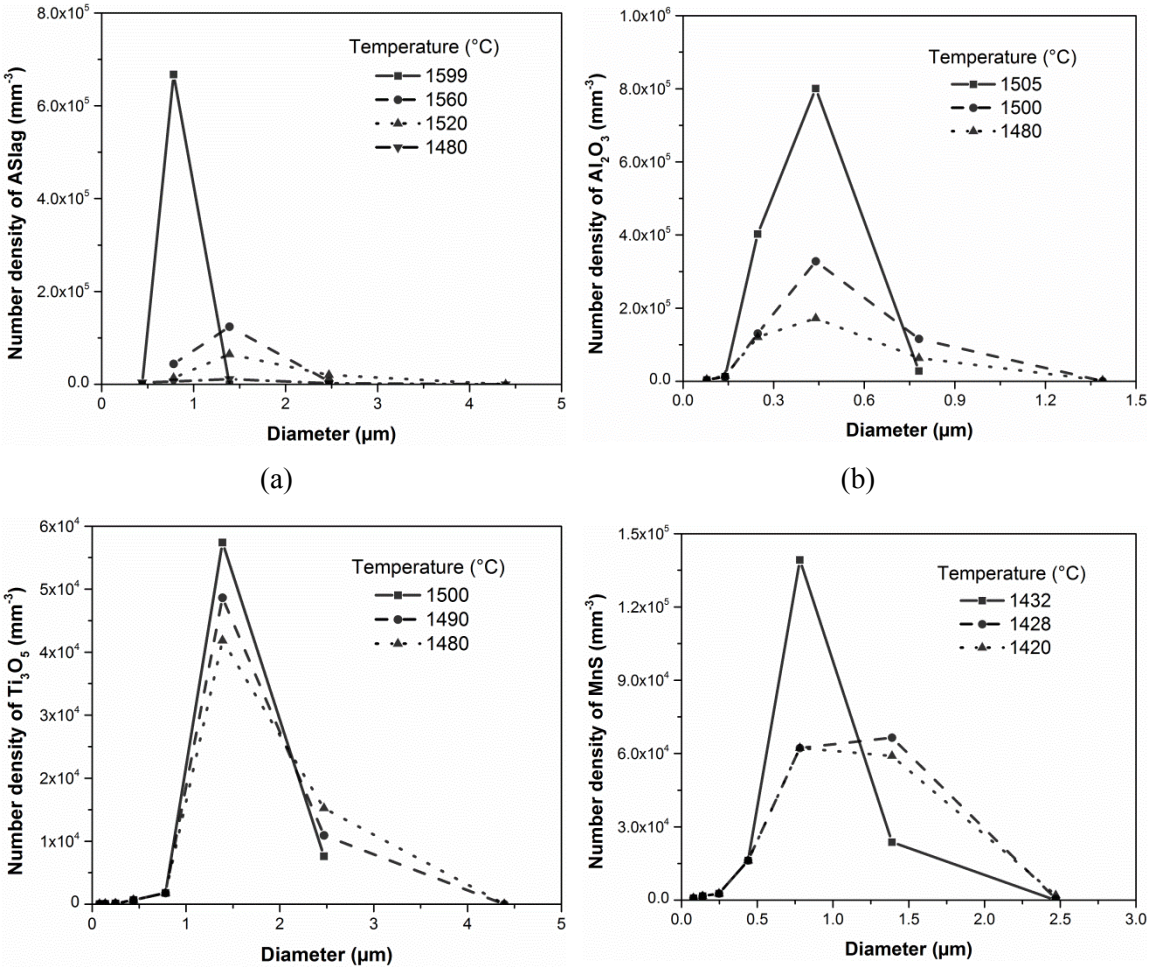

Figure 5.32. The size evolutions of the inclusions formed during cooling and solidification processes in M2 steel (a) ASlag, (b) Al_2O_3, (c) Ti_3O_5 and (d) MnS.

5.3.2.1 Influence of cooling rate

To investigate the effect of cooling rate on the nature, size and composition of oxide inclusions formation, steel M2 was investigated using the comprehensive model under three cooling rates: 50, 10 and 2 Ks^{-1}. The changes of the mass fraction of inclusion and corresponding concentration of dissolved oxygen in the liquid are shown in Figure 5.33. The figure shows that the mass fraction of the different oxides is almost independent from the cooling rate. The same applies when comparing the oxygen concentrations. At the initial stage of ASlag formation (from 1600 to 1580 °C), the highest cooling rate of 50 Ks^{-1} retards the formation of inclusions but the final mass fraction of ASlag is nevertheless similar. When ASlag becomes unstable later on, the particles dissolve slower during cooling at 50 Ks^{-1} which leads to the finally higher mass fraction. The higher mass fraction of ASlag in case of faster cooling is the main reason for a lower fraction of Ti_3O_5 and Al_2O_3. A higher cooling rate results in the lower solidus temperature due to the more pronounced segregation.

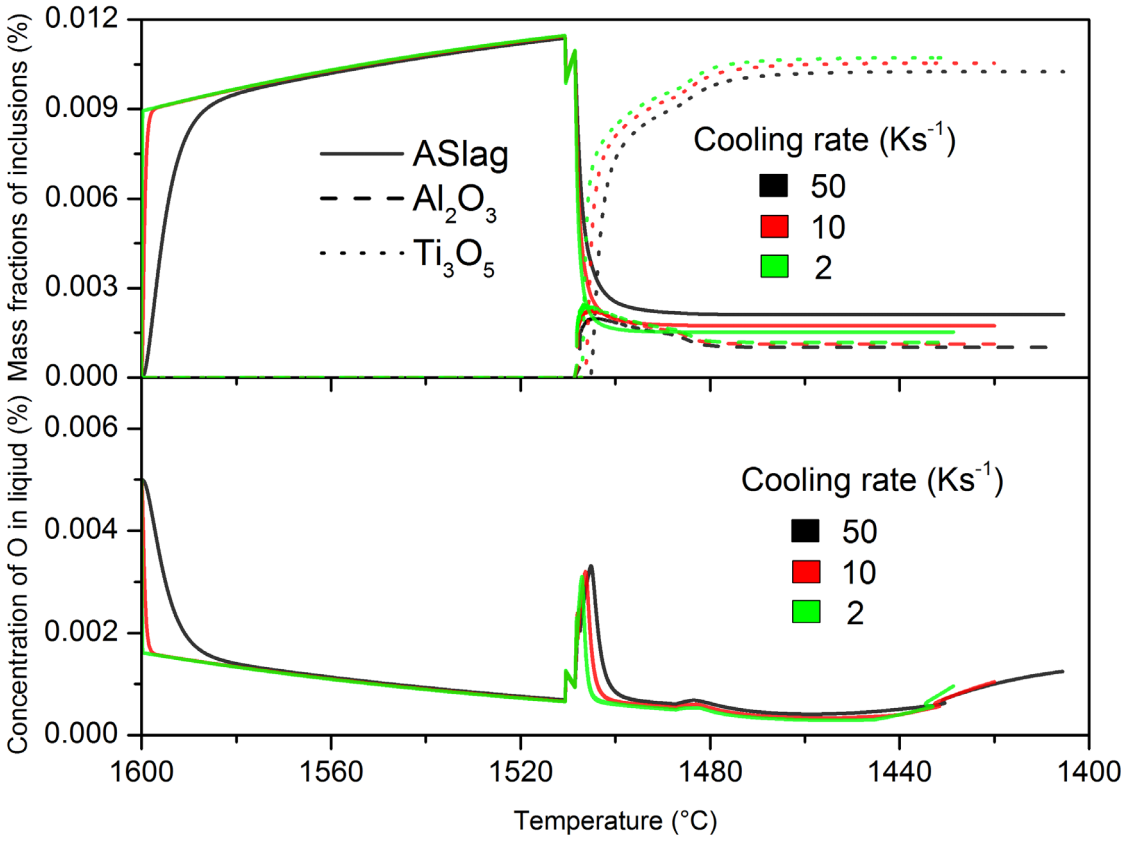

Figure 5.33. Influences of cooling rate on the oxides formation and oxygen concentrations changes.

Figure 5.34 shows the influence of cooling rate on the size distributions of the oxides. Figure 5.34 (a) presents the predicted size distributions of ASlag. With decreasing cooling rate, the maximum diameter of the particles increases from 2.5 to 7.7 µm and the peak number density reduces from appropriate 4×10^4 to 2×10^3 mm^{-3} and the corresponding size enlarges from 0.78 to

2.5 μm. For Al_2O_3 (Figure 5.34 (b)), the peak number density for a cooling rate of 50 Ks^{-1} is much larger than the other predictions but the corresponding size is smaller (about 0.23 μm). The calculated largest diameters are 0.78, 1.35 and 2.5 μm under the cooling rates of 50, 10 and 2 Ks^{-1}, respectively. Figure 5.34 (c) shows that the sizes of Ti_3O_5 with the largest number density are 0.78, 1.35 and 2.5 μm under the cooling rates of 50, 10 and 2 Ks^{-1}, respectively. With the decreasing cooling rates, the peak number densities of Ti_3O_5 significantly decrease and the maximum diameter increases. In common, the size distributions of all the three oxides become more flat and the size ranges broaden under the slower cooling conditions.

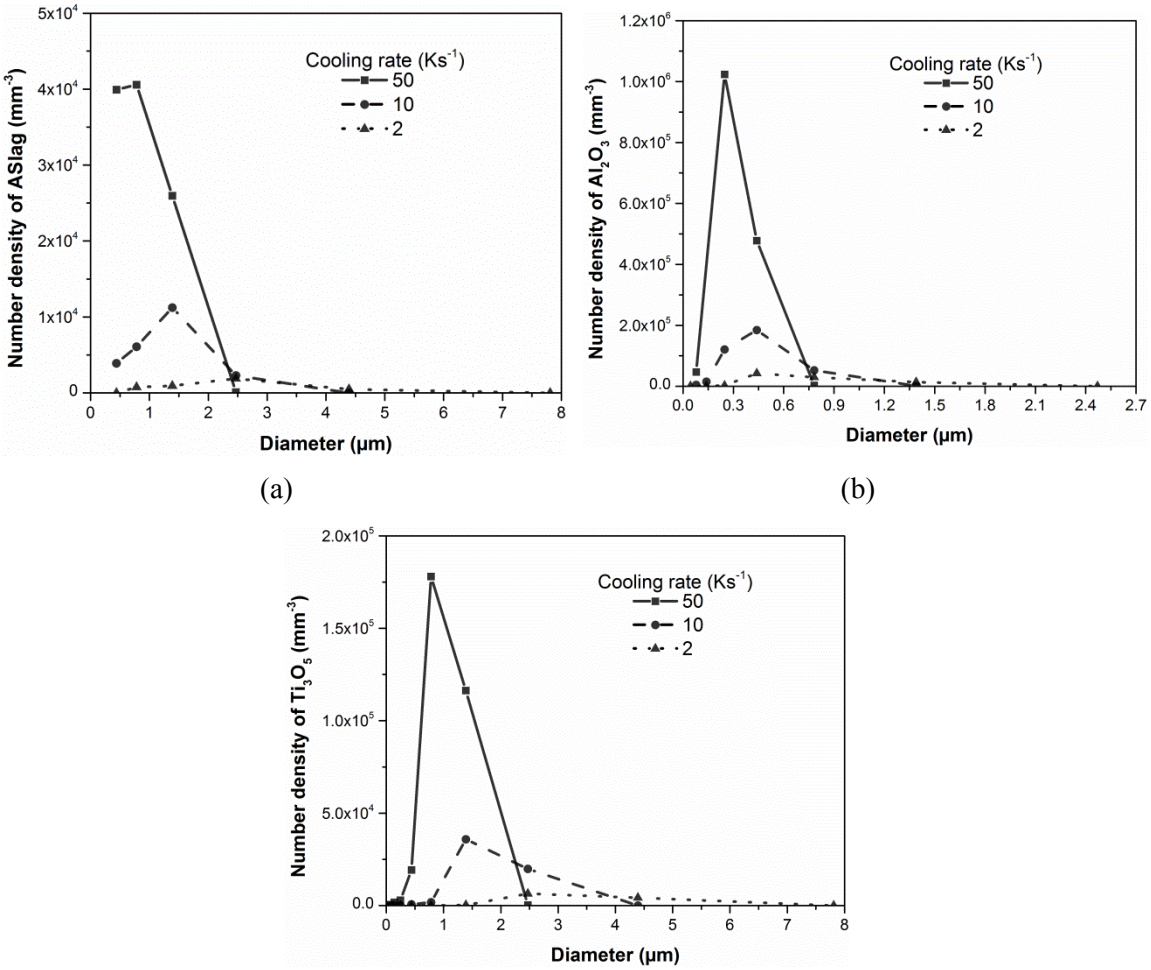

Figure 5.34. Influences of cooling rate on size distributions of (a) ASlag (b) Al_2O_3 and (c) Ti_3O_5.

Figure 5.35 shows the changes of total number and mean diameter of the oxides predicted under the different cooling rates. The figure shows that commonly for all the oxides the total number decreases and the mean diameter enlarges with the lower cooling rate. In details, from Figure 5.35 (a) the mean diameter of ASlag increases from about 0.75 to 2.4 μm with lowering the cooling rate from 50 to 2 Ks^{-1}, while the number density reduces from 1.1×10^5 to 5×10^3 mm^{-3}. Compared with ASlag, under the various cooling rates, the mean diameters of Al_2O_3 are much smaller but with more than 10 times larger number densities, respectively, as shown in Figure

5.35 (c). For Ti_3O_5, when lowering the cooling rate from 50 to 2 Ks^{-1}, the mean diameter increases from 0.9 to 3.1 μm, while the number density decreases to about 1000 mm^{-3}.

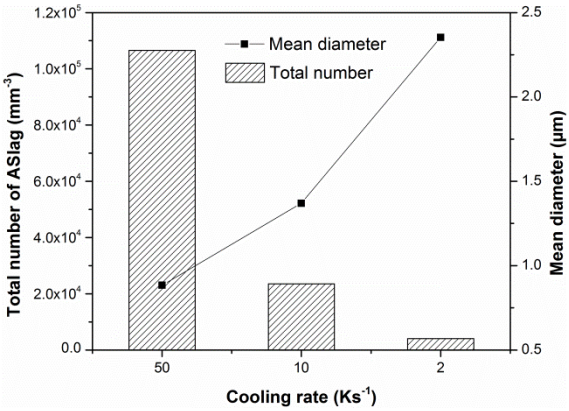

(a)

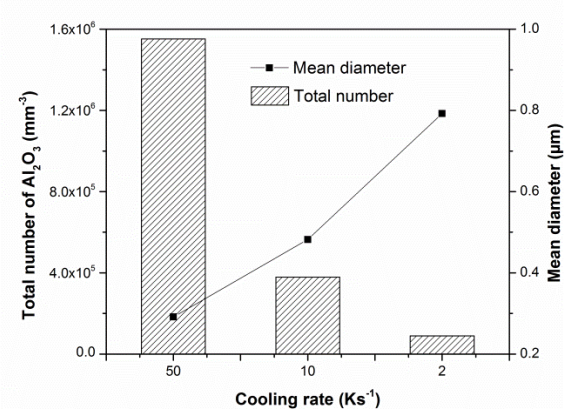

(b)

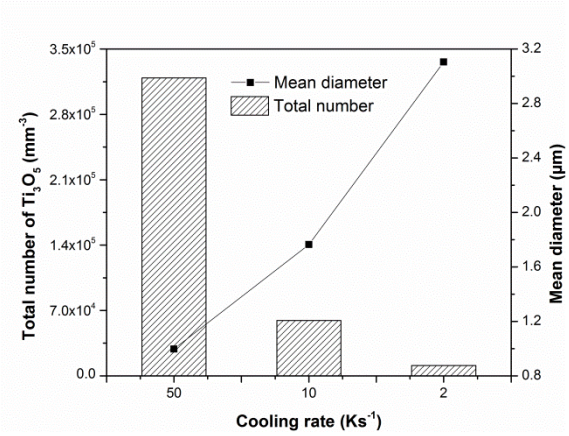

(c)

Figure 5.35. Influences of cooling rate on the number and mean diameter of (a) ASlag, (b) Al_2O_3 and (c) Ti_3O_5.

Combining the above discussions, it is concluded that the variations of cooling rate have little influence on the final inclusions mass fraction but play significant role on the size distributions. The particles under higher cooling rate have less time to grow as referred in Eq. (3.25). This leads to the enrichments of the solutes and increases the supersaturation of the oxides formation. Under given temperature, the higher supersaturation results in larger nucleation rate and number density. Thus, it is helpful to intensify the cooling for achieving fine dispersed oxides, which is beneficial to both grain refining and a minimization of negative effects of inclusions. Acicular ferrite is also promoted by particles with a certain size and composition. Under the cooling rate of 50 Ks^{-1}, a large number of titanium oxides can be generated with the mean diameter of 0.75 μm in the steel which act further on as favorable nucleation sites for acicular ferrite [86,87,194,197]. However, the large number densities of inclusions are not always desirable as they can easily cause defects [162,163]. Summing up, the performed calculations are

meaningful to define the proper cooling conditions for controlling and adjusting the number, composition and size of inclusions.

5.3.2.2 Influence of oxygen content

For studying the influence of oxygen on the formation of various oxides, another two samples with different initial oxygen contents (40 and 30 ppm), but otherwise, the same composition as steel M2 are calculated under the cooling rate of 10 Ks^{-1}. Together with the former calculated M2, the predictions are compared in Figure 5.36, Figure 5.37 and Figure 5.38.

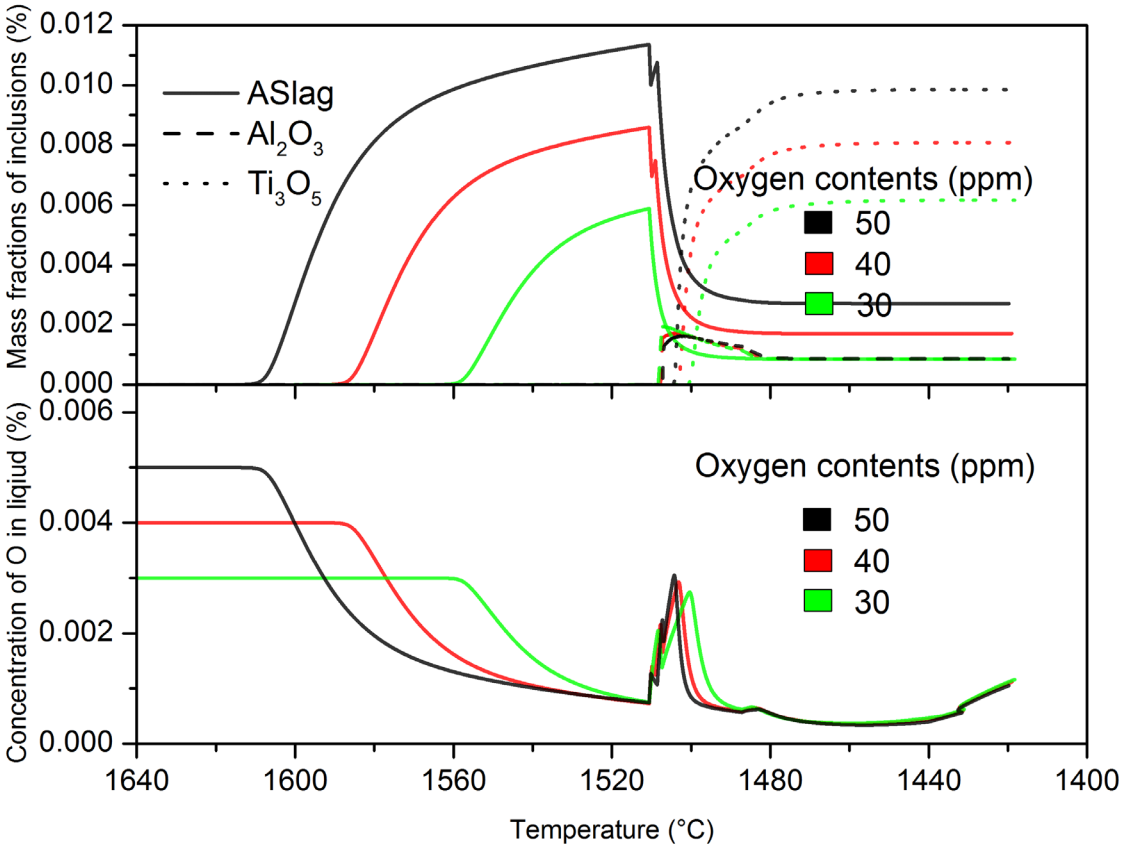

Figure 5.36. Influences of oxygen content on the oxides formation and oxygen concentrations changes.

Figure 5.36 compares the changes of oxides mass fractions and oxygen concentrations during cooling and solidification. With the lower oxygen content, ASlag inclusions precipitate later and, as had to be expected, the mass fraction of formed ASlag is lower, and the oxygen content in liquid steel changes correspondingly. At the beginning of solidification, ASlag dissolves within only ten degrees in temperature due to the thermodynamic instability. The remaining ASlag phase results again from the entrapment of particles at the liquid/solid interface. The sample containing only 30 ppm oxygen achieves finally a lower ASlag mass fraction than the others. For Al_2O_3, the oxygen amount changes in all the samples are similar: the oxygen amount rapidly reaches the maximum and then dissolves gradually, while the final mass fractions of Al_2O_3 in

the different samples are nearly the same. The amount profiles of Ti_3O_5 are similar but distinct. The amount of Ti_3O_5 increases with the increasing oxygen content. The fluctuations of oxygen concentration curves results from the amount changes of ASlag, Al_2O_3 and Ti_3O_5. In addition the dissolution of ASlag leads to the increase of oxygen concentration in the residual liquid at the beginning of the solidification. The Al_2O_3 formation causes the sharp decrease of dissolved oxygen, and after Al_2O_3 becomes unstable, the oxygen concentration increases again until the formation of Ti_3O_5 starts.

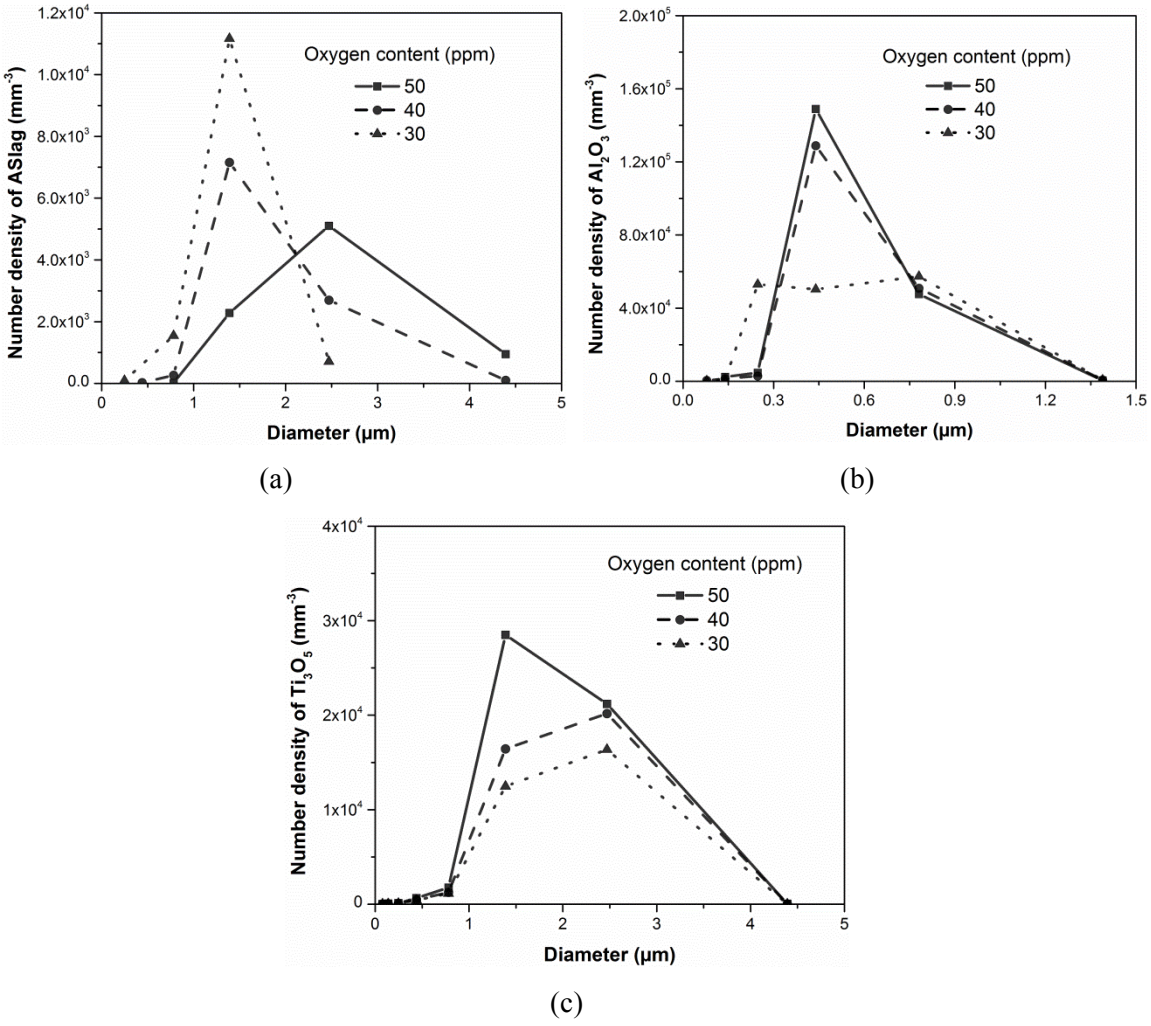

Figure 5.37. Influences of oxygen content on size distributions of (a) ASlag, (b) Al_2O_3 and (c) Ti_3O_5.

In Figure 5.37, the influence of oxygen content on size distributions of the oxides after solidification are presented. Figure 5.37 (a) shows that the maximum number densities of ASlag decrease with the increasing oxygen content, while their corresponding sizes enlarge from 1.5 μm to 2.5 μm. The maximum size of ASlag in the sample containing 30 ppm oxygen is 2.5 μm, while the largest particles in the samples with higher oxygen content are in a diameter range of 4.4 μm. Figure 5.37 (b) shows that the peak number density of Al_2O_3 decreases with the lower oxygen content. The corresponding particle sizes range in the same diameter of

approximate 0.45 μm. The size ranges of the Al_2O_3 particles in the three cases are also similar (from 0.08 to 1.35 μm). Figure 5.37 (c) displays that the number density of Ti_3O_5 decreases with the decreasing oxygen content while the size with the largest number increases from 1.5 μm to 2.5 μm. The maximum sizes in the different samples are the same with a diameter of 4.5 μm.

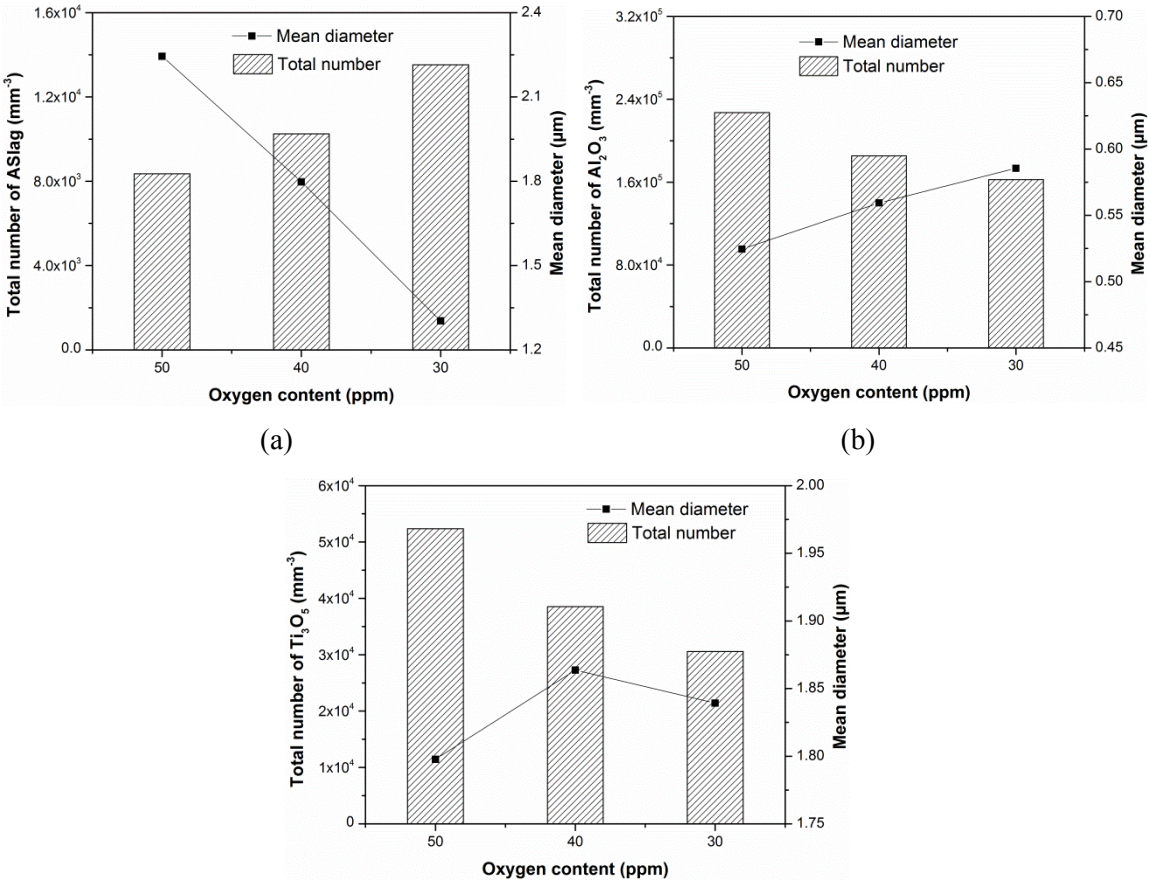

Figure 5.38. Influences of oxygen content on number and mean diameter of (a) ASlag, (b) Al_2O_3 and (c) Ti_3O_5.

Figure 5.38 displays the influence of oxygen content on the total number and mean diameter of the oxides. Unlike the cooling rate, there are no general effects of oxygen content on the total number and mean size for the different oxides. For ASlag (Figure 5.38(a)), the increasing oxygen content leads to large mean diameter and less number density. In contrast to ASlag, with the more oxygen in the samples, Al_2O_3 has higher number density and smaller but close size (Figure 5.38(b)). As shown in (Figure 5.38(c)), Ti_3O_5 has a similar trend that the total number increases with the higher oxygen content and the mean diameters are close (from 1.8 μm to 1.9 μm).

On Figure 5.36, Figure 5.37 and Figure 5.38, the influences of oxygen content on the oxides formation can be explained by the mechanisms of competitive nucleation and growth. With the increasing oxygen content in the samples, ASlag starts to form at significantly higher

temperature. From Eq. (4.29), oxygen diffuses faster at higher temperature. This leads to a faster growth of ASlag particles in the sample containing more oxygen. In the meantime, the growth of ASlag is more favorable than the nucleation in the sample with higher oxygen content as illustrated in Figure 5.39. In this example, the size and number evolutions of ASlag in the samples with 50 and 30 ppm oxygen are compared. For the both cases, ASlag can nucleate and increase in size during the temperature periods; the temperatures decrease by 5 °C under the same cooling rate which ensures the evolution time of ASlag is the same. It shows that the size distribution of ASlag in the sample with 50 ppm oxygen at 1605 °C is similar to that in the sample containing 30 ppm oxygen at 1555 °C. When the temperature decreases from 1605 to 1600 °C, ASlag in the sample with 50 ppm oxygen significantly grow up with the limited increase in number: the size with the largest number density almost become twice and the number density increase just by 30%. In contrast, in the sample with 30 ppm oxygen, after cooling down 5 °C, the peak number density of the particles becomes 2.2 times of the former value and the corresponding diameter remains. From the comparison of these two cases, at higher formation temperature, ASlag is more probable to increase in size than nucleate. In addition, ASlag in the sample with more oxygen precipitate earlier and have longer time to grow which also contributes to its larger size. Based on the above discussion, it is reasonable to find that the total number of ASlag decreases and the mean diameter increases with the increasing oxygen content. In addition, the size distribution of the particles trapped by the solid steel can reflect their characters in the formation process due to the assumed homogeneous distribution in the residual liquid even though the particles experience the dissolution. For the cases of Al_2O_3 and Ti_3O_5 which form during the solidification process, the oxides in the samples containing different oxygen contents start to precipitate at quite close temperature, respectively. From Eq. (3.7), in the sample with higher oxygen content before nucleation (Figure 5.36), the supersaturation and driving force for the oxides formation are higher. This leads to the smaller nucleation barrier as referred in Eq. (3.15). From Eq. (3.16), under the given temperature, the less critical nucleation energy change enlarges the nucleation rate. Thus, the number densities of Al_2O_3 and Ti_3O_5 increase with the increasing oxygen content. At the similar temperature, the diffusivity of the reactants is regarded as the same in different samples. The large number of particles limits the growing driving force of each single particle and further reduces the growth rate. This explains that the mean diameters of Al_2O_3 and Ti_3O_5 particles increase in the samples with less oxygen. The case of Ti_3O_5 in the sample containing 30 ppm oxygen is an exception, which has both smaller number and mean diameter compared to the situation in the sample containing 40 ppm oxygen. This is attributed to the limited oxygen amount in the residual liquid. Based on the presented results in this section, the available oxygen content which is nothing else but the total oxygen content does neither stand automatically for the total amount of various oxides nor for their number or size. According to the different objectives, it needs to specially

focus on the inclusions in different steels and the metallurgical conditions. In this selected steel, when aiming at creating the large number fine particles, the oxygen content of 50 ppm with the high cooling rate is a preferable choice. To prevent large particles, the ASlag particles formed at high temperature should be avoided; accounting both cleanness and creation the desirable oxides, 30 ppm of oxygen can be the preferable choice. The comprehensive adjustment of cooling conditions and steel compositions is the promising method on obtaining the preferable inclusions. In total, to combine a preferably high steel cleanness with the creation of specific inclusion types and sizes for microstructure evolution, comprehensive knowledge on the inclusion formation is needed.

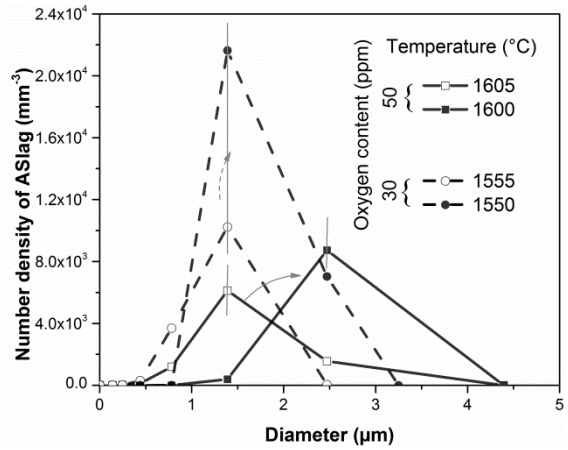

Figure 5.39. Illustration of competitive nucleation and growth in the samples with different oxygen contents.

5.4 Summary

In the present chapter, the step-wise modeling processes were separately and precisely evaluated through comparison of numerical calculation results with analytical solutions and with experimental results. The models were then applied to microsegregation calculations. Assuming the prevention of back diffusion in the solid state, the microsegregation model of Ohnaka transforms into Scheil´s equation. FactSage also offers a standard Scheil module for microsegregation calculations. The comparison of the results from the semi-integral solution of Scheil´s equation by ChemApp and the Scheil module of FactSage on the basis of identical partition coefficients proved an excellent correspondence of the results and thus the proper communication between ChemApp and FactSage.

The semi-numerically solved Ohnaka´s model with local partition coefficients and temperature dependant diffusion coefficients was subsequently used to predict the non-equilibrium solidus temperature for a wide variety of steel grades and to compare the results with Gleeble experiments. The Zero Ductility Temperature (ZDT) corresponds with sufficient precision to a calculated solid fraction close to 1.

A further way of verification of microsegregation calculations is the comparison with the results of microprobe analysis on solidified samples. In the case of Transformation Induced Plasticity (TRIP) steel with elevated manganese and aluminum content, limitations of the quality of commercial databases such as FStel or SGTE become evident. Here, a self optimized excerpt of the SGTE database on the basis of own DSC results helps to overcome the limitations and to achieve an acceptable correspondence between measured and calculated enrichment. The combining of thermodynamics from self optimized databases and solidification kinetics and inclusion kinetics in ChemApp seems to be a promising way to predict microsegregation for higher alloyed steel grades in future.

Combining inclusion kinetics with the microsegregation model, the MnS formation during solidification was simulated. Through comparing with experimental results, some parameters for this case were fitted. Finally, the fitted model was used to predict the influences of cooling rate and sulfur content on MnS formation. The good agreement of predictions and experiments illustrates the validity of the model to simulate the MnS formation during solidification process. By increasing the cooling rate, the size distribution is shifted towards smaller inclusions and the number increases significantly. The mass fraction of manganese sulfide after solidification decreases slightly with increasing cooling rate due to less enrichment of solutes. With decreasing sulfur content, the size of the particles becomes significantly smaller whereas the total number of particles remains more or less constant. Fine manganese sulfides can be achieved through intensive cooling or reduced sulfur content. This is an expected result but nevertheless the fundamental relations seem to be so well described that also results for more complex calculations are trustworthy.

When extending the single inclusion model to the model on multi-phase-inclusions formation, the thermodynamics were first evaluated by experiments. The inclusion formation thermodynamics during solidification are regarded as an independent sub-model. The predicted inclusion types, compositions and nucleation sequence for three investigated steel grades are in good agreement with the experimental results, and this indicates that the prediction of stable inclusion phases is a powerful tool for steel cleanness research.

In a further step, the nucleation kinetics was considered to predict the competitive formation of multi-phase-inclusions in selected Ti-Al-alloyed steel. For the selected steel composition and cooling conditions, ASlag (a multi-phase-oxide) is the only nucleating phase while Al_2O_3 is thermodynamically stable, but the nucleation driving force is not high enough to result in particle nucleation. During solidification, the competition of various oxides results in the dissolution of existing particles and the nucleation and growth of new particles. For the selected case, both growing and dissolving proceed fast at the initial stage and then slow down. The size ranges of all the inclusions increase with the decreasing temperature because of collision growth.

The dissolution of ASlag and Al_2O_3 leads to the appearance of relatively smaller particles and the reduction of number densities. Finally, the effect of cooling rate and oxygen content on the nucleation and growth of oxides was investigated. Cooling rates affect the mass fraction of various inclusions to a lesser extend but have an enormous influence on the size distributions. With decreasing cooling rates, the peak number densities decrease significantly whereas the maximum diameter of the oxides further increases. In contrast, higher cooling rates result in a larger number of small inclusions. The various oxygen contents lead to different evolutions of the oxides. For ASlag (again a multi-phase-oxide melt), with the increasing oxygen, the size distribution is shifted towards larger direction and the number densities reduce. The peak number densities of Al_2O_3 and Ti_3O_5 increase with higher oxygen content while the corresponding size of the particles decrease. The possible explanation for the influences of the oxygen on the oxides formation is the competitive nucleation and growth. In the case of ASlag, the higher oxygen content results in the significantly higher formation temperature and diffusivity of the reactants which increases the growth rate of the particles. Thus, the mean diameter of ASlag enlarges with the increasing the oxygen content while the total number decreases. Al_2O_3 and Ti_3O_5 in the samples containing different oxygen contents form at quite close temperature, respectively. This leads to the higher supersaturation and nucleation rate of the oxides in the samples with more oxygen. Hence, the total numbers of Al_2O_3 and Ti_3O_5 increase with the higher oxygen content, respectively. Then, the large number of particles results in the limited growth and smaller mean diameter.

The comprehensive adjusting of cooling conditions and steel compositions are the promising approach on obtaining the desirable inclusions. To combine a preferably high steel cleanness with the creation of specific inclusion types and sizes for microstructure evolution, comprehensive knowledge on the inclusion formation is needed. The calculations and the predicted trends using the proposed model can deepen the understanding on the multi-phase-inclusions formations though it is just a preliminary version. Future studies will consider the heterogeneous nucleation of different inclusions, and the corresponding experiments also will keep pace with the simulations.

6 Summary, conclusions and outlook

Inclusion engineering has been a widely investigated topic in the last decade mainly driven by the increasing requirements for steel cleanness and mechanical properties. On the one hand, it is dedicated to reduce the population of inclusions and to minimize the negative effects through controlling the compositions, size and number of inclusions; on the other hand, it works on utilizing preferable inclusions to act as heterogeneous nucleation sites and to optimize microstructures. Nonmetallic inclusions determine on the final steel microstructure and properties based on how they nucleate and grow during deoxidation, cooling and solidification of steel. With decreasing temperatures and changing chemistry in the liquid steel during solidification, commonly termed as microsegregation, transformation and dissolution of pre-existing inclusions may appear and new inclusions may nucleate. The modeling of the thermodynamics and kinetics of inclusion formation and growth before and during solidification is the main objective of the present work.

The treatment of microsegregation is a prerequisite when addressing the solidification process. Different solubilities of elements in the liquid and solid matrix results in the partitioning at the solidification interface. Solute enrichment, so-called segregation, in the interdendritic liquid causes inclusion precipitation and defect formation, such as hot tearing and macrosegregation, can further negatively influence the properties of steel products. To predict the microsegregation, analytical as well as numerical solutions exist. Analytical solutions estimate microsegregation based on several simplifying assumptions such as interface advance velocity, dendrite geometry and back diffusion in the matrix. Numerical solutions give more freedom to physical phenomena and can simultaneously predict concentrations in different positions. Compared to numerical solutions, an analytical solution is easier to handle which explains its wide application. However, there the analytical models still need to be further developed: partition and diffusion coefficients should be composition and temperature dependent instead of constant; preferable equilibrium temperature is calculated under the multi-components and multi-phases consideration rather than on the basement of the Fe-C binary phase diagram; and the influence of precipitation of inclusions in the solidification process should be considered.

Depending on the steel composition, various types of inclusions normally generate from different chemical reactions and metallurgical processes. From the specific view of researchers, inclusions were classified according to their composition, sources, formation period and size. Various inclusions play both negative and positive roles on steel properties. To control and utilize the inclusions, the availability of thermodynamics data and the understanding of the kinetics of inclusion nucleation and growth are fundamental. Thermodynamics defines the

stability of inclusions using Gibbs energy functions. Since introducing the CALPHAD method, the rapid development of databases and software made a great difference in the field of thermodynamic calculations. The chemical composition and stability of phases were well predicted. The computational thermodynamics offer a powerful tool to investigate inclusion formation under equilibrium conditions. At the same time, equilibrium calculation provides the chemical driving force for nucleation, growth and dissolution kinetics. Kinetics explains the inclusion nucleation rate including the changes of the number density and size. Classical nucleation theory is valid and widely applied to describe the nucleation behavior in a condense system. For particle growth, several mechanisms were provided such as diffusion controlled growth and coarsening. The influence of collision should also be considered in a liquid system. For competitive growth of a multi-phase-inclusions system, it is necessary to consider the dissolution of less stable inclusions. Based on the fundamentals of inclusion formation, a variety of models were developed and applied. For a broad field of examples, the calculated results correspond well to the measurements; this performance certainly explains the frequent use and popularity of these models on inclusion investigations. Meanwhile, the models can be further improved and extended: the coupling between microsegregation and inclusion formation needs unified thermodynamics; carefully adjusted databases are desirable; collisions of the inclusions cannot be neglected; competitive formation of multi-phase-inclusions are necessary in not only solidification but also the cooling process; and dissolution combined with growth should also be considered.

In the present thesis, the progressive modeling on microsegregation and inclusion formation in the cooling and solidification process of steel was carried out. The core concept of the work is the coupling of metallurgical models with thermodynamic databases. During the programming, FORTRAN was applied as the coding language; ChemApp bridged the metallurgical model and thermodynamic databases; FactSage offered the powerful databases through an output ChemSage datafile. As a first step, a microsegregation model linked with thermodynamic databases was presented based on Ohnaka´s model [10]. In the model, thermodynamic equilibrium is calculated by ChemApp with the database FSstel, from FactSage Version 7.0, which allows the consideration of multicomponent effects and inclusion formation. Thus, more reasonable equilibrium partition coefficient and liquidus temperature were calculated at each solidification step. At the same time, the temperature dependant diffusion coefficients were considered. The peritectic reaction during solidification is implemented by referring to the stability of ferrite and austenite at the liquid/solid interface. Encompassing the model description, the reasonability of parameter selections were well illustrated through the systematic parameters study. Subsequently, a single-phase inclusion (MnS) model coupled with the proposed microsegregation model was developed. In the model, the nucleation, growth and collision of inclusions were considered. The influences of the characteristic parameters in this

model, including step values, interfacial energy, pre-exponent and collision factors on the simulations were investigated. The parameter study provides the fundament for further fitting calculations and applications. Finally on the basement of the single inclusion model, the comprehensive model on multi-phase-inclusions formation during cooling and solidification was programmed. The multi-phase-inclusions formation thermodynamics were basically modeled as a sub-model. The thermodynamic model comprising the microsegregation calculation provides the thermodynamic properties of inclusions to the comprehensive model. The competitive nucleation, growth and dissolution of various oxides were further considered in the comprehensive model.

6.1 Results and conclusions

As the primary part of the present modeling work, the microsegregation model was thoroughly examined. To assure the proper 'communication' among FactSage, ChemApp and the Fortran source codes, the calculations using the present model were compared with those from FactSage. The perfect agreement of the concentrations of various solutes and temperature profiles demonstrated the good connection of the different modules and the stability of the chosen algorithm. Then comparing with the predictions from Lever Rule and Scheil´s [9] model, the solute enrichment in the residual liquid from the current model exhibited their reasonability. Finally, measured Zero Strength (ZST) and Zero Ductility Temperatures (ZDT) from Gleeble experiments were utilized to verify the calculation results for a wide range of steel compositions. As a whole, the above tests illustrate that the proposed model can reasonably predict the microsegregation of steels. In addition to being applied to further model development, the microsegregation model can provide feedback to the database optimizations. As an example, the calculations with both commercial and in-house optimized databases for selected TRIP steel were compared with the experimental results. The predictions using the in-house optimized database are more close to the measured results which indicates the benefits and necessity of the further improvement on databases.

On the single inclusion (MnS) formation, the adjustable parameter -collision factor (f)- in the model was fitted to experimental results of SSCT experiments. The agreement of the mean diameter, total number and the size distribution between measurement and calculation assured that the collision factor of 200 is appropriate to the simulation of the SSCT experiments. The model with the defined parameters was further applied to study the influences of the cooling rate and sulfur content on the MnS formation. From the comparison between calculations and experimental results the following conclusions are drawn:

- The suggested comprehensive model can be applied to simulate the formation of manganese sulfide during solidification. The calculated size distribution of manganese sulfide fits well with experimental results. The influences of sulfur contents and cooling

rates on manganese sulfide formation were well predicted and agree with the experimental results.

- Under increasing cooling rate, the size distribution is shifted towards smaller inclusions and the total number clearly increases. The content of manganese sulfide decreases a bit due to less enrichment of solutes.
- With decreasing sulfur content, the size of the sulfides increases whereas the total number remains fairly constant. The mass fraction significantly increases. Finer manganese sulfide can be achieved through intensive cooling or reduced sulfur content.

When extending single phase inclusion to the multiphase ones, the thermodynamics behind the formation of inclusions was first evaluated. The algorithm of direct coupling of microsegregation and multi-phase-inclusions formation based on a thermodynamic database were tested using overall mass balances. For a Ca-Al containing steel the consistency of the mass balance is in an acceptable range. The inclusions compositions, types and formation sequence were confirmed using dedicated experimental results. This procedure serves also for checking the sub thermodynamic model. Combining the calculations and measurements, the following can be concluded:

- The suggested model can thermodynamically describe the inclusion formation during solidification. The inclusion types and compositions can be predicted well. Through analysis of the calculated precipitation process, the character of the inclusions in the final solidified steel can be understood.
- The proposed model is not yet able to consider heterogeneous nucleation. The order of inclusion formation can be predicted, however, which can indirectly be used to explain the formation of heterogeneous inclusion types.

With reliable thermodynamics, the kinetics on competitive formation of multi-phase-inclusions was further considered and a comprehensive model was developed. The model is a preliminary model which contains the core concept of the single-phase inclusion model under consideration of the inclusion dissolution. The entire process of inclusion formation in the cooling and solidification process is considered. An illustrative example of a Ti-Al alloyed steel was calculated using the proposed model. The effects of cooling rate and oxygen content on the multi-phase-inclusions formation were investigated. The results are summarized as the following:

- In the selected steel, ASlag (a liquid multi-components oxide) is the only existing inclusion in the cooling process while the chemical driving force of Al_2O_3 nucleation is insufficient. The amount of all the inclusions increases rapidly at the initial stage of formation. With the decreasing temperature and segregated concentrations, ASlag

rapidly dissolves and Al_2O_3 becomes stable. Then, the stronger stability of Ti_3O_5 results in the dissolution of Al_2O_3. At the initial stages of nucleation, the size distributions of the inclusions concentrate in a narrow size range with relative large number density. Then the size ranges enlarge with decreasing peak number densities.

- The cooling rate has significant effects on the size and number densities but little influence on the total oxides amount. With the decreasing cooling rate, for all the oxides, the size distribution curves become more flat; the total numbers reduce and mean diameters also enlarge.
- The oxygen content influences the various oxides formation in different ways due to the competitive nucleation and growth. With the increasing oxygen content, ASlag precipitates at higher temperature and grows faster, which further results in the larger size and less number density; for Al_2O_3 and Ti_3O_5, the oxides form at close temperature in the different samples with the higher supersaturation and nucleation rate, which turns be the larger total number and smaller size.

From the simulations and corresponding results, the modeling work in this thesis is quite meaningful for investigating microsegregation and inclusion formation. With the reliable predictions of solutes enrichments, the changes of inclusions, including the chemistry, size and number, are better calculated. The investigations on the related metallurgical parameters can offer valuable references on inclusion engineering and further to improve the qualities of steel products.

6.2 Outlook

This thesis is a primary work on coupled modeling of microsegregation and inclusion formation based on thermodynamic databases. For further enhancement of the models and broad applications, the following aspects are recommended to be focused on:

- Besides general carbon steel, microsegregation of high alloy steel is another important research topic. Due to the high solute concentrations, the influence of the most parameters would be magnified. Hence, parameters in the current model need necessarily to be further investigated, comprising partition coefficients, transformation temperatures and diffusion coefficients. Commercial databases will need to be optimized for better describing the thermodynamic equilibrium of high alloy steels. In the cleanness and casting research group at the Chair of Ferrous Metallurgy, the optimization work is based on extensive DSC measurements. The correspondence between the microsegregation model and the experiments is beneficial to check the validity of the optimized databases. In the meantime, the influence of solute concentrations and the interaction between dissolved elements with respect to solute diffusion should also be considered.

- The present microsegregation model and calculated results can be applied to simulate the solidification process under consideration of heat transfer and solid phase fractions. The simulation of a casting process is achievable.
- To precisely estimate the amount of inclusions in the residual liquid, the behavior of inclusions at solid/liquid interface requires deeper understanding. The interfacial energy between inclusions and solid, liquid matrix are needed not only for this case, but also for the nucleation process.
- It is common to find heterogeneously nucleated inclusions in steel. Further consideration regarding the consideration of heterogeneous nucleation on pre-existing inclusions is necessary. Also, the choice of heterogeneous nucleation sites for the inclusions is another challenge for modeling of inclusion formation. Then, the types (both homogeneous and heterogeneous ones), size distribution and amount of inclusions are more close to the real situation.
- The collision factor of manganese sulfide for one steel composition and specific experimental conditions should be fitted using the size distribution and number densities before application. When dealing with measurements, the small size particles need a second consideration because they can be the precipitations from solid steel. Hence, an ambitious idea is to develop the model accounting subsequent coarsening and precipitation processes in solid.
- The calibration of the multi-phase-inclusions formation model is more complex than for single-phase manganese sulfide. For instance, besides the aforementioned heterogeneous nucleation, the transient phenomenon of inclusion formation should also be considered when performing corresponding experiments. Nevertheless, it is necessary to face the simulations to well established experiments for broader applications.

As a whole, the present models offer a primary tool and method for investigating the microsegregation and inclusion formation during cooling and solidification, and further development and research studies can be carried on the basis of this work.

Bibliography

[1] R. Kiessling. *Clean Steel: a debatable concept*, Met. Sci., 1980, **14**: 161–172.

[2] J. Takamura, S. Mizoguchi. *Metallurgy of Oxides in Steels. I. Roles of Oxides in Steels Performance*, The Sixth International Iron and Steel Congress, 1990: 591–597.

[3] S. Mizoguchi, J. Takamura. *Metallurgy of Oxides in Steels. II. Control of Oxides as Inoculants*, The Sixth International Iron and Steel Congress, 1990: 598–604.

[4] Y. Kang, C. Chang, S. Park, S. Khn, I. Jung and H. Lee. *Thermodynamics of inclusions engineering in steelmaking and refining*, Iron & steel technology, 2006, **3**: 154–162.

[5] Ø. Grong, L. Kolbeinsen, C. van der Eijk and G. Tranell. *Microstructure Control of Steels through Dispersoid Metallurgy Using Novel Grain Refining Alloys*, ISIJ Int., 2006, **46**: 824–831.

[6] O. Wijk. *Inclusion engineering*, 7 th International Conference on Refining Processes, 1995: 35–67.

[7] H. D. Brody, M. C. Flemings. *Solute redistribution in dendritic solidification*, Transactions of the Metallurgical Society of AIME, 1966, **236**: 615–624.

[8] G. H. Gulliver. *The quantitative effect of rapid cooling upon the constitution of binary alloys*, J. Inst. Met, 1913, **9**: 120–157.

[9] E. Scheil. *Bemerkungen zur schichtkristallbildung*, Zeitschrift für Metallkunde, 1942, **34**: 70–72.

[10] I. Ohnaka. *Mathematical analysis of solute redistribution during solidification with diffusion in solid phase*, Trans. ISIJ, 1986, **26**: 1045–1051.

[11] S. Kobayashi. *Solute redistribution during solidification with diffusion in solid phase: a theoretical analysis*, Journal of Crystal Growth, 1988, **88**: 87–96.

[12] T. W. Clyne, W. Kurz. *Solute redistribution during solidification with rapid solid state diffusion*, Metallurgical Transactions A, 1981, **12**: 965–971.

[13] W. Yamada, T. Matsumiya and A. Ito. *Development of simulation model for composition change of nonmetallic inclusions during solidification of steels*, The Sixth International Iron and Steel Congress, 1990: 618–625.

[14] M. Wintz, M. Bobadilla and J. Lehmann. *Microsegregation and precipitation of non metallic inclusions during solidification of steels: a modelling and experimental study*, 4 th Decennial International Conference on Solidification Processing, 1997: 226–229.

[15] M. Wintz, M. Bobadilla, J. Lehmann and H. Gaye. *Experimental Study and Modeling of the Precipitation of Non-metallic Inclusions during Solidification of Steel*, ISIJ Int., 1995, **35**: 715–722.

[16] S. K. Choudhary, A. Ghosh. *Mathematical Model for Prediction of Composition of Inclusions Formed during Solidification of Liquid Steel*, ISIJ Int., 2009, **49**: 1819–1827.

[17] J. Miettinen, S. Louhenkilpi, H. Kytönen and J. Laine. *IDS: Thermodynamic–kinetic–empirical tool for modelling of solidification, microstructure and material properties*, Mathematics and Computers in Simulation, 2010, **80**: 1536–1550.

[18] S. Nurmi, S. Louhenkilpi and L. Holappa. *Thermodynamic Evaluation of Inclusions Formation and Behaviour in Steels during Casting and Solidification*, Steel research international, 2009, **80**: 436–440.

[19] P. Rocabois, J. Lehmann, H. Gaye and M. Wintz. *Kinetics of precipitation of non-metallic inclusions during solidification of steel*, Journal of Crystal Growth, 1999, **198**: 838–843.

[20] H. Gaye, P. Rocabois, J. Lehmann and M. Bobadilla. *Kinetics of inclusion precipitation during steel solidification*, Steel research, 1999, **70**: 356–361.

[21] J. Lehmann, P. Rocabois and H. Gaye. *Kinetic model of non-metallic inclusions' precipitation during steel solidification*, Journal of Non-Crystalline Solids, 2001, **282**: 61–71.

[22] L. H. de Almeida, A. F. Ribeiro and I. Le May. *Microstructural characterization of modified 25Cr–35Ni centrifugally cast steel furnace tubes*, Materials Characterization, 2002, **49**: 219–229.

[23] T. P. Battle, R. D. Pehlke. *Equilibrium partition coefficients in iron-based alloys*, Metallurgical and Materials Transactions B, 1989, **20**: 149–160.

[24] W. Kurz, D. J. Fisher. *Fundamentals of solidification*, Trans. Tech. Publications Ltd., Switzerland, 1986.

[25] U. Feurer, R. Wunderlin. *Einfluss der Zusammensetzung und der Erstarrungsbedingungen auf die Dendritenmorphologie binarer Al-Legierungen*, Fabchbericht der Deutschen Gesellschaft fur Metallkunde, Oberursel, 1977.

[26] G. Salas, J. Ramirez, M. Noguez and T. Robert. *Dentrite arm spacing-local solidification time relationship an experimental model for a 70-30 brass and its comparison with some theoretical models*, Scripta metallurgica materialia, 1995, **32**: 295–299.

[27] M. Melo, E. Rizzo and R. Santos. *Predicting dendrite arm spacing and their effect on microporosity formation in directionally solidified Al-Cu alloy*, Journal of Materials Science, 2005, **40**: 1599–1609.

[28] R. Pierer, C. Bernhard. *On the influence of carbon on secondary dendrite arm spacing in steel*, Journal of Materials Science, 2008, **43**: 6938–6943.

[29] D. H. Kirkwood. *A simple model for dendrite arm coarsening during solidification*, Materials Science and Engineering, 1985, **73**: L1-L4.

[30] A. Mortensen. *On the rate of dendrite arm coarsening*, Metallurgical Transactions A, 1991, **22**: 569–574.

[31] H. Jacobi, K. Wünnenberg. *Solidification structure and micro-segregation of unidirectionally solidified steels*, Steel research, 1999, **70**: 362–367.

[32] M. Bealy, B. G. Thomas. *Prediction of dendrite arm spacing for low alloy steel casting processes*, Metallurgical and materials transactions B, 1996, **27**: 689–693.

[33] Y. Won, B. G. Thomas. *Simple model of microsegregation during solidification of steels*, Metallurgical and materials transactions A, 2001, **32**: 1755–1767.

[34] C. Beckermann, W. Boettinger, H. Combeau, J. Dantzig, A. Ludwig and M. Rappaz. *Solidification Course*, ESI Group, Switzerland, 2007.

[35] C. Bernhard. *Microsegregation and its importance for steelmaking*, Lecture in USTB, Beijing, 2013.

[36] G. Arth, S. Ilie, R. Pierer and C. Bernhard. *Experimental and Numerical Investigations on Hot Tearing during Continuous Casting of Steel*, Berg Huettenmaenn Monatsh, 2015, **160**: 103–108.

[37] C. Bernhard, R. Pierer and C. Chimani. *A new hot tearing criterion for the continuous casting of steel*, 5th Decennial International Conference on Solidification Processing, Sheffield, 2007, **25**: 525–530.

[38] R. Pierer, C. Bernhard. *The nature of internal defects in continuously cast steel and their impact on final product quality*, AIST Proceedings, 2010: 193–203.

[39] J. A. Dantzig, M. Rappaz. *Solidification*, EPFL press, Switzerland, 2009.

[40] T. Matsumiya, H. Kajioka, S. Mizoguchi, Y. Ueshima and H. Esaka. *Mathematical analysis of segregations in continuously-cast slabs*, Transactions of the Iron and Steel Institute of Japan, 1984, **24**: 873–882.

[41] S. Kobayashi. *Mathematical analysis of solute redistribution during solidification based on a columnar dendrite model*, Transactions of the Iron and Steel Institute of Japan, 1988, **28**: 728–735.

[42] T. Kraft, Y. A. Chang. *Predicting microstructure and microsegregation in multicomponent alloys*, JOM, 1997, **49**: 20–28.

[43] B. Sundman, B. Jansson and J. Andersson. *The Thermo-Calc databank system*, Calphad, 1985, **9**: 153–190.

[44] X. Doré. *Modelling of microsegregation in ternary alloys*, Acta Materialia, 2000, **48**: 3951–3962.

[45] Q. Du, A. Jacot. *A two-dimensional microsegregation model for the description of microstructure formation during solidification in multicomponent alloys*, Acta Materialia, 2005, **53**: 3479–3493.

[46] S. C. Michelic, J. M. Thuswaldner and C. Bernhard. *Polydimensional modelling of dendritic growth and microsegregation in multicomponent alloys*, Acta Materialia, 2010, **58**: 2738–2751.

[47] Steeluniversity: *http://www.steeluniversity.org*.

[48] S. Seetharaman. *Fundamentals of metallurgy*, CRC Press, Cambridge, 2005.

[49] AISE Steel Foundation, A. W. Cramb. *The Making, Shaping and Treating of Steel: Casting Volume*, AISE Steel Foundation, Pittsburgh, 2003.

[50] A. Ghosh. *Secondary steelmaking: principles and applications*, CRC Press, New York, 2000.

[51] R. Fandrich, H. Lüngen and C. Wuppermann. *Actual review on secondary metallurgy*, Revue de Métallurgie, 2008, **105**: 364–374.

[52] S. Seetharaman. *Treatise on process metallurgy, volume 3: industrial processes*, Newnes, Oxford, 2013.

[53] The Japan Society for the Promotion of Science. *Sourcebook, Steelmaking Data*, Gordon and Breach Science Publishers, Tokyo, 1988.

[54] E. T. Turkdogan. *Fundamentals of steelmaking*, Maney Pub, London, 1996.

[55] L. Zhang, B. G. Thomas. *State of the art in the control of inclusions during steel ingot casting*, Metallurgical and Materials Transactions B, 2006, **37**: 733–761.

[56] T. Hansén, P. Jonsson, K. Torresvoll and G. Runnsjo. *The LSHR method for determination of inclusion characteristics during steelmaking and casting*, 83rd Steelmaking Conference, 2000: 207–217.

[57] S. K. Michelic, G. Wieser and C. Bernhard. *On the Representativeness of Automated SEM/EDS Analyses for Inclusion Characterisation with Special Regard to the Measured Sample Area*, ISIJ Int., 2011, **51**: 769–775.

[58] M. C. Flemings. *(B) Formation of oxide inclusions during solidification*, International Metals Reviews, 2013, **22**: 201–207.

[59] D. S. Sarma, A. V. Karasev and P. G. Jönsson. *On the Role of Non-metallic Inclusions in the Nucleation of Acicular Ferrite in Steels*, ISIJ Int., 2009, **49**: 1063–1074.

[60] C. van der Eijk, Ø. Grong, F. Haakonsen, L. Kolbeinsen and G. Tranell. *Progress in the Development and Use of Grain Refiner Based on Cerium Sulfide or Titanium Compound for Carbon Steel*, ISIJ Int., 2009, **49**: 1046–1050.

[61] R. Kiessling, N. Lange. *Non-metallic inclusions in steel*, 1968.

[62] H. V. Atkinson, G. Shi. *Characterization of inclusions in clean steels*, Progress in Materials Science, 2003, **48**: 457–520.

[63] A. Nicholson, T. Gladman. *Non-metallic inclusions and developments in secondary steelmaking*, Ironmaking and Steelmaking, 1986, **13**: 53–69.

[64] T. Engh. *Principles of metal refining*, Oxford University Press, Oxford, 1992.

[65] Y. Murakami. *Metal fatigue: effects of small defects and nonmetallic inclusions*, Elsevier, Oxford, 2002.

[66] L. Zhang, B. G. Thomas. *State of the Art in Evaluation and Control of Steel Cleanliness*, ISIJ Int., 2003, **43**: 271–291.

[67] C. Toulouse, A. Pack, A. Ender and S. Petry. *Stable Oxygen Isotopes for Tracing the Origin of Clogging in Continuous Casting Submerged Entry Nozzles*, Steel research international, 2008, **79**: 149–157.

[68] H. Cui, Y. Bao, M. Wang and W. Wu. *Clogging behavior of submerged entry nozzles for Ti-bearing IF steel*, Int. J. Miner. Metall. Mater., 2010, **17**: 154–158.

[69] C. Eijk, Ø. Grong and J. Hjelen. *Quantification of inclusion stimulated ferrite nucleation in wrought steel using the SEM-EBSD technique*, Proc. Int. Conf. on Solid–solid phase transformations, 1999: 1573–1576.

[70] S. Morioka, H. Suito. *Effect of Oxide Particles on δ/γ Transformation and Austenite Grain Growth in Fe–0.05~0.30%C–1.0%Mn–1.0%Ni Alloy*, ISIJ Int., 2008, **48**: 286–293.

[71] H. Suito, H. Ohta and S. Morioka. *Refinement of Solidification Microstructure and Austenite Grain by Fine Inclusion Particles*, ISIJ Int., 2006, **46**: 840–846.

[72] M. Guo, H. Suito. *Influence of Dissolved Cerium and Primary Inclusion Particles of Ce_2O_3 and CeS on Solidification Behavior of Fe-0.20mass%C-0.02mass%P Alloy*, ISIJ Int., 1999, **39**: 722–729.

[73] H. Ohta, R. Inoue and H. Suito. *Effect of TiN Precipitates on Austenite Grain Size in Fe–1.5%Mn–0.12%Ti–Si(<1.1%)–C(0.05 and 0.15%) Alloy*, ISIJ Int., 2008, **48**: 294–300.

[74] P. A. Manohar, M. Ferry and T. Chandra. *Five Decades of the Zener Equation*, ISIJ Int., 1998, **38**: 913–924.

[75] I. Jung, S. A. Decterov and A. D. Pelton. *Computer Applications of Thermodynamic Databases to Inclusion Engineering*, ISIJ Int., 2004, **44**: 527–536.

[76] Y. Kang, H. Lee. *Inclusions Chemistry for Mn/Si Deoxidized Steels*, ISIJ Int., 2004, **44**: 1006–1015.

[77] N. Verma, P. C. Pistorius, R. J. Fruehan, M. S. Potter, H. G. Oltmann and E. B. Pretorius. *Calcium Modification of Spinel Inclusions in Aluminum-Killed Steel*, Metallurgical and Materials Transactions B, 2012, **43**: 830–840.

[78] M. Lind, L. Holappa. *Transformation of Alumina Inclusions by Calcium Treatment*, Metallurgical and Materials Transactions B, 2010, **41**: 359–366.

[79] E.-I. Castro-Cedeño, M. Herrera-Trejo, M. Castro-Román, F. Castro-Uresti and M. López-Cornejo. *Evaluation of Steel Cleanliness in a Steel Deoxidized Using Al*, Metallurgical and Materials Transactions B, 2016, **47**: 1613–1625.

[80] H. Wu, P. Lu, F. Yue, L. Zhou, W. Chen and D. You. *Effect of calciumtreatmenton sulfide inclusions in steel with medium sulphurcontent*, journal of University of Science & Technology Beijing, 2014, **36**: 230–234.

[81] C. Blais, G. L'Espérance, H. LeHuy and C. Forget. *Development of an integrated method for fully characterizing multiphase inclusions and its application to calcium-treated steels*, Materials Characterization, 1997, **38**: 25–37.

[82] D. Loder, S. K. Michelic. *Systematic investigation of acicular ferrite formation on laboratory scale*, Materials Science and Technology, 2016: 1–10.

[83] Q. Huang, X. Wang, M. Jiang, Z. Hu and C. Yang. *Effects of Ti-Al Complex Deoxidization Inclusions on Nucleation of Intragranular Acicular Ferrite in C-Mn Steel*, steel research international, 2016, **87**: 445–455.

[84] M. Song, B. Song, C. Hu, W. Xin and G. Song. *Formation of Acicular Ferrite in Mg Treated Ti-bearing C–Mn Steel*, ISIJ Int., 2015, **55**: 1468–1473.

[85] H. S. Kim, C. Chang and H. Lee. *Evolution of inclusions and resultant microstructural change with Mg addition in Mn/Si/Ti deoxidized steels*, Scripta Materialia, 2005, **53**: 1253–1258.

[86] J. S. Byun, J. H. Shim, Y. W. Cho and D. N. Lee. *Non-metallic inclusion and intragranular nucleation of ferrite in Ti-killed C–Mn steel*, Acta Materialia, 2003, **51**: 1593–1606.

[87] J. H. Shim, Y. J. Oh, J. Y. Suh, Y. Cho, J. D. Shim, J. S. Byun and D. Lee. *Ferrite nucleation potency of non-metallic inclusions in medium carbon steels*, Acta Materialia, 2001, **49**: 2115–2122.

[88] W. Mu, P. G. Jönsson, H. Shibata and K. Nakajima. *Inclusion and Microstructure Characteristics in Steels with TiN Additions*, Steel research international, 2016, **87**: 339–348.

[89] W. Mu, P. G. Jönsson and K. Nakajima. *Prediction of intragranular ferrite nucleation from TiO, TiN, and VN inclusions*, J. Mater. Sci., 2016, **51**: 2168–2180.

[90] W. Mu, P. G. Jönsson and K. Nakajima. *Effect of Sulfur Content on Inclusion and Microstructure Characteristics in Steels with Ti_2O_3 and TiO_2 Additions*, ISIJ Int., 2014, **54**: 2907–2916.

[91] J. M. Gregg, H. Bhadeshia. *Solid-state nucleation of acicular ferrite on minerals added to molten steel*, Acta Materialia, 1997, **45**: 739–748.

[92] A. Einstein. *Albert Einstein: philosopher-scientist*, Library of Living Philosophers, 1949.

[93] Y. B. Kang, H. S. Kim, J. Zhang and H. G. Lee. *Practical application of thermodynamics to inclusions engineering in steel*, Journal of Physics and Chemistry of Solids, 2005, **66**: 219–225.

[94] P. J. Spencer. *A brief history of CALPHAD*, Calphad, 2008, **32**: 1–8.

[95] SGTE: *http://www.sgte.org/*.

[96] Fact: *http://www.crct.polymtl.ca/fact/*.

[97] J. O. Andersson, T. Helander, L. Höglund, P. Shi and B. Sundman. *Thermo-Calc & DICTRA, computational tools for materials science*, Calphad, 2002, **26**: 273–312.

[98] R. H. Davies, A. T. Dinsdale, J. A. Gisby, J. A. Robinson and S. M. Martin. *MTDATA- thermodynamic and phase equilibrium software from the national physical laboratory*, Calphad, 2002, **26**: 229–271.

[99] L. Zhang, S. Jahanshahi, S. Sun, C. Chen, B. Bourke, S. Wright and M. Somerville. *CSIRO's multiphase reaction models and their industrial applications*, JOM, 2002, **54**: 51–56.

[100] J. Lehmann, F. Bonnet and M. Bobadilla. *Thermodynamic description of liquid steels and metallurgical slags by a generalization of the central atoms model*, Iron & steel technology, 2006, **3**: 115–123.

[101] H. Gaye, J. Welfringer. *Modeling of the Thermodynamic Properties of Complex Metallurgical Slags*, Second International Symposium on Metallurgical Slags and Fluxes, 1984, **8**: 357–375.

[102] FactSage: *http://www.factsage.com/*.

[103] Thermo-Calc: *http://www.thermocalc.com/*.

[104] C. Gatellier, H. Gaye, J. Lehmann and Y. Zbaczyniak. *Des outils thermodynamiques pour la maitrise des reactions metallaitier et le controle inclusionnaire des aciers*, Revue de Metallurgie Cahiers D Information Techniques, 1992, **89**: 887–896.

[105] J. Lehmann, H. Gaye and P. Rocabois. *The IRSID slag model for steelmaking process control*, 2nd International Conference Mathematical Modeling and Computer Simulation of Metal Technologies, 2000: 89–96.

[106] MTDATA: *http://resource.npl.co.uk/mtdata/mtdatasoftware.htm*.

[107] C. W. Bale, E. Bélisle, P. Chartrand, S. A. Decterov, G. Eriksson, K. Hack and I. H. Jung et al. *FactSage thermochemical software and databases - recent developments*, Calphad, 2009, **33**: 295–311.

[108] I. H. Jung. *Overview of the applications of thermodynamic databases to steelmaking processes*, Calphad, 2010, **34**: 332–362.

[109]M. Volmer, A. Weber. *Keimbildung in übersättigten Gebilden*, Z. Phys. Chem., 1926, **119**: 277–301.

[110] R. Becker, W. Döring. *Kinetische Behandlung der Keimbildung in übersättigten Dämpfen*, Ann. Phys., 1935, **416**: 719–752.

[111] D. Turnbull, J. C. Fisher. *Rate of Nucleation in Condensed Systems*, The Journal of Chemical Physics, 1949, **17**: 71–73.

[112] J. Frenkel. *Kinetic theory of liquids*, Oxford University Press, Oxford, 1946.

[113] J. B. Zeldovich. *On the theory of new phase formation: cavitation*, Acta physicochim, 1943, **18**: 1–22.

[114] D. A. Porter, K. E. Easterling, M. Sherif. *Phase Transformations in Metals and Alloys, (Revised Reprint)*, CRC Press, New York, 2009.

[115] J. W. Christian. *The theory of transformations in metals and alloys*, Newnes, Oxford, 2002.

[116] M. L. Turpin, J. F. Elliott. *Nucleation of oxide inclusions in iron melts*, J. Iron Steel Inst., 1966, **204**: 217–225.

[117] J. F. Elliott, M. Gleiser, V. Ramakrishna. *Thermochemistry for Steelmaking: Vol. 2. Thermodynamic and Transport Properties*, Addison-Wesley, Reading, 1963.

[118] B. C. Allen, W. D. Kingery. *Surface tension and contact angles in some liquid metal-solid ceramic systems at elevated temperatures*, Transactions of the American institute of mining and metallurgical engineering, 1959, **215**: 30–37.

[119] K. Nogi, K. Ogino. *Role of Interfacial Phenomena in Deoxidation Process of Molten Iron*, Canadian Metallurgical Quarterly, 2013, **22**: 19–28.

[120] T. Nishizawa, I. Ohnuma and K. Ishida. *Correlation between interfacial energy and phase diagram in ceramic-metal systems*, Journal of phase equilibria, 2001, **22**: 269–275.

[121] D. Turnbull. *Kinetics of Solidification of Supercooled Liquid Mercury Droplets*, J. Chem. Phys., 1952, **20**: 411.

[122] P. W. Voorhees. *The theory of Ostwald ripening*, J. Stat. Phys., 1985, **38**: 231–252.

[123] C. Zener. *Theory of Growth of Spherical Precipitates from Solid Solution*, J. Appl. Phys., 1949, **20**: 950-953.

[124] T. Hong, T. Debroy. *Time-temperature-transformation diagrams for the growth and dissolution of inclusions in liquid steels*, Scripta Materialia, 2001, **44**: 847–852.

[125] Y. Wang, J. Yang and Y. Bao. *Characteristics of BN Precipitation and Growth During Solidification of BN Free-Machining Steel*, Metallurgical and Materials Transactions B, 2014, **45**: 2269–2278.

[126] U. Lindborg, K. Torssell. *A collision model for the growth and separation of deoxidation products*, Trans. Metall. Soc. AIME, 1968, **242**: 94–102.

[127] J. Zhang, H. Lee. *Numerical Modeling of Nucleation and Growth of Inclusions in Molten Steel Based on Mean Processing Parameters*, ISIJ Int., 2004, **44**: 1629–1638.

[128] H. Lei, K. Nakajima and J. He. *Mathematical Model for Nucleation, Ostwald Ripening and Growth of Inclusion in Molten Steel*, ISIJ Int., 2010, **50**: 1735–1745.

[129] H. Tozawa, Y. Kato, K. Sorimachi and T. Nakanishi. *Agglomeration and Flotation of Alumina Clusters in Molten Steel*, ISIJ Int., 1999, **39**: 426–434.

[130] I. M. Lifshitz; V. V. Slyozov. *The kinetics of precipitation from supersaturated solid solutions*, Journal of Physics and Chemistry of Solids, 1961, **19**: 35–50.

[131] M. Suzuki, R. Yamaguchi, K. Murakami and M. Nakada. *Inclusion Particle Growth during Solidification of Stainless Steel*, ISIJ Int., 2001, **41**: 247–256.

[132] M. J. Whelan. *On the Kinetics of Precipitate Dissolution*, Metal Science, 2013, **3**: 95–97.

[133] G. Thomas, M. J. Whelan. *Observations of precipitation in thin foils of aluminium +4% copper alloy*, Philosophical Magazine, 1961, **6**: 1103–1114.

[134] G. Eriksson. *Thermodynamics studies of high temperature equilibria. 3. SOLGAS, a computer program for calculating composition and heat condition of an equilibrium mixture*, Acta chemica scandinavica, 1971, **25**: 2651–2658.

[135] C. W. Bale, P. Chartrand, S. A. Degterov, G. Eriksson, K. Hack, R. Mahfoud and J. Melançon et al. *FactSage thermochemical software and databases*, Calphad, 2002, **26**: 189–228.

[136] S. Petersen, K. Hack. *The thermochemistry library ChemApp and its applications*, International Journal of Materials Research, 2007, **98**: 935–945.

[137] L. Holappa, S. Nurmi, S. Louhenkilpi, T. Antola. *Thermodynamic evaluation for inclusion formation in high carbon and spring steels*, 7th International Conference on Clean Steel, 2007: 76-86.

[138] H. Ohta, H. Suito. *Activities in CaO-MgO-Al_2O_3 Slags and Deoxidation Equilibria of Al, Mg, and Ca*, ISIJ Int., 1996, **36**: 983–990.

[139] E. T. Turkdogan. *Nucleation, Growth, and Flotation of Oxide Inclusions in Liquid Steel*, Iron Steel Inst., 1966, **204**: 914-919.

[140] P. M. Mathew, M. L. Kapoor and M. G. Frohberg. *Manganese-Oxygen Equilibrium in Liquid Fe at 1600 C*, Arch. Eisenhuttenwesen, 1972, **43**: 865–872.

[141] S. S. Babu, S. A. David, J. M. Vitek, K. Mundra and T. Debroy. *Development of macro- and microstructures of carbon–manganese low alloy steel welds*, Materials Science and Technology, 1995, **11**: 186–199.

[142] S. S. Babu, S. A. David, J. M. Vitek, K. Mundra and T. D. *Model for inclusion formation in low alloy steel welds*, Science and Technology of Welding and Joining, 1999, **4**: 276–284.

[143] T. Hong, T. Debroy, S. S. Babu and S. A. David. *Modeling of inclusion growth and dissolution in the weld pool*, Metallurgical and Materials Transactions B, 2000, **31**: 161–169.

[144] T. Hong, T. Debroy. *Effects of time, temperature, and steel composition on growth and dissolution of inclusions in liquid steels*, Ironmaking & Steelmaking, 2013, **28**: 450–454.

[145] L. Zhang, W. Pluschkell. *Nucleation and growth kinetics of inclusions during liquid steel deoxidation*, Ironmaking & Steelmaking, 2013, **30**: 106–110.

[146] L. Zhang, W. Pluschkell and B. G. Thomas. *Nucleation and growth of alumina inclusions during steel deoxidation*, Steelmaking Conference Proceedings, 2002: 463–476.

[147] H. Goto, K. Miyazawa and H. Honma. *Effect of the Primary Oxide on the Behavior of the Oxide Precipitating during Solidification of Steel*, ISIJ Int., 1996, **36**: 537–542.

[148] H. Goto, K. Miyazawa, W. Yamada and K. Tanaka. *Effect of Cooling Rate on Composition of Oxides Precipitated during Solidification of Steels*, ISIJ Int., 1995, **35**: 708–714.

[149] H. Goto, K. Miyazawa, K. Yamaguchi, S. Ogibayashi and K. Tanaka. *Effect of Cooling Rate on Oxide Precipitation during Solidification of Low Carbon Steels*, ISIJ Int., 1994, **34**: 414–419.

[150] Z. Ma, D. Janke. *Characteristics of Oxide Precipitation and Growth during Solidification of Deoxidized Steel*, ISIJ Int., 1998, **38**: 46–52.

[151] Z. Liu, J. Wei and K. Cai. *A Coupled Mathematical Model of Microsegregation and Inclusion Precipitation during Solidification of Silicon Steel*, ISIJ Int., 2002, **42**: 958–963.

[152] Y. Ueshima, S. Mizoguchi, T. Matusmiya and H. Kajioka. *Analysis of solute distribution in dendrites of carbon steel with δ/γ transformation during solidification*, Metallurgical Transactions B, 1986, **17**: 845–859.

[153] D. You, S. K. Michelic, C. Bernhard, D. Loder and G. Wieser. *Modeling of Inclusion Formation during the Solidification of Steel*, ISIJ Int., 2016, **56**: 1770–1778.

[154] H. Bester, K. W. Lange. *Estimate of Average Values for the Diffusion of C, O, H, N and S in Solid and Liquid Fe*, Arch. Eisenhuttenwesen, 1972, **43**: 207–213.

[155] E. Schmidtmann, F. Rakoski. *Einfluss des Kohlenstoffgehaltes von 0.015 bis 1% und der Gefügestruktur auf das Hochtemperaturfesttigkeitsuns zähigkeitsverhalten von Baustählen nach der Erstarrung aus der Schmelze*, Arch. Eisenhüttenwes., 1983, **54**: 357–362.

[156] Y. M. Won, K. Kim, T. Yeo and K. H. Oh. *Effect of Cooling Rate on ZST, LIT and ZDT of Carbon Steels Near Melting Point*, ISIJ Int., 1998, **38**: 1093–1099.

[157] Y. M. Won, T. Yeo, D. J. Seol and K. H. Oh. *A new criterion for internal crack formation in continuously cast steels*, Metallurgical and Materials Transactions B, 2000, **31**: 779–794.

[158] K. Kawakami, T. Kitagawa, K. Murakami, Y. Miyashita, Y. Tsuchida and T. Kawawa. *Fundamental research on solidification involved in continuous casting of steel*, Nippon Kokan technical report overseas, 1982: 26–41.

[159] A. Kagawa, T. Okamoto. *Influence of alloying elements on temperature and composition for peritectic reaction in plain carbon steels*, Materials Science and Technology, 1986, **2**: 997–1008.

[160] M. Wolf, Proc. Concast Metall. Semin., Switzerland, 1982.

[161] J. Miettinen, A. A. Howe. *Estimation of liquidus temperatures for steels using thermodynamic approach*, Ironmaking & Steelmaking, 2013, **27**: 212–227.

[162] T. V. Shibaeva, V. K. Laurinavichyute, G. A. Tsirlina, A. M. Arsenkin and K. V. Grigorovich. *The effect of microstructure and non-metallic inclusions on corrosion behavior of low carbon steel in chloride containing solutions*, Corrosion Science, 2014, **80**: 299–308.

[163] A. B. Schmiedt, H. H. Dickert, W. Bleck and U. Kamps. *Evaluation of maximum non-metallic inclusion sizes in engineering steels by fitting a generalized extreme value distribution based on vectors of largest observations*, Acta Materialia, 2015, **95**: 1–9.

[164] G. A. Toledo, O. Campo and E. Lainez. *Influence of sulfur and Mn/S ratio on the hot ductility of steels during continuous casting*, Steel research, 1993, **64**: 292–299.

[165] M. Perez, M. Dumont and D. A. Reyes. *Implementation of classical nucleation and growth theories for precipitation*, Acta Materialia, 2008, **56**: 2119–2132.

[166] T. Nakaoka, S. Taniguchi, K. Matsumoto, S. T. Johansen. *Particle-size-grouping method of inclusion agglomeration and its application to water model experiments*, ISIJ Int., 2001, **41**: 1103–1111.

[167] Y. Ueshima, K. Isobe, S. Mizoguchi, H. Maede and H. Kajioka. *Analysis of the rate of crystallization and precipitation of MnS in a resulphurized free-cutting steel*, Tetsu-to-Hagane, 1988, **74**: 465–472.

[168] K. Oikawa, H. Ohtani, K. Ishida and T. Nishizawa. *The Control of the Morphology of MnS Inclusions in Steel during Solidification*, ISIJ Int., 1995, **35**: 402–408.

[169] M. E. Valdez, Y. Wang and S. Sridhar. *In-situ observation of the formation of MnS during solidification of high sulphur steels*, Steel research international, 2004, **75**: 247–256.

[170] G. Xia. *Untersuchungen über das mechanische Verhalten von erstarrendem Stahl unter stranggußähnlichen Bedingungen*, PHD Dissertation, Montanuniversität Leoben, Leoben, 1992.

[171]P. Atkins, J. de Paula. *Elements of physical chemistry*, Oxford University Press, USA, 2013.

[172] Y. Wang, J. Yang, X. Xin, R. Wang and L. Xu. *The Effect of Cooling Conditions on the Evolution of Non-metallic Inclusions in High Manganese TWIP Steels*, Metallurgical and Materials Transactions B, 2016, **47**: 1378–1389.

[173] P. Maugis, M. Gouné. *Kinetics of vanadium carbonitride precipitation in steel*, Acta Materialia, 2005, **53**: 3359–3367.

[174] J. Zhang, X. Xing, B. Song, X. Guo and C. Xiang. *Metallurgical physical chemistry*, Metallurgical Industry Press, Beijing, 2004.

[175] Chemical databook: *http://www.chemicalbook.com/*.

[176] M. Hillert. *Phase Equilibria, Phase Diagrams and Phase Transformations*, Cambridge University Press, Cambridge, 2007.

[177] G. Shin, T. Kajitani, T. Suzuki and T. Umeda. *Mechanical properties of carbon steels during solidification*, Tetsu-to-Hagane, 1992, **78**: 587–593.

[178] F. Weinberg. *The ductility of continuously-cast steel near the melting point-hot tearing*, Metallurgical transactions B, 1979, **10**: 219–227.

[179] C. H. Yu, M. Suzuki, H. Shibata and T. Emi. *Anomaly in Melting Behavior and Mechanical Properties of Carbon Steels Near Their Solidus Temperature*, Materials Transactions JIM, 1996, **37**: 1251–1257.

[180] H. G. Suzuki, S. Nishimura and Y. Nakamura. *Improvement of hot ductility of continuously cast carbon steels*, ISIJ Int., 1984, **24**: 54–59.

[181] T. Nakagawa, T. Umeda, J. Murata, Y. Kamimura and N. Niwa. *Deformation Behavior during Solidification of Steels*, ISIJ Int., 1995, **35**: 723–729.

[182] H. Nakata, H. Yasunaka. *Influence of Sulfur and Manganese on Hot Ductility of Steel*, Tetsu-to-Hagane, 1990, **76**: 376–382.

[183] D. J. Seol, Y. M. Won, K. H. Oh, Y. C. Shin and C. H. Yim. *Mechanical Behavior of Carbon Steels in the Temperature Range of Mushy Zone*, ISIJ Int., 2000, **40**: 356–363.

[184] P. Presoly, R. Pierer and C. Bernhard. *Linking up of HT-LSCM and DSC measurements to characterize phase diagrams of steels*, IOP Conf. Ser.: Mater. Sci. Eng., 2012, **33**: 12064.

[185] P. Presoly, R. Pierer and C. Bernhard. *Identification of Defect Prone Peritectic Steel Grades by Analyzing High-Temperature Phase Transformations*, Metallurgical and Materials Transactions B, 2013, **44**: 5377–5388.

[186] P. Ackermann, W. Kurz and W. Heinemann. *In Situ tensile testing of solidifying aluminium and Al-Mg shells*, Materials Science and Engineering, 1985, **75**: 79–86.

[187] C. Bernhard, H. Hiebler and M. M. Wolf. *Simulation of Shell Strength Properties by the SSCT Test*, ISIJ Int., 1996, **36**: S163-S166.

[188] M. Nuspl, W. Wegscheider, J. Angeli, W. Posch and M. Mayr. *Qualitative and quantitative determination of micro-inclusions by automated SEM/EDX analysis*, Analytical and bioanalytical chemistry, 2004, **379**: 640–645.

[189] P. Pistorius, A. Patadia. *The steel matrix affects microanalysis of CaO–Al_2O_3–CaS inclusions*, 8th international conference on clean steel proceedings, 2012.

[190] M. D. Higgins. *Closure in crystal size distributions (CSD), verification of CSD calculations, and the significance of CSD fans*, American Mineralogist, 2002, **87**: 171–175.

[191] M. D. Higgins. *Measurement of crystal size distributions*, American Mineralogist, 2000, **85**: 1105–1116.

[192] M. van Ende, M. Guo, E. Zinngrebe, B. Blanpain and I. Jung. *Evolution of Non-Metallic Inclusions in Secondary Steelmaking*, ISIJ Int., 2013, **53**: 1974–1982.

[193] E. Zinngrebe, C. van Hoek, H. Visser, A. Westendorp and I. Jung. *Inclusion Population Evolution in Ti-alloyed Al-killed Steel during Secondary Steelmaking Process*, ISIJ Int., 2012, **52**: 52–61.

[194] Z. Zhang, R. A. Farrar. *Role of non-metallic inclusions in formation of acicular ferrite in low alloy weld metals*, Materials Science and Technology, 2013, **12**: 237–260.

[195] J. Lee. *Evaluation of the nucleation potential of intragranular acicular ferrite in steel weldments*, Acta Metallurgica et Materialia, 1994, **42**: 3291–3298.

[196] S. K. Michelic, M. Hartl, C. Bernhard. *Thermodynamic and Experimental Study on the Modification of Nonmetallic Inclusions Through the Contact with CaO-Al_2O_3-MgO Slags*, Proc. Conf. AISTech, 2011: 618–626.

[197] D. Loder, S. Michelic. *Specific use of non-metallic inclusions for the formation of acicular ferrite structures: Thermodynamic modeling and laboratory experiments*, Clean Steel, 2015: 8–11.

[198] Y. Kang, H. Lee. *Thermodynamic Analysis of Mn-depleted Zone Near Ti Oxide Inclusions for Intragranular Nucleation of Ferrite in Steel*, ISIJ Int., 2010, **50**: 501–508.

Nomenclature

Roman Alphabet

A	Constant
A_{inL}	Interfacial area between inclusion and liquid steel
A_{inM}	Interfacial area between inclusion and mould
a	Activity
B	Constant
b	Molar fraction
C	Concentration
C_0	Initial concentration
C^*	Interfacial concentration
C_L^+	Microsegregation in a subsequent step
C'	Solute concentration after inclusion formation
ΔC_0	Concentration increase
c	Molar fraction
c^*	Constant
D	Diffusion coefficient
D_0	Maximum diffusion coefficient
d	Molar fraction
e_i^j	Interaction coefficient of solute j on i
Fo	Fourier number
f	Collision factor
f_i	Activity coefficient of solute i
f_i^L	Activity coefficient of solute i in liquid steel
f_i^S	Activity coefficient of solute i in solid steel
f_L	Liquid fraction
f_S	Solid fraction
Δf_S	Step value of solid fraction
G	Gibbs energy
G_i	Size group i
G_V^L	Volume Gibbs energy of liquid steel
G_V^{in}	Volume Gibbs energy of inclusion
ΔG	Gibbs energy change

ΔG^0	Standard Gibbs energy change
ΔG_{sol}	Gibbs energy change of solution phase
ΔG_V	Volume Gibbs energy change of inclusion formation
ΔG^*	Critical Gibbs energy change for nucleation
g	Gravitational acceleration
I	Nucleation rate
I_A	Frequency factor of homogeneous nucleation
I_B	Frequency factor of heterogeneous nucleation
J	Molar flux
K	Concentrations product
K^{eq}	Solubility product
k	Partition coefficient
k_b	Boltzmann constant
k_c	Kinetic constant
L	Liquid steel
l	Solidification length
Δl	Radius bin width
M	Molar weight
M_c	Coarsening parameter
m	Mass
m_l	Liquidus slope
Δm	Mass change
N	Inclusions number
N_A	Avogadro constant
N_{ij}	Collision frequency between particles i and j
n	Number density of inclusions
n_{class}	Number of inclusion size calsses
n_0	Number density of nucleus
n_g	Number density after growth
P	Reactant
Q	Reactant
Q_D	Activation energy for diffusion
R	Gas constant
R_C	Cooling rate
R_i	Boundary radius of size group
ΔR	Group width

r	Radius
r_0	Radius of nucleus
r_g	Radius after growth
r^*	Critical radius of nucleus
$\bar{r}$	Mean radius
$\bar{r}_0$	Initial mean radius
S	Solid steel
S_{sat}	Supersaturation
T	Temperature
T_L	Liquidus temperature
T_q	Temperature after heat flux removing
ΔT	Temperature change
ΔT_0	Decrease of the local liquidus temperature
t	Time
t_{dif}	Diffusion time
t_f	Local solidification time
V	Molar volume
v	Interface advancing velocity
v_k	Kinematic viscosity of liquid steel
x	Atom number in molecule
y	Atom number in molecule
y^*	Location of solidification interface
Z	Distance in the solidification direction
z	Diffusion direction

Greek Alphabet

α	Back diffusion coefficient
α_d	Driving force for dissolution
α_T	Turbulent coagulation coefficient
β	Dendritic model
$\beta(r_i, r_j)$	Total collision frequency of particles with radius of r_i and r_j
$\beta'(r_i, r_j)$	Nominal collision frequency of particles with radius of r_i and r_j
$\beta_B(r_i, r_j)$	Brownian motion collision frequency of particles with radius of r_i and r_j

$\beta_S(r_i, r_j)$	Stokes collision frequency of particles with radius of r_i and r_j
$\beta_T(r_i, r_j)$	Turbulent collision frequency of particles with radius of r_i and r_j
Γ	Function of back diffusion coefficient
Γ_g	Gibbs-Thomson coefficient
δ	Thickness of back diffusion layer
ε	Turbulent dissipation rate
ζ	Transformation extent
θ	Contact angle of inclusion and mould
λ_2	Secondary Dendrite Arm Spacing (SDAS)
μ	Dynamic viscosity of liquid steel
μ_i	Chemical potential for solute i
μ_i^0	Standard chemical potential of the solute i
$\mu_i^{0,S}$	Standard chemical potential of the solute i in solid steel
$\mu_i^{0,L}$	Standard chemical potential of the solute i in liquid steel
π	Circumference ratio
ρ	Density
σ	Interfacial energy
σ_{in}	Interfacial energies of inclusion with its vapor
σ_L	Interfacial energies of liquid steel with its vapor
τ	Time period
φ	Contact angle between inclusion and liquid steel
Ω	Treated back diffusion coefficient by Clyne and Kurz

Superscripts, Subscripts and indices

$\square_1$, $\square^1$	Current step
$\square_2$, $\square^2$	Subsequent step
$\square^{Al}$	Aluminum
$\square_{Al_2O_3}$	Alumina Al_2O_3
$\square_{eq}$, $\square^{eq}$	Equilibrium state
$\square\ (f_s)$	Solid fraction f_s
$\square_{hom}$	Homogeneous nucleation
$\square_{het}$	Heterogeneous nucleation
$\square_i$, $\square^i$	Solute i or index number
$\square(i)$	Index number

$\square_{in}$, $\square^{in}$	Inclusion
$\square_{inL}$	Interface between inclusion and liquid steel
$\square_{inM}$	Interface between inclusion and mould
$\square_j$, $\square^j$	Solute j or index number
$\square(j)$	Index number
$\square_L$	Liquid steel
$\square^{L1}$	Current step in liquid steel
$\square^{L2}$	Subsequent step in liquid steel
$\square^{Mn}$	Manganese
$\square_{ML}$	Interface between mould and liquid steel
$\square_{MnO}$	Manganese oxide MnO
$\square_{MnS}$	Manganese sulfide
$\square^N$	Nitrogen
$\square_{nu}$	Nucleus
$\square^O$	Oxygen
$\square_P$, $\square^P$	Solute P
$\square_Q$, $\square^Q$	Solute Q
$\square_S$	Solid steel
$\square^S$	Sulfur
$\square^{S1}$	Current step in solid steel
$\square^{S2}$	Subsequent step in solid steel
$\square_{Sol}$	Solution phase
$\square^{Ti}$	Titanium
$\square_{TiN}$	Titanium nitride
$\square_{TiO_2}$	Titanium oxide TiO_2
$\square_{Ti_2O_3}$	Titanium oxide Ti_2O_3
$\square_{Ti_3O_5}$	Titanium oxide Ti_3O_5
$\square_V$	Volumetric
$\square_\delta$	Ferrite
$\square_\gamma$	Austenite
[% □]	Concentration referred to 1% dilute solution

Acronyms

BOF	Basic Oxygen Furnace
BSE	Backscattered Electron

CALPHAD	CALculation of PHAse Diagrams
CEQCSI	Chemical EQuilibrium Calculation for the Steel Industry
CFD	Computational Fluid Dynamics
CSD	Crystal Size Distributions
DRI	Direct Reduced Iron
EAF	Electric Arc Furnace
ECD	Equivalent Circle Diameter
EDS	Energy Dispersive X-ray Spectrometer
FACT	Facility for the Analysis of Chemical Thermodynamics
IDS	InterDendritic Solidification
LF	Ladle Furnace
MPE	Multiphase Equilibrium
MTDATA	Metallurgical and Thermochemical Databank
PDF	Population Density Function
PSD	Particle Size Distribution
PSG	Particle Size Grouping
RH	Ruhrstahl Heraeus
RH-OB	Ruhrstahl Heraeus-Oxygen Blow
SDAS	Secondary Dendrite Arm Spacing
SEM	Scanning Electron Microscope
SGTE	Scientific Group Thermodata Europe
SSCT	Submerged Split Chill Tensile
TRIP	Transformation Induced Plasticity
VD	*Vacuum Degassing*
VOD	*Vacuum Oxygen Decarburization*
VAD	*Vacuum Arc Degassing*
ZDT	Zero Ductility Temperature
ZST	Zero Strength Temperature

List of Figures

List of Tables

Supplements

A Chemical compositions of steels for microsegregation calculations

Sources	[%C]	[%Si]	[%Mn]	[%P]	[%S]
Schmidtmann and Raposki [155]	0.02	0.37	1.56	0.010	0.013
	0.05	0.35	1.56	0.011	0.013
	0.10	0.34	1.52	0.012	0.015
	0.13	0.28	1.48	0.009	0.011
	0.16	0.29	1.52	0.009	0.015
	0.20	0.41	1.55	0.013	0.015
	0.27	0.32	1.55	0.011	0.013
	0.32	0.37	1.54	0.011	0.015
	0.41	0.38	1.60	0.013	0.017
	0.51	0.39	1.60	0.011	0.017
	0.59	0.40	1.62	0.011	0.017
	0.70	0.21	1.54	0.011	0.012
	0.82	0.31	1.61	0.012	0.014
	0.90	0.42	1.66	0.012	0.015
	1.00	0.32	1.56	0.013	0.015
Weinberg [178]	0.05	0.03	1.93	0.012	0.023
	0.06	0.10	2.38	0.014	0.034
	0.06	0.01	0.34	0.008	0.014
	0.12	0.09	1.13	0.010	0.021
	0.12	0.09	0.62	0.003	0.024
	0.16	0.26	0.89	0.025	0.041
	0.18	0.23	0.45	0.010	0.024
	0.34	0.30	1.03	0.032	0.042
	0.35	0.30	0.98	0.036	0.046
	0.38	0.26	0.81	0.012	0.027
	0.41	0.29	1.31	0.010	0.280
	0.44	0.13	0.73	0.035	0.045
	0.59	0.28	0.86	0.012	0.026
	0.89	0.29	0.73	0.006	0.012
	1.06	0.34	0.47	0.009	0.026

Seol and Won [183]	0.12	0.25	0.59	0.015	0.008
	0.45	0.26	0.73	0.021	0.013
	0.81	0.22	0.50	0.010	0.005
Nakagawa and Umeda [181]	0.13	0.01	1.04	0.001	0.001
	0.14	0.01	1.06	0.001	0.036
	0.14	0.02	1.06	0.098	0.001
	0.53	0.18	0.82	0.016	0.062
	0.60	0.02	1.06	0.001	0.001
	0.82	0.24	0.78	0.012	0.005
Yu and Suzuki [179]	0.003	0.06	0.64	0.05	0.007
	0.04	0.02	0.48	0.008	0.016
	0.11	-	0.34	0.016	0.006
	0.20	0.04	0.71	0.014	0.003
	0.83	0.26	0.48	0.014	0.001
Suzuki and Nishimura [180]	0.03	0.02	0.02	0.003	0.004
	0.05	0.01	0.01	0.002	0.003
	0.11	0.01	0.01	0.002	0.003
	0.15	0.01	0.01	0.002	0.003
	0.19	0.01	0.01	0.002	0.003
	0.21	0.01	0.01	0.002	0.003
	0.40	0.01	0.01	0.002	0.003
	0.61	0.01	0.01	0.003	0.003
	0.79	0.01	0.01	0.003	0.001
	0.88	0.20	0.49	0.003	0.001
	1.03	0.01	0.01	0.001	0.001
	1.33	0.01	0.01	0.001	0.001
	1.60	0.23	0.50	0.004	0.001
Shin and Kajitani [177]	0.06	0.01	1.05	0.001	0.001
	0.13	0.01	1.04	0.001	0.001
	0.18	0.01	1.06	0.001	0.001
	0.27	0.02	1.04	0.001	0.001
	0.41	0.01	1.03	0.001	0.001
	0.60	0.02	1.06	0.001	0.001
Nakata and Yasunaka [182]	0.05	0.3	0.05	0.02	0.0252
					0.0538
					0.0974

	0.18		1.00		0.1031
					0.1848
					0.1986
					0.3161
	0.20		0.27		0.0224
					0.0348
					0.0390
					0.0445
	0.23		0.60		0.0196
					0.0437
					0.0964
					0.1666
					0.1678
					0.2088
					0.2171

B Experimental methods and conditions for measuring the ZST and ZDT

Authors	Experimental methods	Cooling rate (Ks^{-1})	Strain rate (s^{-1})
Schmidtmann [155]	Gleeble, 'in-situ'	10	0.2
Weinberg [178]	Instron, 'as cast'	-	0.017
Seol [183]	Gleeble, 'in-situ'	1	0.01
Nakagawa [181]	High temperature tensile test, 'in-situ'	0.17	0.01
Yu [179]	Instron, 'as cast'	-	0.01
Suzuki [180]	Gleeble, 'in-situ'	20	5
Shin [177]	High temperature tensile test, 'in-situ'	0.17	0.01
Nakata [182]	Tensile test	10	-

C Empirical equations for estimating liquidus temperature

Authors	Equations
IDS [161]	Ferretic low alloy steel: $T_L = 1538 - (76.24[\%C] + 10.3542[\%C]^2 + 11.66[\%Si] + 4.3512[\%C][\%Si] + 5.26[\%Mn] + 0.223[\%C][\%Mn] + 1.95[\%Cr] + 0.0329[\%C][\%Cr] + 2.2[\%Mo] + 0.8451[\%C][\%Mo] + 3.58[\%Ni] + 0.8364[\%C][\%Ni] + 24.78[\%P] + 12.9409[\%C][\%P] + 32.81[\%S] + +17.7234[\%C][\%S])$
	Austenitic low alloy steel: $T_L = 1528 - (60.09[\%C] + 6.1399[\%C]^2 + 11.49[\%Si] + 5.6055[\%C][\%Si] + 4.26[\%Mn] - 0.453[\%C][\%Mn] + 2.47[\%Cr] - 1.3303[\%C][\%Cr] + 4.36[\%Mo] - 0.0701[\%C][\%Mo] + 1.97[\%Ni] - 0.5886[\%C][\%Ni] - 30.92[\%P] + 5.3494[\%C][\%P] + 33.19[\%S] + +10.09[\%C][\%S])$
Wolf [160]	$T_L = 1537.4 - (100.3[\%C] - 22.41[\%C]^2 + 13.55[\%Si] - 0.64[\%Si]^2 + 5.82[\%Mn] + 0.3[\%Mn]^2 + 1.59[\%Cr] - 0.007[\%Cr]^2 + 3[\%Mo] + 4.18[\%Ni] + 0.01[\%Ni]^2 + 4.2[\%Cu])$
Kagawa [159]	Ferretic steel: $T_L = 1534 - (48.24[\%C] + 63.04[\%C]^2 + 14.39[\%Si] + 4.88[\%Mn] + 31.83(\%P) + 37.10[\%S] + 1.04[\%Cr] + 2.6[\%Mo] + 4.69[\%Ni] + 5.32[\%Cu] + 10.24[\%Ti] + 1.46[\%Co] + 0.24[\%W]]$
	Austenitic steel: $T_L = 1491 - (36.33[\%C] - 61.9[\%C]^2 + 17.1[\%Si] + 3.32[\%Mn] + 27.07[\%P] + 30.4[\%S] + 2.61[\%Cr] + 3.25[\%Mo] + 1.6[\%Ni] + 1.7[\%Cu] + 10.17[\%Ti] + 0.86[\%Co] + 2.11[\%W])$
Kawawa [158]	$T_L = 1536 - (78.0[\%C] + 7.6[\%Si] + 4.9[\%Mn] + 34.4[\%P] + 38[\%S] + 4.7[\%Cu] + 3.1[\%Ni] + 1.3[\%Cr] + 3.6[\%Al])$